KU LEUVEN

ARENBERG DOCTORAL SCHOOL
Faculty of Science

Investigating the possible magicity of N=32,34 in exotic Ca isotopes using laser spectroscopy methods

Ronald Fernando Garcia Ruiz

Dissertation presented in partial fulfillment of the requirements for the degree of Doctor in Science

October 2015

المنارة للاستشارات

المنارة للاستشارات

Investigating the possible magicity of N=32,34 in exotic Ca isotopes using laser spectroscopy methods

Ronald Fernando GARCIA RUIZ

Examination committee:
Prof. dr. Mark Huyse, chair
Prof. dr. Gerda Neyens, supervisor
Prof. dr. Thomas Duguet
Prof. dr. Piet Van Duppen
Prof. dr. Riccardo Raabe
Prof. dr. Nathal Severijns

Prof. dr. Jonathan Billows
(The University of Manchester)

Dissertation presented in partial fulfillment of the requirements for the degree of Doctor in Science

October 2015

المنارة للاستشارات

© 2015 KU Leuven – Faculty of Science
Uitgegeven in eigen beheer, Ronald Fernando Garcia Ruiz, Celestijnenlaan 200A box 2402, 3001 Leuven (Belgium)

Alle rechten voorbehouden. Niets uit deze uitgave mag worden vermenigvuldigd en/of openbaar gemaakt worden door middel van druk, fotokopie, microfilm, elektronisch of op welke andere wijze ook zonder voorafgaande schriftelijke toestemming van de uitgever.

All rights reserved. No part of the publication may be reproduced in any form by print, photoprint, microfilm, electronic or any other means without written permission from the publisher.

ISBN

D/

المنارة للاستشارات

Acknowledgements

I would like to express my special thanks to my advisor Gerda Neyens. Her trust and encouragement has made these last four years a very pleasant and stimulating research experience. I will always be grateful for all the wonderful opportunities that I have received.

I would also like to thank to the members of my jury, Mark Huyse, Gerda Neyens, Thomas Duguet, Piet Van Duppen, Riccardo Raabe, Nathal Severijns and Jonathan Billowes. I appreciate the comments and suggestions that you provided to improve this piece of work.

I would like to acknowledge to the IKS team, Camilo Granados, Rafael Ferrer, Yuri Kudryavtsev, the members of the nuclear moments group: Ivan Budincevic, Jasna Papuga, Ruben de Groote, and especially to Hanne Heylen, Wouter Gins and Xiaofei Yang who provided an invaluable support during the last experimental campaign of my PhD work. Many thanks to the secretaries: Danielle Verachtert, Fabienne Vanalphen and Isabelle Boesmans, who always solved my innumerable administrative issues, and to all the technical staff at IKS: Bert Keyaerts, Dries Dirkx, Luc Verwilst, Ludwig Henderix and Willy Schoovaerts.

I am thankful with the members of the COLLAPS and CRIS collaborations: Deyan Yordanov, Jonathan Billowes, Kara Lynch, Kieran Flanagan, Klaus Blaum, Magda Kowalska, Mark Bissell, Rainer Neugart, Stephan Ettenauer, Wilfried Nörthershäuser. I have learned a lot from all of you. Your advice has been key to grow as a scientist. Thanks Kara for the time that you dedicated to check several parts of this manuscript. Your comments and suggestions were very much appreciated.

I would also like to thank to the other members of the ISOLDE community: Jenny Weterings, Maria Borge, Henry Stroke, Vladimir Manea, Frank Wienholtz, Valentin Fedosseev, Bruce Marsh, Sebastian Rothe, Tom Day Goodacre, Ralf Erik Rossel, the solid state team, the members of the target

المنارة للاستشارات

group, all the ISOLDE operators and the people from the workshop. Nothing would work at ISOLDE without your assistance and support. You have made my time at ISOLDE an enjoyable and fruitful experience.

During the development of this work I had the chance to discuss with several theoreticians. I would like to express my gratitude to all our collaborators from theory. Especially to Alfredo Poves, Achim Schwenk, Gaute Hagen, Javier Menendez, Thomas Duguet and Witek Nazarewicz.

Things are much easier with the support from those whom we love most. I can not express how grateful I am to my family, my parents Hernan and Praxedis, my sisters and brother Ingrid, Jennifer and Stiven, and my beloved wife Diana and her family. This journey would not be possible without the support of my great wife. We spent many sleepless nights together. Her endlessness energy and enthusiasm were my strong motivators in any moments of weakness.

When we have the freedom to do what we want we end up doing the things we love!

Ronald
October 2015, Geneva.

المنارة للاستشارات

Preface

The present work is focused on the evolution of the nuclear ground-state properties of Ca isotopes around the neutron numbers $N = 32$ and $N = 34$. Nuclear electromagnetic moments, spin and root-mean squared charge radii were obtained by using the collinear laser spectroscopy technique at the COLLAPS beam line at ISOLDE, CERN. The importance of these properties for testing modern descriptions of the nuclear force and the development of many-body methods is highlighted by comparing our experimental results with state-of-the-art theoretical calculations.
The contents of the thesis is divided in seven chapters. The general introduction of this work is summarized in Chapter 1. Chapter 2 presents an introduction to the study of nuclear electromagnetic properties and their importance in the study of nuclear structure. An extended discussion on the relevant theoretical developments on the Ca isotopes is given in Chapter 3.
Chapter 4 describes the experimental set-up, the analysis procedure of the measured optically detected hyperfine spectra for $^{40,43-52}$Ca, and how nuclear ground-state properties are extracted from the measured hyperfine parameters.

These new results on the ground-state electromagnetic moments and root-mean square charge radii up to $N = 32$ represent an important test to modern nuclear theories based on microscopic interactions derived from chiral effective field theory. In the same chapter, a brief description of laser spectroscopy and its uses for high-precision determination of nuclear structure properties of exotic isotopes is presented.

The discussion of the experimental results, and comparison with different theories are given in Chapter 5. These results have been presented in two articles that have been included in this chapter, along with a few more details on the discussion of electromagnetic moments and charge radii:

- **Ground-state electromagnetic moments of calcium isotopes**
  R. F. Garcia Ruiz, M. L. Bissell, K. Blaum, N. Frömmgen, M. Hammen, J.

المنارة للاستشارات

D. Holt, M. Kowalska, K. Kreim, J. Menéndez, R. Neugart, G. Neyens, W. Nörtershäuser, F. Nowacki, J. Papuga, A. Poves, A. Schwenk, J. Simonis, and D. T. Yordanov
Physical Review C ***91****, 041304(R) (2015)*

- **Unexpectedly large charge radii of neutron-rich calcium isotopes**
  R.F. Garcia Ruiz, M. L. Bissell, K. Blaum, A. Ekström, N. Frömmgen, G. Hagen, M. Hammen, K. Hebeler, J.D. Holt, G.R. Jansen, M. Kowalska, K. Kreim, J. Menéndez, W. Nazarewicz, R. Neugart, G. Neyens, W. Nörtershäuser, T. Papenbrock, J. Papuga, A. Schwenk, J. Simonis, K.A. Wendt and D.T. Yordanov
  Submitted to Nature Physics (2015)

While the direct observation of photons from optical hyperfine structure spectra by collinear laser spectroscopy has been successfully applied in different regions across the nuclear chart, new and striking questions remain unsolved for nuclei at the edge of existence, where only few ions per second can be produced, beyond the limits of sensitivity achieved by fluorescence detection. The exploration of our knowledge on these regions of the nuclear chart is one of the main challenges of modern experimental nuclear physics. Chapter 6 describes the progress on a sensitive technique for high-resolution laser spectroscopy applicable to Ca isotopes. A large part of the work is focused on the development of this particle detection scheme based on radioactive-detection after optical pumping (ROC), aiming to extend the laser spectroscopy measurements of Ca isotopes to $N = 34$. The design, simulations and commissioning of this new sensitive setup for collinear laser spectroscopy at the COLLAPS beam line are presented in this chapter and summarized in the form of a technical article of which a first draft is added as an appendix to this thesis:

- **A sensitive setup for collinear laser spectroscopy experiments at ISOLDE, CERN**
  R. F. Garcia Ruiz, M. Bissell, K. Blaum, R. Neugart, G. Neyens, W. Nörtershäuser, D. T. Yordanov
  To be submitted to Nuclear Instruments and Methods (2015)

The newly designed experimental setup will form part of the Versatile Ion-Polarized Techniques On-line experiment, VITO. Future applications and potential uses of this beam line for experiments based on laser-induced nuclear orientation are included in Chapter 7. Because of my involvement in the design for the new VITO beam line, I have presented an invited talk about the goals

المنارة للاستشارات

of this new experiment at the *"Fifteenth International Symposium on Capture Gamma-Ray Spectroscopy and Related Topics, CGS15, Dresden, Germany* on behalf of Alex Gottberg. The following paper was submitted for the proceedings of the conference.

- **Perspectives for the VITO beam line at ISOLDE, CERN**
  R. F. Garcia Ruiz, M.L. Bissell, A. Gottberg, M. Stachura, L. Hemmingsen, G. Neyens, N. Severijns, and the VITO Collaboration
  EPJ Web of Conferences ***93****, 07004 (2015)*

Finally, the conclusions and the impact of the present work are summarized in chapter 8.

المنارة للاستشارات

المنارة للاستشارات

Abstract

For more than a century physicists have been trying to understand the striking particularities of the atomic nucleus. Although several questions remain open for stable nuclei, our current interest for exploring the properties of exotic species has revealed new and unexpected aspects of nuclear structure. The study of nuclei at extreme conditions is not only relevant for nuclear physics, it can also provide answers to questions related to astrophysical processes such as the origin of elements in the universe and the limits of existence for nuclear matter.

Besides the complexity of the nuclear many-body problem, nuclear structure properties exhibit regular patterns at the so called "magic" numbers of nucleons. The understanding of these apparently simple structures has motivated the development of some of the most elegant models of nuclear physics. Up to now, most of these models have been successfully applied to describe the properties of nuclei in specific regions of the nuclear chart. Even though some models might have a wide range of applicability, they can describe only part of the experimental data available, and generally fail to predict new observations for isotopes far away from stability.

Understanding the properties of the atomic nucleus implies not only a reliable description of the nuclear force but also requires a proper treatment of the many-body problem. During the last few years, considerable progress has been made in both directions. Chiral effective field theory (ch-EFT) has allowed a systematic description of nuclear forces in terms of low-energy degrees of freedom, nucleons and pions, based on the symmetries of the underlying theory, quantum chromodynamics. It allows to explain naturally the hierarchy of many-body forces, and provides a consistent treatment of theoretical uncertainties. Thanks to the advances in ch-EFT, and the development of powerful many-body methods, nuclear physics has made important steps in the construction of an "effective theory of the atomic nucleus". Ab-initio calculations are now available for medium and heavy nuclei, providing an accurate description

المنارة للاستشارات

of experimental properties of doubly- and semi-magic nuclei. Here, the importance of our experimental knowledge of "magic" nuclei to test the contemporary nuclear theories.

Having two doubly-magic isotopes, ^{40}Ca and ^{48}Ca, the calcium isotopes are considered as a prime benchmark for nuclear structure, both from a theoretical and an experimental perspective. A renewed interest has been given to the neutron rich Ca isotopes, as their properties have revealed new aspects of the nuclear forces and many-body physics. Additionally, evidence of doubly-magic features in two new short-lived Ca isotopes has been recently reported in two exotic isotopes, ^{52}Ca and ^{54}Ca.

By using high-resolution bunched-beam collinear laser spectroscopy (COLLAPS) at ISOLDE, CERN, this work presents the first measurements of the ground-state magnetic moments of ^{49,51}Ca, the quadrupole moments of ^{47,49,51}Ca, and the root-mean square charge radii of ^{49,51,52}Ca. Additionally, the ^{51}Ca ground-state spin $I = 3/2$ was determined in a model-independent way.

Ground state electromagnetic moments are compared with state-of-the-art shell-model calculations using both phenomenological interactions and microscopic interactions derived from chiral effective field theory. The results for neutron-rich isotopes are in excellent agreement with predictions of interactions derived from chiral effective field theory including three-nucleon forces, while lighter isotopes illustrate the presence of particle-hole excitations of the ^{40}Ca core in their ground state.

Our measurements of charge radii are complemented by state-of-the-art density functional theory and ab-initio calculations. Ab-initio calculations can accurately reproduce the charge radii of ^{40,48}Ca, but fail to predict the large increase observed beyond $N = 28$. This discrepancy between our unexpected experimental results and the different and theoretical predictions defy the doubly-magic character of ^{52}Ca. This opens up new and intriguing question in our understanding of the atomic nucleus and the evolution of nuclear sizes for neutron-rich systems.

Our findings highlight the importance of extending these experiments further away from stability, especially for the suggested doubly-magic ^{54}Ca nucleus. With a production yield of ~ 300 ions/s, the ^{52}Ca ($N = 32$) isotope is at the limit of the optical-detection techniques. In order to extend the measurements up to ^{53}Ca (< 100 ions/s) and ^{54}Ca (< 10 ions/s), substantial modifications to the COLLAPS beam line were developed to implement a sensitive particle detection scheme. Ions initially in the ground state can be efficiently transferred to a metastable state by using multi-step optical pumping. The difference

المنارة للاستشارات

in neutralization cross section between the metastable and ground state is used to separate atoms and non-neutralized ions after passing the ion beam through a vapor cell. Finally, independent counting of atoms/ions (free of beam contaminants) by detecting the β-radiation of the decaying isotope. Therefore, the resonant signal on the laser-ion interaction is translated into a resonant signal on the β detection.

Numerical calculations of the laser-ion interaction and ion beam optics simulations were performed to choose the design of the different beam line components. The commissioning of the new experimental setup and the first experimental tests are presented.

المنارة للاستشارات

المنارة للاستشارات

Beknopte samenvatting

Reeds meer dan een eeuw pogen fysici de bijzonderheden van de atoomkern te begrijpen. Hoewel er verschillende open vragen zijn omtrent stabiele kernen, heeft onze interesse in het verkennen van de eigenschappen van exotische kernen nieuwe en verrassende aspecten van de kernstructuur onthuld. Het bestuderen van de eigenschappen van exotische, die enkel via kernreacties geproduceerd kunnen worden, is niet enkel relevant voor kernfysica, maar kan ook antwoorden bieden op vragen uit het astrofysisch domein, zoals over de oorsprong van de elementen in het universum en de bestaansgrenzen van nucleaire materie.

Naast de complexiteit van het nucleaire veeldeeltjesprobleem vertonen eigenschappen van de kern structuur regelmatige patronen rond de zogeheten "magische" aantallen van nucleonen. Het begrijpen van deze schijnbare simpele structuren motiveerde de ontwikkeling van enkele van de meest elegante modellen die de kernfysica rijk is. Totnogtoe zijn deze modellen succesvol gebruikt om eigenschappen in specifieke regio's van de kernkaart te beschrijven. Hoewel sommige modellen een brede waaier aan toepassingsmogelijkheden hebben, kunnen ze enkel een deel van de beschikbare experimentele gegevens verklaren, en slagen er in het algemeen niet in om nieuwe data voor exotische kernente voorspellen.

De eigenschappen van de atoomkern begrijpen impliceert niet alleen een betrouwbare beschrijving van de sterke kernkracht maar ook een correcte behandeling van het veeldeeltjesprobleem. Gedurende de laatste paar jaren zijn grote vorderingen geboekt voor beide aspecten. Chirale effectieve veldtheoriën (ch-EFT) staan ons toe een beschrijving te geven van de kernkrachten gebaseerd op laag-energetische vrijheidsgraden, nucleonen en pionen, rekening houdend met de symmetrieën van de onderliggende theorie, de quantumchromodynamica. Op een natuurlijke manier staat deze theorie toe om de hiërarchie van de veeldeeltjeskrachten te verklaren, en biedt een consistente behandeling van theoretische onzekerheden. Dankzij de vorderingen in ch-EFT en de ontwikkeling van krachtige veeldeeltjes methoden heeft

المنارة للاستشارات

de kernfysica belangrijke stappen gezet in de richting van een "effectieve theorie van de atoomkern". Ab-initio berekeningen zijn nu beschikbaar voor middelzware en zware kernen, met een accurate beschrijving van de experimentele eigenschappen van dubbelmagische en semi-magische kernen. Het belang van onze experimentele kennis van magische kernen om de hedendaagse theorieën te testen wordt hier geïllustreerd.

Met de twee dubbelmagische kernen, ^{40}Ca en ^{48}Ca, worden de calcium kernen als uitstekende testers voor kerntheorieën bestempeld, zowel vanuit een theoretisch als een experimenteel oogpunt. Er wordt met vernieuwde interesse naar de neutronrijke calcium isotopen gekeken, aangezien hun eigenschappen nieuwe aspecten van de kernkrachten en veeldeeltjesfysica aan het licht hebben gebracht. Daarenboven zijn er nieuwe aanwijzingen van dubbelmagisch gedrag in twee, kortlevende isotopen, ^{52}Ca en ^{54}Ca.

Door gebruik te maken van hoge resolutie gepulste bundel collineaire laser spectroscopie (COLLAPS) in ISOLDE, CERN presenteert dit werk de eerste metingen van de magnetische momenten van de grondtoestand van ^{49,51}Ca, de quadrupoolmomenten van ^{47,49,51}Ca en de gemiddelde ladingstraal van ^{49,51,52}Ca. Bijkomend is de kernspin vande grondtoestand van ^{51}Ca vastgelegd op $I = 3/2$ op een model-onafhankelijke manier.

Electromagnetische momenten van de grondtoestand worden vergeleken met 'state-of-the-art' schillenmodel berekeningen door gebruik te maken van zowel fenomenologische interacties en microscopische interacties afgeleid uit ch-EFT. De resultaten voor de neutronrijke isotopen stemmen overeen met de voorspellingen van de interacties afgeleid uit ch-EFT en rekening houdend met drie-deeltjes interacties, terwijl de lichtere isotopen de aanwezigheid van gat-deeltje excitaties in de romp van de ^{40}Ca kern in de grondtoestand illustrerem.

Onze meting van de ladingstraal worden gecomplementeerd door 'state-of-the-art' density functional theory en ab-initio berekeningen. Ab-initio berekeningen kunnen accuraat de ladingstraal van ^{40,48}Ca reproduceren, maar slagen er niet in om de grote toename die geobserveerd is na $N = 28$ te voorspellen. Deze discrepantie tussen onze onverwachte experimentele resultaten en de verschillende theoretische voorspellingen spreken het dubbelmagisch karakter van ^{52}Ca tegen. Dit laat nieuwe en intrigerende vragen toe ons begrip betreffende van de atoomkern en de evolutie van de grootte van de kern voor neutronrijke systemen.

Onze bevindingen benadrukken het belang van de studie ver van de stabiliteitsregio, vooral voor de voorgestelde dubbelmagische ^{54}Ca kern. Met een producite van ∼300 ionen/seconde ligt de ^{52}Ca ($N = 32$) isotoop aan de limiet voor optische detectietechnieken. Om de metingen tot ^{53}Ca (<100

المنارة للاستشارات

ionen/seconde) en ^{54}Ca (<10 ionen/s) door te trekken zijn grote aanpassingen gemaakt aan de COLLAPS bundellijn om een gevoelig deeltjesdetectiesysteem te implementeren. Ionen die zich initieel in de grondtoestand bevinden kunnen op een efficiënte wijze naar een meta-stabiele toestand gebracht worden door middel van multi-stap optisch pompen. Het verschil in werkzame doorsnede van de neutralisatie tussen de grondtoestand en de meta-stabiele toestand wordt gebruikt om atomen en niet-geneutraliseerde ionen te scheiden nadat de ionenbundel door een gascel gepasseerd is. Het onafhankelijk tellen van de atomen/ionen (vrij van contaminaties door andere elementen) kan gebeuren door naar de beta-straling van het vervallend isotoop te kijken. Hierdoor wordt een resonant signaal van de laser-ion interactie omgezet naar een resonantie in de beta-detectie. Numerische berekeningen van de laser-ion interactie en ionbundel optica zijn gebruikt om ieder element van de bundellijn op de correcte wijze te ontwikkelen. De inbedrijfstelling van de nieuwe experimentele opstelling en de eerste experimentele data worden hier gepresenteerd.

المنارة للاستشارات

المنارة للاستشارات

Abbreviations

CC	Coupled-Cluster
CCSD	Coupled-Cluster Singles Doubles
CERN	Centre Européen Recherche Nucléaire (European Organization for Nuclear Research)
chEFT	Chiral Effective Field Theory
COLLAPS	COLlinear LAser SPectroscopy at ISOLDE-CERN
EM	Electromagnetic
EW	Electro-Weak
GFMC	Green's Function Monte Carlo
GPS	General Purpose Separator
gs	ground state
hfs	hyperfine structure
HRS	High-Resolution Separator
IA	Impulse Approximation
IM-SRG	In-Medium Similarity Renormalization Group
ISCOOL	ISOLDE beam COOLer
ISOLDE	Isotope Separator On Line DEvice at CERN
LEC	Low Energy Constant
LO	Leading Order
MD	molecular dynamics
MEC	Meson-Exchange Currents
NCSM	No-Core Shell Model

المنارة للاستشارات

NNLO	Next-to-Next Leading Order
OPE	One-Pion Exchange
PSB	Proton Synchrotron Booster
QCD	Quantum Chromodynamics
RG	Renormalization Group
RILIS	Resonance Ionization Laser Ion Source
rms	root mean-square
ROC	Radioactive detection of Optically pumped ions after state selective Charge exchange
SCGF	Self-Consistent Green's Functions
SRG	Similarity Renormalization Group

المنارة للاستشارات

List of Symbols

Λ	Chiral symmetry breaking scale
$\rho_c(r)$	Electromagnetic charge density
e_n	Neutron effective charge
e_p	Proton effective charge
$j_i(r)$	Electromagnetic current density
$\langle r^2 \rangle$	rms charge radius
$\sigma_\mathbf{i}$	Pauli operator
$\mathbf{j}(\mathbf{r})$	Current density
$\mathbf{S_i}$	Spin operator
μ	Nuclear magnetic moment
$\psi(r)$	Nucleon wave function
$\rho(r)$	Charge density
A	Mass number
B	Quadrupole hyperfine coupling constant
$B(E2)$	Reduced transition probability
$B(Z,N)$	Binding energy for a nucleus with Z protons and N neutrons
e	Electron charge
g	Nuclear gyromagnetic factor ($\equiv \mu/I$)
$g_L^{(i)}$	Orbital gyromagnetic ratio of the ith nucleon

المنارة للاستشارات

$g_S^{(i)}$	Spin gyromagnetic ratio of the ith nucleon
I	Nuclear spin
J	Atomic angular momentum
K_{NMS}	Normal mass shift
K_{SMS}	Specific mass shift
M_{lm}	Magnetic multipole moments
N	Neutron number
$P_l(\theta_i)$	Legendre polynomial
Q_{lm}	Electric multipole moments
r_{pp}	Point-proton radius
S_{2n}	Two neutron separation energies
S_{2p}	Two proton separation energies
S_n	One neutron separation energies
T	kinetic energy operator
V	Potential for a given A number of nucleons
$Y_{lm}(\theta_i, \phi_i)$	Normalized spherical harmonic
Z	Proton number

المنارة للاستشارات

Contents

Abstract vii

Contents xix

List of Figures xxiii

List of Tables xxxiii

1 Introduction 1

2 Nuclear structure and the quest for understanding the calcium isotopes 5

2.1 Evidence of shell structures in the nucleus 5

2.2 The multiple “magicity” of Ca isotopes 9

3 The nuclear many-body problem 15

3.1 Generalities of the many-body problem 16

3.2 The nuclear force 17

3.2.1 Phenomenological potentials 17

3.2.2 Chiral effective field theory 19

3.3 Shell-model theories 22

3.3.1 Phenomenological interactions 23

المنارة للاستشارات

3.3.2 Microscopic interactions 24
3.4 *Ab-initio* calculations 29
3.4.1 The frontier of *ab-initio* calculations 29
3.5 Electro-weak currents and effective operators 32
3.5.1 Impulse approximation (IA) 33
3.5.2 Nucleon-nucleon interaction and electro-weak currents . 35
3.5.3 Chiral electro-weak currents 36

4 Collinear laser spectroscopy: Optical detection. 41
4.1 From the atom to the nucleus 41
4.1.1 Hyperfine structure 42
4.2 Experimental Setup 44
4.2.1 COLLAPS beam line 45
4.3 Hyperfine spectra of Ca isotopes 48
4.4 Data Analysis 48
4.4.1 Kepco amplification factor 50
4.4.2 HFS fitting procedure and error estimation 51
4.4.3 ISCOOL voltage calibration 54
4.5 Spin determination of ^{51}Ca 57
4.6 Hyperfine Structure Parameters and Nuclear moments 58
4.7 Isotope Shifts and Charge radii 62

5 Discussion of experimental results 65
5.1 Electromagnetic moments 65
5.1.1 Article I: Ground-State Electromagnetic Moments of Calcium Isotopes 65
5.1.2 Configuration mixing in ^{51}Ca and wave function composition 73

المنارة للاستشارات

5.1.3 Comments on the effective operators 75
5.2 Nuclear charge radii 78
5.2.1 Trend and comparison to different nuclear models . . . 78
5.2.2 Article II: Unexpectedly large charge radii of neutron-rich calcium isotopes 83

6 A sensitive setup for laser spectroscopy 93
6.1 State-selective charge exchange process after optical pumping . 94
6.1.1 Ion-laser interaction and multi-step optical pumping . . 96
6.2 Charge transfer reactions 104
6.3 Previous ROC beam line 112
6.4 Design of the new beam line components and detection set-up . 113
6.4.1 Multi-step optical pumping 115
6.4.2 Deceleration and focus control of atom/ion beam 116
6.4.3 Simultaneous detection of β-decay of atoms and ions . . 119
6.5 Ion beam optics simulations 124
6.6 Commissioning the new ROC setup 128
6.6.1 Installation of beam line components 128
6.6.2 First experimental test of ion beam optics 132
6.7 Article III: Design of a sensitive setup for collinear laser spectroscopy at ISOLDE, CERN 136

7 Perspectives and future application of the newly designed setup 137
7.1 Possible physics cases for the ROC technique 137
7.2 Laser-induced nuclear orientation 138
7.2.1 Article IV: Perspectives for the VITO beam line at ISOLDE, CERN. 139

8 Conclusions 146

المنارة للاستشارات

A Appendix **149**

A.1 Collinear laser spectroscopy 149

A.2 Line shapes in fluorescence spectroscopy 150

A.3 Literature values of hyperfine structure constants and ground-state electromagnetic moments of Ca isotopes 153

A.4 Nuclear mean-squared charge radii of Ca region 155

A.5 Configuration Mixing 156

A.5.1 Useful relations 156

A.5.2 Three valence neutron configurations 157

A.5.3 Ground state wave function of ^{51}Ca 157

A.6 Article III: Design of a sensitive setup for collinear laser spectroscopy at ISOLDE, CERN. 159

Bibliography **175**

المنارة للاستشارات

List of Figures

1.1 Nuclear chart around the Ca region. Stable (blue) and radioactive (red) Ca isotopes across different neutron magic numbers. Black vertical bars show the closed-shell numbers $N = 20, 28, 30, 32$. 2

2.1 Schematic representation of a single-particle potential composed of harmonic oscillator plus an attractive spin-orbit term. The green square marks the region in the vicinity of calcium isotopes. The number within the blue square are the magic numbers found in stable nuclei. The number of nucleons necessary to fill each orbital in the Ca region are shown inside of red squares. 7

2.2 Difference between two neutron separation energies, D_{2n} (upper), and two proton separation energies, D_{2p} (bottom). Courtesy of Frank Wienholtz. Mass values were taken form Ref. [41]. 8

2.3 Values of Δr_{2n} derived form charge radii measurements compiled in Ref. [43]. 10

2.4 Absolute nuclear charge radii for isotopes in the Ca region. The values of charge radii are taken from references [17, 59, 60] (Ca) (see table A.4), [61, 62] (Ar), [63] (K), [64] (Sc), [65] (Ti), and Ref. [43] was used for the remaining isotopes. 11

2.5 Single neutron separation energies for the Ca isotopes. Values are obtained from the mass excess. Experimental data for ^{39,50}Ca was taken from [66] and for ^{51,54}Ca from [11]. 12

المنارة للاستشارات

2.6 Experimental magnetic g-factors ($\equiv \mu/I$) of Ca isotopes. The horizontal lines show the normalized single-particle values for each orbit. The normalization factor of 0.8 is chosen to overlap with the experimental values. (values taken from Ref.[69]). See Ref. [70] for more details. 12

2.7 Excitation energies of the first 2_1^+ (black circles), 4_1^+ (black squares) and 0_2^+ (black triangles) excited states in even calcium isotopes; experimental values are taken from Ref. [74]. For ^{34}Ca (particle unbound) no excitation energies have been measured, but the value of $E(2^+)$ for ^{34}Si ($Z = 14$) [73] is added to the figure to illustrate the importance of $Z, N = 14$. The blue points show the $B(E2)$ values for even calcium isotopes. Experimental values were taken from [74]. See text for more details. 13

3.1 Model of a nuclear potential for different inter nucleon distances in the spin-singlet S-wave channel. Figure taken from Ref. [89]. 18

3.2 Diagram of the nucleon-nucleon interaction. Gluons and quarks degrees of freedom (left) are negligible at low energies, where pions and nucleons are the dominant degrees of freedom (right). Figure taken from Ref. [96]. 19

3.3 Hierarchy of nuclear forces in chiral effective field theory (ch-EFT). Solid lines represent nucleons and dashed lines pions. Small dots, large solid dots, solid squares, and solid diamonds denote vertices of index $\Lambda = 0, 1, 2$, and 4 (Figure taken from [29]). See text for details. 21

3.4 Sketch of the potential well of an harmonic oscillator and the single particle bases used for no-core shell model (left) and "standard" shell model calculations. 24

3.5 Nucleon-nucleon potential and effective interactions developed for Ca isotopes. The "bare" nucleon-nucleon potential is transformed into an "effective" interaction by using the most common methods: G-matrix, SRG, and V_{lowk}. The "effective" Hamiltonian is then used to calculate nuclear structure observables with the shell-model approach or/and *ab-initio* calculations. See text form more details. References: i) [120], ii) [115], iii) [118], iv) [99, 29], v) [121, 122], vi) [123], a) [120] b)[116], c)[117], d) [124, 125], e) [30, 34], f) [126], g) [127], h) [128, 32], i) [31], j) [123]. 25

المنارة للاستشارات

3.6 NN matrix elements expressed in momentum bases for the two major RG methods: a) V_{lowk} with Λ-dependence, and b) SRG with λ-dependence. Figure taken from Ref. [112]. 27

3.7 Example of evolution of NN matrix elements expressed in momentum bases for the $^3S_1$ channel for the phenomenological potential, Argonne ν_{18} [87](top), and a microscopic chiral potential, N^{3}LO [99](bottom). The phenomenological potential is evolved with: c) the traditionally used G-matrix approach, and with b) the SRG method. The chiral potential is evolved with the two major RG methods: e) V_{lowk} (Λ=2 fm^{-1}), and f) SRG (λ=2 fm^{-1}). Figures were adapted from [112]. 28

3.8 Comparison of experimental results with *ab-initio* and shell-model calculations obtained for the S_{2n} values of Ca isotopes. All calculations use interactions derived from ch-EFT. The figure has been modified from Ref. [126, 151]. 33

3.9 Diagrams illustrating one- and two-body electromagnetic current operators entering at order LO (Q^{-2}), NLO (Q^{-1}), NNLO (Q^0) and N3LO (Q^1) in ch-EFT. Solid lines represent nucleons and dashed lines pions. Photons are represented by wavy lines. (Figure taken from Ref. [92]). See text for more details. 37

3.10 Magnetic moments from quantum Monte-Carlo calculations with consistent NN interactions and EW currents derived from ch-EFT. Experimental points are shown as black stars. Blue points show the predicted values considering the IA current only, and red starts show the total many-body current up to o N^{3}LO order. Figure taken from Ref. [167]. 39

4.1 Layout of ISOLDE beam line from the HRS target to the COLLAPS setup. 45

4.2 Applied longitudinal potential in ISCOOL. Ions are trapped by a potential barrier of about 60 V(continuous line), and after a time interval T_2, the voltage is switched from $\sim$ 60V to 0 V to eject the ions (dashed line). 45

المنارة للاستشارات

4.3 Short-lived Ca isotopes are produced from nuclear reactions of high-energy protons impacting on an uranium carbide target. Ca atoms were selectively ionized by using a three-step laser scheme [190]. Ions were extracted from the trap and mass separated to be injected into a radio frequency trap, ISCOOL. Bunches of ions were extracted and redirected into the COLLAPS beam line to perform collinear laser spectroscopy experiments. At COLLAPS, the ions are superimposed with a continuous wavelength laser beam to scan the hyperfine structure in the $4s\ ^2S_{1/2} \rightarrow 4p\ ^2P_{3/2}$ transition of Ca^+ (see text for more details). 46

4.4 Examples of hfs spectra measured for the Ca isotopes in the 393 nm $4s^2S_{1/2} \rightarrow 4p^2P_{3/2}$ ionic transition. The arrows in odd isotopes indicate the centroid of the hyperfine structure. . . . 49

4.5 Kepco factor obtained for the different files saved during the Ca runs. Each color represents a different Fluke. The average value for each fluke is shown with a horizontal line of the same color. The total average $k_{ave} = 50.4268(12)$ is shown using the horizontal black line. 52

4.6 Example of the fit to one of the hfs spectra of ^{47}Ca. Experimental values (points) are fitted to multiple Voigt profiles (continuous line). 53

4.7 Poisson factor x obtained from the fit to the HFS spectra of ^{40}Ca. The horizontal black line shows the weighted average $x = 0.031(2)$. 54

4.8 Fitted isotope shifts as a function of the offset voltage, v_{os} for ^{44}Ca and ^{48}Ca relative to ^{40}Ca. Two different platform potentials were used, 30 kV (red points) and 40 kV (blue points). 56

4.9 Ratio between the hfs constants $A(^2P_{1/2})$ and $A(^2P_{3/2})$. The continuous line shows the average value $A(^2S_{1/2})/A(^2P_{3/2}) = 25.92(3)$. Hyperfine structure spectra of ^{51}Ca were fitted assuming different g.s. spin values of $I = 3/2, 5/2, 7/2$. 57

4.10 King plot: experimental isotope shift as a function of the charge radii obtained by Palmer *et al* [60]. 64

المنارة للاستشارات

5.1 Magnetic moment obtained from the expression 5.2 with $g_s^\nu = -3.826$ as a function of the value a^2. In blue color the values assuming mixing with $f_{7/2}$ only ($|b| = 0$), and with red and green colors assuming that the mixing is only with $p_{1/2}$ ($|c| = 0$). The horizontal black line shows the experimental value. The huge sensitivity of the magnetic moment to the configuration mixing is mainly associated to the off-diagonal term in the case of excitation to a spin-orbit partner orbital. [1] 74

5.2 Experimental results of magnetic moments compared with calculations from the TBCL8 interaction [22]. Effective neutron g-factors were used: $g_s = -3.041$ ($g_s^{eff} = 0.8 g_s^{free}$) and $g_l = 0.000$. 76

5.3 Experimental results for quadrupole moments compared with calculations from the TBCL8 interaction [22]. Two different effective neutron charges were used: $e_n = 0.5e$ (continuous line), and $e_n = 0.84e$ (dotted line). 78

5.4 Changes in the rms charge radii measured for Ca isotopes with respect to ^{40}Ca. Filled circles are from this work. Literature values (filled triangles) are taken from Ref. [59, 200, 17]. . . . 79

5.5 Charge radii of Ca isotopes. Experimental charge radii compared to ab initio calculations with: (a) chiral EFT interactions NNLO$_{sat}$, 2.8/2.0 (EM), 2.0/2.0 (PWA), as well as (b) DFT calculations. Experimental error bars are smaller than the symbols. The absolute values were obtained from the reference radius of ^{40}Ca (Rch = 3.478(2) fm) [224]. Experimental rms charge radius relative to that in ^{48}Ca compared to: (c) the ab initio results as well as (d) those of representative density functional theory (DFT) and different interactions than have been fitted to reproduce the odd-even staggering between $N = 20$ and $N = 28$ (see text for more details). 82

6.1 Layout of the experimental scheme for Radioactive detection of Optically pumped ions after state selective Charge exchange (ROC) . The technique consists of three main processes: *optical pumping, state-selective charge exchange*, and *radioactive detection of atoms/ions*. 95

6.2 Ca^+ energy levels of the low-lying states involved in the optical pumping process. 95

المنارة للاستشارات

6.3 Level scheme of a Ca^+ ion with nuclear spin, $I = 1/2$. A laser field of frequency 393 nm excites the ion from the ground state $S_{1/2}$ to the excited state $P_{3/2}$. When the laser is on resonance with the component $F = 0 \rightarrow F = 1$ or $F = 1 \rightarrow F = 1$, the spontaneous emission spreads the population into the metastable states D_J and the gs components $F = 0, 1$. 99

6.4 Population of the metastable state as a function of the laser frequency scanned over the hyperfine transitions between the $S_{1/2}$ and $P_{3/2}$ levels. Different laser powers were assumed with single-step optical pumping. A ^{53}Ca ($I = 1/2$) ion beam at 30 keV was assumed to interact with the laser beam along an optical pumping region of 2 m length. 100

6.5 Percent of population transferred from the initial ground state into the metastable state via the $F = 1 \rightarrow 2$ transition. The populations is shown as a function of the interaction time for different laser power densities. The laser frequency is fixed at resonance. 101

6.6 Population of the metastable state for single-step optical pumping (SOP) and two-step optical pumping (TSOP). A ^{53}Ca ($I = 1/2$) ion beam at 30 keV is assumed to interact with a laser beam along an optical pumping region of 2 m length. For the TSOP process, the first step was used as scanning frequency, and the frequency of the second step fixed at ν_2. 102

6.7 Population of the metastable state for two-step optical pumping (TSOP). A ^{53}Ca ($I = 1/2$) ion beam at 30 keV is assumed to interact with a laser beam along two optical pumping region of 1 m length each one. The first step is used as scanning frequency, and the frequency of the second step is fixed at ν_2. 103

6.8 Population of the metastable state for four steps optical pumping. The ion beam interacts with four laser fields. First and third laser were allowed to have variable frequency, and the second and fourth field were fixed to any of the possible values ν_1, ν_2 or ν_3 (see text for more details). 104

6.9 Population of the metastable state for different number of steps, using different fixed frequencies. 105

المنارة للاستشارات

6.10 Probability $P(b, v)$ of neutralizing a Ca^+ beam at 5 keV on a Na gas. The probability is calculated as a function of the impact parameter b. The impact parameter is given in units of the Bohr radius, a_0. At b_1 the $\text{sech}^2\left[\frac{\omega}{v}\left(\frac{a_0\pi b_1}{2\gamma}\right)^{1/2}\right]$ (red line) is equal to $4P(b_1, v)$. 108

6.11 Example of the calculated neutralization cross section as a function of the ion energy for three different channels in the reaction Ca^+ + Na. The curves show the cross section for ions in three possible initial states $4s\ ^2S_{1/2}$ (red), $3\ d\ ^2D_{3/2}$ (green), or $3\ d\ ^2D_{5/2}$ (blue). 109

6.12 Ratio of neutralization cross sections between the metastable and ground state of Ca^+ ion in the reaction Ca^+ + Na. Experimental values are taken from [233]. The continuous blue line shows the theoretical predictions for this ratio using a normalization factor of 0.5 (see text for more details). The reaction channels included in the calculations are listed in table 6.1. 110

6.13 CAD model of previous ROC experimental setup. See text for more details. 112

6.14 Complete design of the new ROC experimental setup. As designed with the help of Autodesk Inventor 2013. 114

6.15 Design of the multi-step optical pumping region. The optical pumping region is divided in four independent segments. The first segment is not shown in the figure. A light collection region is placed along the second step for monitoring the fluorescence signals. 116

6.16 SIMION simulations for a simplified setup composed of a decelerator tube, an Einzel lens and a CEC cell. The retarding potential is divided in different steps: a) one slope, b) two slopes and c) three slopes. See text for more details. 120

6.17 CAD design for the ion beam optics after the CEC cell. Independent high efficiency β-detection was implemented of atoms and ions. Details for the β-detector chambers are given in section 6.4.3. 121

المنارة للاستشارات

6.18 CAD design of the high voltage platform. A set of eight HV power supplies are installed with ground reference given by the platform potential (26 keV). 121

6.19 CAD design of the β-detector chamber. Ions are implanted on a movable tape. A collimator prevents the implantation of ions outside the tape. The β-particles are detected by two concentric cylindrical scintillators. The light from the scintillators is collected by a set of PMT tubes attached to the surface of the scinitllators. 123

6.20 Beam line components included in the SIMION simulations. Each electrode with adjustable potential is presented with a different color. The outer chambers were included as a single electrode fixed at ground potential. 125

6.21 Example of a SIMION simulations for the whole ROC setup. a) Potential energy surface view, and b) particle trajectories for the ion beam. A neutralization efficiency of 50 % was assumed for the CEC process at the center of the CEC (see text for more details). 126

6.22 Results of ion beam SIMION simulations for both, atoms(left) and ions(right), assuming two different focal positions for the ion beam entering into the ROC setup: at the entry (upper) and at the end (lower) of the optical pumping region. Colors represent the percent of transmission simulated at the implantation point. 127

6.23 Photograph of the optical pumping region installed at the COLLAPS beam line. The pumping tube connected to the light collection region (left), and a view inside the pumping tube (right). 129

6.24 Photograph of the installation of different beam line elements: the decelerator (left), CEC chamber (center), and HV cage (right) 129

6.25 Photograph of some of the components in the ROC setup. a) A view from the 5^o deflector up to the end of the CEC chamber. The HV cage placed on one side of the CEC chamber. b) The inside of the CEC chamber. c) Re-accelerator for ions after the 35^o deflector and d) Renewed accelerator from the old ROC setup. 130

المنارة للاستشارات

6.26 Photograph of the HV cage and the different components used to control the power supplies floating at 26 keV with respect to the ground potential. 131

6.27 Test of linearity for the high voltage power supplies used to control the ion beam optics inside the CEC chamber. The HV output is measured as a function of the input voltage. 131

6.28 Photograph of the tape stations a) Shows both chambers assembled with the respective tape stations. b) Outer and inner scintillators. c) A view of one detector chamber. d) The inside of one of the tape stations. 132

6.29 Measurements of the XY profile of a collimated ^{19}F ion beam at 30 keV, extracted from the GPS target station. The figures shows the beam profile just after the separator (upper), at midway between the separator and the COLLAPS beam line (center), and just before the COLLAPS beam line (bottom). . 135

A.1 Example of a fit with multiple side peaks on ^{40}Ca. Without side peaks a value of $\chi^2 = 3.2$ is obtained. When side peaks are included (red) the fit converges with a value of $\chi^2 = 2.5$. 152

A.2 Magnetic moment obtained from the expression A.29 as a function of the value $|a|^2$. In blue color the values assuming mixing with $f_{7/2}$ only ($|b| = 0$), and with red and green colors assuming the mixing is only with $p_{1/2}$ ($|c| = 0$). The huge sensitivity of the magnetic moment to the configuration mixing is mainly associated to the off-diagonal term [1] 159

المنارة للاستشارات

المنارة للاستشارات

List of Tables

4.1 Ca isotopes measured during the experiment. Nuclear spin and masses are indicated for each isotope. The yields of each isotope are taken from the ISOLDE yield data base. The masses were taken from Ref. [66] for $^{40-50}$Ca, and from Ref. [194] for ^{51,52}Ca. The total number of runs measured for each isotope is given for the two different V_{ISCOOL} potentials used during the experiments. 50

4.2 Kepco calibration files recorded during the experimental campaign. 51

4.3 Reference Ca isotope shifts measured relative to ^{40}Ca in the $4s\ ^2S_{1/2} \rightarrow 4p\ ^2P_{3/2}$ line. 55

4.4 Values of the ISCOOL offset voltages obtained from isotope shift measurements. 56

4.5 Hyperfine structure values obtained from the fit to the experimental data compared to previous measurements. 58

4.6 Quadrupole and magnetic moments obtained from the measured hfs constants (Table 4.5). The magnetic moments were obtained using the reference isotope ^{43}Ca, with $A(^2P_{3/2}) = -806.40207160(8)$ MHz [203]. Quadrupole moments were extracted using the calculated electric field gradient, $eV_{JJ} = 151.3(7)$ MHzb^{-1} [20]. Data are compared to calculations using the NN+3N interaction. 59

4.7 Calculated electric field gradient for the $4p^2P_{3/2}$ line. Calculated values have been derived using relativistic coupled-cluster theory (RCC), relativistic many body perturbation theory (RMBPT), and RMBPT with single-double all-other method (SD). 60

4.8 B-ratios relative to ^{43}Ca. 61

المنارة للاستشارات

4.9 Measured isotope shifts relative to ^{40}Ca. The errors include statistic and systematic uncertainties given in round and squared brackets, respectively. The systematic uncertainties of our measurements are dominated by the uncertainty in the ion beam energy. Literature values are given in columns 3 and 4. 62

4.10 Values of charge radii obtained from isotope shift measurements. Error bars in square brackets show the uncertainty due to K_{SMS}. 63

5.1 Main components (%) of the wave function obtained from shell model calculations using the different interactions GXPF1A, KB3G, SPDF.SM and NN+3N. 75

6.1 Collision channels included in the calculations of charge transfer cross sections for the reaction $Ca^+ + Na \rightarrow Ca + Na^+ + \Delta E$. The energy values for the different states are taken from Ref [242]. . 111

6.2 Ratio of isobaric contamination for the different isobars of mass $A = 53$ and $A = 54$ identified during the ISOLTRAP experimental campaign (2013) [11, 243]. Half life and Q_β values are taken from [74, 244]. Values in squared brackets show estimated values. 114

6.3 Simplified SIMION simulations for the system composed of a decelerator tube, an einzel lens and a CEC cell. A initial parallel beam at 30 keV is used to illustrate the influence of the deceleration slopes and the Einzel lens potential. The values of V_1 and V_2 are taken relative to the ground potential. The Einzel lens potential, V_L, is given relative to the platform potential (26 kV). Particle trajectories and the potential along the decelerator are shown in Figure 6.16. 119

6.4 Comparison between the old and new ROC setup 124

6.5 Optimum values of the main electrostatic elements of the ROC setup obtained from the ion beam SIMION simulations. The labels (i) and (ii) stands for two different regions of maximum transmission (Figure 6.22). 128

6.6 Experimental values obtained for the main electrostatic elements of the ROC setup. Results are summarized for both target stations: HRS (second column) and GSP (third column). In both cases an ion beam transmission of 90 %, $F_C/F_{ISO} \sim 0.9$, was obtained. 134

المنارة للاستشارات

7.1 ISOLDE yields for unknown exotic isotopes that might be accessible with the ROC technique. Estimated (not measured) yields are in round brackets. 138

A.1 Selected values of hfs constants, B, reported for Ca isotopes. . 153

A.2 Reported quadrupole moments for Ca isotopes. 154

A.3 Literature values of the root-mean squared charge radii, $\langle r^2 \rangle$, of Ca isotopes. 155

المنارة للاستشارات

المنارة للاستشارات

Chapter 1

Introduction

After almost one century of research, the atomic nucleus is still revealing the fascinating physics that survives at the low-energy scale of nuclear physics. New and unexpected nuclear structure features have been observed from the study of short-lived isotopes away from the valley of stability [2, 3, 4, 5]. Special attention has been given to the appearance and disappearance of "magic" (closed-shell) structures in the nucleus at extreme proton-to-neutron ratios [6, 7, 8]. A fundamental understanding of how these closed-shell configurations are formed and how they evolve in unstable nuclei is one of the main challenges of modern experimental and theoretical nuclear physics [9, 10, 11, 12].

The calcium isotopic chain is an excellent example to illustrate the progress of experimental and theoretical nuclear physics in recent decades. With a magic proton number, $Z = 20$, and two naturally occurring doubly magic isotopes, ^{40}Ca ($N = 20$) and ^{48}Ca ($N = 28$), calcium has always been of great interest for the nuclear physics community.
The availability of different naturally occurring Ca isotopes (Figure 1.1) encouraged numerous experiments [13, 14, 15, 16, 17, 18, 19, 20], and theoretical developments [21, 22, 23, 24, 25, 26] on the evolution of the nuclear-structure properties between the two closed shells at $N = 20$ and $N = 28$. In the last decade, since the availability of intense radioactive beams of exotic Ca isotopes, specific interest has been given to the evolution of the nuclear properties of the Ca isotopes beyond $N = 28$, where relative high values of the $E(2^+)$ excitation energies suggest the existence of two additional closed shells at $N = 32$ [27] and $N = 34$ [12]. Indeed, recent mass measurements have provided additional evidence supporting such effects at $N = 32$ [11]. Additionally, other doubly-

المنارة للاستشارات

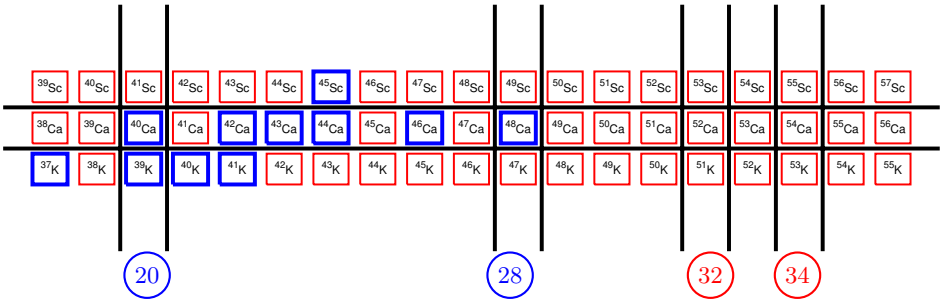

Figure 1.1: Nuclear chart around the Ca region. Stable (blue) and radioactive (red) Ca isotopes across different neutron magic numbers. Black vertical bars show the closed-shell numbers $N = 20, 28, 30, 32$.

magic nuclei may exist further away from stability, e.g., ^{60}Ca at $N = 40$ [28]. This manifestation of multiple closed shells is an exceptional characteristic of the Ca isotopic chain that makes these nuclei particularly attractive for nuclear theory, as they constitute an ideal laboratory to explore the properties of many-body systems, and our understanding of the nuclear force.
During the last few years chiral effective field theory has emerged as a promising path towards the fundamental description of the atomic nucleus, connecting the description of the nuclear force with the underlying theory of the strong interaction, quantum chromodynamics (QCD) [29]. A particular interest has been given to the neutron-rich Ca isotopes as they are at the limit where these state-of-the-art microscopic calculations can be applied [30, 31, 32, 33, 34]. Furthermore, such neutron-rich nuclei have revealed new aspects of the nuclear force, in particular regarding the role of three-nucleon forces (3N-forces) [30, 11]. Hence, the description of Ca isotopes has become a benchmark for the understanding of the atomic nucleus on the basis of first principles.

With lifetimes in the sub-millisecond time scale, the study of exotic nuclei becomes possible thanks to the recent progress at radioactive beam facilities and the development of high-efficiency experimental techniques. As described in the present work, complementary to nuclear-reaction experiments or particle- and gamma-ray spectroscopy, the atomic system can also provide a suitable scenario to extract valuable nuclear structure information. Since electronic energy levels are sensitive to the structure of the nuclear charge distribution, by measuring the transition energies among the atomic hyperfine structure (hfs) levels, the ground state (gs) nuclear electromagnetic moments, nuclear spin and nuclear root mean-square (rms) charge radius can be obtained. As the electrons and the nucleus interact only through the well known electromagnetic force, no

المنارة للاستشارات

nuclear model dependence needs to be introduced to extract these observables from measured hyperfine parameters.

المنارة للاستشارات

المنارة للاستشارات

Chapter 2

Nuclear structure and the quest for understanding the calcium isotopes

The description of the atomic nucleus relies on our knowledge of the not well understood nuclear force, and the proper treatment of the complicated many-body system that the nucleus is. Despite the complexity of this problem, the nucleus seems to exhibit simple structures and regular patterns for certain numbers of protons and neutrons, traditionally referred to as "magic numbers". This chapter presents some of the experimental signatures of nuclear structure that have motivated the development of shell-structure models in atomic nuclei, and have given long life to the nuclear shell model. The discussion is expanded on the importance of the calcium nuclei, and the emergence of new closed-shell structures in exotic isotopes.

2.1 Evidence of shell structures in the nucleus

Rutherford experiments on the size of the nuclear charge distribution provided the first experimental evidences that led to the discovery of the atomic nucleus [35, 36]. Measurements of bulk properties such as the charge radii and the nuclear masses inspired the development of one of the oldest models of nuclear physics, the "liquid drop model" [37]. Although this model was a surprisingly good approximation to the global description of the size and the binding energy

المنارة للاستشارات

of the nucleus, the appearance of structures was rapidly distinguishable as more and more experimental data became available. The regularities observed at the so called "magic numbers", gave birth to another old successful model of nuclear physics, the "nuclear shell model" [38, 39]. Mayer and Jensen demonstrated that a simple single-particle potential composed of harmonic oscillator term plus an attractive spin-orbit term, are the basic ingredients to explain the appearance of such "magic" numbers. The different orbits and occupation numbers generated with this single-particle potential are shown in Figure 2.1.

It is now understood, that just like electrons in the atom, protons and neutrons (nucleons) in the atomic nuclei exist in quantum levels that appear in "shells". These shells are separated by energy gaps, and assumed to be completely filled with protons or neutrons at "magic" numbers. Given the ambiguous use of the terms "magic" and "closed-shell", the term "magic" employed in this work will refer to numbers of nucleons that exhibit similar experimental properties as those observed at the "magic" numbers described by Mayer and Jensen [1] [38]: 2, 8, 20, 28, 50, 82, 126. In this sense, the "magic" character would be purely experimental, without implying the existence of energy gaps, or single-particle energies.

A common indicator of the strength of a closed shell is given by the difference between the two neutron separation energies[2], $D_{2n}(Z,N) = S_{2n}(Z,N) - S_{2n}(Z,N+2)$, with $S_{2n}(Z,N) = B(Z,N) - B(Z,N-2)$, and $B(Z,N)$ the binding energy of a nucleus with Z protons and N neutrons. Equivalently, the quantity D_{2p} is defined to evaluate the strength of a shell closure as a function of the proton number. Up-to-date experimental studies have extended the measurement of nuclear masses in a wide region of the nuclear chart, allowing systematic studies across different numbers of nucleons. For instance, the values D_{2n} and D_{2p} for the available experimental and extrapolated data are shown in Figure 2.2. In regions were data is not yet available, mass models can be used to extrapolate the experimental data. As it is illustrated in the figure, both D_{2n} and D_{2p} exhibit maximum values at "magic" numbers, but the effect is less pronounced for light nuclei at $N, Z = 2, 8, 20$. An enhancement of the binding energy is also observed for nuclei with equal number of protons and neutrons, this extra binding for $Z = N$ nuclei is commonly known as the Wigner effect [42]. In other regions of the nuclear chart, local maxima appear at different numbers of nucleons, i.e., around $N, Z = 14 - 16, 32$ and around $Z = 40$. The emergence of these apparently new "magic" structures, particularly at $N = 32$ and $N = 34$ is one of the main motivations in the study of neutron rich calcium

[1] Note taken from the Nobel lecture of Maria Goeppert Mayer: *"...since they are explained and no longer magic, I shall from here on call them shell numbers." [40]*

[2] Notice that this quantity is meaningful only if correlations are negligible [8].

المنارة للاستشارات

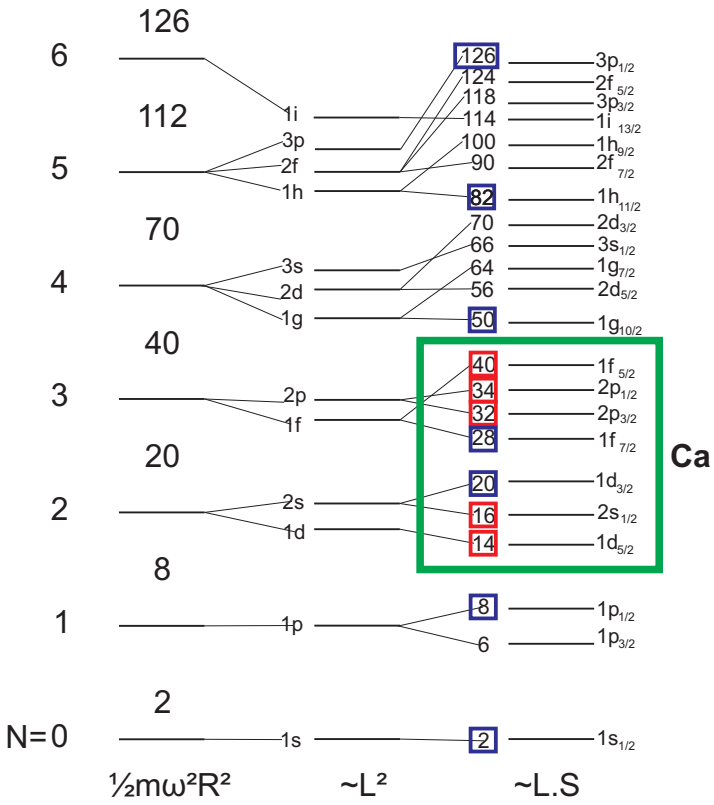

Figure 2.1: Schematic representation of a single-particle potential composed of harmonic oscillator plus an attractive spin-orbit term. The green square marks the region in the vicinity of calcium isotopes. The number within the blue square are the magic numbers found in stable nuclei. The number of nucleons necessary to fill each orbital in the Ca region are shown inside of red squares.

المنارة للاستشارات

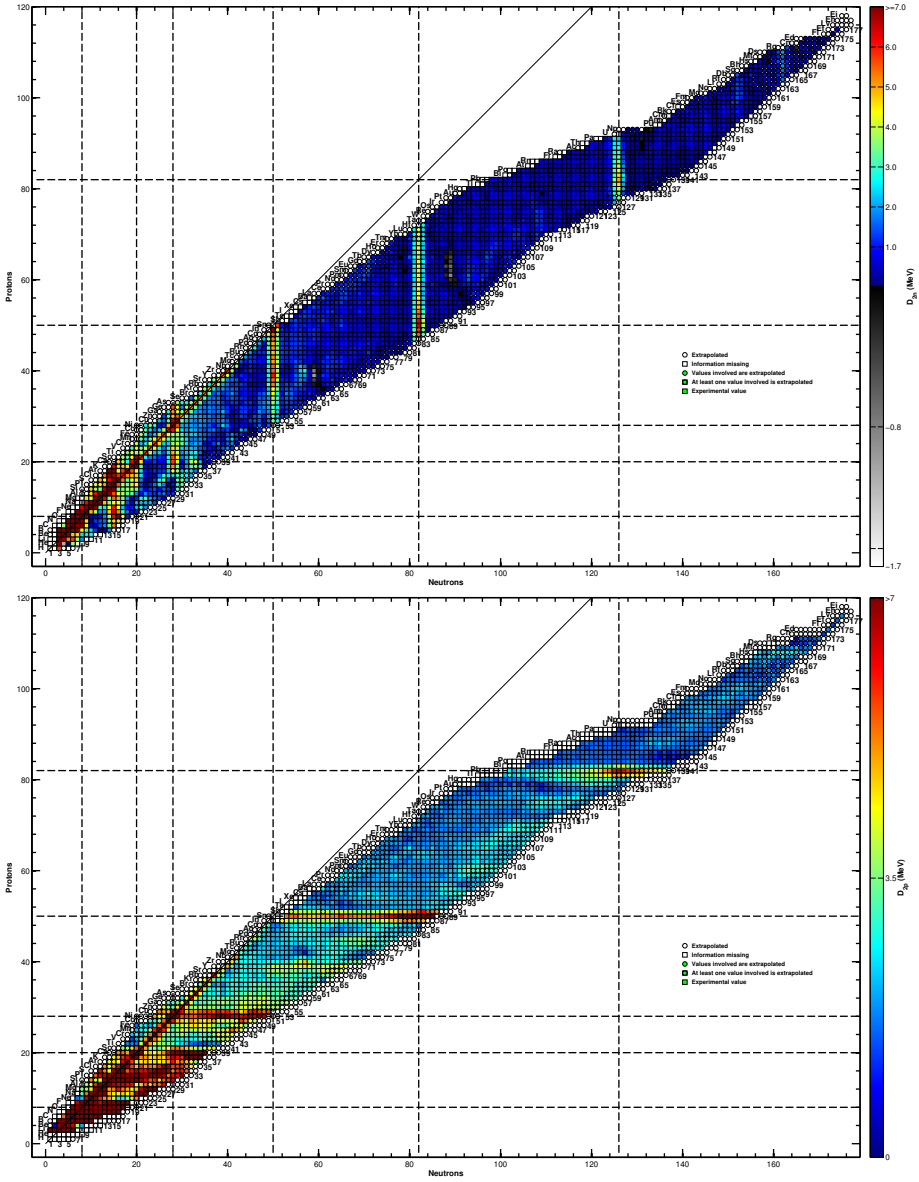

Figure 2.2: Difference between two neutron separation energies, D_{2n} (upper), and two proton separation energies, D_{2p} (bottom). Courtesy of Frank Wienholtz. Mass values were taken form Ref. [41].

المنارة للاستشارات

($Z = 20$) isotopes.

For the charge radii, the available experimental data is more scarce, covering a more limited region of the nuclear chart. Similarly to the binding energies, the existence of a closed-shell can be evaluated from the change of the root-mean square charge radii when two neutrons are added

$$\Delta\langle r^2\rangle^{1/2}_{\Delta N=2} \equiv \Delta\langle r^2\rangle^{1/2}_{2n} = \langle r^2\rangle^{1/2}_{N+1} - \langle r^2\rangle^{1/2}_{N-1}, \tag{2.1}$$

with $\langle r^2\rangle_N$ is the rms charge radius of a nucleus with N number of neutrons. The values of $\Delta\langle r^2\rangle^{1/2}_{2n}$ for the available experimental data [43] are shown in Figure 2.3. The peak values of this quantity are commonly observed across "magic" numbers. A global behaviour of a linear decrease of $\Delta r_{\Delta N=2}$ is observed independent of the proton configuration, and abrupt changes at magic numbers are interpreted as a manifestation of shell structures. There is not a clear signature at $N = 20$, but very few experimental results are available to establish firm conclusions for nuclei with $N \leq 20$. Marked changes in the charge radii between $N = 58$ and $N = 60$ are related with a sudden increase of deformation in this region of the nuclear chart [44].

With the new experimental results on exotic nuclei, the failure of our "old" nuclear models have been exposed, opening new question on the origin of "magic" numbers and its interpreation within the shell-model. Interestingly, it has been shown that equivalent descriptions of a given nucleus can be obtained by employing contradictory schemes, i.e, by assuming single-particle behaviour or by using high configuration mixing [45]. In this regard, the unique determination of shell structures separated by energy gaps in the atomic nucleus is still an ongoing debate. See Ref. [46] for a modern approach to this issue.

2.2 The multiple "magicity" of Ca isotopes

With $Z = 20$ protons, calcium is the only isotopic chain that contains two naturally occurring doubly-magic nuclei, ^{40}Ca($N = 20$) and ^{48}Ca($N = 28$). The natural abundance of six Ca isotopes provided ideal access for the early experimental studies on the evolution of nuclear properties between neutron numbers $N = 20$ and $N = 28$ [47, 48, 49, 50, 51, 52, 53, 54, 55, 13, 25, 56, 14, 15, 16, 17, 18, 19, 20]. These multiple closed-shell structures favored the application of distinct theoretical calculations that were motivated from the experimental results [57, 21, 23, 24, 25, 26, 22]. Moreover, new experimental evidence suggests that new closed-shell structures emerge at neutron numbers $N = 32$ and $N = 34$ [11, 12], giving a renewed interested on the study of exotic

المنارة للاستشارات

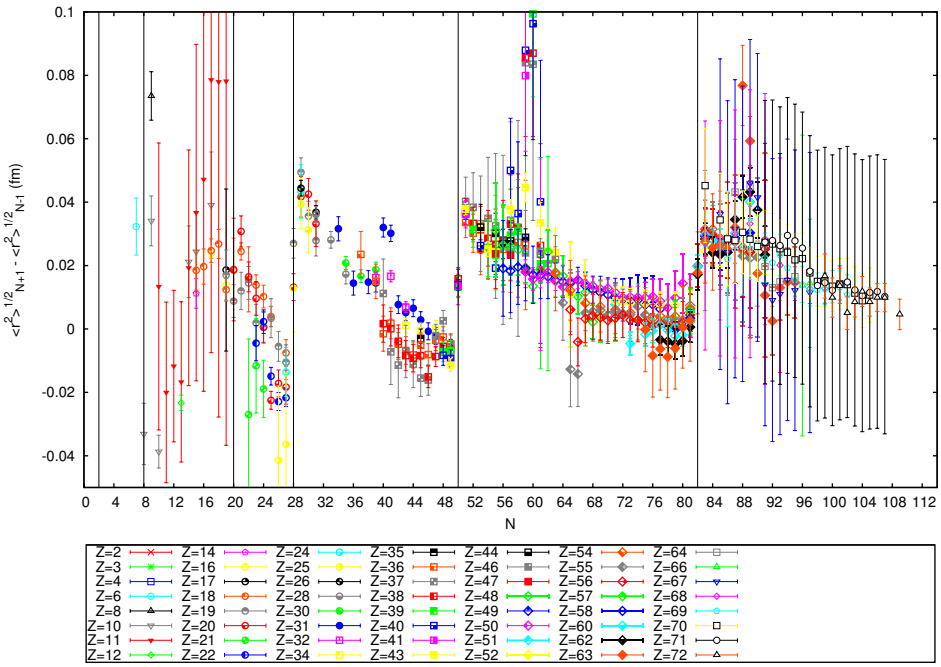

Figure 2.3: Values of Δr_{2n} derived form charge radii measurements compiled in Ref. [43].

neutron-rich isotopes.
In the previous section the global behaviour of bulk properties around magic numbers was discussed. How these properties evolve in the Ca region, and how these structural changes are related with other observables such as $E(2^+)$ excitation energies, $B(E2)$ values, and microscopic properties (the ground state electromagnetic moments) will be discussed below.

The signature of a shell closure is commonly manifested as a pronounced change of the charge radius after a shell closure (kink), with a smooth increase towards closed-shells, and larger increase through the filling of the new open shell [43]. An example of the kink at $N = 28$ is shown in Figure 2.4. This effect is commonly linked to a large decrease of the trend in the neutron-separation energy, S_n, a high 2^+ excitation energy, $E(2^+)$, and a low reduced-transition probability, $B(E2)$ [58]. For Ca isotopes this effect is seen in the S_n values (Figure 2.5). Furthermore, the S_n exhibit a simple linear behaviour between

المنارة للاستشارات

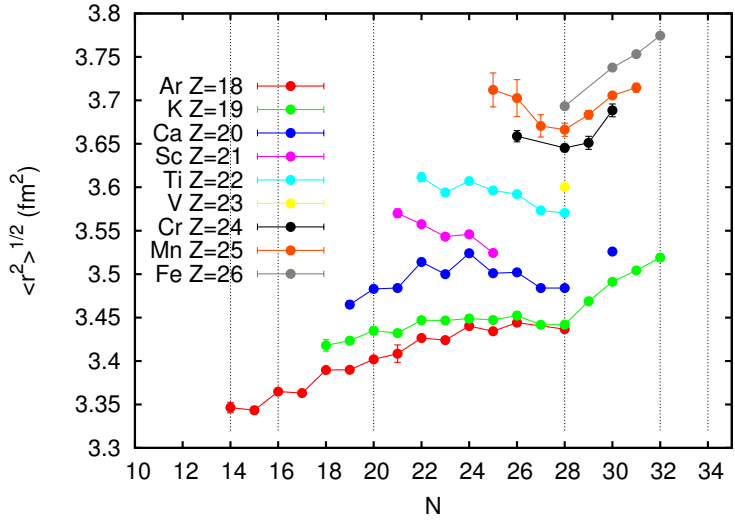

Figure 2.4: Absolute nuclear charge radii for isotopes in the Ca region. The values of charge radii are taken from references [17, 59, 60] (Ca) (see table A.4), [61, 62] (Ar), [63] (K), [64] (Sc), [65] (Ti), and Ref. [43] was used for the remaining isotopes.

magic numbers.

Likewise, the experimental magnetic g-factors ($\equiv \mu/I$) display simple trends, with marked changes at "magic" numbers. The available experimental magnetic g-factors of Ca isotopes are shown in Figure 2.6. The fairly flat trend of g-factors values might be interpreted as a dominant single-particle behaviour [67][3]. As seen in Figure 2.6, the g-factor values are consistent with the filling of the orbit $d_{3/2}$ up to $N = 20$ (see Fig. 2.1), and the filling of the $f_{7/2}$ orbital between $N = 20$ and $N = 28$. The horizontal lines in the figure show the normalized single-particle g-factor values for both orbitals. The normalization factor of 0.8 is chosen to fit with the experimental values. An extended discussion on the origin of these factors is presented in the next chapter.

The values of $E(2^+)$ excitation energies of Ca isotopes are shown in Figure 2.7. The excitation energies of the low lying states $E(2_1^+)$, $E(4_1^+)$ and $E(0_2^+)$, and the $B(E2)$ values are included in the same figure. The characteristic high $E(2^+)$ and low $B(E2)$ values expected at magic numbers are observed at $N = 20, 28$.

[3]For n identical nucleons in a single shell-model orbital, the g-factor is independent of n and I, it is $g(j^n; I) = g(j)$ [68].

المنارة للاستشارات

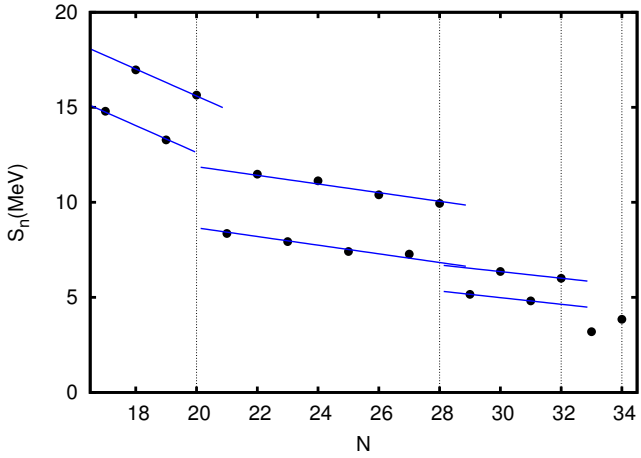

Figure 2.5: Single neutron separation energies for the Ca isotopes. Values are obtained from the mass excess. Experimental data for ^{39,50}Ca was taken from [66] and for ^{51,54}Ca from [11].

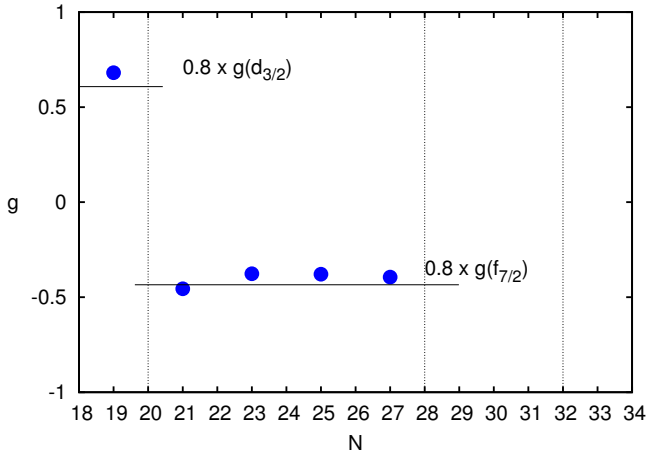

Figure 2.6: Experimental magnetic g-factors ($\equiv \mu/I$) of Ca isotopes. The horizontal lines show the normalized single-particle values for each orbit. The normalization factor of 0.8 is chosen to overlap with the experimental values. (values taken from Ref.[69]). See Ref. [70] for more details.

المنارة للاستشارات

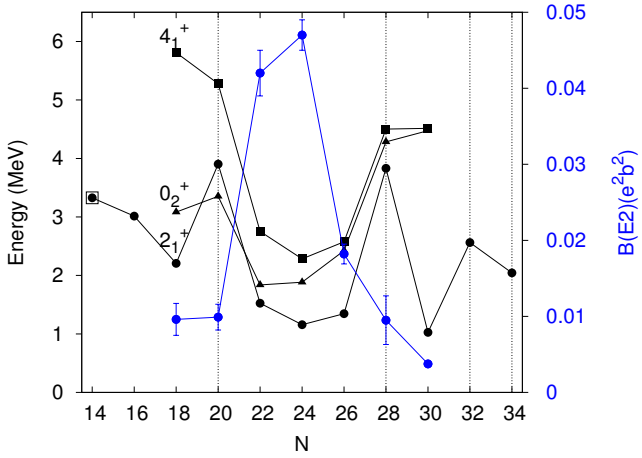

Figure 2.7: Excitation energies of the first 2_1^+ (black circles), 4_1^+ (black squares) and 0_2^+ (black triangles) excited states in even calcium isotopes; experimental values are taken from Ref. [74]. For ^{34}Ca (particle unbound) no excitation energies have been measured, but the value of $E(2^+)$ for ^{34}Si ($Z = 14$) [73] is added to the figure to illustrate the importance of $Z, N = 14$. The blue points show the $B(E2)$ values for even calcium isotopes. Experimental values were taken from [74]. See text for more details.

Additionally, an increased $E(2^+)$ excitation energy is found at $N = 32$, and more recently a relatively high value at $N = 34$, suggested ^{54}Ca as a new doubly-magic nucleus [12].

On the other extreme, towards neutron-deficient Ca isotopes, a relatively high value of $E(2^+)$ at ^{36}Ca ($N = 16$) might be interpreted as a closed shell effect [71, 72]. For ^{34}Ca ($N = 14$), which is already particle unbound, no excitation energies have been measured. Instead, the $E(2^+)$ value of its mirror nucleus, ^{34}Si, is shown in Fig. 2.7 to illustrate the importance of the proton and neutron number $Z, N = 14$. Interestingly, the two mirror nuclei ^{36}S ($Z = 16$) and ^{34}Si ($Z = 14$) have been suggested as doubly-magic nuclei [71, 72, 73].

On the other hand, the presence of a low-lying 0_2^+ excitation energy ($E(0_2^+)$) indicates that multiple correlations are present around ^{40}Ca [75], which is not expected for closed-shell nuclei. This presence of multiple correlations, which points to a rather weak shell closure at $N = 20$, is in agreement with the charge radii trends. The experimental charge radii available around the calcium region are shown in Figure 2.4. The characteristic "kink" commonly observed at closed-shell numbers is not present at $N = 20$, but well pronounced at $N = 28$.

المنارة للاستشارات

A unique characteristic of Ca isotopes is the strong odd-even staggering (Fig. 2.4), which is present but less pronounced among the other isotopes in the region.
In view of the structural changes observed for the neutron separation energies at $N = 32$ and $N = 34$ (Fig. 2.2 and Fig. 2.5), and the $E(2_1^+)$ excitation energies (Fig. 2.7), it is imperative to understand the evolution of other observables such as the charge radii and the electromagnetic properties in these nuclei.

The nucleus, in spite of being a complex nuclear many-body problem, exhibits simple features and regular patterns, such as to the filling of shell structures, with the Ca nucleus providing an interesting example of these phenomena. However, nuclear theory is relied upon to understand the origin of such structures. In the following section we will explore some properties of the nuclear force and the many-body problem in connection with the formation of shell structures in the atomic nucleus. The test and further improvement of microscopic descriptions of the nucleon-nucleon interaction and *ab-initio* many-body methods are some of the major motivations for our study of the calcium isotopes, as these nuclei form bench-marks for most of the theoretical calculations.

المنارة للاستشارات

Chapter 3

The nuclear many-body problem

Certainly, one could think that an ideal description of the atomic nucleus should start from elementary particles and fundamental forces. Such treatment would use quantum chromodynamics, QCD, to describe the strong interaction, creating hadrons from quarks and gluons. Once hadrons (such as protons, neutrons and pions) are built, we could put them together to generate the whole nuclear chart, going from the simplest nucleus ^{1}H up to the most complex superheavy elements. However, the non perturbative low-energy regime of QCD does not allow a feasible description of the nucleons in terms of quarks and gluons. Although attempts to derive the nuclear force including these degrees of freedom have been proposed from lattice QCD [76], a description of the nucleus in terms of quarks and gluons is still not possible.
During the last few years, tremendous progress has been made, not only in the description of the nuclear force, but also in the development of methods to compute the complicated nuclear many-body problem [77, 78]. A systematic treatment of the inter-nucleon force consistent with the underlying theory of the strong interaction, QCD, has been feasible thanks to recent developments in chiral effective field theory [29]. Nuclear physics has found a path to gradually change from "nuclear models" to an "effective theory of the nucleus". We should remember the fact that not a single physical theory works at every scale, and even the standard model is an effective theory that must break down at the Plank scale [79].

This chapter gives a brief introduction to the different theoretical approaches that have been developed during the last few years to create inter-nucleon

المنارة للاستشارات

interactions and solve the many-body Schrödinger equation, with an emphasis on modern descriptions of the inter-nucleon forces based on chiral effective field theory. In the first section (Section 3.1) the generalities of the many-body problem are introduced. The second section (Section 3.2) presents the modern descriptions of the inter-nucleon forces. Shell-model and *ab-initio* strategies developed to solve the many-body Schrödinger equations are illustrated in sections 3.3 and 3.4, respectively. Finally, Section 3.5 extends the discussion on the consistent description of electro-weak currents in the atomic nucleus. Some selected theoretical results on calcium isotopes are presented to illustrate state-of-the-art theoretical calculations. Whereas concepts and methods are revised in a rather simplified way, several references are included to point the reader towards specialized literature.

3.1 Generalities of the many-body problem

The nuclear many-body problem can be expressed as the quantum mechanical many-body Schrödinger equation[1]

$$(T + V)|\Psi\rangle = E|\Psi\rangle, \tag{3.1}$$

with T the kinetic energy operator, and V the potential for a given A number of nucleons

$$V = \sum_{i<j} v_{ij} + \sum_{i<j<k} v_{ijk} + \sum_{i<j<k<l} v_{ijkl} + ..., \tag{3.2}$$

where v_{ij} stands for NN interactions, v_{ijk} for NNN interactions, and so on. Dealing with this problem translates into two main tasks: i) a proper determination of the nuclear Hamiltonian, $T + V$, which entails a consistent treatment of the inter-nucleon interactions, and ii) solving the A-body Schrödinger equation 3.1. Similarly, the electromagnetic charge, $\rho_c(r)$, and current density, $j(r)$, of the nucleus can be expressed as the sum of many-body operators [80]

$$\rho_c(r) = \sum_i \rho_{c,i}(r) + \sum_{i<j} \rho_{c,ij}(r) + \sum_{i<j<k} \rho_{c,ijk}(r) + ..., \tag{3.3}$$

$$j(r) = \sum_i j_i(r) + \sum_{i<j} j_{ij}(r) + \sum_{i<j<k} j_{ijk}(r) + ... \tag{3.4}$$

[1] Relativistic effects are proportional to p_i/m_i. Because the energies of the nucleons are below the nuclear mass, the nonrelativistic treatment is applicable (at least for mid-mass to heavy nuclei).

المنارة للاستشارات

Analogous expressions are required for the weak vector and axial vector charge and current operators. The one-body operators $\rho_{c,i}(r)$ and $j_i(r)$ describe respectively one-body nucleon charge and current density. These operators have been extensively used in nuclear physics. Much less studies consider also higher-order currents, which are commonly included in a phenomenological approach. A consistent treatment of these electro-weak currents is one of the major challenges of chiral effective field theory [81, 82, 83]. As discussed in Sec. 3.5, ch-EFT allows one to connect the low energy constants (LECs) entering in the inter-nucleon interaction (Eq. 3.2) with LECs involved in the expansion of electro-weak currents.

3.2 The nuclear force

The search for a description of inter-nucleon interactions consistent with the first principles of QCD has been one of the main goals of theoretical nuclear physics research. The inherent complexity of this problem led to the development of phenomenological approaches, which were largely adopted to describe the nuclear force and accepted as a unique path towards the microscopic description of the atomic nucleus. During the last decades, a great effort to link the description of the inter-nucleon interactions with the underlying theory of the strong interaction has led to promising results. The long-sought microscopic description of the nucleus is taking strong steps thanks to the developments on chiral effective field theory.

3.2.1 Phenomenological potentials

The starting point to calculate the nuclear Hamiltonian begins with obtaining the most realistic approximation of the inter-nucleon interactions (expression 3.2). For the NN potential, the most general structure of the non-relativistic NN interaction can be expressed as an operator acting on the momentum, spin, and isospin spaces describing nucleon states [84, 85]. The NN potential, can then be expressed in terms of several spin-space structures, whose unknown parameters can be determined from a fit of a large variety of NN scattering data. This has been the approach followed for the construction of high-precision phenomenological potentials such as the Nijmegen I,II [86], Argonne V_{18} [87], and CD-Bonn 2000 [88] potentials. A sketch of some of these phenomenological potentials is shown in Figure 3.1.

The NN phenomenological potential is commonly expressed as the sum of three terms: an electromagnetic (EM) part, the one-pion exchange (OPE) part,

المنارة للاستشارات

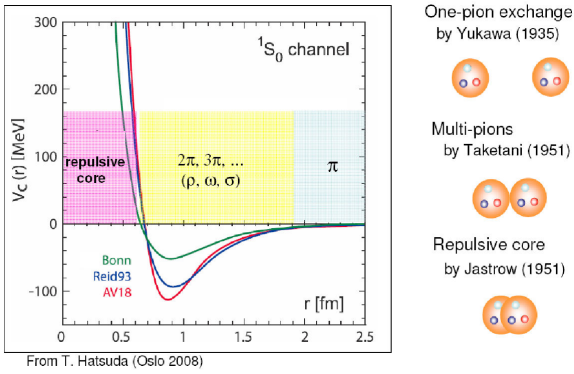

Figure 3.1: Model of a nuclear potential for different inter nucleon distances in the spin-singlet S-wave channel. Figure taken from Ref. [89].

and an intermediate- and short-range phenomenological part [85]

$$v_{ij} = v_{ij}^{\gamma}(\mathrm{EM}) + v_{ij}^{\pi}(\mathrm{OPE}) + v_{ij}^{R}. \tag{3.5}$$

In the attempt to use these NN phenomenological potentials in nuclear structure calculations, the inclusion of three-body forces, 3N, was shown to be essential to obtain an accurate description of nuclear properties [90, 91]. In contrast with NN potentials, 3N phenomenological potentials introduced a large collection of possible structures that can not be fully determined from the very limited experimental data [85]. Therefore, a strong model dependence is inevitable when 3N forces are included. As an example, the Urbana series of potentials [90] include 3N terms as a potential given by

$$v_{ijk} = v_{ijk}^{2\pi,P} + v_{ijk}^{R}, \tag{3.6}$$

where $v_{ijk}^{2\pi,P}$ is used to account for two-pion-exchange P-waves, and v_{ijk}^{R} contains the remaining shorter-range phenomenological part. Although phenomenological potentials including three-nucleon forces can be implemented to improve the description of nuclear structure observables, all phenomenological models lack a consistent treatment of many-body interactions. Overcoming this limitation has been one of the major achievements of chiral effective field theory [92].

المنارة للاستشارات

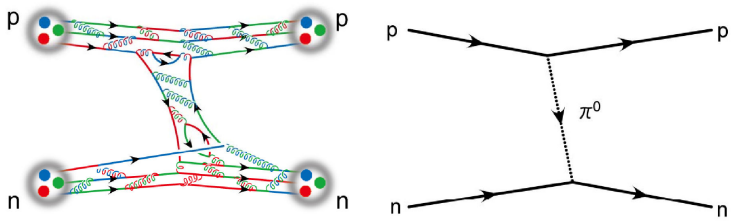

Figure 3.2: Diagram of the nucleon-nucleon interaction. Gluons and quarks degrees of freedom (left) are negligible at low energies, where pions and nucleons are the dominant degrees of freedom (right). Figure taken from Ref. [96].

3.2.2 Chiral effective field theory

The description of nuclear forces in the framework of Effective Field Theories (EFT) goes back to more than 50 years ago [93], but its application as a precision tool in nuclear physics was only possible thanks to the seminal work of Weinberg, originally proposed in 1990 [94]. As illustrated by Weinberg, at the low-energy scale of the nuclear physics, the pions and nucleons are the dominant degrees of freedom (Fig. 3.2), whose interactions are constrained by the broken chiral symmetry. Yukawa introduced the pion(meson) theory to describe the strong interaction between the nucleons much earlier [95], but chiral effective field theory has been the tool necessary to properly treat this problem, consistent with the underlying theory of the strong interaction, QCD. The general idea of effective field theories can be understood by comparing with the multipolar expansion of a charge distribution, $\rho(r)$, in classical electrodynamics [97]. The multipolar expansion can be seen as an approximation of the "underlying theory". If the potential is calculated at the distance R from the charge distribution, the ratio between R and the size of the charge distribution, a, provides a measurement of the "resolution scale". At long distances, $a \ll R$, only a few mutipolar terms might be needed to obtain an accurate description of the potential. Each multipolar term enters into the expansion with a certain weight ("a coupling constant"), i.e, the charge, dipole moment, quadrupole moment, etc. For shorter distances, higher resolution is needed, and higher order multipolar terms must be included.
An analog situation arises in the description of the inter-nucleon interactions. The effective Lagrangian can be expressed as an infinite sum of Feynman diagrams, and chiral effective field theory (chEFT) tell us the importance of the different diagrams (many-body terms) in a systematic expansion of powers, ν. Here the scale parameter is given by (Q/Λ_x), where Q is the generic

المنارة للاستشارات

moment (nucleon three-momentum, pion four-momentum, or a pion mass) and $\Lambda_x \sim 1$ GeV is the chiral symmetry breaking scale [29]. This approach allows a description of the nuclear force as a hierarchy in powers of $\nu = 0, 1, 2, ...$, where many-body terms appears systematically at higher orders. The hierarchy of the different many-body terms is illustrated in Figure 3.3.

Similarly to the expansion of a charge distribution, coupling constants appear with the addition of higher order terms. The leading order (lowest order), LO $\nu = 0$, is given by two momentum-independent contact terms $\sim (Q/\Lambda_x)^0$, shown in the first row of Figure 3.3 (a four-nucleon-leg graph with a small-dot vertex (left), and a static one-pion exchange (right)). The next order, $\nu = 1$, vanishes due to parity and time-reversal invariance. Two-pion exchange currents (2PE) appears in the next-to-leading order, NLO ($\nu = 2$), and seven contact terms emerged, represented by the four-nucleon-leg graph with a solid square in the second row of Figure 3.3. These seven contact terms, appear as low energy coupling constants (LECs), introduced as free parameters that must be fitted to experiments, commonly to NN scattering data and deuteron properties. At next-to-next-to-leading order, NNLO ($\nu = 3$), no new contact terms are introduced, but additional 2PE appear and the three-nucleon forces (3NF) emerge. The two LECs associated with the 3N forces can be fixed to three-body systems, e.g., the ^3H binding energy, and the neutron-deuteron scattering length. Once these constants (nine) are fixed, the theory can be used to predict nuclear structure observables. A detailed explanation of the structure of each term involved in the expansion can be found in Ref. [29].

The expansion at order NNLO has been shown to give a good description of binding energies of light nuclei up to $A \leq 12$ [98]. Adding a higher order, N^{3}LO ($\nu = 4$), increases the number of LECs to 24, but this step is necessary for accurate nuclear structure calculations [99]. The results obtained by including N^{3}LO [99, 100] are at the same level of accuracy of high-precision phenomenlogical potentials, e.g., the Argonne ν_{18} potential [87], which includes about 40 adjustable parameters.

In contrast to the phenomenlogical approaches traditionally used to obtain the nucleon-nucleon potentials (NN), chiral effective field theory allows a consistent treatment of the nuclear force as well as the electro-weak (EW) current operators [29, 81], involving consistent coupling constants in both descriptions. More details on EW currents operators are presented in the last section of this chapter.

Inter-nucleon interactions obtained from ch-EFT have been successfully applied to describe light and medium-mass nuclei [101, 102, 103], with a broad number of numerical methods, as will be discussed in the following sections. Among he major achievements has been the consistent inclusion of three-nucleon forces, wich have played a crucial role in the description of oxygen and calcium isotopes [30, 104, 11, 34].

المنارة للاستشارات

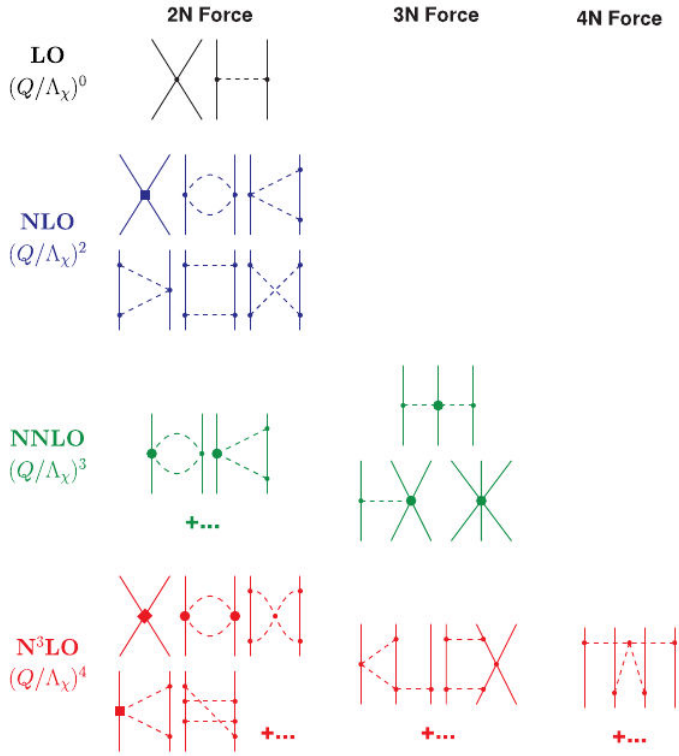

Figure 3.3: Hierarchy of nuclear forces in chiral effective field theory (ch-EFT). Solid lines represent nucleons and dashed lines pions. Small dots, large solid dots, solid squares, and solid diamonds denote vertices of index $\Lambda = 0, 1, 2$, and 4 (Figure taken from [29]). See text for details.

المنارة للاستشارات

Now that we have seen some possible ways to obtain "bare" inter-nucleon interactions, the following sections present several methods used to solve the many-body Schrödinger equation and their use in nuclear structure calculations.

Similarity Renormalization Group(SRG)

The similarity renormalization group (SRG) is based on a family of unitary transformations, $U(\lambda)$, used to divide the original Hamiltonian of a given problem in a diagonal part, $H^d(\lambda)$, and an off-diagonal part, $H^{od}(\lambda)$, such that [105]

$$H(\lambda) = U(\lambda)HU^\dagger(\lambda) \equiv H^d(\lambda) + H^{od}(\lambda) \to H^d(\infty), \tag{3.7}$$

with λ the flow parameter, such that

$$\frac{dH(\lambda)}{d\lambda} = \big[\frac{dU(\lambda)}{d\lambda}U^\dagger(\lambda), H(\lambda)\big]. \tag{3.8}$$

By an appropriate choice of H^d and H^{od}, one can tailor the evolution of the initial Hamiltonian to simplify a particular problem [105, 106]. SRG are widely used in different many-body calculations. Some of its applications are discussed in the following sections.

3.3 Shell-model theories

The single-particle model of the nucleus, as proposed by Mayer and Jensen [38, 39] had great success in explaining the global behaviour of stable nuclei. Since the pioneering work of Talmi [57], two-body interactions and higher order correlations were soon identified as necessary ingredients to describe the details of nuclear structure (see Ref. [107] for a historical review of the shell model). In the current "standard" shell-model calculations, nucleons are constrained inside an effective valence space, and the non-relativistic Schrödinger equation (Eq. 3.1) is solved "exactly"[2] for a given effective NN interaction that includes only one- and two-body terms. A schematic representation of the effective valence space used in standard shell-model calculations is shown in Figure 3.4. It is desired to solve the Schrödinger equation in the full Hilbert space, but given the infinite size of such space, the expression 3.1 must be approximated to a truncated model space of finite dimension d. Consequently, the nuclear

[2]The Schrödinger equation is solved for a truncated model space of finite dimension.

المنارة للاستشارات

Hamiltonian must be transformed to an effective operator, H', that depends on the size of the model space,

$$H'|\Psi_d\rangle = E_d|\Psi_d\rangle, \tag{3.9}$$

with $|\Psi_d\rangle$ the wave function in a truncated model space. Commonly, only two-nucleon interactions are included in the construction of the phenomenological nuclear Hamiltonian (Eq. 3.2), therefore, one- and two-body parts must be re-fitted to experimental data to account for neglected 3N interactions [108]. If the operator H' is renormalized, all physical operators such as rms radius and electromagnetic-moments operators must be renormalized according to the renormalization of the original Hamiltonian[3].
Independently of the path chosen to obtain the "bare" inter-nucleon interactions, the next challenge consists in deriving the "effective" NN interaction for a given model space. The repulsive core of the NN interaction results in an strong short-range repulsion and strong short-range tensor force, preventing a perturbative treatment of this problem. One of the most common methods used in the development of valence-space interactions is the so called Brueckner reaction matrix , G-matrix method [109]. Optionally, two body matrix elements can be derived from phenomenological potentials and re-fitted to experimental data in a particular region of the nuclear chart [110, 111]. Recently, interactions derived from chiral effective field theory have adopted alternative methods such as the low momentum interaction, V_{lowk}, and similarity renormalization group, SRG [112], that can be used to connect the "bare" inter-nucleon interactions with the valence space Hamiltonian. More details on these approaches are presented in the following sections.

3.3.1 Phenomenological interactions

Phenomenological interactions are commonly referred to as valence-space interactions with two-body matrix elements derived from phenomenological potentials (see sec. 3.2.1). The G-matrix method is one of the most used methods adopted to connect "bare" interactions with valence-space potentials. Kuo and Brown were the first to calculate G matrix elements for the sd and pf shells [113, 114], starting from the phenomenological Hamada-Johnston potential [115]. The effective interaction for the pf shell, referred as KB [114], was later re-adjusted to experimental data to obtain the so called KB3G interaction [116], which has been extensively used for nuclear structure calculations around the Ca region.

[3]The inevitable renormalization of operators is commonly used to justify the use of phenomenological "effective" operators in the shell model, but a consistent treatment of these operators is still lacking.

المنارة للاستشارات

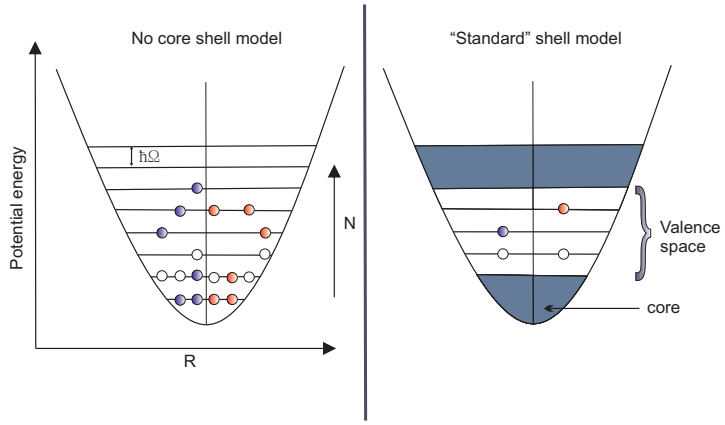

Figure 3.4: Sketch of the potential well of an harmonic oscillator and the single particle bases used for no-core shell model (left) and "standard" shell model calculations.

A different approach has been adopted to obtain the GXPF1A interactions [117], derived for the same region of the nuclear chart. This interaction starts from a G-matrix derived from the phenomenological Bonn-C potential [118], and two-body matrix elements are re-fitted to experimental data in the *pf* shell.
In all cases, the obtained effective phenomenological interaction is readjusted to compensate for initial and final three-body interactions and higher-order correlations that are not included in the construction of the valence-space interaction. It has been shown that a three-body correction affects mainly the monopole term of the effective potential and is indispensable to explain marked differences between theoretical and experimental results in the *p*, *sd* and *pf* shells [119]. A summary of the different effective interactions developed around the Ca region is shown in Figure 3.5. The "bare" inter-nucleon interactions can be transformed into "effective" valence-space interactions, which are then used to calculate nuclear structure observables within the shell-model approach.

3.3.2 Microscopic interactions

Chiral effective field theory, ch-EFT, allows a consistent disentanglement of the many-body forces. Inter-nucleon interactions can be adjusted to reproduce the properties of few-body systems (A $\leq$ 4), and then used to derive effective interactions for a given valence-space or used for *ab-initio* calculations. Such

المنارة للاستشارات

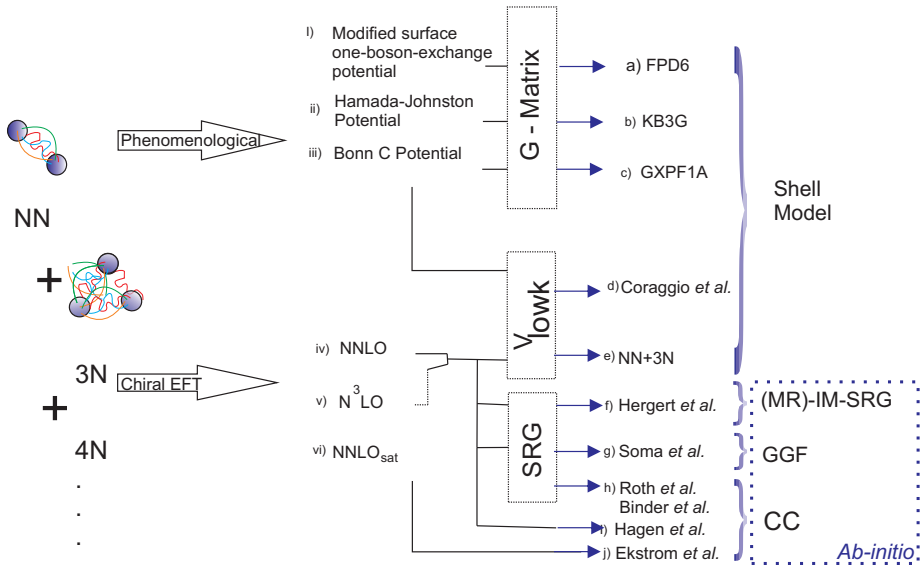

Figure 3.5: Nucleon-nucleon potential and effective interactions developed for Ca isotopes. The "bare" nucleon-nucleon potential is transformed into an "effective" interaction by using the most common methods: G-matrix, SRG, and V_{lowk}. The "effective" Hamiltonian is then used to calculate nuclear structure observables with the shell-model approach or/and *ab-initio* calculations. See text form more details. References: i) [120], ii) [115], iii) [118], iv) [99, 29], v) [121, 122], vi) [123], a) [120] b)[116], c)[117], d) [124, 125], e) [30, 34], f) [126], g) [127], h) [128, 32], i) [31], j) [123].

approaches have successfully been applied to describe the properties of oxygen [103, 129] and calcium isotopes [30, 31, 34].

Renormalization group (RG) transformations [112] can be used to decouple the relevant degrees of freedoms, separating the low momentum interaction [4] without changing the expected value of physical observables. As discussed in section 3.2.2, the hierarchy of many-body forces scales with the factor Q/Λ_x, with Q a generic momentum that depends on the physical process [5], and the parameter Λ the chiral-symmetry breaking scale[6] that defines the

[4] Low momentum interactions (≤ 2 fm^{-1}) are referred to potentials that do not couple low and high momenta.

[5] In the nucleus Q is of the order of the pion mass, m_π.

[6] Typically < 1 GeV

المنارة للاستشارات

convergence in the expansion of the many-body forces. The derived nucleon-nucleon interactions $V_{NN}(\Lambda)$, $V_{3N}(\Lambda)$, $V_{4N}(\Lambda)$,..., depend on the parameter Λ, used to decouple high- and low-momenta. Therefore, the importance of higher order-many body terms runs with the parameter Λ, which defines the resolution scale of the many-body expansion.
Renormalization group transformations allow one to lower Λ and preserve the truncation error [112], by using a unitary transformation, $U(\lambda)$, of the original Hamiltonian, such that

$$\langle\Psi|H|\Psi\rangle = [\langle\Psi|U^{\dagger}]UHU^{\dagger}[U|\Psi\rangle] = \langle\Psi^{\lambda}|H^{\lambda}|\Psi^{\lambda}\rangle. \tag{3.10}$$

The transformed Hamiltonian H^{λ} can be chosen to simplify the many-body calculations. Physical operators must be transformed accordingly, such that the expected values remain unchanged. An example of the evolution of NN matrix elements expressed in momentum bases, $V_{NN}(k,k')$, for different RG transformations is illustrated in Figure 3.6. For the V_{lowk} method, the parameter Λ can be chosen as a cutoff parameter to isolate the potential into a low-momentum interaction, preserving low-energy observables ($k < \Lambda$). Thus, perturbation techniques can be applied for the low-momentum potential, and the size of the bases employed are significantly reduced, accelerating drastically the convergence for numerical calculations (Figure 3.6a). The V_{lowk} potential, can then be used directly in nuclear structure calculations, providing an alternative to the commonly used G-matrix method. There are major differences between G-matrix and V_{lowk} low momentum potentials. The G-matrix is an "in-medium" interaction that depends on the density (on the nucleus) and requires a "starting energy". Furthermore, it does not decouple low- and high-momentum, meaning, it does not allow perturbative expansions [112]. Low momentum interactions by contrast evolve in free space, and decouple the low momentum part, allowing perturbative expansions.
In the SRG approach the off-diagonal terms are suppressed and the matrix elements are restricted to the diagonal part (Figure 3.6b) [105]. In contrast to V_{lowk}, SRG can be used to compute high-energy NN observables, and all operators renormalized under the same transformation.

The power of chiral effective field theory and RG methods, fitted only to a few-nucleon observables, has been shown with the excellent reproduction of nuclear structure observables of light- and medium-mass nuclei, e.g, Oxygen [103] and Calcium isotopes [30]. For Ca isotopes, the valence-space interaction, $NN + 3N$, was derived from the chiral potential N^{3}LO [99]. The use of this valence-space interaction in the valence space (pfg), has provided an excellent description of experimental observables in neutron rich Ca isotopes, such as two neutron separation energy [11], and low-lying excitation energies [34], and were also used in this work to excellently reproduce the ground-state electromagnetic

المنارة للاستشارات

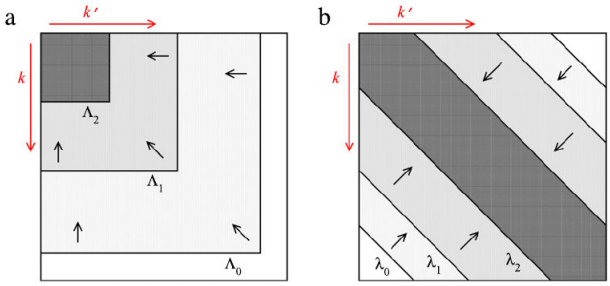

Figure 3.6: NN matrix elements expressed in momentum bases for the two major RG methods: a) V_{lowk} with Λ-dependence, and b) SRG with λ-dependence. Figure taken from Ref. [112].

moments of the neutron-rich Ca isotopes up to $N = 31$ [70][7].
More recent approaches have been proposed to derive nuclear shell-model interactions from "first principles" [130]. The suggested methods start with inter-nucleon interactions derived from chiral effective field theory, and use *ab-initio* calculations to obtain the inert core energy, single-particle energies and effective two-body matrix elements, which are the input for the standard shell-model calculations. Recently, such approach has been applied and compared with NCSM calculations in nuclei up to ^{19}F [131].
The assumption of effective operators has been a key ingredient of nuclear shell-model calculations. Proton and neutron effective charges, and effective nucleon g-factors are commonly introduced to reproduce the electromagnetic properties observed in the nucleus. Phenomenological and microscopic studies [132] have concluded that values significantly differ from the free-nucleon charges are needed to reproduce the observed nuclear electromagnetic properties: $e_p = 1.5e$ and $e_n = 0.5e$ have to be used to obtain a fair description of nuclear electrostatic properties. Magnetic properties by contrast are commonly reproduced by using relatively low quenching of the orbital and spin g-factors. Although the use of effective values is widely accepted as a standard ingredient in shell-model calculations, the origin of these values is not completely understood. As discussed in section 3.5, a consistent description of electro-weak operators from chiral effective field theory is one of the current efforts of modern nuclear theory [80, 133, 81, 83].

[7]Only one-body currents were used in the calculation of electromagnetic operators. The use of consistent operators with ch-EFT has not been implemented yet in medium-mass nuclei.

المنارة للاستشارات

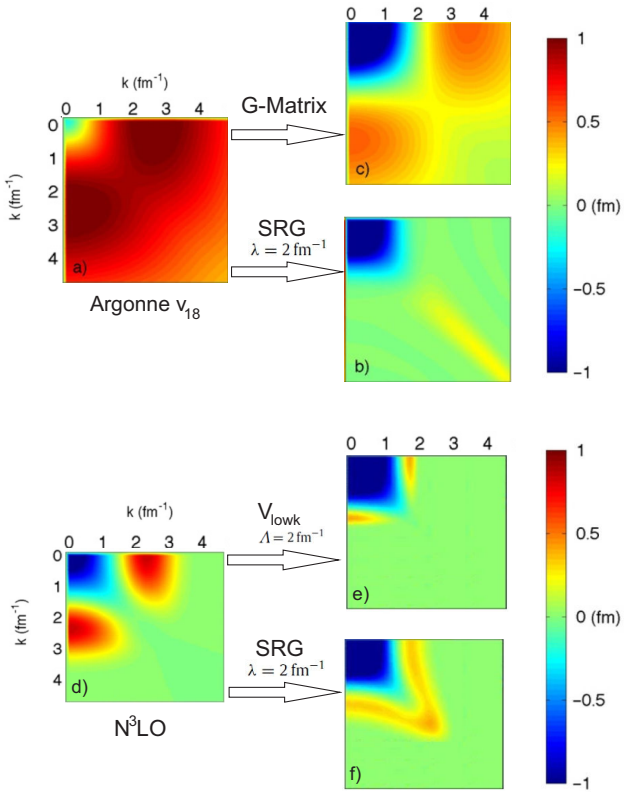

Figure 3.7: Example of evolution of NN matrix elements expressed in momentum bases for the $^3S_1$ channel for the phenomenological potential, Argonne ν_{18} [87](top), and a microscopic chiral potential, N^{3}LO [99](bottom). The phenomenological potential is evolved with: c) the traditionally used G-matrix approach, and with b) the SRG method. The chiral potential is evolved with the two major RG methods: e) V_{lowk} (Λ=2 fm^{-1}), and f) SRG (λ=2 fm^{-1}). Figures were adapted from [112].

المنارة للاستشارات

3.4 *Ab-initio* calculations

Independently of how inter-nucleon interactions are obtained, it is necessary to solve the many-body problem to obtain a description of the atomic nucleus. *Ab-initio* methods have benefited from the developments of ch-EFT, as it provides a consistent treatment of the nuclear force. Many-body terms can be included systematically to obtain the accuracy required for a given problem, and theoretical uncertainties can be controlled with the order of expansion.
One of the main challenges for *ab-initio* calculations is naturally their applicability in heavy and open-shell nuclei. For nuclei with mass number $A \geq 12$, the complexity of the problem requires not only enormous computational power, but also the development of a formalism that can make the problem tractable.

In the following section the most recent developments on *ab-initio* methods are discussed: Nuclear Lattice Effective Field Theory (NLEFT) [134, 135], No-Core Shell Model (NCSM) [136, 137], the in-medium similarity renormalization group approach (IM-SRG) [138], self-consistent Green's functions (SCGF) [33], Green's function Monte Carlo (GFMC) [139], and coupled-cluster expansion (CC) [31, 123].

3.4.1 The frontier of *ab-initio* calculations

Nuclear Lattice Effective Field Theory (NLEFT)

Monte Carlo methods used in lattice QCD calculations are being successfully applied to nuclear physics. In this scheme, the nucleons can be seen as point-like particles positioned on lattice sites, and inter-nucleon interactions are generated using auxiliar fields, consistent with ch-EFT. Calculations in the scheme of NLEFT, were the first *ab-initio* calculations that provided a description of the Hoyle state in ^{12}C [140]. More recently, it has been used to calculate the low-lying energy spectrum as well as electromagnetic properties of ^{16}O [141]. The most recent advances of such calculations have allowed to calculate ground-state energies of alpha-cluster nuclei up to ^{28}Si [134].

No-Core Shell Model (NCSM)

In NCSM calculations, the matrix representation of the nuclear Hamiltonian is constructed using a harmonic oscillator basis, and all nucleons are equally treated in a model space truncated to an excitation energy below $N_{max}\hbar\Omega$

المنارة للاستشارات

(see Figure 3.4). Once the large scale eigenvalue problem is solved, nuclear observables can be computed from the eigenstates [77]. Such approach requires an enormous computational effort, and currently the limits of these calculations have been extended up to ^{16}O [137], and attempts have been explored in heavier nuclei such as ^{19}F [131].

Green's function Monte Carlo (GFMC)

Quantum Monte Carlo methods are based on Feynman path integrals. The GFMC is one of the most accurate methods to calculate nuclear structure properties of light nuclei ($A \leq 12$)[139]. Commonly being used with phenomenological potentials [142], it was recently implemented with nuclear interactions derived from ch-EFT [143] up to $A = 4$ systems [144]. See Ref. [92] for a recent review of quantum Monte Carlo methods applied in nuclear physics.

In-Medium Similarity Renormalization Group(IM-SRG)

Instead of evolving the inter-nucleon interactions in free space (i.e. normal SRG), in-medium SRG (IM-SRG) is used to apply the SRG transformation directly in the many-body system [145]. One starts from the general second-quantized Hamiltonian [145, 146]

$$H = \sum_{ij} T_{ij} a_i^+ a_j + \frac{1}{2!^2} \sum_{ijkl} V^{(2)}_{ijkl} a_i^+ a_j^+ a_l a_k + \frac{1}{3!^2} \sum_{ijklnm} V^{(3)}_{ijklnm} a_i^+ a_j^+ a_k^+ a_n a_m a_l + ... \tag{3.11}$$

where all operators can be normal-ordered with respect to a finite-density reference state $|\Phi\rangle$ (e.g., the Hartree-Fock state):

$$H = E_0 + \sum_{kk'} f_{kk'} a_k^+ a_{k'} + \frac{1}{2!^2} \sum_{kpqr} \Gamma^{(2)}_{kpqr} a_k^+ a_p^+ a_r a_q + \frac{1}{3!^2} \sum_{kpqrst} W^{(3)}_{kpqrst} a_k^+ a_p^+ a_q^+ a_t a_s a_r, \tag{3.12}$$

where the coefficients i E_0, f and Γ are the normal ordered zero-, one-, and two-body operators. In IM-SRG, the flow equations (Eq. 3.7) are truncated to normal-ordered two-body operators. The former coefficients include induced three- and higher-body interactions through density-dependent factors [146]. This approach can be used to calculate nuclear structure observables, but can also be employed to derive effective Hamiltonians for shell-model calculations [147]. Up to day IM-SRG methods have been applied to closed-shell nuclei up to the Ni isotopes [138] and open-shell nuclei up to ^{16}O [148].

المنارة للاستشارات

Self-Consistent Green's Functions (SCGF)

In the second quantization scheme, the A-body Schrödinger equation is given by

$$H|\Psi_k^N = E_k^N|\Psi_k^N\rangle, \tag{3.13}$$

with the A-body Hamiltonian give by Eq. 3.11, and $|\Psi_0^N\rangle$ the A-body ground-state function. The key object of the Green's function formalism is the one-body operator [149]

$$iG_{ab}^{(N,N)}(t,t') = \langle\Psi_0^N|Ta_a(t)a_b^\dagger(t')|\Psi_0^N\rangle, \tag{3.14}$$

where T is the time-ordering operator (earlier times to the right) acting on $a(t)$ and $a^\dagger(t')$ defined in the Heisenberg representation. If G is known, one can compute all one-body operators and the two-body ground-state energy[149]. Similarly, A-body propagators can be defined to evaluate A-nucleon observables.

Different methods have been derived from the SCGF formalism, e.g, Dyson-SCGF have been successfully applied to doubly closed-shell nuclei of mass $A \sim 60$ [150], and more recently the use of self-consistent Gorkov-Green's function theory has allowed to apply these methods to open-shell nuclei up to ^{74}Ni [33, 151]

Coupled-Cluster (CC)

Originally derived for nuclear physics [152], and later used with great success in quantum chemistry [153], coupled-cluster theory has proved to be an efficient and versatile tool for *ab-initio* calculations of many-body systems. Its applications in nuclear physics have been expanding during the last few years [154]. The CC method is based on the similarity transformation

$$H \equiv e^{-T}H_N e^T, \tag{3.15}$$

with H_N the normal-ordered Hamiltonian [152, 153], and the n-particle-n-hole cluster operator $(np-nh)$ given by

$$T = \sum_{k=1}^{A} T_k \equiv \sum_{k=1}^{A} \frac{1}{(k!)^2} \sum_{i_1,\ldots,i_k;a_1,\ldots,a_k} t_{i_1,\ldots,i_k}^{a_1,\ldots,a_k} a_{a_1}^\dagger \ldots a_{a_k}^\dagger a_{i_k}\ldots a_{i_1}. \tag{3.16}$$

The applications in nuclear physics have been mainly restricted to $k = 2$, in the so called coupled-cluster singles doubles (CCSD) approximation [155, 31]. However, extensions to include higher-order correlations have recently been proposed to allow its application to open-shell nuclei [156, 157].

المنارة للاستشارات

The amplitudes t_i^a and t_{ij}^{ab} are obtained from the coupled-cluster equations

$$0 = \langle \phi_i^a | H | \phi \rangle \text{ and } 0 = \langle \phi_{ij}^{ab} | H | \phi \rangle, \tag{3.17}$$

where $|\phi_i^a\rangle = a_a^\dagger a_i |\phi\rangle$ and $|\phi_{ij}^{ab}\rangle = a_a^\dagger a_b^\dagger a_i a_j |\phi\rangle$ are respectively $1p-1h$ and $2p-2h$ excitations of the reference state $|\phi\rangle$.
The computational effort required by the CCSD approximation scales as $n_o^2 n_u^4$ [155], with n_o and n_u the occupied and unoccupied orbitals of the reference state. Hence, the practical applications of this method have been limited to closed-shell (± 1) systems, where calculations have been extended up to nuclei as heavy as ^{132}Sn [128].

Energy density functional

Mean field approaches have been a suitable tool to describe global properties of the atomic nucleus [158]. Although they offer a microscopic description of the nucleus, the coupling constants involved in the parametrization of the nuclear force can not be obtained by *ab-initio calculations*, instead, the inter-nucleon interactions are commonly adjusted to experimental bulk properties (charge radii and nuclear masses) of nuclei close to stability [159]. The fitted interactions can then be used to describe properties of unstable nuclei and global properties of nuclei in the entire nuclear chart, but does not provide a direct understanding of theoretical uncertainties [160].
Chiral effective field theory and RG methods have opened up the possibility to derive energy density functionals from ch-EFT [161]. By using a density matrix expansion (DME) [162], microscopic universal energy functionals can be constructed from low-momentum potentials obtained consistently from ch-EFT. This approach is still in development, and calculations have been reported in nuclei as heavy as ^{208}Pb, but as the authors stated, the results are too premature to be compared with experiment [163].

3.5 Electro-weak currents and effective operators

Our current knowledge of the nuclear force has revealed that the inter-nucleon interactions are mediated by pion exchanges at intermediate- and large-internucleon distances [164, 92]. Such considerations imply directly that electroweak currents (EW) must be expressed as many-body current operators. The influence of meson- and pion-exchange effects in electroweak observables

المنارة للاستشارات

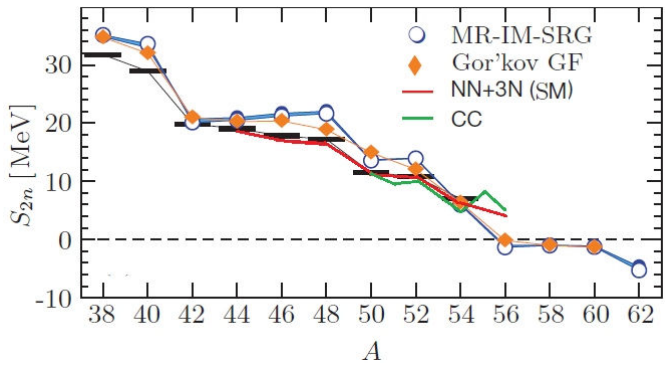

Figure 3.8: Comparison of experimental results with *ab-initio* and shell-model calculations obtained for the S_{2n} values of Ca isotopes. All calculations use interactions derived from ch-EFT. The figure has been modified from Ref. [126, 151].

dates back to Yukawa [95], and the importance of such effects has been widely recognized in observables such as magnetic moments [165]. However, a consistent and model-independent treatment of many-body effects in EW observables is still under development. The advances of chiral effective field theory [166] have opened a path to construct consistent EW operators, but up to recently, it has only been applied to describe electromagnetic properties of few nucleon systems [167, 133].

In this section we will discuss the construction of EW currents operators, starting with the common description of free individual nucleons, in the so-called impulse approximation (IA). Then, the many-body process necessary to obtain a consistent description of the atomic nucleus is introduced, and finally the ch-EFT theory is used to establish a direct link between the inter-nucleons interaction and EW currents.

3.5.1 Impulse approximation (IA)

The electromagnetic properties of the nucleus are given by the movement of protons and neutrons confined in a spatial region. In the impulse approximation

المنارة للاستشارات

the nuclear charge and current density distributions are given by [80]

$$\rho_e^{IA}(r) = \sum_{i=1}^{A} e g_L^{(i)}, \tag{3.18}$$

and

$$\mathbf{j}^{IA} = \frac{e}{2m_n}[g_L^{(i)}\rho_e(r)\mathbf{K_i} + i g_S^{(i)}\sigma_\mathbf{i} \times \mathbf{q}], \tag{3.19}$$

where m_n is the nucleon mass, $\mathbf{S_i}$ is the spin operator proportional to the Pauli operator, $\mathbf{S_i} = \sigma_\mathbf{i}/2$, $g_S^{(\nu)} = -3.826$ and $g_S^{(\pi)} = 5.587$ the spin gyromagnetic factors of the neutron and proton, respectively [168]. Both, protons and neutrons should be considered, since orbital and spins currents contribute to the magnetic distribution. Because the neutrons do not have charge, only protons contribute to the sum, i.e., for protons $g_L^{(\pi)} = 1$, and $g_L^{(\nu)} = 0$ for neutrons. Finally, $\mathbf{K_1} = (p_i' + p_i)/2$ is the average value between the initial momentum, p_i, and final momentum, p_i', of the nucleon i, and q is the transferred momentum[8]. Like in classical electrodynamics, electric and magnetic fields can be described by the electromagnetic multipole moments, with electric multipole moments defined as

$$\mathbf{Q}_{lm} = \int \mathbf{r}_i^l Y_{lm}^*(\theta_i, \phi_i)\rho_e(r)dr, \tag{3.20}$$

where $Y_{lm}(\theta_i, \phi_i)$ is the normalized spherical harmonic function. A similar relation is obtained for the magnetic multipole moments [169]

$$\mathbf{M}_{lm} = \frac{-1}{c(l+1)} \int \mathbf{j}(\mathbf{r}) \cdot (\mathbf{r} \times \nabla)\mathbf{r}_i^l Y_{lm}^*(\theta_i, \phi_i)dr, \tag{3.21}$$

Using approximations detailed in equations 3.18 and 3.19 and combining these equations with equations 3.20, and 3.21, the multipole operators can be re-written as [168]

$$\mathbf{Q}_l = e\sum_{i=1}^{A} g_L^{(i)}\mathbf{r}_i^l P_l(\theta_i), \tag{3.22}$$

and

$$\mathbf{M}_l = \frac{e\hbar}{2mc}\sum_{i=1}^{A}[\nabla \mathbf{r}_i^l P_l(\theta_i)].\left[g_L^{(i)}\frac{2}{l+1}\mathbf{L}^i + g_S^{(i)}\frac{\sigma_\mathbf{i}}{2}\right], \tag{3.23}$$

where, $P_l(\theta_i) = \sqrt{\frac{4\pi}{2l+1}}Y_{l0}(\theta_i, \phi_i)$, are the Legendre polynomials. The parity of these operators is $(-1)^l$ and $(-1)^{l+1}$ for $\mathbf{Q}_l$ and $\mathbf{M}_l$, respectively. Therefore, for nuclear states with definite parity, there are only non-vanishing even electric

[8] Momentum of external field ≡ photon momentum

المنارة للاستشارات

moments and odd magnetic moments [9], given that the expectation values for multipole operators with odd parity vanish. Here, we focus our discussion on the magnetic dipole operator, $\mathbf{M_1}$, and quadrupole moment operator, $\mathbf{Q}_2$, which are given respectively by

$$\mathbf{M}_1 = \sum_i (g_L^{(i)} \mathbf{L_i} + g_S^{(i)} \sigma_\mathbf{i}), \tag{3.24}$$

and

$$\mathbf{Q}_2 = e \sum_{i=1}^{A} g_L^{(i)} \mathbf{r}_i^2 P_2(\theta_i). \tag{3.25}$$

The magnetic moment is commonly expressed in units of nuclear magneton, $\mu_N = \frac{e\hbar}{2mc}$. The magnetic dipole moment, μ, and electrostatic quadrupole moment, Q, are defined as the expectation value of the operators given by expressions 3.24 and 3.25, along the z component, with magnetic substate $m = I$,

$$\mu \equiv \langle I, m = I \mid \mathbf{M_1} \mid I, m = I \rangle. \tag{3.26}$$

and

$$Q \equiv \langle I, m = I \mid \mathbf{Q_2} \mid I, m = I \rangle. \tag{3.27}$$

The proportionality between the magnetic moment and the nuclear spin is the so called g-factor, such that $\mu = gI\mu_N$ [67]. As very small modification of the nuclear states can cause considerable changes in the magnetic moment [171, 172], this factor is therefore commonly used to understand the mixing of different configurations within the shell-model framework [67].

3.5.2 Nucleon-nucleon interaction and electro-weak currents

The gauge invariance of the electromagnetic theory and the requirement of the charge conservation led to a direct link between the Hamiltonian, H, and the EW currents, via the continuity equation [80]

$$\mathbf{q}.\mathbf{j} = [\mathbf{H}, \rho], \tag{3.28}$$

with $\mathbf{q}$ the momentum associated with the external photon field, and ρ and $\mathbf{j}$ the charge and current density, respectively. Considering the IA approximation only, with $\rho_\mathbf{e}^\mathbf{IA}$ and $\mathbf{j}^\mathbf{IA}$ given by expressions 3.18 and 3.19, one can show that expression 3.28 is satisfied only for the kinetic energy part of the nuclear Hamiltonian, i.e.,

$$\mathbf{q}.\mathbf{j}^\mathbf{IA} = [\frac{\mathbf{p_i}}{2m_i}, \rho_\mathbf{e}^\mathbf{IA}]. \tag{3.29}$$

[9] It is strictly valid for non-degenerate states, and applies for the nuclear ground states with center of gravity at rest [170].

المنارة للاستشارات

One thus realizes that the description based on the IA approximation is incomplete. One must find the corresponding charge and current densities that satisfy the continuity equation (eq. 3.28) for each part of the nuclear Hamiltonian. For example, if now we take the standard one-pion exchange (OPE) potential of expression 3.5 as

$$v_{ij}^{\pi}(\mathrm{OPE}) \equiv \nu_{\pi}(\mathbf{k}) = \frac{-g_A^2}{F_\pi^2}\tau_{\mathbf{i}}.\tau_{\mathbf{j}}\frac{\sigma_{\mathbf{i}}.\mathbf{k}\sigma_{\mathbf{j}}.\mathbf{k}}{\omega_k^2}, \tag{3.30}$$

with $\sigma_{\mathbf{i}}$ and $\tau_{\mathbf{i}}$ the nucleonic spin and isospin Pauli matrices, and $\mathbf{k} = p' + p$ being the addition of the momenta of two nucleons with p and p', respectively. The energy of the exchanged pion is given by $\omega_k = \sqrt{k^2 + m_\pi^2}$. The continuity equation is satisfied by using the commonly used OPE current [173]

$$\mathbf{j}_\pi = -ie\frac{g_A^2}{F_\pi^2}(\tau_{\mathbf{i}} \times \tau_{\mathbf{j}})_z\left(\sigma_{\mathbf{i}} - \mathbf{k}_{\mathbf{i}}\frac{\sigma_{\mathbf{i}}.\mathbf{k}_{\mathbf{i}}}{\omega_{k_i}^2}\right)\frac{\sigma_{\mathbf{j}}.\mathbf{k}_{\mathbf{j}}}{\omega_{k_j}^2} + i \rightleftharpoons j, \tag{3.31}$$

such that

$$\mathbf{q}.\mathbf{j}_\pi = [\mathbf{v}_\pi, \rho_{\mathbf{i}}^{\mathbf{IA}} + \rho_{\mathbf{j}}^{\mathbf{IA}}]. \tag{3.32}$$

In this way, one can construct the different phenomenological currents that are consistent with the different structures of the nuclear Hamiltonian, commonly referred as model-independent, due to the fact that they are constrained by the continuity equation. This has been the approach used in different *ab-initio* calculations [174, 175, 164]. However, the continuity equation does not constrain EW currents that are orthogonal to the momentum $\mathbf{q}$. Therefore, this phenomenological approach does not allow a consistent treatment of these currents, which have large contributions to the EW operators, e.g., transverse meson-exchange currents (MEC). Systematic studies of EW properties in light nuclei have shown that these transverse currents contribute with up to ~ 50 % of the IA results [139, 142].

3.5.3 Chiral electro-weak currents

The great advantage introduced by chiral effective field theory regarding the consistent treatment of many-body forces (Sec. 3.2.2), also concerns electroweak currents in the atomic nucleus. The structure and hierarchy of many-body currents can be introduced consistently with the one at play for inter-nucleon interactions. In contrast with the phenomenological approach, transverse currents emerge naturally in ch-EFT.

Electromagnetic current operators scaling with pion and nucleon momenta, Q, at different orders in ch-EFT are shown in Figure 3.9. The leading order, LO,

المنارة للاستشارات

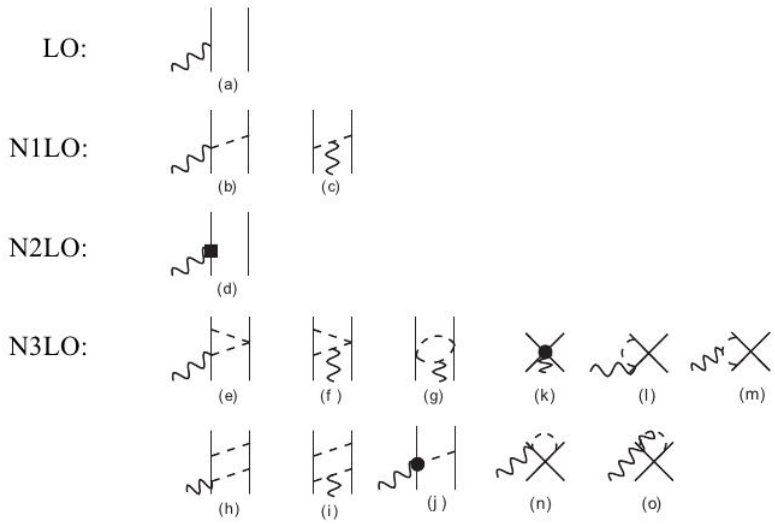

Figure 3.9: Diagrams illustrating one- and two-body electromagnetic current operators entering at order LO (Q^{-2}), NLO (Q^{-1}), NNLO (Q^0) and N3LO (Q^1) in ch-EFT. Solid lines represent nucleons and dashed lines pions. Photons are represented by wavy lines. (Figure taken from Ref. [92]). See text for more details.

corresponds to the commonly known one-body current [167]

$$\mathbf{j^{LO}} \equiv \mathbf{j^{IA}} = \frac{e}{2m_n}[2e_{N,1}\mathbf{K_1} + i\mu_{N,1}\sigma_\mathbf{1} \times \mathbf{q}], \tag{3.33}$$

with

$$e_{N,i} = (G_E^S(q^2) + G_E^V(q^2)\tau_{i,z})/2,\ \mu_N = (G_M^S(q^2) + G_M^V(q^2)\tau_{i,z})/2 + 1 \rightleftharpoons 2, \tag{3.34}$$

where τ_z is the Pauli isospin projection equal to $+1$ for protons, and -1 for neutrons. $G_E^S(G_E^V)$ and $G_M^S(G_M^V)$ are the isoscalar (isovector) combinations of the proton and neutron electric (E) and magnetic (M) form factors, normalized as $G_E^S(0) = G_E^V(0) = 1$, $G_M^S(0) = 0.880\ \mu_N$, and $G_M^V(0) = 4.706\ \mu_N$ [176]. Therefore, the well known one-body current contribution to the nuclear magnetic dipole moment is given by

$$\mu = \frac{1}{2}\sum_i \mathbf{r_i} \times \mathbf{j^{LO}} = \sum_i (e_{N,i}\mathbf{L_i} + 2\mu_{N,i}\mathbf{S_i}), \tag{3.35}$$

المنارة للاستشارات

Constants $e_{N,\pi} = 1$ and $2\mu_{N,\pi} = 5.586$ are the so called free orbital and spin gyromagnetic ratio of the proton, with $e_{N,\nu} = 0$ and $2\mu_{N,\nu} = -3.826$ denoting the same for the neutron. The latter correspond to the factors $g_S^{(\nu)}$ and $g_S^{(\pi)}$ in expression 3.19.

The next-to-leading order, NLO, includes the seagull and in-flight long range contributions due to one-pion exchange (OPE), represented in Fig. 3.9b and 3.9c, respectively. Their explicit structure given by [177] is

$$\mathbf{j_b^{NLO}} = -ie\frac{g_A^2}{F_\pi^2}(\tau_\mathbf{1} \times \tau_\mathbf{2})_z \sigma_\mathbf{1} \frac{\sigma_\mathbf{2}.\mathbf{k_2}}{\omega_{k_2}^2} + 1 \rightleftharpoons 2, \tag{3.36}$$

$$\mathbf{j_c^{NLO}} = ie\frac{g_A^2}{F_\pi^2}(\tau_\mathbf{1} \times \tau_\mathbf{2})_z \frac{\mathbf{k_1} - \mathbf{k_2}}{\omega_{k_1}^2 \omega_{k_2}^2} \sigma_\mathbf{1}.\mathbf{k_1} \sigma_\mathbf{2}.\mathbf{k_2}, \tag{3.37}$$

with $k_i = p_i' - p_i$. These isovector currents contain two known low-energy constants (LECs): the axial coupling constant $g_A = 1.29$ and the pion decay amplitude $F_\pi = 184.6$ MeV [167]. These are the same LECs that enter in the description of the inter-nucleon interactions.

The next-to-next-to-leading order contributions, N2LO, correspond to relativistic corrections to the LO current, such that no new LEC is introduced. The explicit form of this current and of the magnetic dipole moment contribution can be found in Ref. [177] and [167], respectively. At next-to-next-to-next-to-leading order, N3LO, six types of currents arise, including one-loop diagrams displayed in Figure 3.9e -3.9i and Figure 3.9l -3.9o. These contributions come from purely isovector currents, and only involve the known LECs, g_A and F_π. Up to these diagrams, no new parameters have been introduced.

New LECs appear in the diagrams (j) and (k) in Figure 3.9. The current due to diagram 3.9(j) can be separated in minimal, $\mathbf{j_{j,min}^{N3LO}}$, and nonminimal, $\mathbf{j_{j,nm}^{N3LO}}$, contributions [167]. The former involve seven LECs, which are directly connected with interactions derived from ch-EFT. On the other hand $\mathbf{j_{j,nm}^{N3LO}}$ involves two new LECs, and three new LECs arise from the N3LO OPE current (Figure 3.9(k)). These new five LECs do not appear in the inter-nucleon interactions, and thus, need to be fixed to EM observables, e.g., magnetic moments of light nuclei, Δ-resonance saturation [176, 178], and/or Gamow-Teller matrix elements [179].

Up to know, the description of EM properties in the framework of ch-EFT has only been possible in light nuclei [167, 176, 180]. Magnetic moments have been shown to be particularly sensitive to two-body currents. Figure 3.10 shows the results of magnetic moments from quantum Monte-Carlo calculations with consistent EW currents and inter-nucleon interactions derived from ch-EFT. For instance, QMC calculations have revealed that MEC currents induce changes of the order of 40 % in the magnetic moment of ^{9}C [167]. For medium- and heavy-mass nuclei, the electromagnetic properties are commonly

المنارة للاستشارات

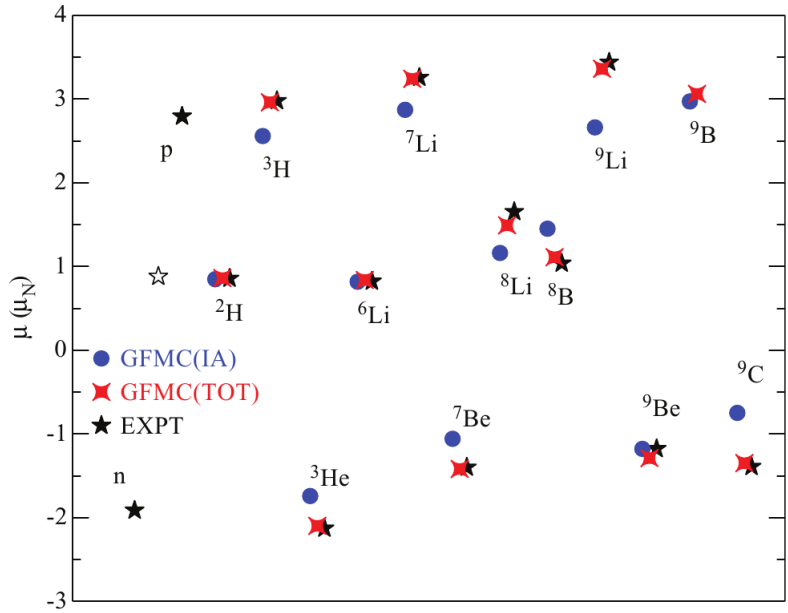

Figure 3.10: Magnetic moments from quantum Monte-Carlo calculations with consistent NN interactions and EW currents derived from ch-EFT. Experimental points are shown as black stars. Blue points show the predicted values considering the IA current only, and red starts show the total many-body current up to o N^{3}LO order. Figure taken from Ref. [167].

approximated by the LO operator without explicit inclusion of higher-order many-body currents, such that effective coupling constants are introduced in a rather phenomenological way. In view of a microscopic description of the atomic nucleus, a consistent description of EM operators is thus one of the main current goals of ch-EFT [82, 181, 182, 83].

Nuclear charge radius

The root-mean square (rms) charge radius is defined as a measurement for the spatial extension of the nuclear charge density

$$r_{ch}^2 = \frac{\int \rho_c(r) r^2 d^3r}{\int \rho_c(r) d^3r}, \tag{3.38}$$

المنارة للاستشارات

with $\rho_c(r)$ the charge density given by expression 3.18. To our knowledge the many-body terms present in the charge density expansion have not been studied yet within the framework of ch-EFT. Effects beyond the one-body term ($\rho_{c,i}(r)$) have been recognized in the literature [183], but only included in a phenomenological way. The rms charge radius is commonly expressed as [184]

$$\langle r_{ch}^2 \rangle = \langle r_{pp}^2 \rangle + \langle R_p^2 \rangle + \frac{N}{Z} \langle R_n^2 \rangle + \frac{3\hbar^2}{4m_p^2 c^2} + r_{SO}^2 + r_{MEC}^2, \tag{3.39}$$

where r_{pp} is the point-proton radius, $\frac{3\hbar^2}{4m_p^2 c^2} = +0.033$ fm^2 is the Darwin-Foldy correction [184], while $R_n^2 = -0.1149(27)$ fm^2 [43] and $R_p = +0.8775(51)$ fm [185] denote the rms radius of the neutron and proton, respectively. The terms r_{SO}^2 and r_{MEC}^2 stand respectively for the spin-orbit [186] and meson-exchange corrections [184].

المنارة للاستشارات

Chapter 4

Collinear laser spectroscopy: Optical detection.

The optical hyperfine structure (hfs) spectra of neutron-rich $^{40-52}$Ca isotopes were measured by using high-resolution bunched-beam collinear laser spectroscopy at the COLLAPS beam line. The first part of this chapter presents a description of the experimental setup and the procedure followed to analyze the measured hfs spectra. In a second part it is explained how and which nuclear properties were determined for the first time: the ground state spin of ^{51}Ca, the gs quadrupole moments of ^{47,49,51}Ca, gs magnetic moments of ^{49,51}Ca, and rms charge radii of ^{49,51,52}Ca.

4.1 From the atom to the nucleus

It is the main goal of our study to understand the atomic nucleus, but as will be described in this section, the atomic system provides a suitable scenario to extract valuable nuclear structure information. By observing the hyperfine structure (HFS) of an atom (or ion), the nuclear electromagnetic moments, spin and changes in the rms charge radius can be obtained independently of any model of nuclear forces.

المنارة للاستشارات

4.1.1 Hyperfine structure

The size and the shape of the nucleon distribution influence the energy of the surrounding electrons. The magnetic and electric interactions between the nucleus and the electrons cause the splitting of electronic fine structure energy levels, leading to the hyperfine structure. The nuclear magnetic dipole moment, μ, interacts with the magnetic field, B_e, produced by the electrons. This effect results in the coupling of the nuclear spin $\boldsymbol{I}$, with the atomic angular momentum $\boldsymbol{J}$, yielding a total angular momentum

$$\boldsymbol{F} = \boldsymbol{I} + \boldsymbol{J}, \tag{4.1}$$

Then, one hyperfine multiplet contains $2J + 1$ or $2I + 1$ (the smaller of these two) different components. The magnetic interaction is then given by[187]

$$E_\mu = \langle \boldsymbol{\mu}.\boldsymbol{B_e} \rangle = \frac{AC}{2}, \tag{4.2}$$

with

$$A = \frac{\mu_I B_e(0)}{IJ}, \tag{4.3}$$

and

$$C = F(F+1) - I(I+1) - J(J+1). \tag{4.4}$$

On the other hand the interaction between the electrostatic nuclear quadrupole moment, Q_s, and the electric field gradient $\dfrac{\partial^2 V}{\partial^2 z}$ along the symmetry axis, z, produced by the electrons is given by:

$$E_Q = \frac{B}{4} \frac{(3/2)C(C+1) - 2I(I+1)J(J+1)}{I(2I-1)J(2J-1)}, \tag{4.5}$$

where C is the same constant as in Eq. 4.4, and the hyperfine coupling constant, B, is defined as

$$B = eQ_s \frac{\partial^2 V}{\partial^2 z}. \tag{4.6}$$

Therefore, if the hyperfine parameters, A (Eq. 4.3) and B (Eq. 4.6) are known, the nuclear magnetic moment and nuclear quadrupole moment can be obtained, provided that the magnetic field and the electric field gradient produced by the electrons are known. If the nuclear structure parameters and hyperfine structure constants are known for a reference isotope, $B_e(0)$ can be extracted from expression 4.3

$$B_e(0)|_{ref} \equiv \frac{A_{ref} I_{ref} J}{\mu_{I_{ref}}}, \tag{4.7}$$

المنارة للاستشارات

where A_{ref} is the reference isotope magnetic dipole constant, and I_{ref}, $\mu_{I_{ref}}$ are the nuclear magnetic dipole moment and nuclear spin of the reference isotope, respectively. Thus, the magnetic moments of other isotopes can then be obtained as

$$\mu_I = \frac{AIJ}{B_e(0)|_{ref}} = AI\frac{\mu_{I_{ref}}}{A_{ref}I_{ref}}. \tag{4.8}$$

Similarly, if the quadrupole hyperfine constant and nuclear quadrupole moment are known for a reference isotope $\left(\frac{\partial^2 V}{\partial^2 z}|_{ref} \equiv B_{ref}/Q_{s_{ref}}\right)$, the nuclear quadrupole moment can be obtained form the measured quadrupole hyperfine structure constant via

$$Q_s = B\left(e\frac{\partial^2 V}{\partial^2 z}|_{ref}\right)^{-1} = B\frac{Q_{s_{ref}}}{B_{ref}}. \tag{4.9}$$

Isotope shifts and nuclear charge radii

A change of the number of neutrons causes a redistribution of the protons, modifying slightly the energy of the electrons. This shift of energy between two isotopes A and A' is the so called isotope shift, $\delta\nu^{A,A'}$.
The isotope shift is caused by two effects: the change of the kinetic energy of the nuclear motion in the rest frame when neutrons are added or removed, known as a mass shift, and a field shift that is proportional to the rms nuclear charge radius

$$\delta\nu^{A,A'} = K_{MS}\frac{M_{A'} - M_A}{M_{A'}M_A} + F\delta\langle r^2\rangle^{A,A'}, \tag{4.10}$$

where M_i is the mass of the isotope i, F is the field shift factor, K_{MS} is a factor which is transition dependent, and can be divided in two parts: $K_{MS} = K_{NMS} + K_{SMS}$. The factor $K_{NMS} = m_e\nu_0$, with ν_0 the transition frequency, is the normal mass shift factor related to a shift in the transition frequency. The specific mass shift, K_{SMS}, takes into account the effect of the nucleus on the electron momenta. Therefore, if K_{MS} and F are known, a measurement of the isotope shift, $\delta\nu^{A,A'}$, can be used to obtain the change in rms nuclear charge radius, via the expression

$$\delta\langle r^2\rangle^{A,A'} = \frac{\delta\nu^{A,A'}}{F} - K_{MS}\frac{M_{A'} - M_A}{FM_{A'}M_A}. \tag{4.11}$$

المنارة للاستشارات

4.2 Experimental Setup

The experiments were performed in the Isotope Separation Online DEvice, ISOLDE [188]. ISOLDE is part of the great complex of experimental facilities that is located at the European Organization for Nuclear Research, CERN. At ISOLDE, exotic nuclei are produced from nuclear reactions induced by high-energy proton beams (1.4 GeV) impinging on heavy targets. Pulses of protons from the proton synchrotron booster (PSB) can be directed to one of the two target stations available at ISOLDE. The first one is attached to a General Purpose Separator (GPS) providing a mass-resolving power of about 1000. An independent second station is connected to the High-Resolution Separator (HRS), reaching a higher resolving power of more than 5000.
The exotic Ca isotopes studied in this thesis were extracted from reactions of 1.4 GeV proton pulses of 5 μC on an uranium carbide target at the HRS station. The typical temporal spacing between proton pulses was around of 2.4 s. Since a large variety of different nuclei are produced in the reaction, the Ca isotopes were selected from the reaction products by using a three-step laser ionization scheme provided by the Resonance Ionization Laser Ion Source (RILIS) [189, 190]. The selected ions are extracted from the ion source and accelerated up to 30 keV or 40 keV (see section 4.2.1) to be mass separated by the two electromagnets of the HRS separator. A layout of the ion path from the target area to the COLLAPS beam line is shown in figure 4.1. After mass separation, ions are injected into the ISOLDE radio-frequency quadrupole (RFQ) beam cooler, ISCOOL [191]. This gas-filled linear Paul trap (ISCOOL), is used to bunch the beam. It also reduces the transverse and longitudinal energy spread of the ions[1], although the observed Doppler-broadening line width is not significantly different when using or not using the cooler. The electrode potentials can be tuned remotely to modify the cooling potential and control the trapping time in the milli-second scale. A sketch of the cooling process is shown in Figure 4.2. A trapping potential (solid line) is applied to reduce the energy and accumulate the incoming ions during a given time, T_1. After the accumulation time the electrode potential is swapped to ejection mode (dashed line). The ion beam is extracted from the cooler in bunches of low energy spread (< 5 eV) and well defined time structure (~ 5 μs). The beam energy of each bunch is given by the ISCOOL platform potential, V_{ISCOOL}, which is approximately the same voltage applied to the target potential.

[1] The reduction is mainly appreciable for plasma ion sources.

المنارة للاستشارات

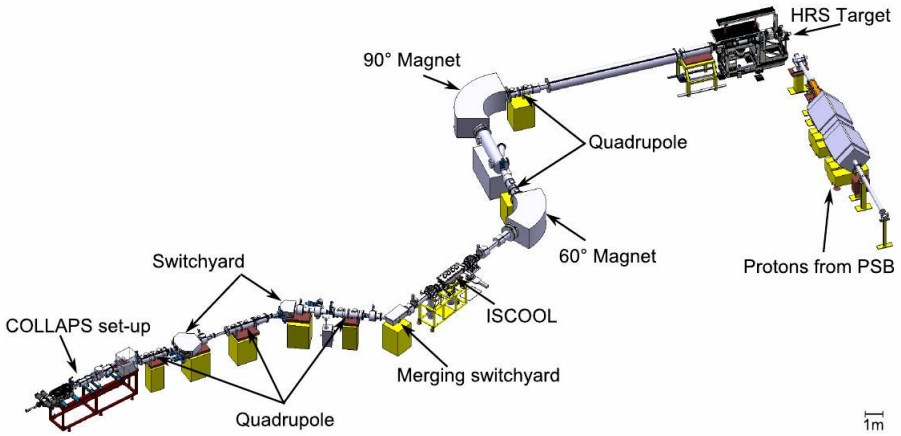

Figure 4.1: Layout of ISOLDE beam line from the HRS target to the COLLAPS setup.

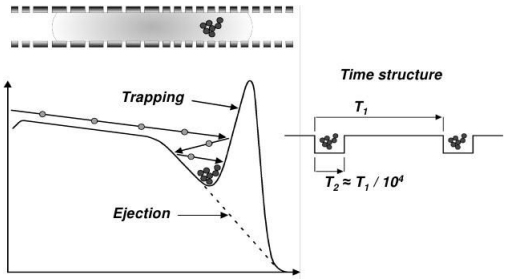

Figure 4.2: Applied longitudinal potential in ISCOOL. Ions are trapped by a potential barrier of about 60 V(continuous line), and after a time interval T_2, the voltage is switched from $\sim$ 60V to 0 V to eject the ions (dashed line).

4.2.1 COLLAPS beam line

A sketch of the different experimental processes from the ion-beam production to fluorescence detection is shown in Figure 4.3. The Ca ions were trapped for approximately 50 ms, and extracted in bunches of about 5 μs temporal width. They were directed to the dedicated beam line for collinear laser spectroscopy experiments, COLLAPS. At COLLAPS, the bunches of ions at energy eV_{ISCOOL} were superimposed with a continuous wave (cw) laser beam fixed at $\sim$393-nm wavelength, close to the $4s\ ^2S_{1/2} \rightarrow 4p\ ^2P_{3/2}$ transition in

المنارة للاستشارات

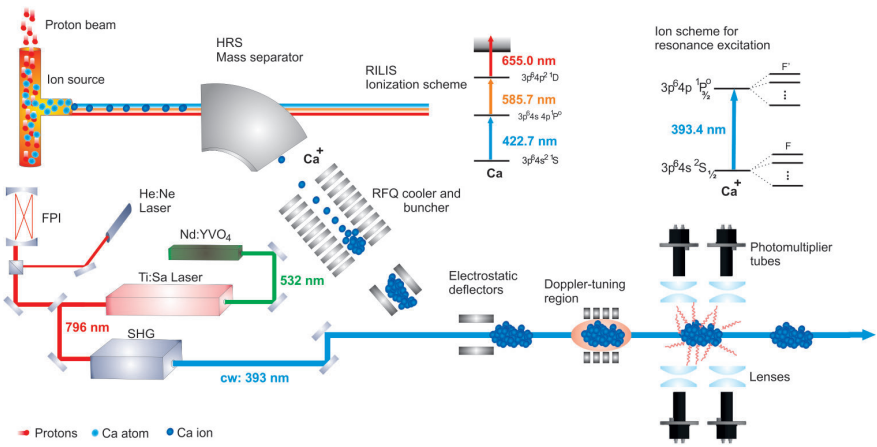

Figure 4.3: Short-lived Ca isotopes are produced from nuclear reactions of high-energy protons impacting on an uranium carbide target. Ca atoms were selectively ionized by using a three-step laser scheme [190]. Ions were extracted from the trap and mass separated to be injected into a radio frequency trap, ISCOOL. Bunches of ions were extracted and redirected into the COLLAPS beam line to perform collinear laser spectroscopy experiments. At COLLAPS, the ions are superimposed with a continuous wavelength laser beam to scan the hyperfine structure in the $4s\ ^2S_{1/2} \rightarrow 4p\ ^2P_{3/2}$ transition of Ca^+ (see text for more details).

المنارة للاستشارات

Ca^+. The cw laser beam at ∼393-nm wavelength was obtained from a second-Harmonic generation (SHG) [2] of a Ti:Sa laser [3], pumped with 532 nm light from a cw Nd:YVO_4 laser. The laser frequency was locked to a Fabry-Perot interferometer, which was in turn locked to a polarization-stabilized HeNe laser, reducing the laser frequency drift to < 10 MHz per day.

For the experiments described in this work, two different platform potentials V_{ISCOOL}=30 kV and V_{ISCOOL}=40 kV were used. Along the COLLAPS setup, the ions are exposed to two different potentials. A fixed potential, V_{prema}, typically between ±10 kV is used to shift the laser frequency in the ions reference frame to a value close to the frequency of the ionic transition, which is different for each isotope due to the kinematic and isotope shifts. Thereupon, a second scanning potential, is applied to Doppler-tune the laser frequency over the whole hyperfine pattern. The total external potential applied to the ion beam at the end of the COLLAPS beam line can be expressed as

$$V \equiv V_{total} = V_{ISCOOL} + V_{prema} + kV_{line}. \tag{4.12}$$

The post-acceleration voltage, V_{prema}, is set to a fixed value and recorded automatically at the start of each hfs measurement with a digital multimeter, Prema 6040, connected to a voltage divider (1:1000). The platform potential V_{ISCOOL} is constantly monitored and recorded during the experiment.
The scanning potential, kV_{line}, is provided by amplifying a 18 Bit analog output (-10 V$< V_{line} <$ +10 V). The amplification factor, k, is referred as the *kepco factor*. It takes typical values of ~ 50, and should be constantly calibrated as it could fluctuate during each experiment.

Doppler tuning of the laser frequency through the scanning potential kV_{line} was used to scan the hyperfine structure (hfs) levels around the $4s\ ^2S_{1/2} \rightarrow 4p\ ^2P_{3/2}$ transition. At resonance frequencies, transitions between the lower and upper hfs levels were excited, and the fluorescence photons were detected by four photomultipliers tubes (PMT) at the end of the beam line (see Refs. [63, 192] for details). The photon signals were accepted only when the ion bunch passed in front of the light collection region, reducing the background counts from scattered laser light and PMT dark counts by a factor of $\sim 10^4$.

[2] External cavitiy frequency doubler: Wavetrain manufactured by Spectra Physics
[3] Actively Stabilized Titanium:Sapphire Ring Laser: Matisse TS manufactured by Sirah Lasertechnik

المنارة للاستشارات

4.3 Hyperfine spectra of Ca isotopes

The hyperfine structure for the $4s\ ^2S_{1/2} \rightarrow 4p\ ^2P_{3/2}$ transition in Ca^+ was measured by detecting the fluorescence photons as a function of the Doppler-tuning voltage. The laser frequency in the lab frame, ν_0, was locked at 25449.2478 cm^{-1} ($\sim$ 393 nm), which is transformed to the ion rest frame by using the expression

$$\nu = \nu_0 \frac{(1 - \beta \cos\theta)}{\sqrt{1 - \beta^2}}, \tag{4.13}$$

where θ is the angle between the ion velocity vector and the direction of the interacting photon, and the factor β given by

$$\beta = \sqrt{1 - \frac{1}{\left(\frac{eV_{total}}{M_{II}c^2} + 1\right)^2}}, \tag{4.14}$$

with M_{II} the rest mass of the single ionized Ca [4], and V_{total} the total potential applied to the ion beam (expression 4.12). The masses and nuclear spin for the isotopes measured in the experimental campaign are shown in Table 4.1. Additionally, the total number of hfs scans measured for each isotope at the two different V_{ISCOOL} potentials employed during the experiments are also listed. The yields of each isotope are taken from the ISOLDE yield data base. These values agree with the values estimated during the current experiments, as well as the yields obtained from previous ISOLTRAP measurements.

Some examples of the measured hyperfine structure spectra are shown in Figure 4.4. The number of PMT counts per proton pulse are plotted as a function of the laser frequency in the ion rest frame.

4.4 Data Analysis

The uncertainty of the frequency measurements in the hyperfine spectra are directly linked with the uncertainty in the total acceleration voltage. Hence, a precise determination of each one of the factors involved in the total acceleration voltage is necessary (see Equation 4.12). These calibrations will be described in the present section.

[4]The rest mass of the single ioinized Ca can be obtained from the mass of the atom, M_I, using the expression

$$M_I c^2 + E_{ionization} = m_e c^2 + M_{II} c^2, \tag{4.15}$$

where m_e is the electron mass and $E_{ionization}$ the ionization energy, 6.11315509(25) eV [193].

المنارة للاستشارات

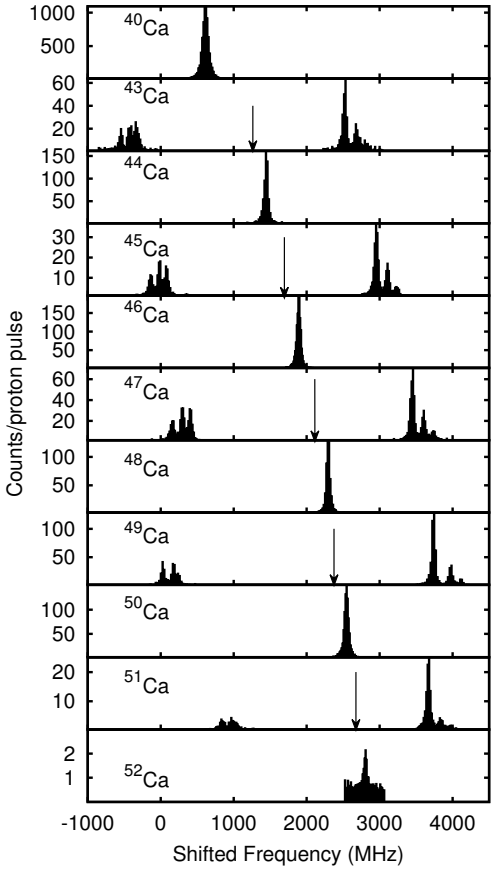

Figure 4.4: Examples of hfs spectra measured for the Ca isotopes in the 393 nm $4s^2S_{1/2} \rightarrow 4p^2P_{3/2}$ ionic transition. The arrows in odd isotopes indicate the centroid of the hyperfine structure.

المنارة للاستشارات

Isotope	Half life	Yield (ions/μC)	Spin	Atomic mass (u)	# runs 40 kV	30 kV
^{40}Ca	stable		0	39.962590863 (22)	39	72
^{43}Ca	stable		7/2	42.95876634 (24)	-	5
^{44}Ca	stable		0	43.95548134 (34)	4	4
^{45}Ca	162.61 d	$> 10^7$	7/2	44.9561861 (39)	-	2
^{46}Ca	stable		0	45.9536873 (24)	-	2
^{47}Ca	162.61 d	$> 10^7$	7/2	46.9545407 (24)	-	2
^{48}Ca	stable		0	47.9525241 (23)	5	8
^{49}Ca	8.718 m	2.5×10^5	3/2	48.9556641 (23)	5	7
^{50}Ca	13.9 s	2.4×10^4	0	49.9575004 (37)	5	4
^{51}Ca	10.0 s	1.0×10^3	(3/2)	50.960989 (24)	-	17
^{52}Ca	4.6 s	1.0×10^2	0	51.963237 (65)	5	6

Table 4.1: Ca isotopes measured during the experiment. Nuclear spin and masses are indicated for each isotope. The yields of each isotope are taken from the ISOLDE yield data base. The masses were taken from Ref. [66] for $^{40-50}$Ca, and from Ref. [194] for ^{51,52}Ca. The total number of runs measured for each isotope is given for the two different V_{ISCOOL} potentials used during the experiments.

4.4.1 Kepco amplification factor

The scanning voltage in expression 4.12 is generated from the amplification of an analog out signal $|V_{line}| \leq 10$ V by using a Kepco linear-amplifier. Calibration measurements for the kepco amplification factor, k, are obtained recording the amplified output as a function of V_{line}. As the amplification device is sensitive to temperature fluctuations, it is important to repeat these calibration measurements at different times throughout the experiment. In total 14 different calibration measurements were taken over the ~ 8 days of measurements. The file name, day and time of each measurement are shown in the table 4.2.

As three different Fluke power supplies were used during the experimental campaign, each power supply requires an independent calibration. The results from the Kepco calibration for each Fluke are shown in the figure 4.5. An average kepco factor, $k_{ave} = 50.4268(12)$, was obtained from the total number of measurements. The small fluctuations in the Kepco amplification lead to a voltage uncertainty of at most 0.05 V, which corresponds to an uncertainty in the frequency of less than 0.15 MHz. This uncertainty is significantly smaller compared to the other uncertainties discussed further.

المنارة للاستشارات

Name	Day	Time
Ca_a_024	04/04/12	10:37
Ca_a_025	04/04/12	11:06
Ca_a_031	05/04/12	07:53
Ca_a_033	05/04/12	08:25
Ca_a_035	05/04/12	09:26
Ca_a_058	06/04/12	01:36
Ca_a_066	06/04/12	10:20
Ca_a_173	06/04/12	20:55
Ca_a_201	10/04/12	9:56
Ca_a_202	10/04/12	14:22
Ca_a_203	10/04/12	15:00
Ca_a_204	10/04/12	15:21
Ca_a_236	11/04/12	13:19
Ca_a_237	11/04/12	15:20

Table 4.2: Kepco calibration files recorded during the experimental campaign.

4.4.2 HFS fitting procedure and error estimation

The raw data are recorded as the number of photon counts in each PMT as a function of the Doppler-tuning voltage. A script **getfreq.sh** in *bash* language was written to read the .mcp files and extract prema voltages, V_{prema}, scanning voltage, V_{line}, and number of counts for each PMT row. The total acceleration voltage, V_{total}, is then calculated from equation 4.12, using the kepco amplification factor, k, and the recorded values for V_{ISCOOL}. Expression 4.13 is used to convert the voltage data into frequency values. The data of each run was divided in two hfs spectra, corresponding to each PMT row, to be analyzed independently.

A simple model of asymmetric errors [195] was used for the PMT counts. These asymmetric errors are important when low count rates are measured. As typical frequency values are numbers with many significant digits, it is convenient to shift the frequency range by subtracting the value of the transition frequency 4p $^2S_{1/2} \rightarrow$ 4s $^2P_{3/2}$ of Ca II, 7.619047×10^{14} Hz [196]. (393.3663 nm $\equiv$ 7.619047×10^{14} Hz $\equiv$ 25414.40 cm^{-1} $\equiv$ 3.151390 eV).

Once the file is transformed to frequency, a code with ROOT instructions [197] is used to fit the hyperfine structure spectra. The standard MINUIT fitting package was used for the χ^2-minimization procedure. The peaks in the hfs spectra are fitted to Voigt profiles as indicated in expression A.12, with the Gaussian (σ) and Lorentzian (Γ_L) widths as free parameters in the fit of each

المنارة للاستشارات

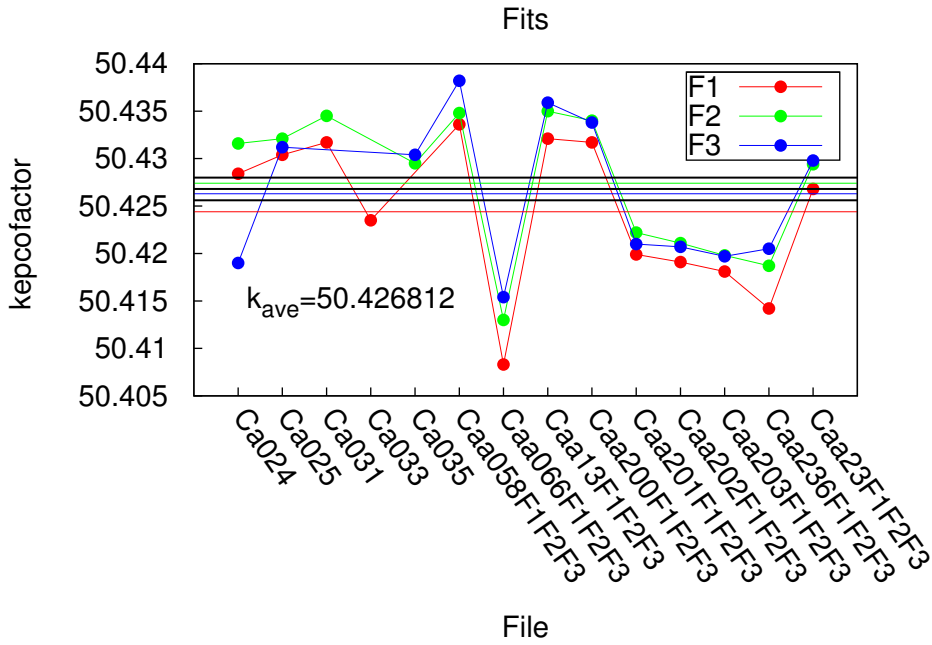

Figure 4.5: Kepco factor obtained for the different files saved during the Ca runs. Each color represents a different Fluke. The average value for each fluke is shown with a horizontal line of the same color. The total average $k_{ave} = 50.4268(12)$ is shown using the horizontal black line.

hfs spectrum. For the transition $^2P_{3/2} \rightarrow ^2 S_{1/2}$, each peak position is given

$$\nu_i = C_1 A(^2S_{1/2}) + C_2 A(^2P_{3/2}) + C_3 B(^2P_{3/2}) + \nu_0, \tag{4.16}$$

where the constants C_i are defined by the atomic and nuclear angular momentum numbers (see eq. 4.4). The hyperfine structure constants $A(^2S_{1/2})$, $A(^2P_{3/2})$ and $B(^2P_{3/2})$ and the centroid, ν_0, are included as free parameters in each fit. The difference between the centroids of two isotopes is the so-called isotope shift. An example of the fit for the hfs spectrum of ^{47}Ca is shown in Figure 4.6. The measured spectrum (points) is fitted to multiple Voight profiles (continuous line).

The peak intensities are included as free parameters. The position of each peak is constrained by expression 4.16. Side peaks were included to account for the asymmetry observed in the line shapes. As explained in sec. A.2, multiple-Voigt profiles are added following a Poisson distribution (eq. A.13). The distance

المنارة للاستشارات

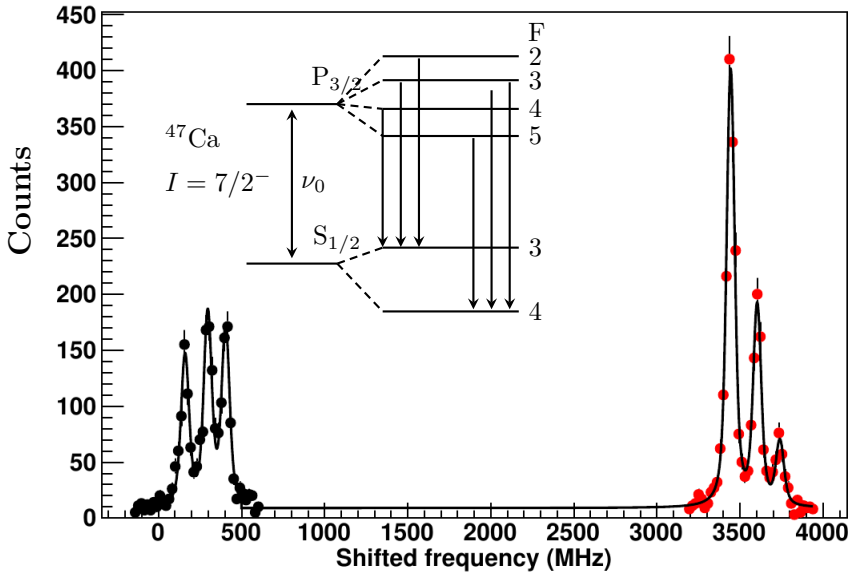

Figure 4.6: Example of the fit to one of the hfs spectra of ^{47}Ca. Experimental values (points) are fitted to multiple Voigt profiles (continuous line).

between the main peaks and the subsequent side peak was fixed at a muliple of the average transition energy (~ 3.1 eV) of the two possible populated states in CaII, 4p $^2S_{1/2} \rightarrow$ 4s $^2P_{3/2}$ and 4p $^2S_{1/2} \rightarrow$ 4s $^2P_{1/2}$. The Poisson factor, x, was obtained from the fit to the hfs spectra of the reference isotope ^{40}Ca, assuming up to three side-peaks. The Poisson factors for the total number of measured spectra are shown in Figure 4.7. For the analysis of the other isotopes the Poisson factor was fixed to the weighed average $x = 0.031(2)$ obtained from the reference isotope.

The fit results provide the hyperfine structure parameters and centroid of each hfs spectrum. Realistic error estimations for the fit results were obtained using the MINUIT application for error analysis, namely MINOS[5] [198]. The error estimation of each parameter corresponds to a 68.3 % confidence level. Final values are calculated as the weighted average, $\bar{X}$, obtained from total number

[5]MINOS procedure takes into account both parameter correlations and non-linearities. The MINOS error intervals are in general asymmetric.

المنارة للاستشارات

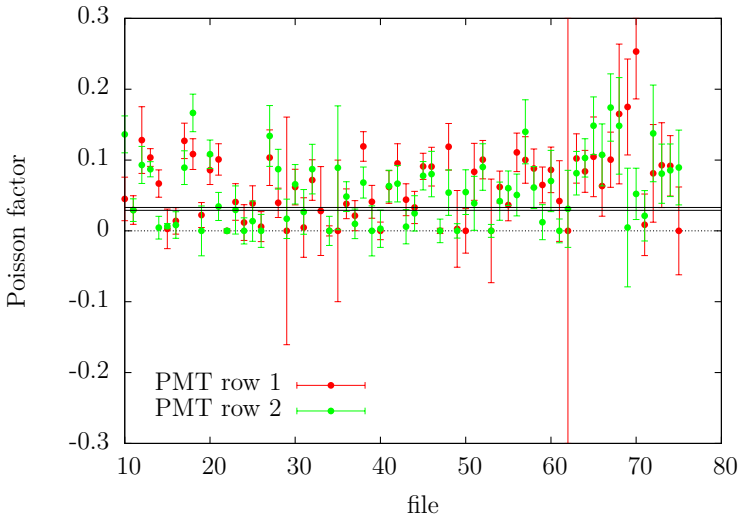

Figure 4.7: Poisson factor x obtained from the fit to the HFS spectra of ^{40}Ca. The horizontal black line shows the weighted average $x = 0.031(2)$.

of measurements for each isotope

$$\bar{X} = \frac{\sum_{i=1}^{n} X_i/\sigma_i^2}{\sum_{i=1}^{n} 1/\sigma_i^2} \pm \sqrt{\frac{1}{\sum_{i=1}^{n} 1/\sigma_i^2}}, \tag{4.17}$$

where σ_i is the uncertainty associated to the value X_i, and n the total number of measurements. The scattering error, $\sigma_{\bar{X}}$, takes into account the scattering among individual measurements, and is expressed as

$$\sigma_{\bar{X}}^2 = \frac{1}{\sum_{i=1}^{n} 1/\sigma_i^2} \frac{1}{n-1} \sum_{i=1}^{n} \frac{(X_i - \bar{X})^2}{\sigma_i^2}. \tag{4.18}$$

The final uncertainty of $\bar{X}$ is taken as the larger of the statistical error, $\sqrt{\frac{1}{\sum_{i=1}^{n} 1/\sigma_i^2}}$, and the scattering error.

4.4.3 ISCOOL voltage calibration

The voltage reading of the cooler platform was obtained by using a high-voltage divider with an accuracy of 2 V in 1 kV. This uncertainty of just few volts

المنارة للاستشارات

can cause a notable change in the measured isotope shift. Therefore, the reading from the voltage divider, named *ISCOOL voltage*, V_{ISCOOL}, needs to be corrected by comparing the measured isotope shifts with previously reported values. The reading provided by the voltage divider is assumed to have an offset voltage, v_{os}, therefore the real ISCOOL voltage is given by

$$V'_{ISCOOL} = V_{ISCOOL} - v_{os}. \tag{4.19}$$

To find the offset voltage, the isotope shifts, $\delta\nu_{cal}^{A_i,A'}(v_{os})$, were calculated for different v_{os} values and compared with reference values from literature, $\nu_{ref}^{A_i,A'}$ [199, 200]. The reference isotope shifts used for the v_{os} calibration are listed in Table 4.3.

Table 4.3: Reference Ca isotope shifts measured relative to ^{40}Ca in the $4s\ ^2S_{1/2} \rightarrow 4p\ ^2P_{3/2}$ line.

Isotope	Pendrill et al [200] (MHz)	TRIGA-LASER [199] (MHz)
^{42}Ca	-430(18)(4)	-426.4(15)(10)
^{44}Ca	842(13)(8)	850.1(10)(20)
^{48}Ca	1699(19)(16)	1710.6(35)(42)

To investigate the effect of the offset voltage on the isotope shift, the frequency conversion was recalculated for different v_{os} voltages, and the centroids were re-fitted each time for ^{40}Ca, ^{44}Ca, and ^{48}Ca. Figure 4.8 shows the calculated isotope shifts relative to ^{40}Ca for different offset voltages. Points were fitted to the linear equation

$$\delta\nu^{A_1,A_2} = \delta\nu_0^{A_1,A_2} + v_{os}\kappa, \tag{4.20}$$

where $\delta\nu_0^{A_1,A_2}$ is the calculated isotope shift without offset voltage, and κ is the frequency change per voltage unit, which can be obtained from the linear fit of the straight line $\delta\nu^{A_1,A_2}$ vs v_{os}.

Once κ was calculated[6], the expression 4.20 was used to obtain the offset voltage, v_{os}, needed to reproduce the reference isotope shifts showed in Table 4.3. The isotope shift of ^{44}Ca relative to ^{40}Ca, $\delta\nu^{44,40}$, coincides with the reference value (Table 4.3) when v_{os} takes the values 8.1(1.5) V and 9.9(1.7) V, corresponding to ISCOOL voltages of 30 kV and 40 kV, respectively. For $\delta\nu^{48,40}$, the values obtained for v_{os} are 6.9(2.0) V and 7.1(2.2) V, for ISCOOL voltages of 30 kV and 40 kV, respectively. The weighted average of v_{os} for each ISCOOL potential is shown in Table 4.4.

[6]The frequency change per voltage unit is different for each isotope

المنارة للاستشارات

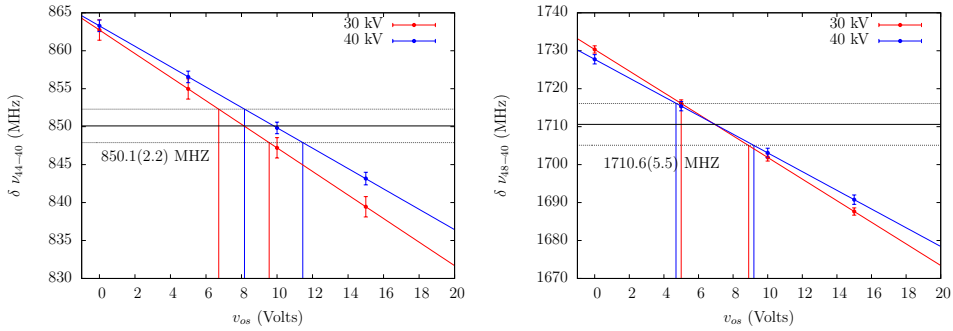

Figure 4.8: Fitted isotope shifts as a function of the offset voltage, v_{os} for ^{44}Ca and ^{48}Ca relative to ^{40}Ca. Two different platform potentials were used, 30 kV (red points) and 40 kV (blue points).

Table 4.4: Values of the ISCOOL offset voltages obtained from isotope shift measurements.

V_{ISCOOL}	v_{os} (Volts)
40 kV	8.8(1.3)
30 kV	7.7(1.2)

المنارة للاستشارات

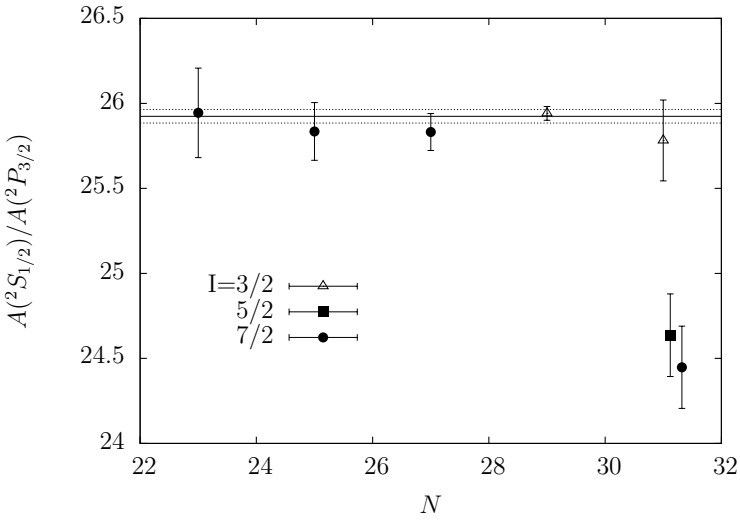

Figure 4.9: Ratio between the hfs constants $A(^2P_{1/2})$ and $A(^2P_{3/2})$. The continuous line shows the average value $A(^2S_{1/2})/A(^2P_{3/2}) = 25.92(3)$. Hyperfine structure spectra of ^{51}Ca were fitted assuming different g.s. spin values of $I = 3/2, 5/2, 7/2$.

4.5 Spin determination of ^{51}Ca

As described in eq. 4.16, the hyperfine structure peak positions depend on the electronic spin, J, and the nuclear spin, I. If the nuclear spin is unknown, it can be determined by using different values in the minimization procedure. Since a different set of hfs constants is obtained for a given spin, the ratio, $R = A(^2P_{3/2})/A(^2S_{1/2})$, can be used to determine the correct spin for each isotope, as this ratio should be a constant over the entire isotopic chain (neglecting a possible small hyperfine anomaly that is usually much smaller than the error on the ratio value). Figure 4.9 shows the ratio R for the isotopes measured in the experimental campaign. The ratio remains constant along the Ca isotopes up to ^{49}Ca, using the earlier determined g.s. spins in the fitting procedure. For ^{51}Ca, we postulated three possible spins for its ground state. Only when $I = 3/2$ is used, the ratio of the fitted hfs parameters is consistent with those from the other isotopes. This is a clear prove that $I = 3/2$ is the g.s. spin of ^{51}Ca, confirming earlier tentative assignments [201, 202], and in agreement with expectations from the shell model.

المنارة للاستشارات

Table 4.5: Hyperfine structure values obtained from the fit to the experimental data compared to previous measurements.

A	I^π	$A(^2S_{1/2})$ (MHz)	$A(^2P_{3/2})$ (MHz)	$B(^2P_{3/2})$ (MHz)	Ref.
43	$7/2^-$	-806.87(42)	-31.1(3)	-4.2 (1.3)	This work
		-806.40207160(8)			[203]
		-805(2)	-31.9(2)	-6.7(1.4)	[15]
			-31.0(2)	-6.9(1.7)	[204]
45	$7/2^-$	-811.99(44)	-31.43(19)	3.1(1.0)	This work
47	$7/2^-$	-860.96(28)	-33.33(13)	12.68(96)	This work
49	$3/2^-$	-1971.02(30)	-75.98(11)	-5.53(40)	This work
51	$3/2^-$	-1499.22(94)	-58.15(54)	5.4(1.8)	This work

4.6 Hyperfine Structure Parameters and Nuclear moments

As illustrated in section 4.4.2, the peak positions in the hfs spectrum define the centroid, ν_0, of the hfs spectrum and the hfs parameters of the ionic ground state $A(^2S_{1/2})$, and the excited state, $A(^2P_{3/2})$ and $B(^2P_{3/2})$. The four hfs spectra for each isotope were divided in two PMT rows, and the weighted average from the fit of the total number of runs were adopted as the final values. The results for the different hfs constants are shown in Table 4.5. The hfs parameters for ^{43}Ca are compared with literature values. Our results are in good agreement with the literature values.

The g.s. magnetic moments were extracted from the magnetic hfs constant of the lower state, $A(^2S_{1/2})$, following the expression (4.8), and using the high-precision values of $A(^2S_{1/2}) = -806.40207160(8)$ MHz [203] and $\mu = -1.3173(6)$ [49] for ^{43}Ca. Taking the ratio of the hyperfine parameters for two isotopes, as defined in (4.8), the magnetic moment of one isotope can be extracted relative to the reference isotope by using

$$\mu(^A\mathrm{Ca}) = \left[IA(^2S_{1/2})\right]_{^A\mathrm{Ca}} \left[\frac{\mu}{IA(^2S_{1/2})}\right]_{^{43}\mathrm{Ca}}. \tag{4.21}$$

The results for the magnetic moments and previously reported values for ^{45}Ca and ^{47}Ca are presented in Table 4.6.

The gs quadrupole moments, Q, were obtained from the quadrupole hfs constant, by using expression (4.6). The electric field gradient (EFG) produced by the electrons at the nucleus, $eV_{zz}(\equiv B/Q)$, is needed to extract the

المنارة للاستشارات

Table 4.6: Quadrupole and magnetic moments obtained from the measured hfs constants (Table 4.5). The magnetic moments were obtained using the reference isotope ^{43}Ca, with $A(^2P_{3/2}) = -806.40207160(8)$ MHz [203]. Quadrupole moments were extracted using the calculated electric field gradient, $eV_{JJ} = 151.3(7)$ MHzb^{-1} [20]. Data are compared to calculations using the NN+3N interaction.

A	$\mu(\mu_N)$	$\mu(\mu_N)$ (NN+3N)	Q (b)	Q (b) (NN+3N)	Ref.
41	−1.594781(9)				[205]
			−0.080(8)		[206]
43		−1.56	−0.028(9)	−0.0246	This work
	−1.3173(6)[b]				[49]
			−0.043(9)		[15]
			−0.049(5)		[206]
			−0.0408(8)		[207]
			−0.0444(6)		[20]
45	−1.3264(13)	−1.45	+0.020(7)	+0.0252	This work
	−1.3278(9)				[56]
			+0.046(14)		[206]
47	−1.4064(11)	−1.38	+0.084(6)	+0.0856	This work
	−1.380(24)				[14]
49	−1.3799(8)	−1.40	−0.036(3)	−0.0422	This work
51	−1.0496(11)	−1.04	+0.036(12)	+0.0425	This work

[b] Reference value.

quadrupole moment. The EFG for the $^2P_{3/2}$ can be calculated from atomic physics theory or from the measured B/Q ratio, provided a reliable value for the latter is available.

For the $^2P_{3/2}$ level, the experimental $B(^2P_{3/2})$ factor is known with large relative uncertainty because of its very small value. Furthermore, there is a rather poor agreement among the reported gs quadrupole moments of ^{43}Ca, which would be used as a reference value[20]. Therefore, we have used the calculated electric field gradient (EFG) for the $P_{3/2}$ level to extract all quadrupole moments from the measured $B(^2P_{3/2})$ factors.

There are several (independent) atomic physics calculations reporting EFGs for the $4p^2P_{3/2}$ level. All of these values agree within 3%. The agreement is excellent for both hfs constants A and B, which gives reliability to the calculated values. The results from different calculations of the EFG for the $4p^2P_{3/2}$ line are shown in Table 4.7. Given the agreement between different

المنارة للاستشارات

Table 4.7: Calculated electric field gradient for the $4p^2P_{3/2}$ line. Calculated values have been derived using relativistic coupled-cluster theory (RCC), relativistic many body perturbation theory (RMBPT), and RMBPT with single-double all-other method (SD).

eV_{zz} (MHz b^{-1})	Theory	Reference
151.3(7)	RCC	[20]
151.798	RMBPT	[208]
155	RMBPT	[209]
153.99	SD	[210]

atomic physics calculations (see Table 4.7), the calculated EFG from Ref. [20] was used to extract the gs quadrupole moments from the measured quadrupole hfs constant, $B(^2P_{3/2})$. The results are presented in Table 4.6.

When comparing the present results with previous reported quadrupoles moments, it is not trivial to chose a proper set of "literature values". Several values for the gs quadrupole moment of ^{41,43,45}Ca isotopes have been reported, but most of them use common experimental results, and “re-calculated” electric field gradients. A summary of reported quadrupole hfs constants and quadrupole moments for Ca isotopes is listed in Appendix A.3. Only the isotope ^{43}Ca has been studied previously in the ionic transition used during the current experiment, and our results are in agreement within 1.1 standard deviation. For ^{41}Ca and ^{45}Ca, the quadrupole hfs constants have been reported in the atomic level system, both relative to that of ^{43}Ca [55, 206], yielding the ratios $B(^{41}\text{Ca})/B(^{43}\text{Ca}) = 1.63(1)$, and $B(^{45}\text{Ca})/B(^{43}\text{Ca}) = -0.94(27)$. The values are presented in Table 4.8. The B-factor ratio equals the ratio of the quadrupole moments. Thus we can compare the ratio of our B-values, measured in the ionic system $B(^{45}\text{Ca})/B(^{43}\text{Ca}) = -0.74(31)$ (see Table 4.8), to the latter value. They are in agreement within the error bars.

المنارة للاستشارات

Table 4.8: B-ratios relative to ^{43}Ca.

Ca	Transition	$\frac{B(^{41}\text{Ca})}{B(^{43}\text{Ca}}$	$\frac{B(^{45}\text{Ca})}{B(^{43}\text{Ca})}$	$\frac{B(^{47}\text{Ca})}{B(^{43}\text{Ca})}$	Ref.
I	$4s4p^3P_1$	1.54(17)	-1.08(32)	-	[55]
I	$4s4p^3P_1$	1.630(11)	-0.94(26)	-	[206]
II	$4p^2P_{3/2}$		-0.74(31)	-3.02(32)	This work

المنارة للاستشارات

4.7 Isotope Shifts and Charge radii

Before and after taking each hfs spectrum, the reference isotope, ^{40}Ca, was measured to control possible systematic errors related to the observed absolute transition frequencies during the experiment. The isotope shifts were then obtained as the difference between the measured centroid, ν^A, relative to the centroid of ^{40}Ca, ν^{40} (obtained from the measured hfs spectrum closest in time).
The measured isotope shifts relative to ^{40}Ca, $\delta\nu^{40,A} = \nu^A - \nu^{40}$, are presented in Table 4.9. Statistical and systematic errors are given in round and squared brackets, respectively. Statistical errors correspond to the uncertainty in the determination of the peak positions in the hfs spectra. Systematic errors are mainly due to the uncertainty in the ion beam energy. High precision values for isotope shifts measured in transitions 4s $^2S_{1/2} \rightarrow$ 4p $^2P_{3/2}$ [199] were used as reference values to re-calibrate the absolute potential applied to the ion beam, thereupon, to obtain a high-precision value of the ion beam energy (see sec. 4.4.3).

Table 4.9: Measured isotope shifts relative to ^{40}Ca. The errors include statistic and systematic uncertainties given in round and squared brackets, respectively. The systematic uncertainties of our measurements are dominated by the uncertainty in the ion beam energy. Literature values are given in columns 3 and 4.

	This work	Literature values	
	4s $^2S_{1/2} \rightarrow$ 4p $^2P_{3/2}$		
A	$\nu^{40,A}$(MHz)	TRIGA (2015) [199]	Pendrill *et al* [200]
40	0	0	0
42	-	426.4(1.5)[1.0]	425(4)[4]
43	683.0(12)[16]	-	672(9)[6]
44	851.1(6)[21]	850.1(1.0)[2.0]	842(3)[8]
45	1103.5(7)[25]	-	1091(4)[10]
46	1301.0(6)[30]	-	1287(3)[12]
47	1524.8(8)[35]	-	
48	1706.5(8)[38]	1710.6(3.5)[4.2]	1696(4)[16]
49	1854.7(10)[43]	-	
50	1969.2(9)[47]	-	1951(9)[20]
51	2102.6(9)[51]	-	
52	2219.2(14)[56]	-	

المنارة للاستشارات

Changes in the rms charge radii were deduced from the isotope shifts following the relation 4.11. The specific mass shift, $K_{SMS} = -9.2(3.8)$ GHz.u, and field shift factor, $F = -283(6)$ MHz/fm^2, were taken from reference [17]. The calculated values are shown in Table 4.10.

Table 4.10: Values of charge radii obtained from isotope shift measurements. Error bars in square brackets show the uncertainty due to K_{SMS}.

	This work		Literature	
A	$\delta\langle r^2\rangle$ (fm^2) [a]	$\delta\langle r^2\rangle$ (fm^2) [b]	Vermeeren *et al* [17][c]	Palmer *et al* [60]
40	0	0	0	0
42	-	-	0.203(15)	0.215(5)
43	0.109(4)[28]	0.114(4)[8]	0.125(30)	0.125(3)
44	0.278(2)[33]	0.288(2)[6]	0.280(11)	0.283(6)
45	0.118(3)[40]	0.125(3)[8]	0.126(15)	0.119(6)
46	0.117(3)[46]	0.125(2)[8]	0.124(11)	0.124(5)
47	-0.003(2)[53]	0.002(3)[9]	-	0.005(13)
48	-0.004(3)[59]	0.001(3)[10]	-0.022(15)	-0.004(6)
49	0.090(4)[66]	0.098(4)[12]	-	
50	0.277(3)[71]	0.291(3)[12]	0.276(34)	
51	0.375(3)[76]	0.392(3)[13]	-	
52	0.510(5)[83]	0.531(5)[15]	-	

[a]Values of $K_{SMS} = -9.2(3.8)$ GHz.u and $F = -278(6)$ MHz/fm^2 were taken from literature [17]. In square brackets the systematic errors associated to these factors.

[b]Values of $K_{SMS} = -8.8(5)$ GHz.u and $F = -276(8)$ MHz/fm^2 were taken from the king-plot results. In square brackets the systematic errors associated to these factors.

[c]Calculated from isotope shifts values reported in [17] and using the new reported mass values[66]

To reduce the uncertainty in the charge radii due to the large error on K_{SMS} (square bracket), an alternative method was used to determine the mass and field shift factors, K_{SMS} and F, using a King-plot analysis [211]. The expression 4.11 can be reordered as

$$\mathcal{M}\delta\nu^{A,A'} = F\mathcal{M}\delta\langle r^2\rangle^{A,A'} + K_{MS}, \tag{4.22}$$

with $\mathcal{M} = \dfrac{M_{A'}M_A}{M_{A'} - M_A}$. Therefore, in a plot of $\mathcal{M}\delta\nu^{A,A'}$ vs $\mathcal{M}\delta\langle r^2\rangle^{A,A'}$ (King's plot), the gradient and the intercept would provide F and K_{MS} respectively. The present measurements of isotope shifts and previous reported values of rms charge radii were used to extract the specific mass shift and the field shift factor from the King plot shown in Figure 4.10. The values of rms charge radii were taken from a combined analysis of optical and muonic experiments [60]. The values obtained from the King plot, i.e., $K_{SMS} = -8.8(5)$ GHz.u

المنارة للاستشارات

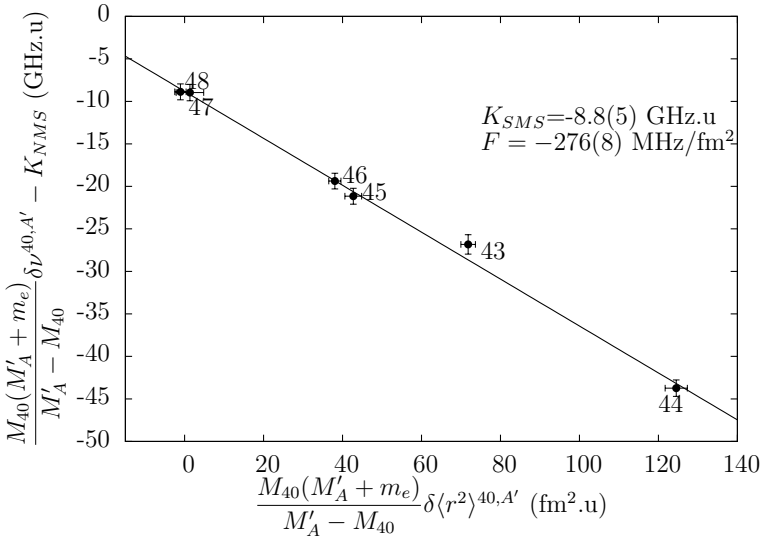

Figure 4.10: King plot: experimental isotope shift as a function of the charge radii obtained by Palmer *et al* [60].

and $F = -276(8)$ MHz/fm^2, agree with the previously reported values, but the error on K_{SMS} is reduced by nearly an order of magnitude [17]. The re-calculated rms charge radii are shown in the third column of Table 4.10. The results are in very good agreement with the literature values, where available. The importance of these new results and their impact in the understanding of the nuclear structure of neutron-rich calcium isotopes and on the development of modern nuclear theories will be discussed in the following chapter.

المنارة للاستشارات

Chapter 5

Discussion of experimental results

This chapter presents the discussion on the nuclear observables obtained from the hfs spectra analyzed in the previous chapter. The results on electromagnetic moments are compared with phenomenological and microscopic shell-model interactions. The interpretation of these results has been presented in Article I, which is added below. After the paper, we add some more information on a simple configuration mixing calculation which helps to understand the extreme sensitivity of the ^{51}Ca g-factor to a few % mixing with neutron configurations in the higher pf-orbits.

The nuclear charge radii on the other hand are presented in a separate paper, in comparison with *ab initio* and mean field calculations using newer and still in development nuclear theories. This is presented in Article II.

5.1 Electromagnetic moments

5.1.1 Article I: Ground-State Electromagnetic Moments of Calcium Isotopes

This article reports the experimental ground-state nuclear magnetic moments and quadrupole moments of neutron-rich Ca isotopes towards the supposedly

المنارة للاستشارات

new magic number $N = 32$. Our experimental results are compared with state-of-the-art shell-model calculations using both phenomenological interactions and microscopic interactions derived from chiral effective field theory. These new results provide a critical test of modern nuclear theories, and give direct answer to the evolution of ground-state electromagnetic properties in the Ca isotopic chain.
I was involve in the experiment. As a main contribution to the article I performed the data analysis and prepared the initial draft of the manuscript. I performed shell-model calculations using the phenomenological interactions KB3G and GXPF1A, and contacted the collaborators from theory to include microscopic shell-model calculations with the NN+3N interaction. I was in charge of the submission process.

المنارة للاستشارات

RAPID COMMUNICATIONS

PHYSICAL REVIEW C **91**, 041304(R) (2015)

Ground-state electromagnetic moments of calcium isotopes

R. F. Garcia Ruiz,[1,*] M. L. Bissell,[1] K. Blaum,[2] N. Frömmgen,[3] M. Hammen,[3] J. D. Holt,[4,5,6] M. Kowalska,[7] K. Kreim,[2] J. Menéndez,[4,5,8] R. Neugart,[2,3] G. Neyens,[1] W. Nörtershäuser,[4] F. Nowacki,[9] J. Papuga,[1] A. Poves,[10] A. Schwenk,[4,5] J. Simonis,[4,5] and D. T. Yordanov[2]

[1]*KU Leuven, Instituut voor Kern-en Stralingsfysica, B-3001 Leuven, Belgium*
[2]*Max-Plank-Institut für Kernphysik, D-69117 Heidelberg, Germany*
[3]*Institut für Kernchemie, Universität Mainz, D-55128 Mainz, Germany*
[4]*Institut für Kernphysik, Technische Universität Darmstadt, D-64289 Darmstadt, Germany*
[5]*Extreme Matter Institute EMMI, GSI Helmholtzzentrum für Schwerionenforschung GmbH, D-64291 Darmstadt, Germany*
[6]*TRIUMF, 4004 Wesbrook Mall, Vancouver, British Columbia, V6T 2A3, Canada*
[7]*CERN, European Organization for Nuclear Research, Physics Department, CH-1211 Geneva 23, Switzerland*
[8]*Department of Physics, University of Tokyo, Hongo, Tokyo 113-0033, Japan*
[9]*IPHC, IN2P3-CNRS and Universite Louis Pasteur, F-67037 Strasbourg, France*
[10]*Departamento de Física Teórica and IFT-UAM/CSIC, Universidad Autónoma de Madrid, E-28049 Madrid, Spain*

(Received 10 November 2014; revised manuscript received 8 April 2015; published 30 April 2015)

Background: The neutron-rich calcium isotopes have gained particular interest as evidence of closed-shell structures has recently been found in two exotic nuclei, at $N = 32$ and $N = 34$. Additionally, the study of such neutron-rich systems has revealed new aspects of nuclear forces, in particular regarding the role of three-nucleon forces.

Purpose: We study the electromagnetic properties of Ca isotopes around the neutron number $N = 32$.

Methods: High-resolution bunched-beam collinear laser spectroscopy was used to measure the optical hyperfine spectra of the $^{43-51}$Ca isotopes.

Results: The ground-state magnetic moments of ^{49,51}Ca and quadrupole moments of ^{47,49,51}Ca were measured for the first time, and the ^{51}Ca ground-state spin $I = 3/2$ was determined in a model-independent way. Our experimental results are compared with state-of-the-art shell-model calculations using both phenomenological interactions and microscopic interactions derived from chiral effective field theory.

Conclusions: The results for the ground-state moments of neutron-rich isotopes are in excellent agreement with predictions of interactions derived from chiral effective field theory including three-nucleon forces. Lighter isotopes illustrate the presence of particle-hole excitations of the ^{40}Ca core in their ground state. Our results provide a critical test of modern nuclear theories, and give direct answer to the evolution of ground-state electromagnetic properties in the Ca isotopic chain across three doubly closed-shell configurations at $N = 20$, 28, 32 of this unique system.

DOI: 10.1103/PhysRevC.91.041304 PACS number(s): 21.10.Ky, 21.45.Ff, 21.60.Cs, 42.62.Fi

The existence of doubly magic nuclei has played a key role in our understanding of nuclear structure. Doubly magic nuclei have been the basis to develop the shell model, and are an ideal probe to test our knowledge of nuclear interactions by comparing experimental data with shell-model predictions [1,2]. Such shell-model calculations depend on the effective Hamiltonian used, a suitable valence space to capture the low-energy degrees of freedom, and consistent effective operators. Although effective charges and g factors are widely used in shell-model calculations, they are not completely understood. Furthermore, their orbital [3] and valence-space [4] dependence and connection to two-body currents (meson-exchange currents), known to be important for magnetic moments in light nuclei [5], are under discussion.

Having a closed proton shell, $Z = 20$, and two naturally occurring doubly magic isotopes, ^{40}Ca and ^{48}Ca, the calcium isotopic chain has always been considered a prime benchmark for nuclear structure, both from a theoretical [6] and an experimental perspective [7]. Recently, special attention has turned to the evolution of the structure beyond $N = 28$, where additional shell closures have been suggested at $N = 32$ [8] and $N = 34$ [9]. These neutron-rich calcium isotopes have also gained exceptional interest from the theoretical side [10–14], as their properties reveal new aspects of nuclear forces, in particular regarding the role of three-nucleon ($3N$) forces [10,11] (for a review on $3N$ forces see [15]).

Spectroscopic properties in the Ca region are well described by phenomenological shell-model interactions, such as KB3G [16] and GXPF1A [17]. These interactions start from a ^{40}Ca core and two-nucleon (NN) forces and refit part of the interactions to experimental data in the pf shell, to compensate for neglected many-body effects (both due to $3N$ and many-body correlations) [2]. Normal and superdeformed bands in ^{40}Ca have been understood as due to particle-hole excitations of protons and neutrons from the sd shell into the pf orbits, and have been well described

*ronald.fernando.garcia.ruiz@cern.ch

Published by the American Physical Society under the terms of the Creative Commons Attribution 3.0 License. Further distribution of this work must maintain attribution to the author(s) and the published article's title, journal citation, and DOI.

المنارة للاستشارات

using the SDPF.SM shell model interaction starting from a virtual ^{28}Si core [18]. These calculations showed that the ^{40}Ca ground state is very correlated. In the last years, valence-shell interactions have been derived from NN and $3N$ forces based on chiral effective field theory [10], fitted only to few-nucleon systems. Investigating the reliability of these microscopic $NN + 3N$ interactions is a matter of general interest as they have direct implications for the modeling of astrophysical systems [19]. The $NN + 3N$ interactions provide a good description of the shell structure and the spectra of neutron rich calcium isotopes in an extended valence space ($fpg_{9/2}$) [14]. The electric quadrupole ($E2$) transitions obtained from both phenomenological and microscopic interactions exhibit good agreement using the neutron effective charge: $e_n = 0.5e$. On the other hand, phenomenological interactions and $NN + 3N$ disagree in effective nucleon g factors needed to reproduce the magnetic ($M1$) transition strengths [14].

Despite the remarkable differences, both phenomenological and microscopic $NN + 3N$ interactions give a similar description of neutron separation (binding) energies and low-lying excitation energies of Ca isotopes from $N = 22$ up to $N = 32$ [8,9,20]. As illustrated in [21], such observables might however be insensitive to cross-shell correlations. Therefore, there is a need to measure additional observables like electromagnetic moments, which further test the above models and might provide a deeper insight to developing improved shell-model interactions.

Magnetic moments and g factors, $g = \mu/(I\mu_N)$, of isotopes near shell closures are very sensitive to the occupancy of particular orbitals by valence particles (or holes). The quadrupole moments on the other hand are directly sensitive to nuclear shell structure [22]. While the terms *closed shell* or *magic number* may lack a rigid definition, the electromagnetic moments provide a more direct probe of the structure involved including cross-shell effects [23,24].

In this Rapid Communication, we report the first measurements of the quadrupole moment of the closed shell -1 isotope ^{47}Ca, and the quadrupole and magnetic moment of the closed-shell $+1$ isotope ^{49}Ca.[1] Also the magnetic and quadrupole moments of ^{51}Ca, having a single-hole with respect to the new $N = 32$ subshell closure, are presented, as well as its ground state (g.s.) spin. The experimental data are compared to shell-model calculations using phenomenological interactions, and to calculations including $3N$ forces based on chiral effective field theory.

At ISOLDE, CERN, exotic Ca isotopes were produced from nuclear reactions induced by a high-energy proton beam (1.4 GeV; pulses of 2 μC typically every 2.4 s) impinging on a uranium carbide target. High selectivity for the Ca reaction products was accomplished by laser ionization [25]. Ions were extracted from the ion source and accelerated up to 30 keV or 40 keV to be mass separated, after which they were injected into the ISOLDE radiofrequency quadrupole (RFQ) beam cooler, ISCOOL [26]. Ions were trapped for approximately 50 ms, and extracted bunches of 5 μs temporal width were distributed to a dedicated beam line for collinear laser spectroscopy experiments (COLLAPS). At COLLAPS, the ion beam was superimposed with a continuous wave (CW) laser beam from a frequency-doubled Ti:Sa laser, providing a 393-nm laser wavelength to excite the $4s\ ^2S_{1/2} \rightarrow 4p\ ^2P_{3/2}$ transition in Ca^+. The laser frequency was locked to a Fabry-Perrot interferometer, which was in turn locked to a polarization-stabilized HeNe laser, reducing the laser frequency drift to <10 MHz per day.

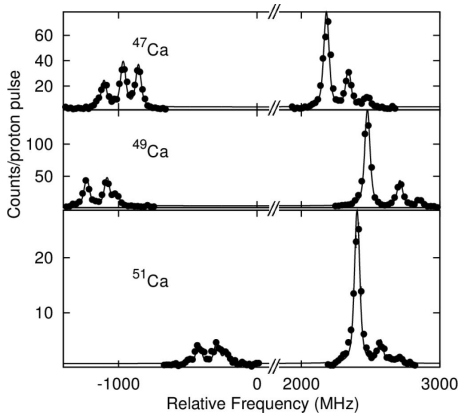

FIG. 1. Examples of hfs spectra measured for the Ca isotopes in the 393 nm $4s\ ^2S_{1/2} \rightarrow 4p\ ^2P_{3/2}$ ionic transition. The lines show the fit with a Voigt profile. Frequency values are relative to the centroid of ^{43}Ca.

By changing the ion velocity, and thereby Doppler tuning the laser frequency in the ion rest frame, hyperfine structure (hfs) components could be scanned. Fluorescence photons were detected by a set of four photomultipliers (PMT) at the end of the beam line (see Refs. [27,28] for details). By only accepting signals from the PMT while the ion bunch passed in front of them, background from scattered laser light and PMT dark counts was reduced by a factor of $\sim 10^4$. Sample hfs spectra measured during the experiment are shown in Fig. 1. The magnetic hfs constants, $A(^2S_{1/2})$, $A(^2P_{3/2})$, and quadrupole hfs constants, $B(^2P_{3/2})$, were extracted from the fit of Voigt profiles to the experimental spectra by using a χ^2-minimization technique as explained, e.g., in Ref. [29]. The values are listed in Table I. Only ^{43}Ca has been studied before in this ionic transition, and our values are in agreement within 1.1 standard deviations. For ^{41}Ca and ^{45}Ca, two measurements of the quadrupole hfs constants have been reported in the atomic level system, both relative to that of ^{43}Ca [30,31], yielding the ratios $B(^{41}\text{Ca})/B(^{43}\text{Ca}) = 1.63(1)$, and $B(^{45}\text{Ca})/B(^{43}\text{Ca}) = -0.94(27)$. The B-factor ratio equals the ratio of the quadrupole moments. Thus we can compare the ratio of our B values, measured in the ionic system

[1] A previous value for the magnetic moment of ^{49}Ca was suggested from a partial measurement of its hfs and assuming a value for its unknown isotope shift [52].

المنارة للاستشارات

TABLE I. Hyperfine structure values obtained from the fit to the experimental data compared to previous measurements.

A	I^π	$A(^2S_{1/2})$ (MHz)	$A(^2P_{3/2})$ (MHz)	$B(^2P_{3/2})$ (MHz)	Ref.
43	$7/2^-$	−806.87(42)	−31.10(30)	−4.2(1.3)	
		−806.40207160(8)			[32]
		−805(2)	−31.9(2)	−6.7(1.4)	[33]
			−31.0(2)	−6.9(1.7)	[34]
45	$7/2^-$	−811.99(44)	−31.43(19)	3.1(1.0)	
47	$7/2^-$	−860.96(28)	−33.33(13)	12.68(96)	
49	$3/2^-$	−1971.02(30)	−75.98(11)	−5.53(40)	
51	$3/2^-$	−1499.22(94)	−58.15(54)	5.4(1.8)	

$B(^{45}\mathrm{Ca})/B(^{43}\mathrm{Ca}) = -0.74(31)$, to the latter value. They are in agreement within the error bars.

The nuclear spin, I, is required to calculate each peak position in the minimization procedure. Since a different set of hfs constants is found for a given spin, the ratio, $R = A(^2P_{3/2})/A(^2S_{1/2})$, can be used to determine the correct spin for each isotope, as this ratio should be a constant over the entire isotopic chain (neglecting a possible small hyperfine anomaly). As can be seen from Fig. 2, the ratio R remains constant along the Ca isotopes up to ^{49}Ca, using the earlier determined g.s. spins in the fitting procedure. For ^{51}Ca we assumed three possible spins for its ground state and only when $I = 3/2$ is used, the ratio of the fitted hfs parameters is consistent with those from the other isotopes. Thus $I = 3/2$ is the g.s. spin of ^{51}Ca, confirming earlier tentative assignments [35,36], and in agreement with expectations from the shell model.

Magnetic moments were extracted from the lower state magnetic hfs constants, $A = \mu_I B_0/(IJ)$, where B_0 is the magnetic field produced by the electrons at the nucleus, and J is the electronic total angular momentum. Since high-precision values of $A(^2S_{1/2}) = -806.40207160(8)$ MHz [32] and $\mu = -1.3173(6)$ [37] are known for ^{43}Ca, this isotope was used as a reference to calculate the other magnetic moments from the measured A values. The results are shown in Table II, where we compare our data to earlier reported values for ^{45}Ca and ^{47}Ca.

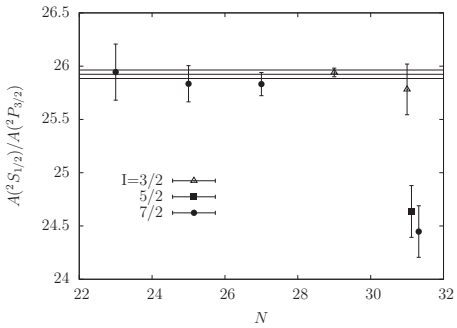

FIG. 2. Ratio between the hfs constants $A(^2P_{1/2})$ and $A(^2P_{3/2})$. The continuous line shows the average value $A(^2S_{1/2})/A(^2P_{3/2}) = 25.92(3)$. Hyperfine structure spectra of ^{51}Ca were fitted assuming different g.s. spin values of $I = 3/2,5/2,7/2$.

Quadrupole moments, Q, were obtained from the quadrupole hfs constant, $B = eQV_{JJ}$, with e the electron charge, and V_{JJ} the electric field gradient (EFG) produced by the electrons at the nucleus, the latter being isotope independent. To extract quadrupole moments from the measured hfs B parameters, a calculated value for the EFG, $eV_{JJ} = 151.3(7)$ MHz/b, was taken from atomic-physics calculations based on relativistic coupled-cluster theory (RCC) [40]. Independent values calculated from many-body perturbation theory (MBPT) [43,44] agree with the value from RCC within 3%. The extracted quadrupole moments are shown in Table II. The deviation of our value for ^{43}Ca from the literature values is attributed to the low statistics of our data for this isotope combined with a poorly resolved hyperfine splitting in the excited state. Note however that our ratio of the ^{45}Ca to ^{43}Ca quadrupole moment is consistent with the value measured in the atomic system.

Since the g factors are sensitive to the valence-particle configuration, it is illustrative to study their evolution along the Ca isotopic chain. The horizontal lines in Fig. 3 show the effective single-particle values ($g^\nu_{\mathrm{eff}} = 0.8g^\nu_{\mathrm{free}}$) for the different shell-model orbits. The isotope ^{39}Ca ($N = 19$) has a g factor close to the $d_{3/2}$ effective single-particle value, confirming the hole nature of this isotope. Once the $d_{3/2}$ orbit is filled, the fairly constant g-factor values from $N = 21$ up to $N = 27$ are in agreement with that of an odd neutron in the $f_{7/2}$ orbital.

As expected, the measured g factor of ^{49}Ca is close to the effective single-particle value of the $p_{3/2}$ orbit, and a similar value would be expected for ^{51}Ca. However, a deviation from this value is observed, indicating an appreciable contribution from the mixing with configurations due to neutron excitations across $N = 32$, which seems to contradict the closed-shell nature of $N = 32$. The isotope ^{51}Ca is an exceptional case for testing different shell-model interactions as excitations across $N = 32$ can be of $M1$-type (from $p_{3/2}$ into $p_{1/2}$) and therefore even a one percent mixing of those configurations in the wave function is sufficient to induce a ∼20% change of the g factor [46].

The measured and calculated magnetic moments of the Ca isotopes are shown in the upper panel of Fig. 4. A ^{40}Ca core is assumed in the calculations with the GXPF1A and KB3G phenomenological interactions, as well as for the calculations with the microscopic $NN + 3N$ interaction. To investigate the effect of breaking the ^{40}Ca core we also compare to a large-scale shell model calculation using the phenomenological interaction SDPF.SM starting from a virtual ^{28}Si core. For the KB3G and GXPF1A interactions, neutrons were allowed to occupy the pf shell, while an extended valence space including the $0g_{9/2}$ orbital ($pfg_{9/2}$ space) was used for the $NN + 3N$ calculations. Excitations of neutrons and protons from the upper sd shell into the pf shell are allowed with the SDPF.SM interaction. Bare spin and orbital

المنارة للاستشارات

TABLE II. Quadrupole and magnetic moments obtained from the measured hfs constants (Table I). The magnetic moments were obtained using the reference isotope ^{43}Ca, with $A(^2P_{3/2}) = -806.40207160(8)$ MHz [32]. Quadrupole moments were extracted using the calculated electric field gradient, $eV_{JJ} = 151.3(7)$ MHz/b [40]. Data are compared to calculations using the $NN + 3N$ interaction.

A	$\mu(\mu_N)$	$\mu(\mu_N)$ $(NN+3N)$	Q (b)	Q (b) $(NN+3N)$	Ref.
41	−1.594781(9)				[38]
			−0.080(8)		[31]
43		−1.56	−0.028(9)	−0.0246	This work
	−1.3173(6)[a]				[37]
			−0.043(9)		[33]
			−0.049(5)		[31]
			−0.0408(8)		[39]
			−0.0444(6)		[40]
45	−1.3264(13)	−1.45	+0.020(7)	+0.0252	This work
	−1.3278(9)				[41]
			+0.046(14)		[31]
47	−1.4064(11)	−1.38	+0.084(6)	+0.0856	This work
	−1.380(24)				[42]
49	−1.3799(8)	−1.40	−0.036(3)	−0.0422	This work
51	−1.0496(11)	−1.04	+0.036(12)	+0.0425	This work

[a]Reference value.

g factors were used in all theories to calculate the magnetic moments.

The disagreement between the shell-model calculations starting from a ^{40}Ca core and the experimental magnetic moments of ^{41,43,45}Ca suggests that nucleon excitations across the sd shell are important in the vicinity of $N = 20$. Indeed, large-scale shell model calculations using the SDPF.SM interaction are closer to the experimental values. These calculations include up to 6p-6h for ^{41}Ca, 4p-4p for ^{43}Ca, and 2p-2p for the other isotopes. A similar conclusion on the importance of cross-shell correlation across $N = 20$ was obtained from experimental $g(2^+)$ factors and $B(E2)$ values of ^{42,44}Ca [47,48] as well as the calcium isotope shifts [49]. For the heavier Ca isotopes, all theoretical calculations describe the experimental value rather well (see Fig. 4), indicating that from $N = 27$ and beyond, the assumption of a rigid ^{40}Ca core works well. Especially, the calculations with the $NN + 3N$ interaction give a very good agreement for ^{47,49,51}Ca. Considering that from the measured g factor a mixed ground state wave function is expected (Fig. 3), the excellent agreement for the microscopic calculations, which are not fitted to this mass region, is remarkable. The fact that the calculated values for the phenomenological KB3G and GXPF1A lay on opposite side of the experimental value is due to the different contributions of $(p_{1/2})^2(p_{3/2})^1$ and $(p_{1/2})^1(p_{3/2})^2$ configurations. Certainly, the magnetic moment is highly sensitive to matrix elements involving the $p_{3/2}$-$p_{1/2}$ spin-orbit partners. The ratio of $(p_{1/2})^1(p_{3/2})^2$ to $(p_{3/2})^3$ configurations in ^{51}Ca is a measure for these cross-shell excitations across $N = 32$: it is almost twice larger with $NN + 3N$ and GXPF1A (3.5% and 4.0%, respectively) than in KB3G (2.0%). Larger cross-shell excitations reduce the absolute value of the magnetic moment. On the other hand, due to stronger pairing, the $NN + 3N$ and KB3G interactions have a two times larger ratio of $(p_{1/2})^2(p_{3/2})^1$ over $(p_{1/2})^1(p_{3/2})^2$ configurations than GXPF1A, 1.6 and 1.9 compared to 0.9. These cross-shell excitations increase the absolute value of the magnetic moment.

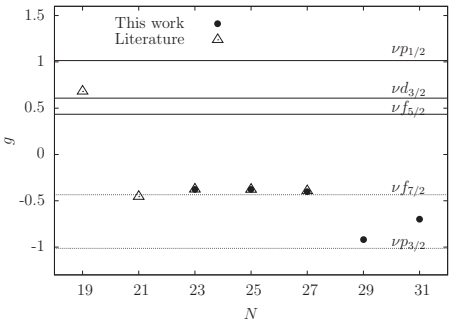

FIG. 3. Measured g factors compared with literature values and effective single-particle values (lines) using $g_s^\nu = -3.041$ and $g_l^\nu = 0.0$ ($g_{\rm eff}^\nu = 0.8 g_{\rm free}^\nu$). The magnetic moment of ^{39}Ca was taken from Ref. [45]. The experimental error bars are smaller than the symbols.

In the lower panel of Fig. 4, the experimental and calculated quadrupole moments are shown. The theoretical results assume neutron and proton effective charges, $e_n = 0.5e$ and $e_p = 1.5e$, respectively (protons in the valence space are allowed for the SDPF.SM interaction only). All interactions exhibit in general a good description of the experimental quadrupole moments. The only deviation exists for $N = 27$, where KB3G and GXPF1A slightly disagree with the experimental value, while $NN + 3N$ and SDPF.SM agrees nicely. The agreement between calculated and experimental values also confirms the values of effective charges used around $N = 20$ [18,49], and more recently around $N = 28$ [50]. Earlier studies of $N \sim Z$

المنارة للاستشارات

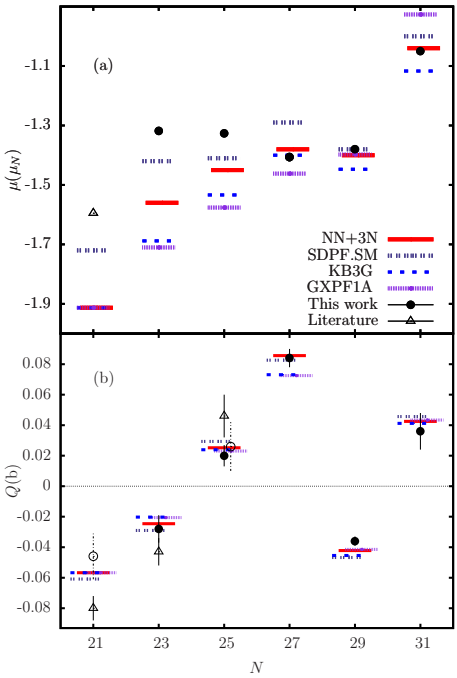

FIG. 4. (Color online) Measured magnetic and quadrupole moments of Ca isotopes. Results are compared with theoretical predictions from phenomenological interactions (KB3G, GXPF1A, SDPF.SM) and calculations including three-nucleon forces ($NN + 3N$). Experimental literature values (empty triangles) are given in Table II. The open circles show the values calculated from the ratios $B(^{41}\text{Ca})/B(^{43}\text{Ca}) = 1.63(1)$, $B(^{45}\text{Ca})/B(^{43}\text{Ca}) = -0.94(27)$ [31] and relative to our value of $Q(^{43}\text{Ca})$.

isotopes, where the $f_{7/2}$ orbital is dominant, suggested values of $e_n = 0.8e$ and $e_p = 1.15e$ [51], opening a discussion on the possible orbital dependence of the effective charges in the pf shell [3].

In summary, bunched-beam collinear laser spectroscopy was used to measure the hfs spectra in the Ca II resonance transition from $^{43-51}$Ca. Our results allowed a direct g.s. spin determination for ^{51}Ca. The quadrupole moments of ^{47,49,51}Ca, and magnetic moments of ^{49,51}Ca were measured for the first time. We compared these results with new shell-model calculations using a microscopic interaction derived from chiral effective field theory, including $NN + 3N$ forces, and fitted only to isotopes up to mass $A = 4$. Comparison was also made with existing and new calculations using phenomenological interactions. Large discrepancies among the measured magnetic moments and the calculated values using a ^{40}Ca core were observed around $N = 20$. Large-scale shell model calculations in the sd-pf valence space are required to reproduce better the observed magnetic moments. Further developments of microscopic interactions in the complete sd-pf valence space for both protons and neutrons are needed to provide a consistent description for all observables of Ca isotopes from below $N = 20$ up to above $N = 32$. For $N \geqslant 27$, the calculations with $NN + 3N$ forces derived from chiral effective field theory provide excellent agreement for both the magnetic and quadrupole moments. Through the gradual filling of the $f_{7/2}$ and $p_{3/2}$ orbits, our results provide a comprehensive study of the basic ingredients employed in shell-model calculations over a wide range of neutrons. At the level of precision of our experimental results, the g.s. quadrupole moments do not reveal any orbital dependence of the effective charges. The larger difference in calculated magnetic moments compared to electric quadrupole moments highlights the need of improved theoretical calculations, e.g., including two-body currents from chiral effective field theory, that compared to the present measurements may provide new insights on the magnetic operator and effective g factors.

This work was supported by the IAP-project P7/12, the GOA grant 15/010 KU Leuven, NSF Grant No. PHY-1068217, the BMBF Contracts No. 05P12RDCIC and No. 06DA70471, the Max-Planck Society, the EU FP7 via ENSAR No. 262010, the DFG through Grant No. SFB 634, ERC Grant No. 307986 STRONGINT, the Helmholtz Alliance HA216/EMMI, and MINECO (SPAIN) (FPA2011-29854). Computations were performed on JUROPA at the Jülich Supercomputing Center. We would like to thank the ISOLDE technical group for their support and assistance. International Research Fellowship of the Japan Society for the Promotion of Science (JSPS) and JSPS KAKENHI Grant No. 26.04323.

[1] B. A. Brown, Prog. Part. Nucl. Phys. **47**, 517 (2001).
[2] E. Caurier *et al.*, Rev. Mod. Phys. **77**, 427 (2005).
[3] J. J. Valiente-Dobon *et al.*, Phys. Rev. Lett. **102**, 242502 (2009).
[4] I. Stetcu and J. Rotureau, Prog. Part. Nucl. Phys. **69**, 182 (2013).
[5] S. Pastore, S. C. Pieper, R. Schiavilla, and R. B. Wiringa, Phys. Rev. C **87**, 035503 (2013).
[6] I. Talmi, Rev. Mod. Phys. **34**, 704 (1962).
[7] W. H. King, *Isotope Shifts in Atomic Spectra*, 1st ed. (Plenum Press, New York/London, 1984).
[8] F. Wienholtz *et al.*, Nature **498**, 346 (2013).
[9] D. Steppenbeck *et al.*, Nature **502**, 207 (2013).
[10] J. D. Holt *et al.*, J. Phys. G **39**, 085111 (2012).
[11] G. Hagen, M. Hjorth-Jensen, G. R. Jansen, R. Machleidt, and T. Papenbrock, Phys. Rev. Lett. **109**, 032502 (2012).
[12] R. Roth *et al.*, Phys. Rev. Lett. **109**, 052501 (2012).
[13] V. Somà, A. Cipollone, C. Barbieri, P. Navrátil, and T. Duguet, Phys. Rev. C **89**, 061301(R) (2014).
[14] J. D. Holt, J. Menéndez, J. Simonis, and A. Schwenk, Phys. Rev. C **90**, 024312 (2014).
[15] H.-W. Hammer, A. Nogga, and A. Schwenk, Rev. Mod. Phys. **85**, 197 (2013).
[16] A. Poves *et al.*, Nucl. Phys. A **694**, 157 (2001).

المنارة للاستشارات

[17] M. Honma, T. Otsuka, B. A. Brown, and T. Mizusaki, Phys. Rev. C **69**, 034335 (2004).
[18] E. Caurier, J. Menéndez, F. Nowacki, and A. Poves, Phys. Rev. C **75**, 054317 (2007).
[19] K. Helbert *et al.*, Astrophys. J. **773**, 11 (2013).
[20] A. T. Gallant *et al.*, Phys. Rev. Lett. **109**, 032506 (2012).
[21] P. Isacker and I. Talmi, J. Phys. Conf. Ser. **267**, 012029 (2011).
[22] C. H. Townes, H. M. Foley, and W. Low, Phys. Rev. **76**, 1415 (1949).
[23] R. J. Blin-Stoyle, Rev. Mod. Phys. **28**, 75 (1956).
[24] G. Neyens, Rep. Prog. Phys. **66**, 633 (2003).
[25] V. N. Fedosseev *et al.*, Rev. Sci. Instrum. **83**, 02A903 (2012).
[26] E. Mané *et al.*, Eur. Phys. J. A **42**, 503 (2009).
[27] J. Papuga *et al.*, Phys. Rev. Lett. **110**, 172503 (2013).
[28] K. Kreim *et al.*, Phys. Lett. B **731**, 97 (2014).
[29] M. Kowalska *et al.*, Phys. Rev. C **77**, 034307 (2008).
[30] E. Bergmann *et al.*, Z. Phys. A **294**, 319 (1980).
[31] M. Arnold *et al.*, Z. Phys. A **314**, 303 (1983).
[32] F. Arbes *et al.*, Z. Phys. D **31**, 27 (1994).
[33] R. E. Silverans *et al.*, Z. Phys. D **18**, 351 (1991).
[34] W. Nörtershauser *et al.*, Eur. Phys. J. D **2**, 33 (1998).
[35] F. Perrot *et al.*, Phys. Rev. C **74**, 014313 (2006).
[36] B. Fornal *et al.*, Phys. Rev. C **77**, 014304 (2008).
[37] L. Olschewski, Z. Phys. **249**, 205 (1972).
[38] E. Brun *et al.*, Phys. Rev. Lett. **9**, 166 (1962).
[39] D. Sundholm and J. Olsen, J. Chem. Phys. **98**, 7152 (1993).
[40] B. K. Sahoo, Phys. Rev. A **80**, 012515 (2009).
[41] M. Arnold *et al.*, Hyperfine Interact. **9**, 159 (1981).
[42] A. Andl *et al.*, Phys. Rev. C **26**, 2194 (1982).
[43] K. Z. Yu, L. J. Wu, B. C. Gou, and T. Y. Shi, Phys. Rev. A **70**, 012506 (2004).
[44] A.-M. Mårtensson-Pendrill and S. Salomonson, Phys. Rev. A **30**, 712 (1984).
[45] T. Minamisono *et al.*, Phys. Lett. B **61**, 155 (1976).
[46] R. J. Blin-Stoyle and M. A. Perks, Proc. Phys. Soc. A **67**, 885 (1954).
[47] S. Schielke *et al.*, Phys. Lett. B **571**, 29 (2003).
[48] M. J. Taylor *et al.*, Phys. Lett. B **605**, 265 (2005).
[49] E. Caurier *et al.*, Phys. Lett. B **522**, 240 (2001).
[50] L. A. Riley *et al.*, Phys. Rev. C **90**, 011305(R) (2014).
[51] R. du Rietz *et al.*, Phys. Rev. Lett. **93**, 222501 (2004).
[52] L. Vermeeren *et al.*, *Proceedings of the 6th International Conference on Nuclei Far from Stability and the 9th International Conference on Atomic Masses and Fundamental Constants, Bernkastel-Kues, Germany, 1992*, edited by R. Neugart and A. Wöhr (Institute of Physics, Bristol, 1993), p. 193.

المنارة للاستشارات

5.1.2 Configuration mixing in ^{51}Ca and wave function composition

To illustrate the high sensitivity due to the mixing with the spin-orbital partner, the gs magnetic moment of ^{51}Ca is calculated as the one given by three neutrons in the orbitals $p_{1/2}$, $p_{3/2}$ and $f_{5/2}$. Thus, the gs wave function is assumed as a mix of these orbitals

$$|^{51}\mathrm{Ca}, I = 3/2^-\rangle = a|(\nu p^3_{3/2})_{3/2}\rangle + b|[(\nu p^2_{3/2})_2(\nu p^1_{1/2})]_{3/2}\rangle + c|[(\nu p^2_{3/2})_2(\nu f^1_{5/2})]_{3/2}\rangle, \tag{5.1}$$

with a, b and c the mixing coefficients, such that $|a|^2 + |b|^2 + |c|^2 = 1$. Using the free g-factors values for a neutron: $g_l = 0$ and $g_s = g_s^\nu$, the ground-state magnetic moment of ^{51}Ca can be calculated as

$$\langle^{51}\mathrm{Ca}, I = 3/2^-|\boldsymbol{\mu}|^{51}\mathrm{Ca}, I = 3/2^-\rangle = g_s^\nu\left[\frac{1}{2}|a|^2 + \frac{7}{10}|b|^2 - \frac{5}{42}|c|^2 - \frac{\sqrt{10}}{5}(a^*b + b^*a)\right] \tag{5.2}$$

The details for the calculations used to obtain the expression 5.2 are given in the appendix A.5. The dependence of this expression as function of $|a|^2$ is shown in Figure 5.1. For a neutron in a $p_{3/2}$ ($|a|^2 = 1$, $|b| = 0$ and $|c| = 0$) orbit, the magnetic moment is equal to the free single-particle value $\mu = -1.913\mu_N$. If the mixing is only with the $f_{5/2}$ orbital ($|b| = 0$), the magnetic moment varies linearly proportional to the factor $|c|^2$ (blue curve in Figure 5.1). If the mixing is due to excitation into the spin-orbital partner level, $p_{1/2}$, in addition to a linear term proportional to $|b|^2$, a nonlinear factor proportional to ab contributes to the magnetic moment (red and green curves in Figure 5.1). Thus, a small percent of mixing between $p_{3/2}$ and $p_{1/2}$ ($|b| \neq 0$) has a huge sensitivity on the magnetic moment, due mainly to the off-diagonal term $|[(\nu p^2_{3/2})_2(\nu p^1_{1/2})]_{3/2}\rangle$ [1]. The horizontal black line in the same figure shows the experimental magnetic moment. In this simple model, ~ 4 % of mixing with $p_{1/2}$ causes a change of ~ 45 % in the magnetic moment, and is enough to reproduce the experimental value.

A more realistic estimation of configuration mixing in the gs wave function can be obtained by comparing the experimental magnetic moment with shell-model calculations. The measured magnetic moments of the Ca isotopes and calculated values obtained from different valence-space interactions are shown in Figure 4 of Article I. The details of the shell-model calculations and the different interactions used to obtain the ground electromagnetic moments are presented in Article I (see sec. 5.1.1)

The dominant component in the ^{51}Ca wave function[1] is about 85-87% with

[1]This model-dependent analysis is meaningful only within the same framework of shell-model calculation in the same valence-space. Although the wavefunction is not an observable,

المنارة للاستشارات

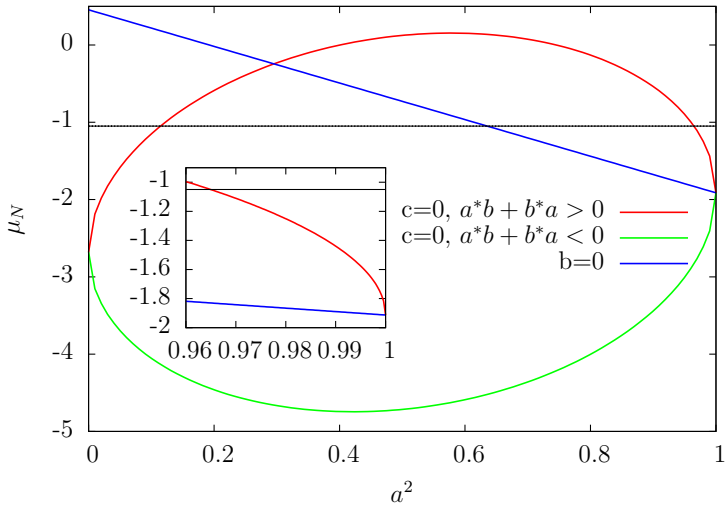

Figure 5.1: Magnetic moment obtained from the expression 5.2 with $g_s^\nu = -3.826$ as a function of the value a^2. In blue color the values assuming mixing with $f_{7/2}$ only ($|b| = 0$), and with red and green colors assuming that the mixing is only with $p_{1/2}$ ($|c| = 0$). The horizontal black line shows the experimental value. The huge sensitivity of the magnetic moment to the configuration mixing is mainly associated to the off-diagonal term in the case of excitation to a spin-orbit partner orbital. [1] .

the empirical shell model interactions, while it is only 78% with the NN+3N interaction (Table 5.1). Configurations with neutrons excited across $N = 32$ are highly fragmented and are more important with the latter interaction. This and Figure 3 in Article I suggests that correlations above $N = 32$ are not negligible for the magnetic moments in these isotopes. The $N = 32$ gap is due to a large spin-orbit splitting between the orbits $p_{3/2}$ and $p_{1/2}$. This gap is bigger for KB3G, which translates as an smaller percent of cross-shell configurations with $(p_{3/2})^2(p_{1/2})^1$, it is 1.7 %, compared with 2.8-3.3% for NN+3N and GXPF1A. A small $(p_{1/2})^1$ component means large magnetic moment, as it is observed for KB3G in ^{49}Ca. The calculated values for the phenomenological KB3G and GXPF1A lay on the opposite side of the experimental value, which is due to the different contributions of $(p_{1/2})^2(p_{3/2})^1$ and $(p_{1/2})^1(p_{3/2})^2$ configurations. As was previously discussed, the magnetic moment is highly sensitive to matrix elements involving the $p_{3/2}$-$p_{1/2}$ spin-

it is illustrative to compare the dominant configuration obtained for different shell-model interactions.

المنارة للاستشارات

Table 5.1: Main components (%) of the wave function obtained from shell model calculations using the different interactions GXPF1A, KB3G, SPDF.SM and NN+3N.

A	$((d_{3/2})^4 \otimes \nu)$	GXPF1A	KB3G	SDPF.SM	NN+3N
51	$(p_{3/2})^3$	87.2	84.6	86.0	78.3
	$(p_{3/2})^2(p_{1/2})^1$	3.3	1.7	2.0	2.8
	$(p_{3/2})^1(p_{1/2})^2$	3.1	3.3	3.0	4.4
	$(p_{3/2})^1(p_{1/2})^2/(p_{3/2})^2(p_{1/2})^1$	0.9	1.9	1.5	1.6

orbit partners. Due to stronger pairing, the NN+3N and KB3G interactions have a two times larger ratio of $(p_{1/2})^2(p_{3/2})^1$ over $(p_{1/2})^1(p_{3/2})^2$ configurations than GXPF1A, 1.6 and 1.9 compared to 0.9. These cross-shell excitations increase the absolute value of the magnetic moment. A small ratio of these configurations translates into a small magnetic moment, which is the case of GXPF1A for ^{51}Ca.

Finally, it should be emphasized that the calculations of the magnetic moments do not include contributions from two-body (or meson-exchange) currents. Two-body currents are predicted in chiral-effective field theory, and have been shown to be crucial for the magnetic moments in light nuclei $A \leqslant 9$ [167]. Work is in progress to include two-body currents in medium-mass nuclei [212, 82]. Comparison of these theoretical results with the present measurements would provide new insights on the magnetic operator and effective g-factors.

5.1.3 Comments on the effective operators

Effective g-factors and model space

We have concluded that the disagreement between the shell-model calculations and the experimental magnetic moments for ^{41,43,45}Ca is due to the importance of nucleon excitations across the sd-shell, which are not included if a ^{40}Ca core is used in shell-model calculations. There is no *a priori* reason to adopt bare g-factors ($g_s^{eff} \equiv g_s^{free}$, $g_l^{eff} \equiv g_l^{free} = 0$) in the different calculations, but it has been justified by the excellent agreement between theory and experiment on neutron-rich isotopes. In contrast, previous shell-model calculations of $M1$ transition strength around mass $A \sim 50$, concluded that an effective g-factor, $g_s^{eff} = 0.75(2) g_s^{free}$ is needed to reproduce the experimental results [213]. Effective g-factors are expected to compensate effects not included in the calculations, i.e, the use of a limited valence space, and/or the incomplete definition of the magnetic operators. From our results, we can assume that the

المنارة للاستشارات

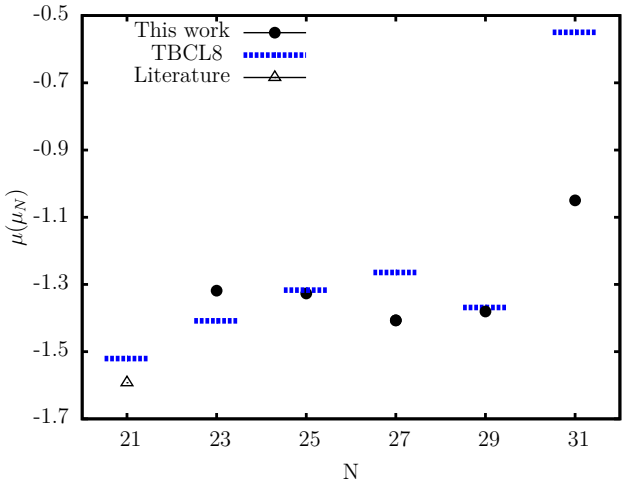

Figure 5.2: Experimental results of magnetic moments compared with calculations from the TBCL8 interaction [22]. Effective neutron g-factors were used: $g_s = -3.041$ ($g_s^{eff} = 0.8 g_s^{free}$) and $g_l = 0.000$.

model space is sufficiently large to include the important degrees of freedom on neutron-rich Ca isotopes, and higher order corrections to the magnetic moment operator are negligible for these nuclei, i.e, two-body currents.
As a didactic exercise, we compare the experimental results with a phenomenological interaction previously developed in a truncated space, which allows only 1p-1h excitations from the $f_{7/2}$ to the $p_{3/2}$, $p_{1/2}$, and $f_{5/2}$ orbits [22]. Here effective g-factors are justified to account for the neglected degrees of freedom due to this highly constrained space. Indeed, a very good agreement with the experimental low-lying excitation energies and gs electromagnetic moments of nuclei around mass $A = 41 - 66$ is found with this interaction, named the TBCL8 interaction [22]. Theoretical predictions and experimental values for the magnetic moment of Ca isotopes are shown in Figure 5.2.

Notice the relatively good agreement for $^{41-49}$Ca isotopes. These predictions suggest fairly pure $f_{7/2}$ configurations between $N = 21$ and $N = 27$, which could be seen as a contradiction of our previous conclusions on the need of including cross-shell excitations across $N, Z = 20$. Hence we stress that effective g-values can be introduced to improve the agreement with the experiment, but they must be used consistently to avoid misinterpretation.

المنارة للاستشارات

Effective charges

It has been seen that the ground-state quadrupole moments are in very good agreement with the results from different shell-model calculations using the neutron effective charge $e_n = 0.5e$ (Figure 4 in Article I). For the SPDF.SM interaction a proton effective charge value $e_p = 1.5e$ was assumed, and there are no protons in the valence space for the KB3G, GXPF1A and NN+3N interactions. The values for the neutron- and proton-effective charges are empirical results, obtained from the comparison between experimental electromagnetic properties and shell-model calculations [108]. There have been several attempts to derive the effective charges from microscopic theories, but the results are usually lower than the empirical values, see for example [214, 132, 215]. Within the uncertainty of our measurements, these values are equally in agreement with our experimental quadrupole moments.
The apparent linearity of the quadrupole moments through the filling of the $f_{7/2}$ and $p_{3/2}$ orbits (Fig. 4 in Article I) suggests a dominant single particle behavior, which can be easily understood in the seniority scheme. For n particles in an orbital j, the quadrupole moment can be expressed as [216]

$$\langle j^n|Q|j^n\rangle = \frac{2j+1-2n}{2j+1-2\nu}\langle j^\nu|Q|j^\nu\rangle, \tag{5.3}$$

where ν is the seniority number for the pure $|j^n; J\rangle$ configuration. Considering one unpaired valence nucleon, $\nu = 1$, this expression shows that the odd-N quadrupole moments in a single-j shell are linearly proportional to the effective single particle quadrupole moment, $\langle j^\nu|Q|j^\nu\rangle$. The dashed lines in Figure 5.3 show the fit to the expression 5.3 for the orbits $f_{7/2}$ and $p_{3/2}$, from which we obtain the corresponding slopes $\langle f_{7/2}|Q|f_{7/2}\rangle$=-82(4) mb ($21 \leq N \leq 27$), and $\langle p_{3/2}|Q|p_{3/2}\rangle$ =-36(3) mb ($29 \leq N \leq 31$). Values of effective charges in each orbital can be obtained from the ratio between the fitted effective single particle value and the free single particle value

$$Q_{sp} = -\langle r^2\rangle(2j-1)/(2j+2), \tag{5.4}$$

where $\langle r^2\rangle$ the mean square radius of the corresponding orbit. Using the calculated mean square radius: $\langle r^2\rangle_{f_{7/2}} \sim 17.5$ fm^2 and $\langle r^2\rangle_{p_{3/2}} \sim 21$ fm^2 [217], the effective charges $e_n = 0.69(4)e$ and $e_n = 0.43(6)e$ are extracted for $f_{7/2}$ and $p_{3/2}$, respectively. Notice that this simple approximation is model dependent, and assumes a pure single particle behaviour, which is only appropriate for Ca isotopes around $N \sim 28$. Due to the strong $N = 28$ closed shell the single-particle behaviour is more pronounced for the $p_{3/2}$ orbit. These extracted

المنارة للاستشارات

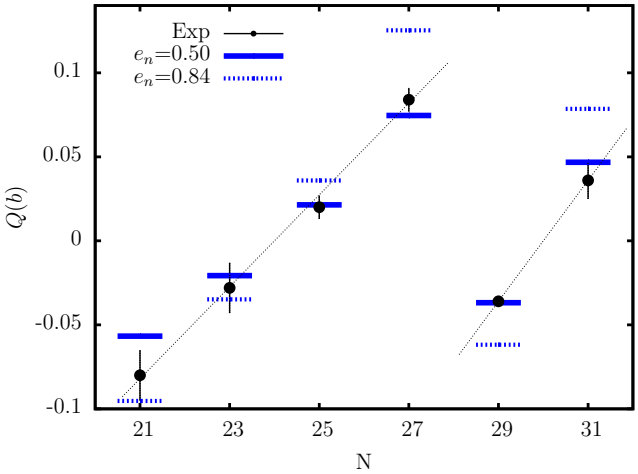

Figure 5.3: Experimental results for quadrupole moments compared with calculations from the TBCL8 interaction [22]. Two different effective neutron charges were used: $e_n = 0.5e$ (continuous line), and $e_n = 0.84e$ (dotted line).

neutron effective charge[2] for this orbit is in agreement with the results from shell-model calculations and the one derived microscopically [214].

5.2 Nuclear charge radii

5.2.1 Trend and comparison to different nuclear models

Modern nuclear theories such as shell-model calculations based on phenomenological and microscopic interactions have provided an excellent description of the neutron rich Ca isotopes, e.g., the binding energy [11], $E(2^+)$ excitation energies [12], and as was shown in the previous section, electromagnetic properties are also in good agreement with experiment, but the description of its charge radii goes beyond the scope of these models. Even though the size of the nucleus is closely linked to its binding energy, a satisfactory simultaneous description of these two properties is considered as a major puzzle [123]. Solving this problem is an important step towards an accurate and unified description of the nuclear force, which is important not only for the understanding of the atomic nucleus, but also has a direct impact in the modelling of astrophysical

[2]Notice that the extracted value for the neutron effective charge depends on the assumed electric field gradient, $e\dfrac{\partial^2 V}{\partial^2 z}$, used to derive the experimental quadrupole moments (Eq. 4.9).

المنارة للاستشارات

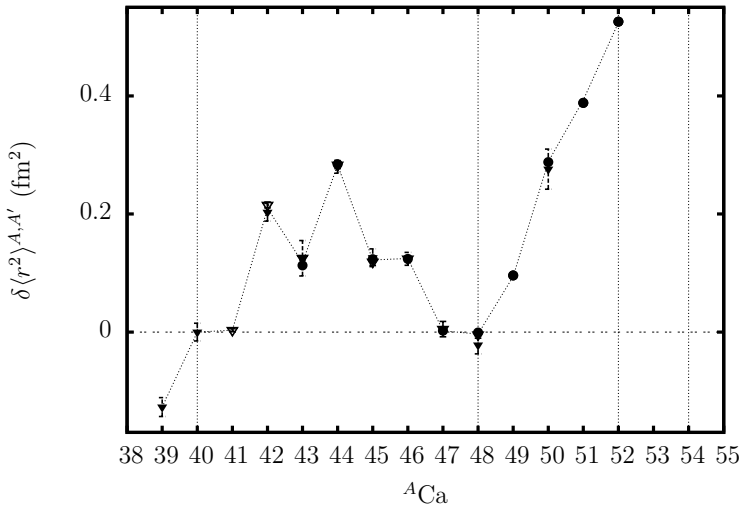

Figure 5.4: Changes in the rms charge radii measured for Ca isotopes with respect to ^{40}Ca. Filled circles are from this work. Literature values (filled triangles) are taken from Ref. [59, 200, 17].

processes [218]. Thus, it is essential to predict correctly the boundaries of the nuclear landscape, and to understand the origin of the elements in the universe [158].

While most of the properties around the Ca region display the simple patterns commonly observed in stable nuclei, the charge radii on the other hand, exhibit anomalous behaviour not observed in any other region of the nuclear chart, defying our simple picture of nuclear structure. Nuclear theory has satisfactorily explained most of the measured properties of Ca isotopes, but the fundamental description of its charge radii dependence has been a major challenge (see, e.g., [219, 220]). Phenomenological models have been proposed to account for some of the particularities observed in the charge radii of Ca isotopes [221, 220, 222], but so far there is a lack of a microscopic description.

The literature values and rms charge radii measured in this work are shown in Figure 5.4. When neutrons are added to the nucleus ^{40}Ca, the size of the charge distribution is showing a remarkable odd-even staggering effect on top of a parabolic shape. A stunning result is observed for ^{48}Ca: despite of an excess of eight neutrons, it has the same charge radius as ^{40}Ca.

So far, the only charge radius measured beyond ^{48}Ca had been ^{50}Ca, resulting in a large relative increase, $\delta\langle r^2\rangle^{50,48} = 0.293(37)$ fm^2 [17]. This result opened

المنارة للاستشارات

even more exciting questions on the charge radii evolution of Ca isotopes. Based on these antecedents, the prominent odd-even staggering could be even more pronounced beyond ^{48}Ca, and a reduction of the charge radius at $N = 32$ would be expected as a consequence of a suggested doubly-magic ^{52}Ca. This possible new parabolic behaviour between $N = 28$ and $N = 32$ is predicted from recent phenomenological studies that have succesfully reproduced the relative behaviour between $N = 20$ and $N = 28$ [223].

Mean field approaches have been a suitable tool to describe global properties of the atomic nucleus [158]. Although they offer a microscopic description of the nucleus, the coupling constants involved in the parametrization of the nuclear force can not be obtained by *ab initio* calculations. Instead, the nucleon-nucleon interaction is adjusted to experimental bulk properties (charge radii and nuclear masses) of nuclei close to stability [159]. The fitted interaction can then be used to describe properties of unstable nuclei and global properties throughout the nuclear chart [158]. Self-consistent calculations of charge radii are in good agreement with the experimental trends of heavy systems, but these conventional models fail to reproduce the marked details observed for the charge radii in the Ca region. The main reason is attributed to the poorly known density dependence of the nucleon-nucleon interaction [222], which is also essential for extrapolating predictions of nuclear properties far away from stability [158].

Chiral effective field theory has emerged as a promising path towards the fundamental description of the atomic nucleus, connecting our knowledge of the nuclear force with the underlying theory of the strong interaction, quantum chromodynamics (QCD). It allows a consistent disentanglement of the many-body forces in their leading components, and the details of the nucleon-nucleon interaction are usually adjusted to reproduce the properties of few-body systems ($A \leq 4$) only. This conventional approach has successfully described the nuclear charge radius and binding energy of light systems [102]. A notable problem appears for medium mass nuclei ($A \gtrsim 10$): while binding energy is predicted with good accuracy, the charge radius is always underestimated. This is a persistent problem in the current constructions of chiral Hamiltonians, and the effect is known to increase with the mass number [128].

Recently, an attempt to overcome the unabated problem attached to the charge radii description has proposed an alternative route to obtain the components of the nucleon-nucleon interaction. Coupled-cluster calculations based on a new parametrization of the nuclear force, NNLO$_{sat}$, have been successfully applied to accurately reproduce both charge radius and binding energies on medium mass doubly-magic systems up to ^{40}Ca [123]. Testing the reliability of this new interaction on heavier nuclei, and its predictive power on neutron-rich systems, provides not only a deeper understanding of the nuclear force, but offer us

المنارة للاستشارات

a first-principles approach to describe the properties of nuclear matter [218]. Therefore, the experimental determination of the charge radii of ^{49,51,52}Ca not only solves intriguing questions on the evolution of the anomalous Ca charge radii and is necessary to understand the possible doubly-magic character of ^{52}Ca, but also constitutes a striking test to our understanding of the atomic nucleus.

Our results for the charge radii of Ca isotopes are shown in Figure 5.5. The values of absolute charge radii shown in figure 5.5 are obtained from the rms charge radii (Table 4.10). The absolute charge radius of ^{40}Ca was used as a reference value [224]. The experimental results are compared with the different theoretical predictions from *ab initio* calculations (Fig 5.5a) using the newly developed Ch-EFT interactions NNLO$_{sat}$ [123], and two additional Ch-EFT interactions that predict fairly good nuclear matter saturation: 2.8/2.0 (EM), 2.0/2.0 (PWA) [225]. Figure 5.5b compares the experimental absolute charge radius with density functional calculations with the interactions Sly4, sv-min, UNEDF0 [158], HFB-24 [226], DS1+corr [227]. A very good description of the charge radii of Ca isotopes between $N = 20$ and $N = 28$ can be achieved if three- and four-body forces are introduced via a density-dependent pairing interaction, namely DF3-a interaction [222, 228] (Figure 5.5b). However, it fails shortly to reproduce the values beyond $N = 28$.
Shell-model calculations can not describe the absolute charge radius values, but the proton occupation of the fp-shell has been proposed to explain the relative changes of the rms charge radii between $N = 20$ and $N = 28$ [220]. The results for the rms charge radii obtained with the recently modified shell-model interaction ZBM2 [229] as well as a modern phenomenological model fitted to the Ca radii (Wang *el al.* [223]) are shown in Figure 5.5d.

The rms charge radius of ^{49}Ca presents a considerable increase with respect to ^{48}Ca, and an unexpected large increase is observed at ^{52}Ca. This increase towards $N = 32$ is similar to the large increase observed for open-shell nuclei like Fe ($N = 26$) [224], where there is not a sizable shell gap at $N = 32$. A similar increase was observed recently also in the K($Z = 19$) isotopes up to ^{51}K [63]. The parabolic behaviour and marked odd-even staggering between $N = 20$ and $N = 28$ is not reproduced by conventional mean field calculations. The phenomenological descriptions of the charge radii that have been proposed to explain the relative changes of charge radii between $N = 20$ and $N = 28$ [220, 222, 223], fail to describe the experimental values beyond $N = 32$, and none of the available theories can predict the large increase of the charge radii beyond $N = 28$. In a recent study of the neutron-deficient K isotopes [230] the K and Ca changes in rms charge radii have been compared to shell-model calculations up to $N = 32$. While these can reproduce the odd-even trend between $N = 20$ and $N = 28$, they fail to reproduce the very steep increase

المنارة للاستشارات

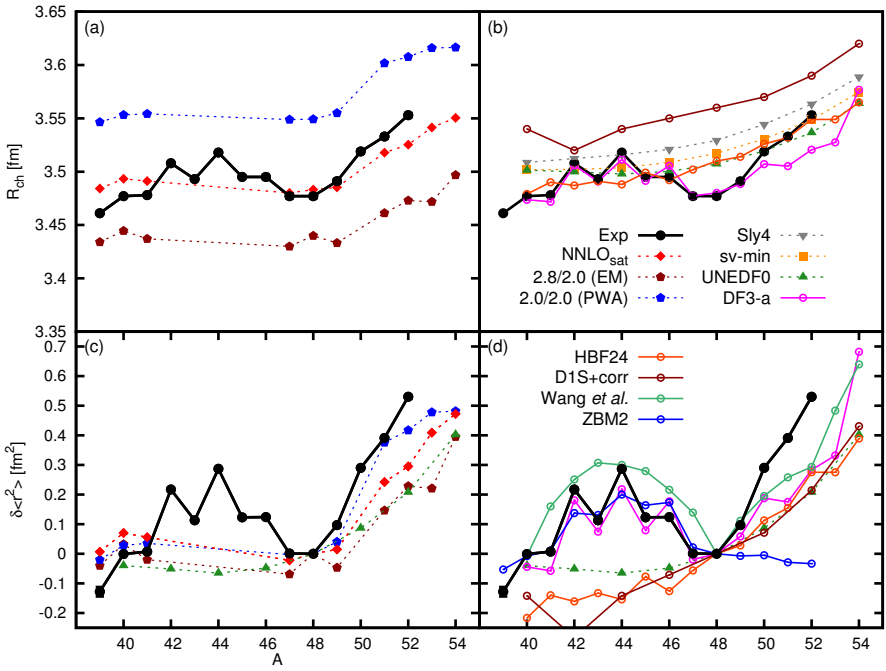

Figure 5.5: Charge radii of Ca isotopes. Experimental charge radii compared to ab initio calculations with: (a) chiral EFT interactions NNLO$_{sat}$, 2.8/2.0 (EM), 2.0/2.0 (PWA), as well as (b) DFT calculations. Experimental error bars are smaller than the symbols. The absolute values were obtained from the reference radius of ^{40}Ca (Rch = 3.478(2) fm) [224]. Experimental rms charge radius relative to that in ^{48}Ca compared to: (c) the ab initio results as well as (d) those of representative density functional theory (DFT) and different interactions than have been fitted to reproduce the odd-even staggering between $N = 20$ and $N = 28$ (see text for more details).

المنارة للاستشارات

beyond $N = 28$. All of these results suggest that new details of the effective many-body force should be included to understand the density-dependence of the nucleon-nucleon interaction on neutron-rich isotopes.

This discrepancy between our unexpected experimental results and the theoretical predictions beyond ^{48}Ca defy the doubly-magic character of ^{52}Ca, and raises new intriguing questions on the evolution of nuclear sizes far away from stability. These findings emphasize the importance of charge radii measurements further away from stability, especially the nucleus ^{54}Ca where a new magic number has been suggested at $N = 34$. Notice that the rapid increase observed for the charge radii contrasts with the slow and relatively flat behaviour of the binding energy observed on neutron-rich Ca isotopes [31], confronting the possible limits of existence for these isotopes [30, 31, 158]. An extended discussion of our experimental results and the calculations obtained from different theories are presented in Article II.

5.2.2 Article II: Unexpectedly large charge radii of neutron-rich calcium isotopes

This article summarizes the results obtained for the charge radii of Ca isotopes. It has been submitted to Nature Physics. The discussion is focused on the evolution of charge radii towards the newly suggested magic numbers $N = 32$ and $N = 34$. A relatively large increase of the charge radius at $N = 32$ defies the doubly-magic nature of ^{52}Ca raising new questions on the evolution of nuclear structure properties far away from stability.

While most of the spectroscopic properties of Ca isotopes have been reproduced by nuclear theory, the simultaneous prediction of both binding energy and charge radii has been a long-standing problem in the development of microscopic interactions. Very recently, a new interaction derived from chiral effective field theory has been developed to overcome this limitation. Our experimental results are compared with *ab initio* calculations based on this new interaction. These calculations reproduce relatively well the absolute charge radii of ^{40,41,47,48}Ca isotopes, but underestimate the large increase observed beyond $N = 28$. Besides of being a direct test to modern descriptions of the nuclear force, our results constitute an important step in the search of a unified description of the atomic nucleus, which is also of importance of the description of nuclear mater.

I performed the data analysis. I was involved in the discussion with the different collaborators. I prepared the figures and the different drafts of the manuscript.

المنارة للاستشارات

I was in charge of including all revision and for the submission process.

المنارة للاستشارات

Unexpectedly large charge radii of neutron-rich calcium isotopes

R.F. Garcia Ruiz[1], M. L. Bissell[1,2], K. Blaum[3], A. Ekström[4,5], N. Frömmgen[6], G. Hagen[4], M. Hammen[6], K. Hebeler[7,8], J.D. Holt[11], G.R. Jansen[4,5], M. Kowalska[9], K. Kreim[3], W. Nazarewicz[4,10,12], R. Neugart[3,6], G. Neyens[1], W. Nörtershäuser[6,7], T. Papenbrock[4,5], J. Papuga[1], A. Schwenk[7,8], J. Simonis[7,8], K.A. Wendt[4,5] and D.T. Yordanov[3,13]

[1]KU Leuven, Instituut voor Kern-en Stralingsfysica, B-3001 Leuven, Belgium [2]School of Physics and Astronomy, The University of Manchester, Manchester M13 9PL, United Kingdom [3]Max-Planck-Institut für Kernphysik, D-69117 Heidelberg, Germany [4]Physics Division, Oak Ridge National Laboratory, Oak Ridge, Tennessee 37831, USA [5]Department of Physics and Astronomy, University of Tennessee, Knoxville, Tennessee 37996, USA [6]Institut für Kernchemie, Universität Mainz, D-55128 Mainz, Germany [7]Institut für Kernphysik, Technische Universität Darmstadt, 64289 Darmstadt, Germany [8]ExtreMe Matter Institute EMMI, GSI Helmholtzzentrum für Schwerionenforschung GmbH, 64291 Darmstadt, Germany [9]CERN, European Organization for Nuclear Research, Physics Department, CH-1211 Geneva 23, Switzerland [10]Department of Physics and Astronomy and NSCL/FRIB Laboratory, Michigan State University, East Lansing, Michigan 48824, USA [11]TRIUMF, 4004 Wesbrook Mall, Vancouver, British Columbia, V6T 2A3, Canada [12]Institute of Theoretical Physics, Faculty of Physics, University of Warsaw, Pasteura 5, PL-02-093 Warsaw, Poland [13]Institut de Physique Nucléaire d'Orsay, CNRS/IN2P3, Université Paris-Sud, F-91406 Orsay Cedex, France.

Despite being a complex many-body system, the atomic nucleus exhibits simple structures for certain "magic" numbers of protons and neutrons. The calcium chain in particular is both unique and puzzling: evidence of doubly-magic features are known in ^{40,48}Ca, and recently suggested in two radioactive isotopes, ^{52,54}Ca. Although many properties of experimentally known Ca isotopes have been successfully described by nuclear theory, it is still a challenge to predict their charge radii evolution. Here we present the first measurements of the charge radii of ^{49,51,52}Ca, obtained from laser spectroscopy experiments at ISOLDE, CERN. The experimental results are complemented by state-of-the-art theoretical calculations. The large and unexpected increase of the size of the neutron-rich calcium isotopes beyond $N = 28$ challenges the doubly-magic nature of ^{52}Ca and opens new intriguing questions on the evolution of nuclear sizes away from stability, which are of importance for our understanding of neutron-rich atomic nuclei.

Similar to the electrons in the atom, protons and neutrons (nucleons) in atomic nuclei occupy quantum levels that appear in "shells" separated by energy gaps. The number of nucleons that completely fill each shell define the so called "magic" numbers, known in stable nuclei as $2, 8, 20, 28, 50, 82, 126$[1]. A fundamental understanding of how these magic configurations evolve in unstable neutron-rich nuclei, and how they impact the charge radius, is one of the main challenges of modern experimental and theoretical nuclear physics[2–9].

The calcium isotopic chain ($Z = 20$) is a unique nuclear system to study how protons and neutrons interact inside the atomic nucleus: two of its stable isotopes are magic in both their proton and neutron number (^{40}Ca and ^{48}Ca), while experimental evidence of doubly-magic features in two short-lived calcium isotopes have been reported recently, based on precision measurements of nuclear masses for ^{52}Ca ($N = 32$)[6] and 2^+ excitation energies for ^{54}Ca ($N = 34$)[7]. Possibly, additional doubly-magic isotopes might exist even further away from stability[10]. As a local change in the behaviour of the charge radius is expected in doubly-magic nuclei[11], it is important to pin down the charge radius in these exotic isotopes to understand how shell structure evolves and impacts the limits of stability.

Although the average distance between the electrons and the nucleus in an atom is about 5000 times larger than the nuclear radius, the size of the nuclear charge distribution is manifested as a perturbation of the atomic energy levels. A change in the nuclear size between two isotopes gives rise to a shift of the atomic hyperfine structure levels. This shift between two isotopes, commonly known as the isotope shift, $\delta\nu^{A,A'}$, includes a part that is proportional to the change in the nuclear mean square charge radii, $\delta\langle r^2\rangle^{A,A'}$ (see expression (1) in methods). Isotope shifts of stable Ca isotopes have been extensively studied in the literature[13], revealing the unusual evolution of their charge radii. Despite an excess of eight neutrons, ^{48}Ca exhibits the striking feature that it has essentially the same charge radius as ^{40}Ca. A fundamental explanation of these anomalous features has been a long-standing problem for nuclear theory for more than three decades (see, e.g.,[14,15]). Quantitative scenarios have been proposed to account for some of these properties[14,16,17], but so far a microscopic description was lacking.

A first estimate for the charge radius of the radioactive ^{49}Ca isotope was based on a failure to observe its resonance in a dedicated measurement of its isotope shift. The resulting conclusion that $\delta\nu^{48,49} \leq 50\,\text{MHz}$ suggested an enormous increase of the charge radius $\delta\langle r^2\rangle^{48,49} \geq 0.5\ \text{fm}^2$[18], reflecting the strong magicity of ^{48}Ca. So far, the only charge radius measured beyond

المنارة للاستشارات

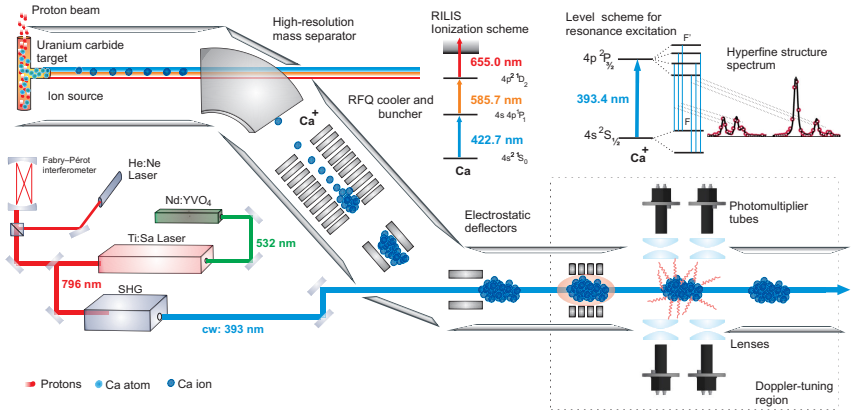

FIG. 1. High-resolution bunched collinear laser spectroscopy at ISOLDE, CERN. Short-lived calcium isotopes are produced from nuclear reactions of high-energy protons impacting on an uranium carbide target. Ca atoms were selectively ionized by using a three-step laser scheme[12]. Ions were extracted from the source and mass separated to be injected into a radiofrequency trap, where they are accumulated for typically 100 ms. Bunches of ions were extracted and redirected into the COLLAPS beam line to perform collinear laser spectroscopy experiments. At COLLAPS, the ions are superimposed with a continuous wavelength laser beam to scan the hyperfine structure in the $4s\ ^2S_{1/2} \rightarrow 4p\ ^2P_{3/2}$ transition of Ca^+ (see text for more details).

^{48}Ca has been for ^{50}Ca, resulting in a large increase of $\delta\langle r^2\rangle^{48,50} = 0.293(37)$ fm^2[19]. These results raised even more exciting questions on the charge radii evolution of

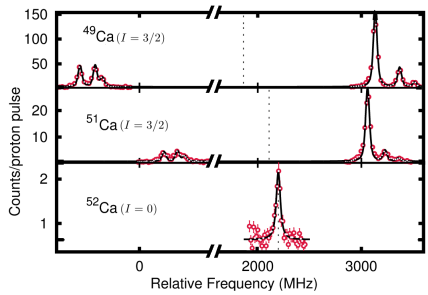

FIG. 2. Examples of hyperfine structure spectra measured for the Ca isotopes in the 393-nm $4s\ ^2S_{1/2} \rightarrow 4p\ ^2P_{3/2}$ ionic transition. The solid lines show the fit with a Voigt profile. Frequency values are relative to the centroid of ^{40}Ca. The position of each hfs centroid is indicated by the dashed lines.

Ca isotopes. It suggested that the prominent odd-even staggering of their charge radii could be even more pronounced beyond ^{48}Ca since a reduction of the charge radius for ^{52}Ca would be expected as a consequence of a suggested doubly-magic nature of this isotope. Thus, the experimental determination of the charge radii of ^{49,51,52}Ca not only addresses fundamental questions regarding the size of atomic nuclei, but are also important for understanding the possible doubly-magic character of ^{52}Ca. By using high-resolution bunched-beam collinear laser spectroscopy at ISOLDE, CERN, changes in the charge radii for $^{40-52}$Ca isotopes were obtained from the measured optical isotope shifts (see Table I). With a production yield of only a few hundred ions per second, our measurement of ^{52}Ca represents one of the highest sensitivities ever reached by using fluorescence detection techniques.

The isotope shift is typically 10^6 times smaller than the absolute transition frequency between two atomic levels, and the relevant part is in turn only a small fraction of the total shift. Thus a measurement of such a tiny change is only possible by using ultra-high resolution techniques. Collinear laser spectroscopy has been established as a unique method to reach such high resolution and has been applied with different detection schemes to study a variety of isotopes[22–24].

المنارة للاستشارات

TABLE I. **Measured isotope shifts and corresponding rms charge radii.** Statistical and systematic uncertainties are given in round and squared brackets, respectively.

	$\delta\nu^{40,A}$ (MHz)			$\delta\langle r^2\rangle$ (fm^2)		
A	This work	Literature		This work	Literature	
40	0	0[a]	0[b]	0[c]	0[d]	0[e]
42	–	426.4(15)[10]	425(4)[4]		0.203(15)	0.215(5)
43	683.0(12)[16]		672(9)[6]	0.114(4)[8]	0.125(30)	0.125(3)
44	851.1(6)[21]	850.1(10)[20]	842(3)[8]	0.288(2)[6]	0.280(11)	0.283(6)
45	1103.5(7)[25]		1091(4)[10]	0.125(3)[8]	0.126(15)	0.119(6)
46	1301.0(6)[30]		1287(3)[12]	0.125(2)[8]	0.124(11)	0.124(5)
47	1524.8(8)[35]			0.002(3)[9]		0.005(13)
48	1706.5(8)[38]	1710.6(35)[42]	1696(4)[16]	0.001(3)[10]	−0.022(15)	−0.004(6)
49	1854.7(10)[43]			0.098(4)[12]		
50	1969.2(9)[47]		1951(9)[20]	0.291(3)[12]	0.276(34)	
51	2102.6(9)[51]			0.392(3)[13]		
52	2219.2(14)[56]			0.531(5)[15]		

[a] High-precision measurements of isotope shifts of stable Ca isotopes[20].
[b] Data from Ref[19].
[c] Values of $K_{SMS} = -8.8(5)$ GHz u and $F = -276(8)$ MHz/fm^2 were taken from the King-plot results (see methods). In square brackets are listed the systematic errors associated to these factors, which are related to the uncertainty of the kinetic energy of the ion beam.
[d] Recalculated from isotope shift values reported in[19] using the newly reported mass values[21].
[e] Taken from Ref.[13].

A major challenge of exotic nuclei is that they are produced in very low quantities and exist only for a fraction of a second. Therefore, continuous improvements have been made during the past decades to enhance the experimental sensitivity, without sacrificing resolution. Since the introduction of an ion cooler-buncher for collinear spectroscopy that allows bunching radioactive beams[25], the sensitivity of the conventional fluorescence laser spectroscopy has been improved by two to three orders of magnitude. It is now possible to routinely perform experiments with beams of $\sim 10^4$ ions/s[26]. In this work, we have further optimized the photon detection sensitivity and at the same time reduced further the photon background events[8], now allowing to study calcium isotopes produced with a yield of only a few hundred ions per second. While preserving the high resolution, this sensitivity surpasses the previous limit by two orders of magnitude, achieved by an ultra-sensitive particle detection technique employed on Ca isotopes[19].

The short-lived Ca isotopes studied in this work were produced at the ISOLDE on-line isotope separator, located at the European Center for Nuclear Research, CERN. High-energy proton pulses with intensities of $\sim 3 \times 10^{13}$ protons/pulse at 1.4 GeV impinged every 2.4 seconds on an uranium carbide target to create radioactive species of a wide range of chemical elements. The Ca isotopes were selected from the reaction products by using a three-step laser ionization scheme provided by the Resonance Ionization Laser Ion Source (RILIS)[12]. A detailed sketch of the different experimental processes from the ion beam production to the fluorescence detection is shown in Fig. 1.

After selective ionization, Ca ions (Ca^+) were extracted from the ion source and accelerated up to 40 keV. The isotope of interest was mass-separated by using the High-Resolution Mass Separator (HRS). The selected isotopes were injected into a gas-filled radiofrequency trap (RFQ) to accumulate the incoming ions. After a few milliseconds, bunches of ions of $\sim 5\mu$s temporal width were extracted and redirected into a dedicated beam line for collinear laser spectroscopy experiments (COLLAPS). At COLLAPS, the ion beam was superimposed with a continuous wave laser beam fixed at 393-nm wavelength (see methods), close to the $4s\ ^2S_{1/2} \rightarrow 4p\ ^2P_{3/2}$ transition in the Ca^+. The laser frequency was fixed to a constant value, while the ion velocity was varied inside the optical detection region. A change in the ion velocity corresponds to a variation of laser frequency in the ion rest frame. This Doppler tuning of the laser frequency was used to scan the hyperfine structure (hfs) components of the $4s\ ^2S_{1/2} \rightarrow 4p\ ^2P_{3/2}$ transition. At resonance frequencies, transitions between different hfs levels were excited, and subsequently the fluorescence photons were detected by a light collection system consisting of four lenses and photomultipliers tubes (PMT) (see Refs.[8] for details). The photon signals were accepted only when the ion bunch passed in front of the light collection region, reducing the background counts from scattered laser light and PMT dark counts by a factor of $\sim 10^4$. A sample of the hfs spectra measured during the experiment is shown in Fig. 2.

The isotope shifts were extracted from the fit of the hfs experimental spectra, assuming multiple Voigt profiles in the χ^2-minimization (see methods). The measured isotope shift relative to the reference isotope ^{40}Ca,

المنارة للاستشارات

and the corresponding change in the mean-square charge radius are shown in Table I. Statistical errors (parentheses) correspond to the uncertainty in the determination of the peak positions in the hfs spectra. The systematic errors in the isotope shift (square brackets) are mainly due to the uncertainty in the beam energy, which is also the main contribution to the uncertainty in the charge radius. Independent high-precision measurements of isotope shifts on stable Ca isotopes[20] were used for an accurate determination of the kinetic energy of each isotope. The stability of the beam energy was controlled by measuring the stable ^{40}Ca, before and after the measurement of each isotope of interest.

Our experimental results (Table I and Fig. 3) show that the root-mean-square (rms) charge radius of ^{49}Ca presents a considerable increase with respect to ^{48}Ca, $\delta\langle r^2\rangle^{48,49} = 0.097(4)$ fm^2, but much smaller than previously suggested[18]. The increase continues towards $N = 32$, resulting in a very large charge radius for ^{52}Ca, with an increase relative to ^{48}Ca of $\delta\langle r^2\rangle^{48,52} = 0.530(5)$ fm^2. This increase observed beyond the neutron number $N = 28$ is as large as the values observed for open-shell nuclei like Fe[27], where there is not a sizable shell gap at $N = 32$. Thus, the charge radius of ^{52}Ca is found to be much larger than expected for a doubly-magic nucleus.

With advances in chiral effective field theory (EFT) and the development of powerful many-body methods, nuclear structure theory has entered a new era in recent years. Chiral EFT allows to systematically derive nuclear forces in terms of low-energy degrees of freedom, nucleons and pions, based on the symmetries of the fundamental theory, Quantum Chromodynamics. Chiral EFT provides systematically improvable Hamiltonians, explains naturally the hierarchy of two-, three-, and higher-body forces, and allows to estimate theoretical uncertainties[28].

Ab initio calculations based on chiral EFT interactions are able to correctly predict properties of light nuclei[31] and oxygen isotopes[32]. In addition, many-body calculations starting from a ^{40}Ca core provide an excellent description of the binding energies of neutron-rich Ca isotopes[6], 2^+ excitation energies[4,5,33] and ground-state electromagnetic moments[34]. However, there are also clear indications for deficiencies of some chiral EFT interactions: ground-state energies of heavier nuclei turn out to be systematically too large and radii are significantly too small[9,35].

Very recently, this problem was addressed by an optimization of chiral EFT interactions[9] that also included binding energies and radii of selected nuclei up to mass number $A = 25$ in addition to data from two- and few-body systems. Ab initio coupled-cluster calculations based on the resulting interaction (NNLO$_{\rm sat}$) accurately reproduce both charge radii and binding energies of nuclei up to ^{40}Ca, and the empirical saturation point of symmetric nuclear matter. In addition to NNLO$_{\rm sat}$, we employ two chiral interactions[36], SRG1 and SRG2, de-

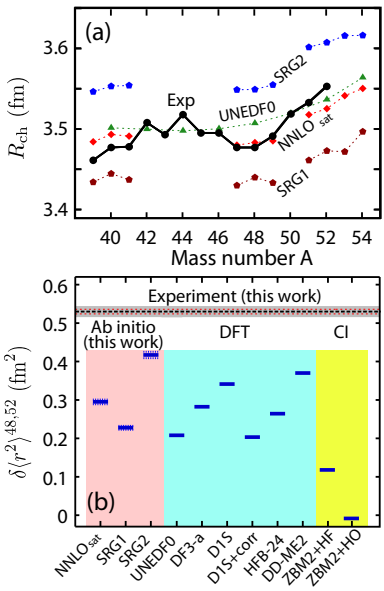

FIG. 3. Charge radii of Ca isotopes. (a) Experimental charge radii compared to ab initio calculations with chiral EFT interactions NNLO$_{\rm sat}$, SRG1, SRG2, as well as DFT calculations with the UNEDF0 functional. Experimental error bars are smaller than the symbols. The absolute values were obtained from the reference radius of ^{40}Ca ($R_{\rm ch} = 3.478(2)$ fm)[27]. The values of ^{39}Ca and ^{41,42}Ca are taken from Ref.[29] and Ref.[30], respectively. A systematic theoretical uncertainty of 1% is estimated for the absolute values due to the truncation level of the coupled-cluster method and the finite basis-space employed in the computation. (b) Experimental rms charge radius in ^{52}Ca relative to that in ^{48}Ca compared to the ab initio results as well as those of representative density functional theory (DFT) and configuration interaction (CI) calculations. The systematic uncertainties in the theoretical predictions are largely cancelled when the differences between rms charge radii are calculated (dotted horizontal blue lines). Experimental uncertainties are represented by the horizontal red lines (statistical) and the gray shaded band (systematic).

rived from renormalization group techniques[37] (see methods for details), which are fit only to properties of $A \leq 4$ and predict nuclear matter saturation within theoretical uncertainties.

In Fig. 3 we compare the experimental results to the charge radii obtained in our ab initio calculations and to other theoretical predictions. Figure 3 (a) shows that our calculations correctly yield similar charge radii

المنارة للاستشارات

for ^{40}Ca and ^{47,48}Ca for the chiral EFT interactions employed. These calculations are based on the single-reference coupled-cluster method, which is ideally suited for nuclei with at most one or two nucleons outside a closed (sub-) shell[38]. Thus, we do not give theoretical results for the mid-shell isotopes $^{42-46}$Ca and ^{50}Ca. We note that absolute values of charge radii are very well reproduced by NNLO$_{\rm sat}$. The interactions SRG1 and SRG2 also reproduce well the overall trend, but as they were not optimized to saturation properties can give either somewhat too low or too high saturation densities, corresponding to larger or smaller charge radii. Also shown are nuclear DFT results obtained with the Skyrme energy density functional UNEDF0[39], which fails to describe the fine details of the experimental trend.

Figure 3 (b) shows the difference in rms charge radii between ^{52}Ca and ^{48}Ca predicted with different methods and models; all being representative of modern approaches to charge radii. In general, for neutron-rich isotopes beyond ^{48}Ca, our ab initio calculations consistently predict an increase in charge radii for ^{50,52}Ca but fail short of describing the data. Similarly, DFT predictions with various models[40–45]; configuration interaction (CI) calculations[45] obtained from large-scale shell-model calculations with the ZBM2 interaction[14,46] using Skyrme-Hartree-Fock (ZBM2+HF) and harmonic oscillator (ZBM2+HO) wave functions, all considerably underestimate the large charge radius of ^{52}Ca. The standard explanation involving quadrupolar correlations[14,45] does not seem to improve this, as can be seen by comparing the D1S and D1S plus quadrupolar correlations (D1S+corr) results[42] in Fig. 3 (b). (For more discussion of the impact of dynamical quadrupole and octupole effects on charge radii in the Ca chain, see also Ref.[17].) Thus, our experimental results are truly unexpected. Speculating about the reason for these theoretical shortcomings we note that all theoretical approaches are lacking in the description of deformed intruder states associated with complex configurations. To develop large-scale ab-initio, CI, and multi-reference DFT frameworks with optimized input, capable of treating deformed intruder states, constitutes an ambitious future program for the era of exascale computing.

To assess the impact of core breaking effects, which turned out to be important for the description of electromagnetic moments in this region[34], we studied the proton occupancies of natural orbitals above the naively filled $Z = 20$ shell. Our ab initio calculations show a weak, but gradual erosion of the proton core as neutrons are added. While this defies the simple pattern of a rigid proton core expected for the magic Ca isotopes, the estimated magnitude of core breaking effects, including coupling to the neutrons, is not sufficient to explain the large charge radius of ^{52}Ca.

In summary, the charge radii of ^{49,51,52}Ca were measured for the first time, extending the picture for the evolution of charge radii over three neutron shell closures; a unique scenario found in the entire nuclear chart. We find that between ^{48}Ca and ^{52}Ca the charge radius exhibits a strong increase that considerably exceeds theoretical predictions. This is a surprising finding, considering that ^{40}Ca and ^{48}Ca have similar charge radii[19], which are significantly smaller than the charge radius of ^{52}Ca. Our measurements are complemented by ab initio calculations that reproduce the similarities of charge radii in ^{40,48}Ca but cannot account for the unexpected increase in $R_{\rm ch}$ to ^{52}Ca. These calculations also show an increase in proton occupancies outside the $Z = 20$ core as more neutrons are added to ^{40}Ca, hinting at a progressive weakening of the $Z = 20$ shell closure in the neutron-rich calciums. Future experiments aim at extending the current studies to isotopes even further away from stability, especially for the possibly doubly-magic nucleus ^{54}Ca[7]. These results open intriguing questions on the evolution of charge radii away from stability and constitute a major challenge in the search of a unified description of the atomic nucleus.

المنارة للاستشارات

METHODS

Laser setup The continuous wave laser beam at 393-nm wavelength was obtained from a second-harmonic generation of a Ti:Sa laser output, pumped with 532 nm light from a cw Nd:YVO_4 laser. To reduce the laser frequency drift to less than 10 MHz per day, the laser frequency was locked to a Fabry-Perrot interferometer, which was in turn locked to a polarization-stabilized HeNe laser (see Figure 1).

Chiral EFT interactions The ab initio calculations in this work are based on interactions derived within chiral effective field theory. The interaction $\mathrm{NNLO_{sat}}$ includes contributions to nucleon-nucleon and three-nucleon forces up to third order in the chiral expansion, which have been fitted to selected properties of nuclei up to ^{24}O, so as to include information on saturation properties (see Ref.[9] for details). The interactions SRG1 and SRG2 are derived from the fourth-order chiral nucleon-nucleon interaction of Ref.[47] by performing an evolution to lower resolution scales via the the similarity renormalization group[36]. The three-nucleon interactions include contributions up to third order in the chiral expansion and are fit to the binding energy of ^{3}H and the charge radius of ^{4}He at the low resolution scales. The interaction SRG1 refers to an interaction at the the resolution scales $\lambda/\Lambda_{\mathrm{3NF}} = 2.8/2.0$ fm^{-1}(EM c_i's) and SRG2 to $\lambda/\Lambda_{\mathrm{3NF}} = 2.0/2.0$ fm^{-1}(PWA c_i's) (see Table 1 in Ref.[36]).

Coupled-cluster calculations Our coupled-cluster (CC) calculations are performed starting from a closed-shell Hartree-Fock reference state computed from 15 harmonic-oscillator shells with an oscillator frequency of $\hbar\Omega$ =22 MeV. In CC theory correlations are included via a similarity transformation, which generates particle-hole excitations to all orders in perturbation theory. In our calculations the cluster operator is truncated at the singles and doubles level (CCSD), and also includes triples excitations in a nonperturbative but approximate way (see Ref.[38] for details). Contributions from three-nucleon forces are taken into account up to $E_{3\mathrm{max}} = 18\ \hbar\Omega$ for $\mathrm{NNLO_{sat}}$ and $E_{3\mathrm{max}} = 16\ \hbar\Omega$ for SRG1 and SRG2 in the normal-ordering approximation, which has been demonstrated to be an excellent approximation for medium-mass nuclei[48]. Based on the size-extensitivity of the CC method, the uncertainty of the radius results is estimated to 1% in the CCSD approximation. The uncertainties of the *ab-initio* results shown in Fig. 3 (b) are very small, because they are differences of correlated and very small (1%) uncertainties of each individual radius. We find 0.006 fm^2, 0.005 fm^2, and 0.008 fm^2 for the uncertainties of $\delta\langle r^2\rangle$[48,52] for the interactions $\mathrm{NNLO_{sat}}$, SRG1, and SRG2, respectively.

The results for the charge radii are computed from the point-proton radius starting from the intrinsic operator. We then correct the point-proton radius for the finite proton and neutron charge sizes, for the relativistic Darwin-Foldy term, and the spin-orbit correction. The latter is calculated consistently in CC theory. Finally, we note that the DFT results also include this spin-orbit correction. If not added in the original reference, we adopt spin-orbit corrections given by the mean of CC theory and relativistic mean-field theory.

Data analysis The measured hyperfine structure spectra were fitted with Voigt profiles of common widths for the different hfs components. The peak positions are constrained by the functional expression for the hyperfine structure splitting in the ionic ground- and excited states. The hfs centroid obtained for each isotope were used to extract the isotope shifts, $\delta\nu^{A,A'}$, and calculate the corresponding change in rms charge radius, $\delta\langle r^2\rangle^{A,A'}$, following the expression

$$\delta\langle r^2\rangle^{A,A'} = \langle r^2\rangle^{A'} - \langle r^2\rangle^{A} = \frac{1}{F}\left(\delta\nu^{A,A'} - K_{\mathrm{MS}}\frac{M_{A'}-M_A}{M_A M_{A'}}\right). \quad (1)$$

The mass shift, K_{MS}, is the sum of the normal mass shift, K_{NMS}, and the specific mass shift, K_{SMS}. The value $K_{\mathrm{NMS}} = 417.97$ GHz u was obtained from the energy of the $4s\ ^2S_{1/2} \rightarrow 4p\ ^2P_{3/2}$ transition of Ca^+. The electronic field factor, F, and the specific mass shift factor, K_{SMS}, were obtained by comparing with independent measurements of charge radii in a King-plot analysis[13]. The results: $F = -276(8)$ MHz/fm^2 and $K_{\mathrm{SMS}} = -8.8(5)$ GHz u, are in good agreement with the literature values[30].

Acknowledgments This work was supported by the IAP-project P7/12, the FWO-Vlaanderen, GOA grants 10/010 and 15/010 from KU Leuven, the Max-Planck Society, the ERC Grant No. 307986 STRONGINT, the BMBF contract 05P12RDCIC and 05P15RDCIA, the U.S. Department of Energy, Office of Science, Office of Nuclear Physics under Award Numbers DEFG02-96ER40963 (University of Tennessee), DE-SC0013365 (Michigan State University), DE-SC0008499 and DE-SC0008511 (NUCLEI SciDAC collaboration), the Field Work Proposal ERKBP57 at Oak Ridge National Laboratory (ORNL), and Contract No. DE-AC05-00OR22725 (ORNL). Computer time was provided by the Innovative and Novel Computational Impact on Theory and Experiment (INCITE) program. This research used resources of the Oak Ridge Leadership Computing Facility at ORNL, and used computational resources of the National Center for Computational Sciences, the National Institute for Computational Sciences. We thank Javier Menéndez for very useful discussions. We would like to thank the ISOLDE technical group for their support and assistance.

Author contributions R.F.G.R., M.L.B., N.F., M.H., M.K., K.K., R.N., W.Nö., J.P., and D.T.Y. performed the experiment. R.F.G.R. performed the data analysis and prepared the figures. G.H. and G.R.J. performed the coupled-cluster calculations. R.F.G.R, K.B., G.H., K.H., G.N., W.Na., W.Nö., T.P., and A.S. prepared the manuscript. All authors discussed the results

المنارة للاستشارات

and contributed to the manuscript at all stages.

Author information Reprints and permissions information is available at www.nature.com/reprints. The authors declare no competing financial interests. Readers are welcome to comment on the online version of the paper. Correspondence and requests for materials should be addressed to R.F.G.R (ronald.fernando.garcia.ruiz@cern.ch)

[1] Goeppert Mayer, M. On closed shells in nuclei. *Phys. Rev. C* **75**, 1969 (1949).

[2] Fridmann, J. *et al.* Magic nucleus ^{42}S. *Nature* **435**, 922 (2005).

[3] Jones, K. *et al.* The magic nature of ^{133}Sn explored through the single-particle states of ^{133}Sn. *Nature* **465**, 454 (2010).

[4] Holt, J. D., Otsuka, T., Schwenk, A. & Suzuki, T. Three-body forces and shell structure in calcium isotopes. *J. Phys. G* **39**, 085111 (2012).

[5] Hagen, G., Hjorth-Jensen, M., Jansen, G. R., Machleidt, R. & Papenbrock, T. Evolution of shell structure in neutron-rich calcium isotopes. *Phys. Rev. Lett.* **109**, 032502 (2012).

[6] Wienholtz, F. *et al.* Masses of exotic calcium isotopes pin down nuclear forces. *Nature* **498**, 346 (2013).

[7] Steppenbeck, D. *et al.* Evidence for a new nuclear 'magic number' from the level structure of ^{54}Ca. *Nature* **502**, 207 (2013).

[8] Kreim, K. *et al.* Nuclear charge radii of potassium isotopes beyond N=28. *Phys. Lett. B* **731**, 97 (2014).

[9] Ekström, A. *et al.* Accurate nuclear radii and binding energies from a chiral interaction. *Phys. Rev. C* **91**, 051301 (2015).

[10] Gade, A. *et al.* Nuclear structure towards $N = 40$ ^{60}Ca: In-beam γ-ray spectroscopy of ^{58,60}Ti. *Phys. Rev. Lett.* **112**, 112503 (2014).

[11] Angeli, I. *et al.* N and Z dependence of nuclear charge radii. *J. Phys. G* **36**, 085102 (2009).

[12] Marsh, B. *et al.* RILIS applications at CERN/ISOLDE. *Hyper. Int.* **227**, 101 (2014).

[13] Palmer, C. W. P. *et al.* Laser spectroscopy of calcium isotopes. *J. Phys. B.* **17**, 2197 (1984).

[14] Caurier, E., Langanke, K., Martínez-Pinedo, G., Nowacki, F. & Vogel, P. Shell model description of isotope shifts in calcium. *Phys. Lett. B* **522**, 240 (2001).

[15] Bender, M., Heenen, P.-H. & Reinhard, P.-G. Self-consistent mean-field models for nuclear structure. *Rev. Mod. Phys.* **75**, 121 (2003).

[16] Talmi, I. On the odd-even effect in the charge radii of isotopes. *Nucl. Phys. A* **423**, 189 (1984).

[17] Fayans, S., Tolokonnikov, S., Trykov, E. & Zawischa, D. Nuclear isotope shifts within the local energy-density functional approach. *Nucl. Phys. A* **676**, 49 (2000).

[18] Andl, A. *et al.* Isotope shifts and hyperfine structure of the $4s^2\ ^1S_0$-$4s4p\ ^1P_1$ transition in calcium isotopes. *Phys. Rev. C* **26**, 2194 (1982).

[19] Vermeeren, L. *et al.* Ultrasensitive radioactive detection of collinear-laser optical pumping: Measurement of the nuclear charge radius of ^{50}Ca. *Phys. Rev. Lett.* **68**, 1679 (1992).

[20] Gorges, C. *et al.* High-precission isotope shift measurements of stable Ca isotopes. *Submitted* (2015).

[21] Wang, M. *et al.* The AME2012 atomic mass evaluation. *Chinese Phys. C* **36**, 1603 (2012).

[22] Geithner, W. *et al.* Measurement of nuclear moments and radii by collinear laser spectroscopy and by β-NMR spectroscopy. *Hyper. Int.* **129**, 271 (2000).

[23] Cheal, B. & Flanagan, K. Progress in laser spectroscopy at radioactive ion beam facilities. *J. Phys. G: Nucl. Part. Phys* **37**, 113101 (2010).

[24] Blaum, K., Dilling, J. & Nörtershäuser, W. Precision atomic physics techniques for nuclear physics with radioactive beams. *Phys. Scr.* **T152**, 014017 (2013).

[25] Nieminem, A. *et al.* On-line ion cooling and bunching for collinear laser spectroscopy. *Phys. Rev. Lett.* **88**, 094801 (2002).

[26] Vingerhoets, P. *et al.* Nuclear spins, magnetic momnets, and quadrupole moments of Cu isotopes from N=28 to N=46: Probes for core polarization effects. *Phys. Rev. C* **82**, 064311 (2010).

[27] Fricke, G. & Heilig, K. *Nuclear Charge Radii* (Springer, 2004).

[28] Epelbaum, E., Hammer, H.-W. & Meißner, U.-G. Modern theory of nuclear force. *Rev. Mod. Phys.* **81**, 1773 (2009).

[29] Vermeeren, L. *et al.* The mean square nuclear charge radius of ^{39}Ca. *J. Phys. G: Nucl. Part. Phys.* **22**, 1517 (1996).

[30] Martensson-Pendrill, A. M. *et al.* Isotope shifts and nuclear-charge radii in singly ionized $^{40-48}$Ca. *Phys. Rev. A* **45**, 4675 (1992).

[31] Navrátil, P., Gueorguiev, V. G., Vary, J. P., Ormand, W. E. & Nogga, A. Structure of $A = 10 - 13$ nuclei with two- plus three-nucleon interactions from chiral effective field theory. *Phys. Rev. Lett.* **99**, 042501 (2007).

[32] Hergert, H., Binder, S., Calci, A., Langhammer, J. & Roth, R. Ab Initio Calculations of Even Oxygen Isotopes with Chiral Two-Plus-Three-Nucleon Interactions. *Phys. Rev. Lett.* **110**, 242501 (2013).

[33] Coraggio, L., Covello, A., Gargano, A. & Itaco, N. Spectroscopic study of neutron-rich calcium isotopes with a realistic shell-model interaction. *Phys. Rev. C* **80**, 044311 (2009).

[34] Garcia Ruiz, R. F. *et al.* Ground-state electromagnetic moments of calcium isotopes. *Phys. Rev. C* **91**, 041304(R) (2015).

[35] Binder, S., Langhammer, J., Calci, A. & Roth, R. Ab initio path to heavy nuclei. *Phys. Lett. B* **736**, 119 (2014).

[36] Hebeler, K., Bogner, S., Furnstahl, R., Nogga, A. & Schwenk, A. Improved nuclear matter calculations from chiral low-momentum interactions. *Phys. Rev. C* **83**, 031301(R) (2011).

[37] Furnstahl, R. & Hebeler, K. New applications of renormalization group methods in nuclear physics. *Rep. Prog. Phys.* **76**, 126301 (2013).

[38] Hagen, G., Papenbrock, T., Hjorth-Jensen, M. & Dean, D. Coupled-cluster computations of atomic nuclei. *Rep. Prog.*

المنارة للاستشارات

Phys. **77**, 096302 (2014).

[39] Kortelainen, M. *et al.* Nuclear energy density optmization. *Phys. Rev. C* **82**, 024313 (2010).

[40] Erler, J. *et al.* The limitis of the nuclear landscape. *Nature* **486**, 509 (2012).

[41] Saperstein, E. & Tolokonnikov, S. Self-consistent theory of finite fermi systems and radii of nuclei. *Phys. Atom. Nucl.* **74**, 1277 (2011).

[42] Delaroche, J.-P. *et al.* Structure of even-even nuclei using a mapped collective hamiltonian and the D1S Gogny interaction. *Phys. Rev. C* **81**, 014303 (2010).

[43] Roca-Maza, X., Viñas, X., Centelles, M., Ring, P. & Schuck, P. Relativistic mean-field interaction with density-dependent meson-nucleon vertices based on microscopical calculations. *Phys. Rev. C* **84**, 054309 (2011).

[44] Goriely, S., Chamel, N. & Pearson, J. M. Further explorations of Skyrme-Hartree-Fock-Bogoliubov mass formulas. XIII. the 2012 atomic mass evaluation and the symmetry coefficient. *Phys. Rev. C* **88**, 024308 (2013).

[45] Rossi, D. M. *et al.* Charge radii of neutron-deficient ^{36}K and ^{37}K. *Phys. Rev. C* **92**, 014305 (2015).

[46] Bissell, M. L. *et al.* Proton-neutron pairing correlations in the self-conjugate nucleus ^{38}K probed via a direct measurement of the isomer shift. *Phys. Rev. Lett.* **113**, 052502 (2014).

[47] Entem, D. & Machleidt, R. Accurate charge-dependent nucleon-nucleon potential at fourth order of chiral perturbation theory. *Phys. Rev. C* **68**, 041001(R) (2003).

[48] Roth, R. *et al.* Medium-mass nuclei with normal-ordered chiral NN+3N interactions. *Phys. Rev. Lett.* **109**, 052501 (2012).

المنارة للاستشارات

Chapter 6

A sensitive setup for laser spectroscopy

With production yields estimated to be less than $\sim$ 100 ions/s and $\sim$ 10 ions/s for ^{53}Ca and ^{54}Ca, respectively, a measurement of the hyperfine structure of these isotopes is beyond the limits of sensitivity obtained by optical detection techniques. In order to extend these measurements to ^{53}Ca and ^{54}Ca, a more sensitive detection scheme is needed. The earlier measurement of ^{50}Ca (5×10^4 ions/s) was based on a sensitive particle detection scheme, in combination with the state-selective collisional neutralization [17]. This technique is sensitive enough for isotopes without hyperfine splitting (like ^{50}Ca), but requires further development to make it also sensitive for hyperfine-split isotopes such ^{53}Ca. Furthermore, substantial modifications of the earlier setup are needed to push the sensitivity towards 10 ions/s. This new desing is supposed to be very close to the ideal conditions suggested by P. Lievens et al. [231] ($\sim$100% optical pumping, $\sim$100 % beam transmission, $\sim$100 % detection efficiency) to be able to measure Ca ions with yields of less than 10 ions/s.

This chapter presents the current developments necessary to reach the sensitiviy limits that will allow to obtain hfs measurements on isotopes produced at rates of only few ions/s. The first section presents the principles of the experimental method. A detailed explanation of the laser-ion interaction and ion beam optics simulations used to choose the design of each beam line component are illustrated in the second part. Finally, the commissioning of the new experimental setup and the first experimental tests with stable beams are presented.

المنارة للاستشارات

6.1 State-selective charge exchange process after optical pumping

A layout of the experimental scheme for Radioactive detection of Optically pumped ions after state selective Charge exchange (ROC) is shown in Figure 6.1. The technique consists of three main steps: *optical pumping, state-selective charge exchange*, and *radioactive detection*. First, the ions in the ground state are resonantly excited to a short-lived excited state, and subsequent spontaneous decay from this level populates a low-lying metastable state in the Ca ion (see Figure 6.2). An efficient population of the metastable state is achieved by superimposing the laser and the ion beam in collinear geometry along a sufficiently long optical pumping region. Afterwards, the ions (mostly in the metastable state, some in the ionic ground state) are deflected from the laser beam and decelerated in order to then be efficiently neutralized by passing the ion beam through a charge exchange cell. Finally, an electric field is applied to separate the remaining ions from the neutralized atoms. As the neutralization cross section depends on the initial state of the ionic system (the metastable state is 3 times more efficiently neutralized), the resonant interaction between the laser and the ions in the first step[1] is turned into a resonant change in the ion/atom counting rate after the charge-exchange process. Thus the hyperfine structure can be observed in the atom and ion count rate as a function of the laser frequency[2].

The applicability of this technique is restricted to the existence of a low-lying metastable state that can be optically pumped from the ground state, with a near-resonance charge-exchange reaction for only one of these states. This type of three-level scheme is commonly found in alkaline-earth ions such as Ca, Sr, Ba and Ra. An illustration of the level scheme of Ca^+ is shown in figure 6.2. The ions, initially in the ground state, $ns^2S_{1/2}$, interact with a laser beam, and are resonantly excited to the np^2P_J states. Subsequently, spontaneous emission populates the metastable $(n-1)d^2D_J$ states. For isotopes with nuclear spin $I = 0$, approximately 100 % of the ions can be transferred to the metastable state. Therefore, the pumping efficiency depends mainly on the laser power and the interaction time (length of the optical pumping region in Figure 6.1). For a nuclear spin $I \neq 0$, the pumping efficiency is strongly affected by trapping into the different hyperfine components of the states involved in the pumping process.

The sensitivity of the technique is dominated by the ratio between the metastable and ground state neutralization cross sections. Considering a charge

[1] It includes scanning over the hyperfine structure
[2] Here as a function of voltage, as we scan Doppler shifted observed frequency

المنارة للاستشارات

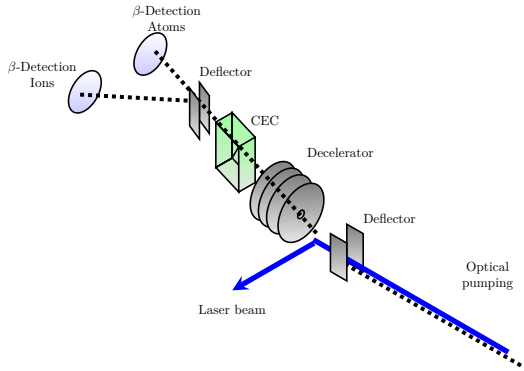

Figure 6.1: Layout of the experimental scheme for Radioactive detection of Optically pumped ions after state selective Charge exchange (ROC) . The technique consists of three main processes: *optical pumping, state-selective charge exchange*, and *radioactive detection of atoms/ions*.

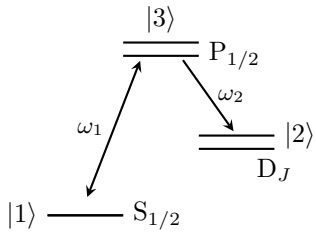

Figure 6.2: Ca^+ energy levels of the low-lying states involved in the optical pumping process.

exchange process of an ion A^+ colliding with an atom B, the neutralization mechanism can be expressed as

$$A^+ + B \rightarrow A + B^+ + \Delta E, \tag{6.1}$$

where ΔE is the so called energy defect [232]. The neutralization cross section related to this process depends on the ion impact velocity and the ionic state [233]. In the case of Ca^+, the ratio between the neutralization cross section for the metastable state, σ_D, and the neutralization cross section for the ground state, σ_S, reaches a maximum value of $\sigma_D/\sigma_S \sim 3$ at kinetic ion energies of ~ 4 keV [233]. Hence, the sensitivity is maximized if the ions are decelerated before the charge exchange process to about 4 keV. As shown in Figure 6.1, the

المنارة للاستشارات

laser beam must be separated from the ion beam path to prevent interference of the laser light on the particle detectors used for atom counting.
The direct ion/atom detection might be altered by contamination of other isotopes in the ion beam [234], but this can be avoided by counting the charged particles emitted by the radioactive isotopes, instead of directly measuring the beam intensity. An extended discussion of the different processes involved in the experimental technique are explained in the following sections.

6.1.1 Ion-laser interaction and multi-step optical pumping

Consider a three level system with a ground state $\mid 1\rangle$, a meta-stable state $\mid 2\rangle$, and an excited level $\mid 3\rangle$ (Figure 6.2), with population densities N_1, N_2, and N_3, respectively. Both spontaneous and induced emission are allowed from the excited state to the ground state, as well as spontaneous decay to the meta-stable state (this latter process will be responsible for the pumping into this level). If the frequency of the external laser field, ν_{13}, takes values around the energy difference between states $\mid 3\rangle$ and $\mid 1\rangle$, resonant excitation from the ground state to the exited state occurs. Thus, the evolution of the population for the different states can be expressed as [235]

$$\begin{aligned}
\frac{dN_3}{dt} &= -(A_{31}+A_{32})N_3 - \rho(\nu_{13})B_{31}N_3 + \rho(\nu_{13})B_{13}N_1, \\
\frac{dN_2}{dt} &= A_{32}N_3, \qquad (6.2) \\
\frac{dN_1}{dt} &= A_{31}N_3 - \rho(\nu_{13})B_{13}N_1 + \rho(\nu_{13})B_{31}N_3, \qquad (6.3)
\end{aligned}$$

with A and B the Einstein's coefficients introduced to account for the different processes of spontaneous emission (A_{31}, A_{32}), stimulated absorption (B_{13}) and stimulated emission (B_{31}).
The spontaneous emission coefficients, A_{if}, between an initial state i and a final state f (with i and f characterized by their hyperfine quantum numbers I, J, F, M) is given by [236]

$$\begin{aligned}
A_{if} &= \tau^{-1}(2J_i+1)(2F_i+1)(2F_f+1) \\
&\quad \times \begin{pmatrix} F_f & 1 & F_1 \\ -M_f & M_f - M_i & M_i \end{pmatrix}^2 \begin{Bmatrix} J_f & F_f & I \\ F_i & J_i & 1 \end{Bmatrix}^2 \qquad (6.4)
\end{aligned}$$

المنارة للاستشارات

For an ion exposed to an electromagnetic field with spectral energy density $\rho(\nu)$, the probability per unit time of absorption of photons, transferring the ion from the state $\mid i\rangle$ to a final state $\mid f\rangle$, is given by $\rho(\nu)B_{if}$. The absorption cross section $\sigma(\nu)$ is equal to the absorbed energy per intensity unit (I) of the external radiation per unit time [236]

$$\sigma(\nu) = \frac{B_{fi}\rho(\nu)h\nu}{I}, \tag{6.5}$$

expressed as [3]

$$\sigma(\nu) = A_{if}\frac{c^2}{8\pi\nu_0^2}\frac{1}{\pi}\frac{\Gamma/4\pi}{(\nu-\nu_o)^2+(\Gamma/4\pi)^2}, \tag{6.6}$$

where $\Gamma = \tau^{-1}$ is the natural linewidth, and ν_0 the transition frequency. If different hyperfine sub-states are included for each level, the expression 6.3 can be expressed as

$$\frac{dN_i}{dt} = -N_i\sum_{j=g'}^{g''-1}(A_{ij}+D_{ij}) + \sum_{j=g'}^{g''-1}N_jD_{ji} - N_i\sum_{j=g''}^{g-1}A_{ij} \tag{6.7}$$

$$i = 0, 1, ..., g'-1.$$

$$\frac{dN_i}{dt} = \sum_{j=0}^{g'-1}A_{ji}N_j \tag{6.8}$$

$$i = g'', g''+1, ..., g-1.$$

$$\frac{dN_i}{dt} = \sum_{j=0}^{g'-1}(A_{ji}+D_{ji})N_j - N_i\sum_{j=0}^{g'-1}D_{ij} \tag{6.9}$$

$$i = g', g'+1, ..., g''-1.$$

with $D_{if} = B_{if}\rho(\nu)$, g the total number of states, $g''-g' = (2I+1)(2J_1+1)$ the number of states in the level $\mid 1\rangle$, $g-g'' = (2I+1)(2J_2+1)$ the number of states in the level $\mid 2\rangle$, and $\mid 3\rangle$ given by $g' = (2I+1)(2J_3+1)$ for the state $\mid 3\rangle$.
Since the electric dipole transition is forbidden among multiplets, the equations 6.10 can be expressed as

$$\dot{N}_{g\times 1} = M_{g\times g}.N_{g\times 1}, \tag{6.10}$$

[3]The expression 6.6 is derived from the optical Bloch equations [236].

المنارة للاستشارات

with

$$\begin{matrix} M_{if} \\ 0 \leq i \leq g' - 1 \end{matrix} = \left\{ \begin{array}{ll} D_{ji}, & i \neq j \\ D_{ji} - \sum_{j=g'}^{g''-1}(A_{ij} + D_{ij}) - \sum_{k=g''}^{g-1} A_{ij}, & i = j \end{array} \right\} \tag{6.11}$$

$$\begin{matrix} M_{if} \\ g'' \leq i \leq g - 1 \end{matrix} = A_{ji}, \quad i \neq j \tag{6.12}$$

and

$$\begin{matrix} M_{if} \\ g' \leq i \leq g'' - 1 \end{matrix} = \left\{ \begin{array}{ll} A_{ji} + D_{ji}, & i \neq j \\ A_{ji} + D_{ji} - \sum_{k=0}^{g'-1} D_{ik}, & i = j. \end{array} \right\} \tag{6.13}$$

The population of the different states involved in the optical pumping process were calculated by numerically solving the expression 6.10. The final population of each state is obtained from the sum of the populations of the different hyperfine levels after a given laser-ion interaction time. The c++ code written for this calculations is an extension of the code written for a two level system [237].

Single-step

The isotope $^{53}Ca^{+}$ was chosen as the test case to illustrate the influence of multiple steps in the optical pumping process. The Ca^{+} was assumed to interact with a laser field of frequency values around the $S_{1/2} \rightarrow P_{3/2}$ transition. This transition was used as a resonance transition to populate the metastable states D_J (see Figure 6.2). The ratio between the magnetic dipole hfs constants, $A_{S_{1/2}}/A_{P_{3/2}}$, was fixed to the average experimental value ∼25.92(3) [70].
A scheme for a laser field interaction with a Ca^{+} with nuclear spin, $I \neq 0$, is shown in Figure 6.3. For ions with spin $I \neq 0$, the population of the metastable state via some of the hyperfine transitions is reduced due to trapping into another hyperfine component of the ground state.

Figure 6.4 shows the population of the metastable state after resonant excitation of the ^{53}Ca ions with a single laser field, named single-step optical pumping (SSOP). The figure shows the results for different laser power densities and 6 μs interaction time, which is equivalent to an ion beam at 30 keV passing

المنارة للاستشارات

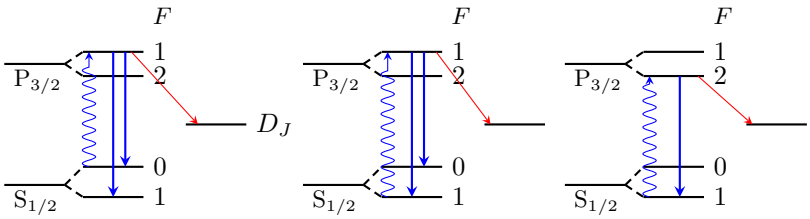

Figure 6.3: Level scheme of a Ca^+ ion with nuclear spin, $I = 1/2$. A laser field of frequency 393 nm excites the ion from the ground state $S_{1/2}$ to the excited state $P_{3/2}$. When the laser is on resonance with the component $F = 0 \rightarrow F = 1$ or $F = 1 \rightarrow F = 1$, the spontaneous emission spreads the population into the metastable states D_J and the gs components $F = 0, 1$.

through an interaction region of 2 m long. A nuclear spin $I = 1/2$ was assumed for ^{53}Ca. When the laser is at resonance with the $F' = 1$ excited hyperfine level, by excitation from the $F = 0$ or from the $F = 1$ ground state level (see Figure 6.3), part of the spontaneous decay de-populates into the non-excited gs hyperfine level. This fraction of ions is lost for the remaining of the optical pumping process, which proceeds through the spontaneous decay from excited state hyperfine levels to the metastable D state. Thus, in Figure 6.4 only one hyperfine transition efficiently pumps the ions into the metastable state, namely the one that populates the $F' = 2$ level can not decay back to the $F = 0$ ground state. Therefore, only one of the three hyperfine transitions has a significantly large amplitude to be detected in the experiment.

A high pumping efficiency can be reached either by increasing the length of the pumping zone (interaction time) or by increasing the laser power. In practice, laser powers up to maximum 100 mW/cm^2 can be obtained for the laser frequency used to excite Ca^+ ($\sim$393 nm)[4]. Figure 6.5 shows the population as a function of the interaction time for different laser powers. Because the exponential behaviour of the pumping efficiency, at laser power densities above 40 mW/cm^2, an interaction time of about 3 μs (pumping zone of 1 m length) results in about 85 % of pumping efficiency into the meta-stable state. Higher laser power densities can be applied at the cost of power broadening, reducing the signal to background ratio.

[4] 100 mW/cm^2 corresponds to 50 mW uniformly distributed on a spot of 8 mm diameter.

المنارة للاستشارات

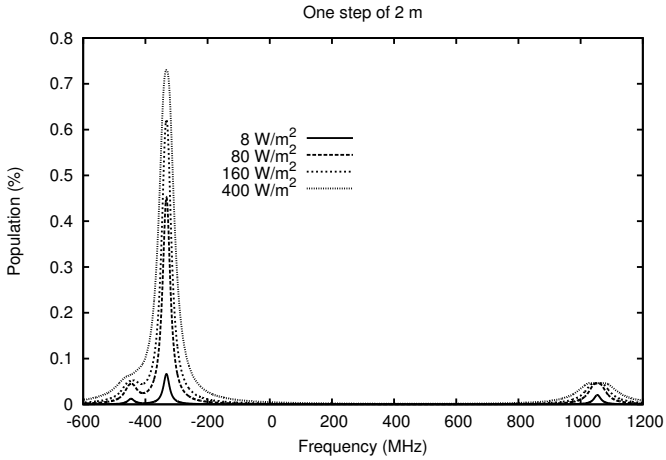

Figure 6.4: Population of the metastable state as a function of the laser frequency scanned over the hyperfine transitions between the $S_{1/2}$ and $P_{3/2}$ levels. Different laser powers were assumed with single-step optical pumping. A ^{53}Ca ($I = 1/2$) ion beam at 30 keV was assumed to interact with the laser beam along an optical pumping region of 2 m length.

Two-step

In order to observe the three hyperfine components with a similar signal strength, we plan to use a two-step optical pumping (TSOP) scheme [238, 239]. Simultaneous pumping from different hfs components can be used to avoid the trapping of population. The two-step optical pumping is based on the interaction of an ion beam with two laser fields of different frequency. A comparison of the results of numerical calculations for both SSOP and TSOP are shown in Figure 6.6. In the SSOP process, the ion interacts during 6 μs with only one laser of variable frequency, allowing to scan the hyperfine structure but with only the $F = 1 \rightarrow 2$ transition leading to efficient pumping. The two other hyperfine transitions are very inefficient in the pumping due to their spontaneous decay into the "dark" hyperfine partner level. To apply two laser frequencies in the optical pumping section for TSOP, two different potentials will be applied along the beam path, such that the observed laser frequency is changed in subsequent pumping sections (details follow in section 6.4). In the first section the ion interacts with a laser field of variable frequency during 3 μs (so the potential is changed to scan the observed laser frequency), and in the next pumping section, it interacts during another 3 μs with a laser frequency

المنارة للاستشارات

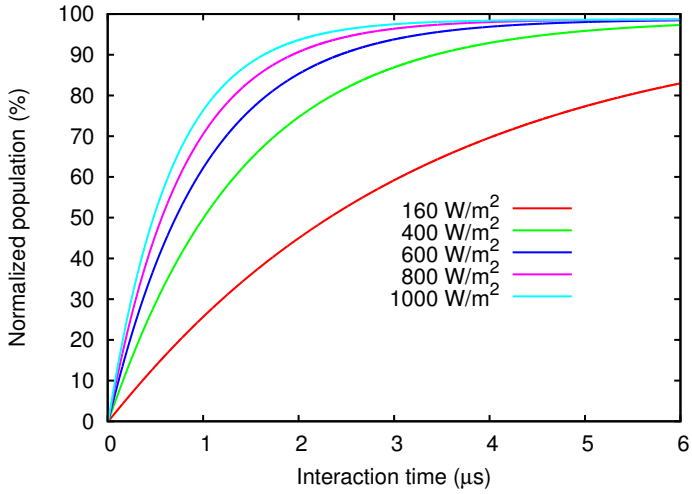

Figure 6.5: Percent of population transferred from the initial ground state into the metastable state via the $F = 1 \rightarrow 2$ transition. The populations is shown as a function of the interaction time for different laser power densities. The laser frequency is fixed at resonance.

fixed at the value of the dominant component, ν_2 ($F = I+1/2 \rightarrow F' = I+3/2$) (by applying a fixed potential).
If the frequency seen by the ion in the first step is outside of resonance, no change of population occurs. In this case only the ions observing a fixed frequency in the second section will initiate excitation of the state $F = I+1/2$ and pumping into the meta-stable states will take place. This signal will be our base line. Then, when the first laser frequency is scanned across the hyperfine resonances, e.g. with ν_1 ($F = I-1/2 \rightarrow F' = I+1/2$), the state $F = I-1/2$ is completely depopulated transferring some of the ions to the metastable states D_J, but most of the decay goes to the gs component $F = I + 1/2$.
When the first laser is at resonance with frequency ν_3 ($F = I + 1/2 \rightarrow F' = I - 3/2$), an opposite effect is observed. First, the state $F = I + 1/2$ is depopulated partially into the meta-stable state, but mostly to the state $F = I-1/2$. As the state $F = I-1/2$ can not be depopulated with the second laser field, the net population of the meta-stable state is reduced significantly. This is observed as a decrease in the meta-stable state population at ν_3 (Fig. 6.6).

The dependence of the metastable population for different laser power densities is shown in Figure 6.7. As in the former case, the first step was used as scanning

المنارة للاستشارات

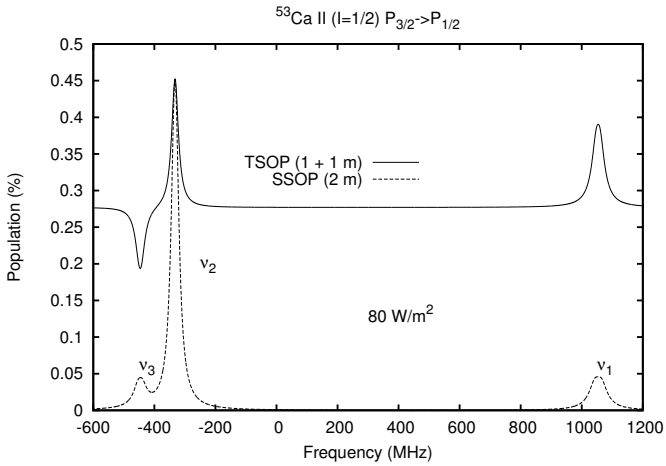

Figure 6.6: Population of the metastable state for single-step optical pumping (SOP) and two-step optical pumping (TSOP). A ^{53}Ca ($I = 1/2$) ion beam at 30 keV is assumed to interact with a laser beam along an optical pumping region of 2 m length. For the TSOP process, the first step was used as scanning frequency, and the frequency of the second step fixed at ν_2.

frequency, and the frequency of the second step fixed at ν_2. For TSOP the pumping efficiency plays a different role. As previously discussed, the fixed frequency of the second step (ν_2) transfers the ions into the meta-stable state and defines the base line of the TSOP spectrum. As can be seen in Figure 6.7, if the this second step is saturated, the peak corresponding to ν_2 in the TSOP spectrum is not visible. An optimum balance of the different peak intensities and low power broadening is found for steps of 1 m length and 160 W/m^2 power density (Figure 6.7). It corresponds to about 50 % population efficiency for each step (Figure 6.5).

Multiple-step

More than two laser fields can be used to obtain further control for the meta-stable state population. Multiple-step optical pumping can be performed with various laser fields of different frequencies. An example for meta-stable state population of a four-step optical pumping is shown in Figure 6.8. The first and third laser were allowed to have variable frequency, and the second and fourth field were fixed to any of the possible values ν_1, ν_2 or ν_3. In the sequence

المنارة للاستشارات

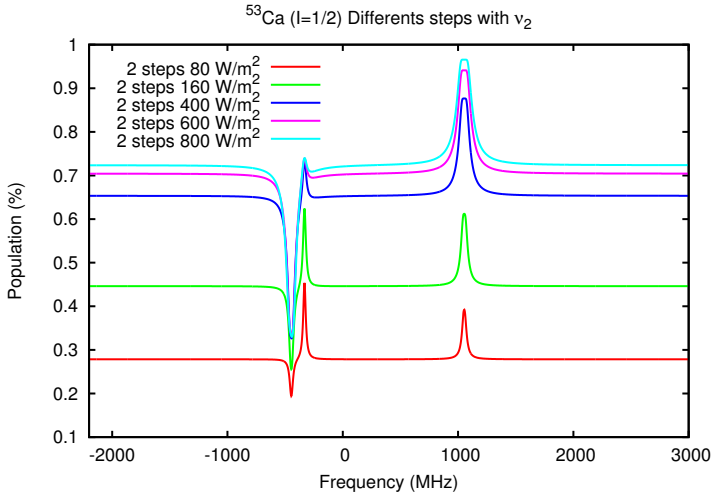

Figure 6.7: Population of the metastable state for two-step optical pumping (TSOP). A ^{53}Ca ($I = 1/2$) ion beam at 30 keV is assumed to interact with a laser beam along two optical pumping region of 1 m length each one. The first step is used as scanning frequency, and the frequency of the second step is fixed at ν_2.

$\nu_i - \nu_1 - \nu_i - \nu_1$ for example, the ion interacts with a laser field of variable frequency during the first step, and with a laser field of fix frequency ν_1 in the second step. The sequence is repeated, applying a variable field in the third step, and finally a fix frequency ν_1 for the last step. An interaction time of 1.5 μs was used for each step.

المنارة للاستشارات

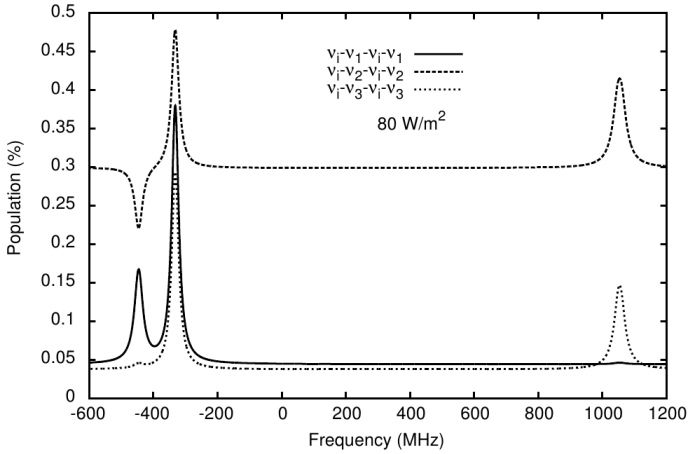

Figure 6.8: Population of the metastable state for four steps optical pumping. The ion beam interacts with four laser fields. First and third laser were allowed to have variable frequency, and the second and fourth field were fixed to any of the possible values ν_1, ν_2 or ν_3 (see text for more details).

As can be seen, this type of four step process is equivalent to a sequence of two TSOP, and might be used to enhance the population at frequency ν_3. Multiple steps with different values of fixed frequencies might be implemented to enhance the relative population of a specific hfs component. In Figure 6.9, for example, the ion beam interacts with three laser fields. The first one is fixed at ν_3. In the second step a laser of variable frequency is applied, and finally the ion interacts with a field of fixed frequency ν_2. Notice a clear enhancement of the component at ν_1, which for this frequency is better than TSOP, but decreases the signal amplitude at ν_2 and ν_3.

To summarize, TSOP produces a good balance for the signal observed in the meta-stable state population, but multiple steps with different fixed frequencies could be implemented to populate or depopulate a specific hfs component.

6.2 Charge transfer reactions

The charge-exchange process that takes place in the charge exchange cell (CEC) neutralizes the Ca ion beam. As the gas of atoms in the CEC(B) are different

المنارة للاستشارات

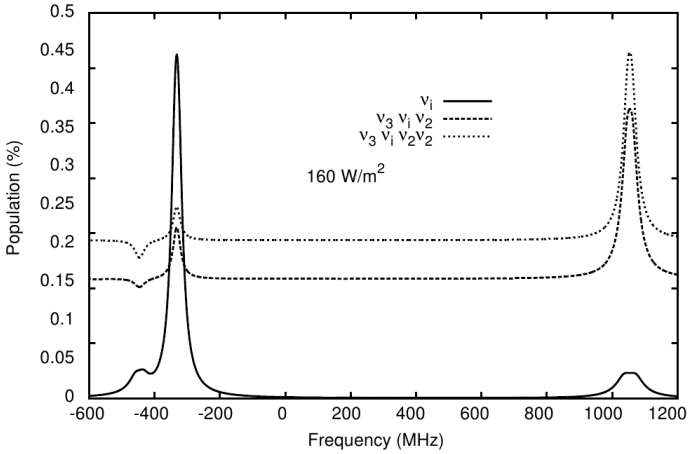

Figure 6.9: Population of the metastable state for different number of steps, using different fixed frequencies.

than the ion beam elements (A^+), this is called an asymmetric charge transfer reaction [232]:

$$A^+ + (B^+ + e) \rightarrow (A^+ + e) + B^+ + \Delta E. \tag{6.14}$$

In this expression, ΔE is the energy defect given by the difference between the ionization potentials of A and B. A semi-classical approximation was introduced by Rapp and Francis [232] to describe such charge-exchange processes, and its dependence on the relative energy of the beam and gas particle. The reaction velocities considered in this work are of the order of 10^4-10^5 cm/s[5], which corresponds to the so called "intermediate" velocity region[6] [232]. At this energy, the mechanical-wave treatment is simplified by neglecting low phase shifts, and the electron orbital velocity is relatively large to allow for the Born-Oppenheimer approximation.
Following Rapp and Francis's theory, the wave function for the electron, ψ, during the reaction 6.14 can be approximated by a linear combination of the

[5]This corresponds to an ion beam energy about of 4 keV

[6]Velocities bellow $10^5/\mu^{1/2}$ cm/s, with μ the reduced mass in amu, are considered within the low velocity range [232]

المنارة للاستشارات

electron wave function in both projectile, ϕ_A, and target, ϕ_B, given by [232, 240]

$$\psi = C_A(t)\phi_A \exp(-i\omega_A t) + C_B(t)\phi_B \exp(-i\omega_B t), \tag{6.15}$$

with

$$\phi_j(r_j) = (\pi a_0^3)^{-1/2}(\gamma_j)^{3/4} \exp\left(-\gamma_j \frac{r_j}{a_0}\right), \tag{6.16}$$

the electron wave function in a s-like orbital of radius r_j, bound by a potential V_j with ionization energy I_j, and $\gamma_j \equiv \sqrt{\frac{I_j}{13.6\text{eV}}}$. If the electron is not in an s orbital, the expression 6.16 is used only as an approximation to correlate the size of the orbital with the ionization potential.
The time-dependent Schrödinger equation of the electron transfer reaction can be expressed as two coupled differential equations for $C_A(t)$ and $C_B(t)$,

$$i\frac{dC_B(t)}{dt} = \kappa_A \exp(i\omega t)C_A(t) + \eta_A C_B(t), \tag{6.17}$$

$$i\frac{dC_A(t)}{dt} = \eta_B C_A(t) + \kappa_B \exp(i\omega t)C_B(t), \tag{6.18}$$

where $\omega \equiv \omega_B - \omega_A$, with $\omega_i = I_i/\hbar$, and

$$\kappa_j \equiv \frac{(V_j)_{jk} - F(V_j)_{kk}}{(1-F^2)\hbar},\ j,k \in \{A,B\}. \tag{6.19}$$

The constants η_j are defined as

$$\eta_j \equiv \frac{(V_j)_{kk} - F(V_j)_{kj}}{(1-F^2)\hbar}, \tag{6.20}$$

where $(V_i)_{jk} = \int \phi_j \left(-\frac{1}{r_j}\right)\phi_k$, for $i \in \{A,B\}$ is the exchange integral for the electron in the atom ($i = A$) and gas ($i = B$), and $F \equiv \int \phi_A \phi_B$ is the overlap of the ion and gas atom electron wave functions. The explicit expressions of these integrals are given in Ref. [240]:

$$F = \frac{8(\gamma_A\gamma_B)^{3/2}[(\gamma_A^2 R - 4\gamma_B - \gamma_B^2 R)\gamma_A e^{\gamma_A R} - (\gamma_B^2 R - 4\gamma_A - \gamma_A^2 R)\gamma_B e^{\gamma_B R}]}{e^{(\gamma_A+\gamma_B)R}(\gamma_A+\gamma_B)^3(\gamma_A-\gamma_B)^3 R}, \tag{6.21}$$

$$(V_j)_{jk} = \frac{-4(\gamma_j\gamma_k)^{3/2}[(\gamma_j^2 R - 2\gamma_k - \gamma_k^2 R)e^{\gamma_j R} - 2\gamma_k e^{\gamma_k R}]}{e^{(\gamma_j+\gamma_k)R}(\gamma_j+\gamma_k)^2(\gamma_j-\gamma_k)^2 R},\ j \neq k, \tag{6.22}$$

المنارة للاستشارات

and

$$(V_j)_{ii} = -\frac{1}{R} + \frac{1+\gamma_i R}{e^{2\gamma_i R}R},\ .i \neq j. \tag{6.23}$$

Therefore, the probability of finding the electron bound to A^+ after the charge transfer reaction is calculated as

$$P(b,v) = |C_A(\infty)|^2, \tag{6.24}$$

where b is the impact parameter, and $C_A(t)$ can obtained by solving the differential equations 6.18, with the initial conditions $C_B(-\infty) = 1$ and $C_A(-\infty) = 0$ (electron is bound only to B^+ before the reaction). The solution of equation 6.24 is given by [232, 241]

$$P(b,v) = fP_0(b,v)\text{sech}^2\left[\left(\frac{\omega a_0}{\gamma b}\right)(\gamma b/a_0)\exp(\gamma b/a_0)\left(K_0(\gamma b/a_0)+\frac{K_1(\gamma b/a_0)}{\gamma b/a_0}\right)\right], \tag{6.25}$$

with

$$P_0(b,v) = \sin^2\left[\frac{2Ib^2}{a_0\hbar v}\left(K_0(\gamma b/a_0) + \frac{K_1(\gamma b/a_0))}{\gamma b/a_0}\right)\right], \tag{6.26}$$

f is a statistical wight factor. K_0 and K_1 are the zero- and first-order Bessel functions of second kind. Figure 6.10 shows the probability $P(b,v)$ to neutralize A as a function of the impact parameter b and for a fixed velocity, corresponding to a projectile with mass $A = 40$ at 5 keV.

The cross section of the charge exchange process can be expressed as

$$\sigma(v) = 2\pi\int_0^\infty P(b,v)b\_db, \tag{6.27}$$

which can be rewritten as [232, 241]

$$\sigma(v) = \frac{f}{2}2\pi\int_0^{b_1}\text{sech}^2\left[\frac{\omega}{v}\left(\frac{a_0\pi b}{2\gamma}\right)^{1/2}\right]b\_db, \tag{6.28}$$

To evaluate the cross section (Eq. 6.28) a factor $b = b_1$ must be chosen. This factor is usually approximated as the average value of the reaction. As the probability (Eq. 6.26) is normalized and is given by a squared sinusoidal function, the average value of this function is 1/4. Thus, b_1 is obtained as the value for which $|P_0(b_1,v)| = 1/2$ [232, 240].

Due to the different approximations used in the theory of Rapp and Francis [232], the derived expressions are not expected to predict the absolute value of the experimental cross sections, but they can be used to predict results of the same order of the experimental values and provide a good description of the global behaviour to study the velocity and state dependence [233].

المنارة للاستشارات

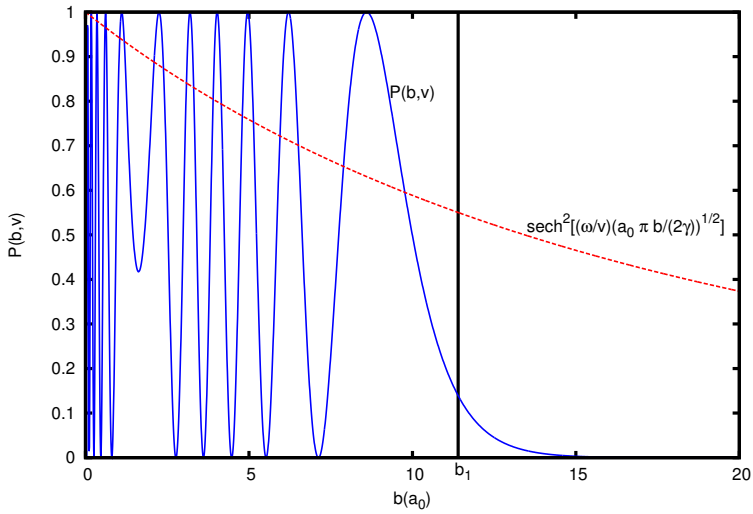

Figure 6.10: Probability $P(b,v)$ of neutralizing a Ca^+ beam at 5 keV on a Na gas. The probability is calculated as a function of the impact parameter b. The impact parameter is given in units of the Bohr radius, a_0. At b_1 the $\text{sech}^2\left[\frac{\omega}{v}\left(\frac{a_0\pi b_1}{2\gamma}\right)^{1/2}\right]$ (red line) is equal to $4P(b_1,v)$.

The expression 6.28 was used to estimate the neutralization cross section of Ca^+ in a Na gas. An example of the cross section dependence with the ion energy and initial ionic state is shown in Figure 6.11.
The cross section is closer to resonance ($\Delta E \sim 0$) when the ions are initially in the metastable states D_J. Consequently, the neutralization cross section $\sigma(D_J)$ is expected to have a larger value than the neutralization cross section for ions in the ground state, $\sigma(S_{1/2})$. According to the calculated values (Figure 6.11), the ratio $\sigma(D_J)/\sigma(S_{1/2})$ is maximum at low energies (<5 keV). Experimentally, this maximum value has been found to be at ~ 4 keV [233].
The total cross section must be calculated as the sum of all possible collision channels. Only channels with energy defect up to $\Delta E = 1.6$ eV were considered in the present calculations (Table 6.1). The ratio of neutralization cross sections between the metastable and ground state as a function of the beam energy is shown in Figure 6.12. Although the experimental absolute values are not well reproduced by the theory, the global behaviour and order of magnitude is in good agreement. A normalization factor is included to reproduce the absolute experimental values. As previously discussed, the theoretical approach is expected to be valid at intermediate energies only. For low energy the

المنارة للاستشارات

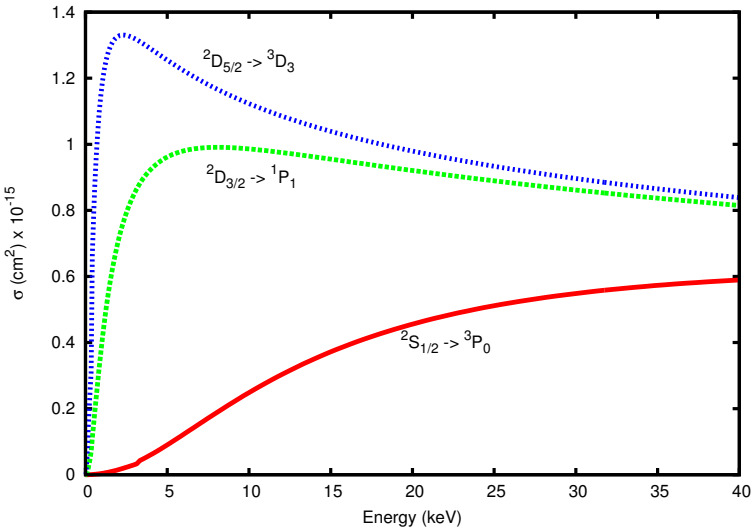

Figure 6.11: Example of the calculated neutralization cross section as a function of the ion energy for three different channels in the reaction $Ca^+ + Na$. The curves show the cross section for ions in three possible initial states $4s\ ^2S_{1/2}$ (red), $3\ d\ ^2D_{3/2}$ (green), or $3\ d\ ^2D_{5/2}$ (blue).

calculated values for the ground state cross section tends to decrease towards zero rapidly. Consequently, the cross section ratio diverges towards large values for low energies.

المنارة للاستشارات

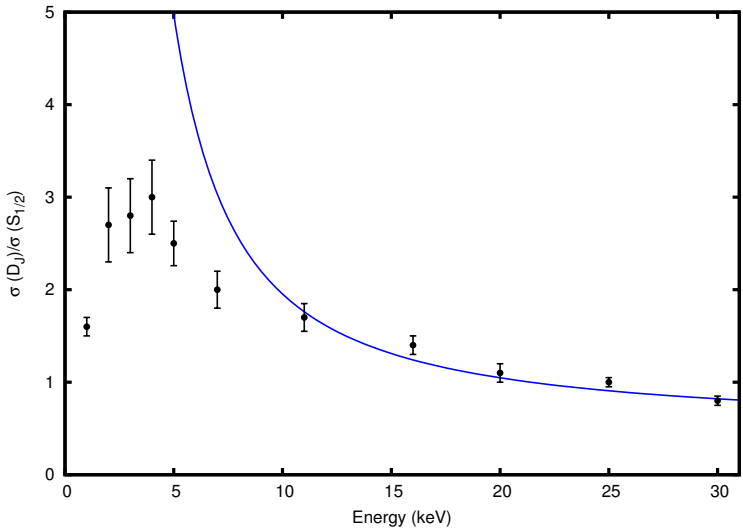

Figure 6.12: Ratio of neutralization cross sections between the metastable and ground state of Ca^+ ion in the reaction Ca^+ + Na. Experimental values are taken from [233]. The continuous blue line shows the theoretical predictions for this ratio using a normalization factor of 0.5 (see text for more details). The reaction channels included in the calculations are listed in table 6.1.

المنارة للاستشارات

Table 6.1: Collision channels included in the calculations of charge transfer cross sections for the reaction $Ca^+ + Na \rightarrow Ca + Na^+ + \Delta E$. The energy values for the different states are taken from Ref [242].

Initial state	Energy (eV)	Final state	Energy (eV)	$\lvert\Delta E\rvert$ (eV)
$4s\ ^2S_{1/2}$	0	$4s^2\ ^1S_0$	0	0.974
$4s\ ^2S_{1/2}$	0	$4s4p\ ^3P_0$	1.879	0.905
$4s\ ^2S_{1/2}$	0	$4s4p\ ^3P_1$	1.886	0.912
$4s\ ^2S_{1/2}$	0	$4s4p\ ^3P_2$	1.899	0.925
$4s\ ^2S_{1/2}$	0	$3d4s\ ^3D_1$	2.521	1.547
$4s\ ^2S_{1/2}$	0	$3d4s\ ^3D_2$	2.521	1.547
$4s\ ^2S_{1/2}$	0	$3d4s\ ^3D_3$	2.526	1.552
$3\ d\ ^2D_{3/2}$	1.692	$4s^2\ ^1S_0$	0.000	2.666
$3\ d\ ^2D_{3/2}$	1.692	$4s4p\ ^3P_0$	1.879	0.787
$3\ d\ ^2D_{3/2}$	1.692	$4s4p\ ^3P_1$	1.886	0.781
$3\ d\ ^2D_{3/2}$	1.692	$4s4p\ ^3P_2$	1.899	0.768
$3\ d\ ^2D_{3/2}$	1.692	$3d4s\ ^3D_1$	2.521	0.145
$3\ d\ ^2D_{3/2}$	1.692	$3d4s\ ^3D_2$	2.521	0.145
$3\ d\ ^2D_{3/2}$	1.692	$3d4s\ ^3D_3$	2.526	0.141
$3\ d\ ^2D_{3/2}$	1.692	$3d4s\ ^1D_2$	2.709	0.043
$3\ d\ ^2D_{3/2}$	1.692	$3s4p\ ^1P_1$	2.933	0.266
$3\ d\ ^2D_{3/2}$	1.692	$3s5s\ ^3S_1$	3.910	1.244
$3\ d\ ^2D_{3/2}$	1.692	$3s5s\ ^1S_0$	4.131	1.464
$3\ d\ ^2D_{5/2}$	1.700	$4s^2\ ^1S_0$	0.000	2.674
$3\ d\ ^2D_{5/2}$	1.700	$4s4p\ ^3P_0$	1.879	0.795
$3\ d\ ^2D_{5/2}$	1.700	$4s4p\ ^3P_1$	1.886	0.788
$3\ d\ ^2D_{5/2}$	1.700	$4s4p\ ^3P_2$	1.899	0.775
$3\ d\ ^2D_{5/2}$	1.700	$3d4s\ ^3D_1$	2.521	0.153
$3\ d\ ^2D_{5/2}$	1.700	$3d4s\ ^3D_2$	2.521	0.153
$3\ d\ ^2D_{5/2}$	1.700	$3d4s\ ^3D_3$	2.526	0.148
$3\ d\ ^2D_{5/2}$	1.700	$3d4s\ ^1D_2$	2.709	0.035
$3\ d\ ^2D_{5/2}$	1.700	$3s4p\ ^1P_1$	2.933	0.259
$3\ d\ ^2D_{5/2}$	1.700	$3s5s\ ^3S_1$	3.910	1.236
$3\ d\ ^2D_{5/2}$	1.700	$3s5s\ ^1S_0$	4.131	1.457

المنارة للاستشارات

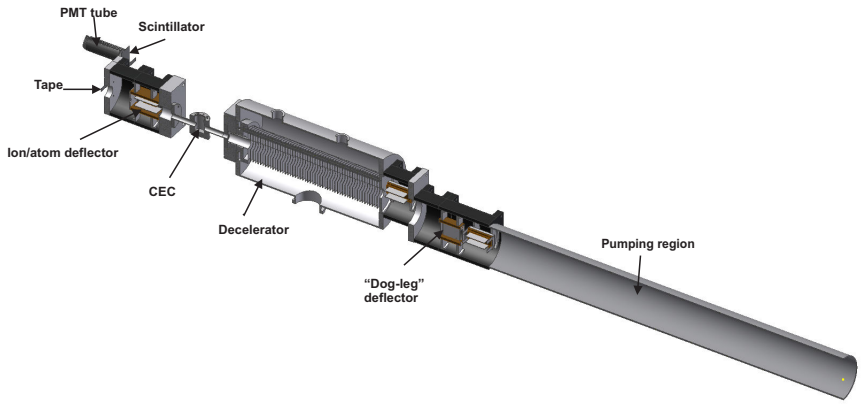

Figure 6.13: CAD model of previous ROC experimental setup. See text for more details.

6.3 Previous ROC beam line

A drawing of the previous ROC beam line, as used in Ca experiment to study the isotope shift of ^{50}Ca [17] is shown in figure 6.13. In the former experiment, ions at 34 keV were sent into the ROC setup and overlapped with a laser beam along an optical pumping region of 1.5 m long. The laser was separated from the ion beam by using a "dog-leg" deflector. The ion beam was decelerated down to 4 keV and passed though a charge exchange cell. The charge-exchange cell was placed outside of vacuum at a fixed potential of 30 kV. After the neutralization process, the ions and atoms were separated by a pair of electrostatic deflectors, and the atoms were implanted in a movable tape. Subsequently, the β-particles emitted from the decay of the implanted Ca isotopes were detected by a plastic scintillator of 2 mm thickness, with an angular coverage of $\sim$25 %. More details of the old setup and previous experimental results are found in Ref. [17].
Odd isotopes were not accessible in this previous experiment because the signal-to-background ratio, S/B, is reduced to less than 10% of the value obtained for even isotopes, due to spontaneous decay into different hyperfine components. Furthermore, measurements on even isotopes beyond ^{50}Ca were impossible due to an increase of the background signals resulting from radioactive contamination implanted around the β-detectors.

المنارة للاستشارات

6.4 Design of the new beam line components and detection set-up

With the goal of improving the limits of sensitivity of the ROC technique by at least three orders of magnitude to study ^{53,54}Ca, a new experimental setup has been designed. The new ROC setup is expected to solve the shortcomings identified during previous experiments, and includes improvements on beam transmission, laser-ion interaction, β-detection efficiency, and background reduction. Furthermore, multiple-step optical pumping and simultaneous detection of atoms and ions was implemented.
The sensitivity of the previous ROC experiment on ^{50}Ca was considerably reduced due to a low S/N signal caused by radioactive isobaric contamination, which was partially implanted in the detection zone, inhibiting a possible measurement of ^{52}Ca. Thanks to the laser ionization ion source, the beam contamination is now strongly reduced as compared to previous experiments using surface-ionization, allowing an improvement of the S/N signal. The isobaric contamination ratios for ^{53}Ca and ^{54}Ca measured during the ISOLTRAP experimental campaign (2013) [11] are listed in Table 6.2. Energy discrimination has been implemented in the new β-detector setup to allow a clear separation of the β-counts coming from ^{54}Ca (Sec. 6.4.3). Furthermore, several ion beam optics elements have been implemented in the new setup to guarantee a safe implantation of both ion and atom beams on the different tape stations (Sec. 6.4.3). The simultaneous detection of both beams allows a normalization to the total beam current, removing the dependence of the β-count signals with ion beam intensity.

An overview of the new design is shown in Figure 6.14. The total length of the new ROC setup is $\sim$ 4 m. The laser interacts with the ion beam along an optical pumping zone of 2 m long. As can be seen in Figure 6.5, a longer interaction region (2 m) guarantees $\sim$100 % pumping efficiency for transferring the ground-state population into metastable states (see Figure 6.5). The introduction of multiple potentials along the pumping region allows the pumping of different hyperfine components, enhancing the signal of weakly populated hfs transitions in odd-isotopes by more than one order of magnitude, depending on the nuclear spin and the number of pumping steps (Sections 6.1.1-6.1.1). For steps of 1m length, a pumping efficiency of about 50% can be reached for a laser power density of 160 W/m^2 (Figure 6.5). These are the optimum parameters to obtain equally distributed peak intensities for each hfs transition in the metastable state population (Figure 6.7).

After the optical pumping process, the ion beam is separated from the laser beam by a 5 degree deflector, and directed into the decelerator. The deflection

المنارة للاستشارات

Table 6.2: Ratio of isobaric contamination for the different isobars of mass $A = 53$ and $A = 54$ identified during the ISOLTRAP experimental campaign (2013) [11, 243]. Half life and Q_β values are taken from [74, 244]. Values in squared brackets show estimated values.

Isobar X	Half life	Q_β (MeV)	^{53}X/^{53}Ca	^{54}X/^{54}Ca
^{53}Ca	90(15) ms	[11.5]	1	
^{53}Cr	stable		300	
^{53}Ti	32.7 s	5	3	
^{53}K	30(5) ms	[16]	~ 0.3	
^{54}Ca	86(7) ms	10.3(8)		1
^{54}Cr	stable			928
^{54}Ti	1.5 s	[4.2]		3
unknown molecules[7]	stable			2

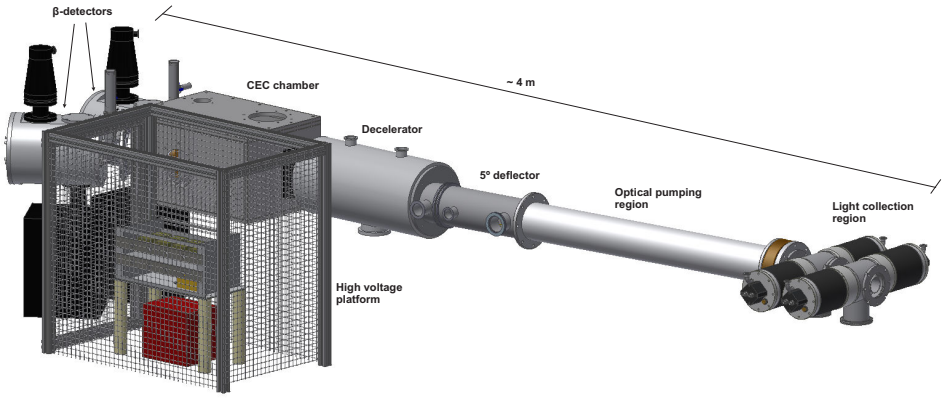

Figure 6.14: Complete design of the new ROC experimental setup. As designed with the help of Autodesk Inventor 2013.

المنارة للاستشارات

is achieved by a couple of cylindrical lenses of long curvature radius ($\sim$ 2 m), which preserve the plane of motion for the ion beam, and minimized undesired focusing effects. This is in contrast with the previous "dog leg" deflector composed of two couples of parallel plates used to change the horizontal plane of motion and introducing a strong focus on the vertical plane, reducing the overall ion beam transmission.
After deceleration, the ion beam is passed through a charge exchange cell, and independent counting of neutralized and non-neutralized particles is performed by two independent tape stations at the end of the beam line. High transmission for the simultaneous detection of both atoms and ions after the deceleration and the neutralization processes is achieved by introducing multiple ion beam optics components floating at the CEC potential. A detailed explanation of each new beam line component is presented in the following sections.

6.4.1 Multi-step optical pumping

As explained in section 6.1.1, the length of the optical pumping region (interaction time) and the laser power density are critical parameters affecting the population of the metastable state. For ions with nuclear spin $I = 0$, no hyperfine components are present, and up to 100% of optical pumping efficiency can be achieved. When $I \neq 0$, the population of the metastable state is significantly reduced due to the trapping into the different hyperfine structure components, hence multi-step optical pumping needs to be employed to depopulate these "dark" states [238, 239]. In practice, multi-step optical pumping is achieved by dividing the optical pumping region in different segments maintained at different potentials. It is the equivalent to using multiple laser frequencies as explained in section 6.1.1.
The optical pumping region for the new design is shown in figure 6.15. The ion beam is superimposed with the laser beam along a pumping zone divided in four segments with lengths of 40 cm, 60 cm, and two of 50 cm. The first segment corresponds to a pumping tube of 40 cm length (not shown in the figure). A light collection region is installed along the second pumping segment for monitoring the resonant fluorescence signal during the experiments. This light collection region is the same one used in the previous optical hfs experiments on Ca and K isotopes [70, 245, 246, 63].

In the experiment, the hfs spectrum of a particular nucleus is scanned by changing the potential of the optical pumping region. Regardless of the voltage applied to the optical pumping zone ($\pm$ 5 keV), the ion beam transmission up to the end of the beam line should remain unaltered. To avoid abrupt changes between the optical pumping zone and the ground potentials, a five-

المنارة للاستشارات

step accelerator(decelerator) set connects the beginning(end) of the optical pumping region with the rest of the beam line. For ions with nuclear spin $I = 0$, all pumping segments are fixed at the same potential, and the Doppler-tuning voltage is applied to the whole optical pumping region. For odd ions ($I \neq 0$), independent potentials can be applied to each pumping segment for multi-step optical pumping (see section 6.1.1). When the TSOP scheme is used, the last two sections are set at a constant voltage corresponding to the most intense resonance peak in the hyperfine spectrum. Scanning across the full hyperfine structure is then performed by scanning the voltage on the first and second section (both on the same potential).

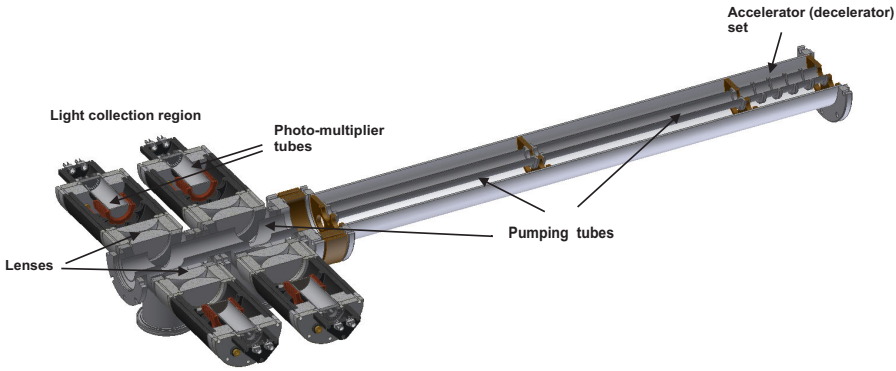

Figure 6.15: Design of the multi-step optical pumping region. The optical pumping region is divided in four independent segments. The first segment is not shown in the figure. A light collection region is placed along the second step for monitoring the fluorescence signals.

6.4.2 Deceleration and focus control of atom/ion beam

As the ratio of neutralization cross section between the metastable state and the ground state reaches the maximum value at 4 keV, the initial ion energy (30 keV) should be reduced by a factor of ∼10. This energy reduction has the highest influence on the overall beam transport. Beam divergences, and undesired focusing points can be easily introduced during the deceleration. Besides requiring maximum beam transport efficiency, the possibility to control

المنارة للاستشارات

the focus of the decelerated beam is essential, as both ions and atoms must be separated and implanted simultaneously on two independent tape stations of 10 mm width. Radioactive nuclei were implanted outside the tape, creating a large background due to radioactive contamination implanted around the β-detectors [17]. In order to preserve the beam quality in the deceleration process, the ion beam is passed through an array of 52 equidistant disks of 1.5 mm thickness. Each disk has an outer diameter of 14 cm, and a concentric hole of 4cm diameter. The decelerator system is the same as used in the previous ROC setup, but an adjustable slope for the deceleration potential, and an einzel lens between the decelerator and CEC were implemented to control simultaneously the focus of both atom and ion beam.

Assuming an initial ion beam at 30 keV, the simplest approach to reduce the beam energy to 4 keV, might be feasible by applying a linear retarding potential along the beam direction, starting from the first disk at 0 V, and increasing the potential linearly up to 26 keV on the last disk. To illustrate the sensitivity of the focal point position to the shape of the retarding potential, ion beam simulations were performed for a simplified setup composed of a decelerator, an Einzel lens and a CEC cell. The results from the SIMION simulations are shown in Figure 6.16. As it can be seen in Figure 6.16a, the focal position for this case is generated after the CEC. The ion beam can be later refocused by introducing additional electrostatic elements after the CEC, but for atoms the focal point shall be fixed before the neutralization.
A common method used to control the focus introduced by a decelerator with cylindrical geometry consists in applying an exponential retarding potential field instead of a linear one [247]. Using the paraxial approximation [248], a charged particle in an axially symmetric field along the z direction, follows a trajectory, $r(z)$, described by

$$\frac{d^2r}{dz^2} + \frac{1}{2V(z)}\frac{dV(z)}{dz}\frac{dr}{dz} + \frac{r}{4V(z)}\frac{d^2V(z)}{dz^2} = 0, \tag{6.29}$$

where $V(z)$ is the potential along the z direction.
For an retarding potential given by an exponential form

$$V(z) = V_0(1 - e^{-\alpha z}), \tag{6.30}$$

with V_0 and α constants that depend on the initial conditions. The solution, $r(z)$, of equation 6.29 is given by [247]

$$r(z) = 2\alpha\sqrt{(4\theta_0^2 - 2\theta_0 r_0\alpha + r_0^2\alpha^2)/3}e^{\alpha z/4}\sin(\sqrt{3}\alpha z/4 + \phi), \tag{6.31}$$

where θ_0 is the entrance angle, and r_0 is the initial distance from the symmetric axis. At the focal point, z_1, the distance of each particle to the symmetric axis

المنارة للاستشارات

is minimized, such that $r(z_1) = 0$. Therefore, the first focal point is located at

$$z_1 = \frac{4\pi}{\sqrt{3}\alpha}. \tag{6.32}$$

Hence, the focal position can be moved by varying the parameter α of the exponential function that defines the shape of the retarding potential. Experimentally, an exponential potential can be implemented by choosing appropriate resistor values connecting the different disks in the decelerator. This approach, although it is feasible, does not allow an easy control of the exponential factor, because the whole set of resistors would need to be replaced to change the focal position. Instead of using an exponential potential, a similar effect can be produced by dividing the deceleration potential in three steps of different slope. Each step is connected by a linear resistor chain of different value, and a floating power supply on the top of the CEC potential can be added to control the slopes of retarding potential. The idea is outlined in Figure 6.16. It can be seen as three-points linear interpolation of an exponential function, and it is equivalent to have several decelerators in series [249, 250].
The deceleration potential can be applied in three different ways: by using only one slope (figure 6.16a), two slopes (figure 6.16b) and three slopes (figure 6.16c). By varying the slope of each step, the focal position can be adjusted. The focus can be located inside the decelerator, an einzel lenses can be added to send the next focal point to the desired position.
In the experiment the focal position should be located at the implantation points, just in front of the tape stations, at a distance l_4 from the end of the CEC (see figure 6.16). For the ion beam simulations, an array of 51 disks was divided in three sets of 17 disks each one. The potential of each disk was increased linearly along the z axis, using different slopes for each set of disks. The results from the SIMION simulations are summarized in the table 6.3.

The results for the SIMION simulations using retarding potentials of different slopes are shown in Figure 6.16. For a linear potential with a single slope the focal point is located at the exit of the charge exchange cell and the beam diverges quickly at short distances (Figure 6.16a). At the point of the tape station the beam diameter for this case is about four times the tape width ($\sim$ 40 mm). Because the focus occurs after the CEC, the Einzel lens is useless in this situation. Using two slopes (Figure 6.16b), the focal point can be moved to the end of the decelerator, and if three slopes are used (Figure 6.16c), the focal point is sent into the decelerator. Therefore, the ion beam can be re-focused by the Einzel lens, allowing full control of the focal position after the CEC. In this case the beam diameter at the implantation point can be reduced to a few millimeters, assuring a safe implantation on the tape station.
A parallel beam of 10 mm diameter entering into the decelerator tube at 30 keV was assumed in the simulations. The results are similar for a divergent ion

المنارة للاستشارات

Table 6.3: Simplified SIMION simulations for the system composed of a decelerator tube, an einzel lens and a CEC cell. A initial parallel beam at 30 keV is used to illustrate the influence of the deceleration slopes and the Einzel lens potential. The values of V_1 and V_2 are taken relative to the ground potential. The Einzel lens potential, V_L, is given relative to the platform potential (26 kV). Particle trajectories and the potential along the decelerator are shown in Figure 6.16.

V_1	V_2	V_L	Final beam diameter (mm)
8667	17333	0	43
13000	26000	0	23
24600	26000	0	14
24600	26000	-6500	6

beam as the strong focus induced in the deceleration is almost independent of the initial beam divergence. This dominant focus can be taken as an advantage for the new experimental setup. The voltage applied to the optical pumping region for the Doppler-tunning of hfs components modifies the focal point for the ion beam before the decelerator, but the focus induced in the deceleration dominates the final focal position. Consequently, very little influence on the overall beam transmission and on the focal position is expected at the tape position.

6.4.3 Simultaneous detection of β-decay of atoms and ions

Once the ion beam is decelerated and passed trough the charge exchange cell, the ions are separated from the neutralized particles by a pair of electrostatic cylindrical plates as shown in Figure 6.17. Horizontal and vertical correction plates were added to control the position of the implantation point. The atoms follow a straight path towards the tape station, located at 53 cm from the end of the CEC. The ions are deflected 35^o towards a second tape station at 68 cm from the end of the CEC. Because both β-detection stations are at ground potential, a post-accelerator can be used to gradually decrease the potential seen by the ion beam, from 26 keV to 0 keV. This re-acceleration process is accomplished by a set of 18 equidistant disks connected by resistors of equal value. As the tape station is close to the end of the accelerator, no further focus control is needed.

المنارة للاستشارات

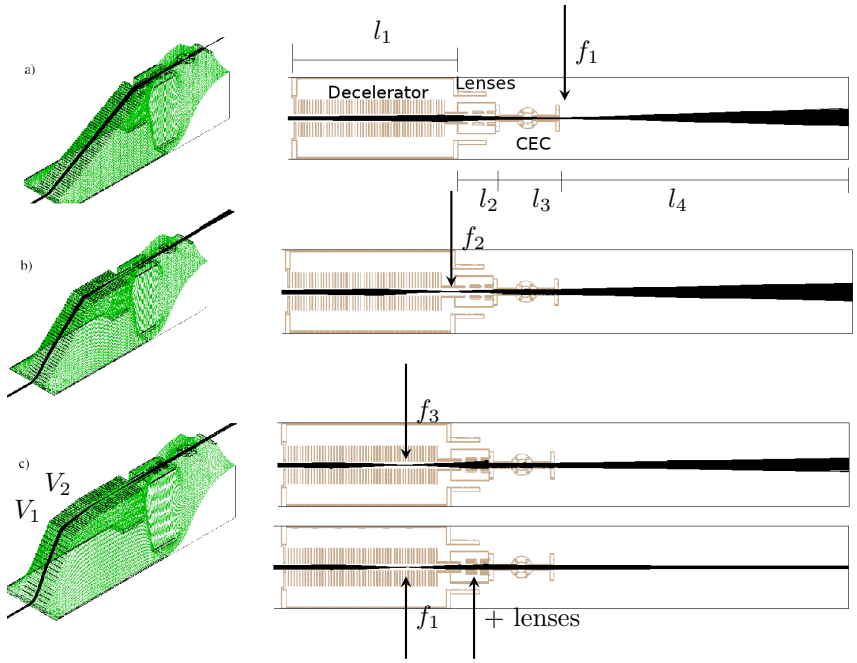

Figure 6.16: SIMION simulations for a simplified setup composed of a decelerator tube, an Einzel lens and a CEC cell. The retarding potential is divided in different steps: a) one slope, b) two slopes and c) three slopes. See text for more details.

Power supply control of ion beam optics

As the CEC is at 26 keV, the voltages applied to the beam optics components inside the CEC chamber should float on top of this potential. A HV platform was designed to operate up to 50 keV (Figure 6.18). It is used to provide the HV voltages required by the different electrostatic components. The HV platform potential is provided by an external power supply. On the top of the HV platform, eight power supplies are installed with a ground reference provided by the platform potential. Two negative HV powers supplies are used to control the Einzel lens potential, and the slopes of the deceleration voltage (V_1). Two HV supplies of opposite polarity are used for the 35^o deflector, and two HV supplies with the same polarity are connected to a pair of parallel plates for horizontal correction. Similarly, two extra HV supplies are used for vertical corrections. As the cables connecting the HV supplies with the electrostatic

المنارة للاستشارات

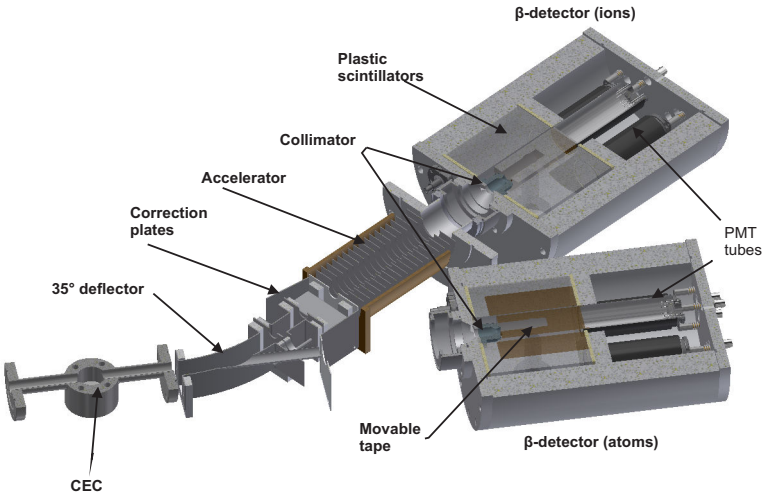

Figure 6.17: CAD design for the ion beam optics after the CEC cell. Independent high efficiency β-detection was implemented of atoms and ions. Details for the β-detector chambers are given in section 6.4.3.

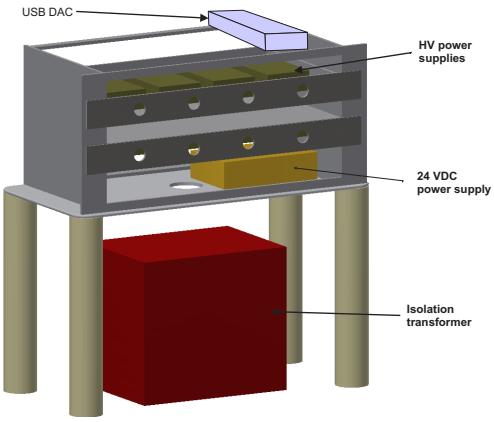

Figure 6.18: CAD design of the high voltage platform. A set of eight HV power supplies are installed with ground reference given by the platform potential (26 keV).

المنارة للاستشارات

elements inside the CEC chamber are floating at the HV platform potential (26 keV), it is necessary to construct a HV cage to prevent electrical hazards. The CAD design of the HV cage was shown in Figure 6.14. The HV cage is placed next to the CEC chamber.
The HV platform and HV cage were built following the guidelines for safety practices in high-voltage and high-power testing, recommend by the IEEE STD 510-1983 [251]. The minimum approach distance between the HV cage and exposed conductors inside the cage was maintained to a value higher than the 32 cm recommended for voltages up to 33 kV [252]. For places where the minimum distance was lower than this value an extra isolation sheet was attached to the wall of the HV platform to prevent the risk of sparks.
A high current (12.5 A) 24 VDC power supply was used to provide the power required for the different HV supplies. The output value of each HV supply was controlled by an analog signal between 0 to 10 V, from a digital to analog converter, DAC. The DAC device was controlled by a computer outside the HV cage via an optical link. The technical details of each of these component are given in section 6.6.

High efficiency β-detection

A direct detection of atoms and ions is sensitive to isobaric contamination present in the ion beam. Nevertheless, a selective measurement of the number of particles for the ion of interest can be obtained by counting the β-particles emitted from the beta-decaying nuclei. β detection removes completely the background associated with stable contaminants. The background emanating from radioactive isobars (mainly Ti) can also be reduced if additional energy discrimination is implemented. The endpoint energy for ^{53,54}Ti beams is around 4-5 MeV, while it is above 10 MeV for Ca beams (see Table 6.2).
A view inside the β-detector chamber is shown in Figure 6.19. Each chamber is composed of two concentric cylindrical scintillators with inner and outer radius of 50 mm and 190 mm respectively. The axis of each cylinder coincides with the beam direction. A movable tape perpendicular to the beam direction can circulate through the center of both cylinders. This configuration allows for a geometrical efficiency of $\sim 4\pi$ at the implantation point. Particle coincidences between the inner and outer cylinder are used to discriminate the β-particles from other sources of radiation, e.g., γ-radiation. The intrinsic β-detection efficiency of this setup is expected to be $> 80\%$. The thickness of the outer detector was chosen to stop all β-particles emitted with energies below 12 MeV. It allows full energy reconstruction of the β-particles by adding the signals of all 5 PMTs. Event by event information will be obtained using the ISOLDE DAQ system, allowing the selection of different energy cuts for the offline analysis. For online monitoring, a simple DAQ system will be used to monitor β-signals.

المنارة للاستشارات

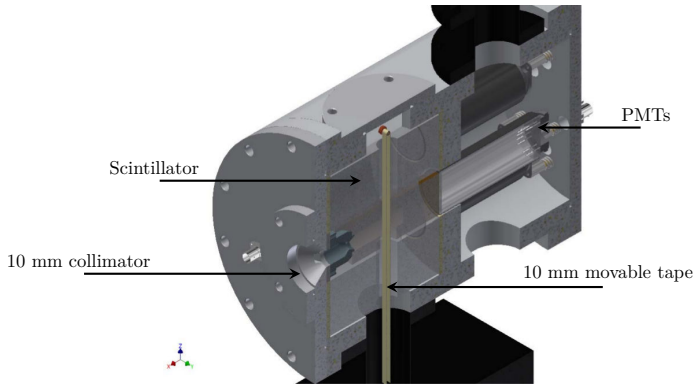

Figure 6.19: CAD design of the β-detector chamber. Ions are implanted on a movable tape. A collimator prevents the implantation of ions outside the tape. The β-particles are detected by two concentric cylindrical scintillators. The light from the scintillators is collected by a set of PMT tubes attached to the surface of the scinitllators.

The discriminator level of each PMT signal can be adjusted to provide online "Hardware" energy cuts.

The β-particles emitted from the radioactive isotopes implanted on the tape are recorded on the site of implantation point. After few hundreds of milliseconds [8], the contaminated part of the tape is removed, and a clean section of the tape is placed in front of the beam path at the center of the β-detectors. Each collection time is synchronized with a change of the ion velocity (Doppler-tuning of the laser frequency).
A collimator of 10 mm aperture is placed at the entrance of each chamber to prevent the implantation of the radioactive contamination outside of the tape. The light resulting from the β-decaying particles passing through the scintillators is detected by a set of photomultiplier tubes. Four PMTs are attached to the surface of the outer cylinder, and one PMT on the surface of the inner cylinder.

A summary with the improvements and new features implemented in the new experimental setup are listed in Table 6.4.

[8] For ^{54}Ca ($T_{1/2} = 86(7)$ ms) the detection time is around 400 ms

المنارة للاستشارات

Table 6.4: Comparison between the old and new ROC setup

Parameter	Old	New
Interaction region	1.5 m	2 m
Light collection	No	Yes
Multi-step optical pumping	No	Yes
Deceleration	Yes	Yes
Slope control of retarding potential	No	Yes
Focus control after Deceleration	No	Yes
Atom counting	Yes	Yes
Ion counting	No	Yes
Angular coverage for β-detection	$\sim$ 25 %	$\sim$100%
Scintillator detectors per chamber	1	2
Protection of β-detectors against contamination	No	Yes
β-energy discrimination	No	Yes
Overall ion beam transmission (simulated)	$<$70 %	$>$90 %

6.5 Ion beam optics simulations

The beam line components included in the ion beam optics simulations are shown in Figure 6.20. Electric fields and particle trajectories were calculated by using the ion beam simulation software SIMION-8.1.
The 3D CAD designs of each beam line component were imported to SIMION by using the STL tools included in the same software. The outer chambers for the whole beam line were included as a single electrostatic component (electrode) fixed at ground potential. Each internal component was imported as an independent electrostatic device with an adjustable potential. The electrodes included in the ion beam simulations are shown in Figure 6.20. Different colors represent independent electrodes. For simulations of the whole ROC setup, a grid unit equivalent to 1.6 mm was chosen. Independent beam line segments were simulated with higher resolution ($<$ 1 mm) to explore specific details on the beam transmission.
The simulations were performed assuming different initial conditions for the ion beam entering into the beam line. The focus of the incoming beam was placed at different positions assuming a beam emittance of around $\sim$3-5 π mm.mrad, similar to the typical values observed at HRS [191] and GPS ion source targets [253].

An example of a SIMION simulation for the whole ROC setup is shown in Figure 6.21. The upper figure shows the potential energy surface view. An

المنارة للاستشارات

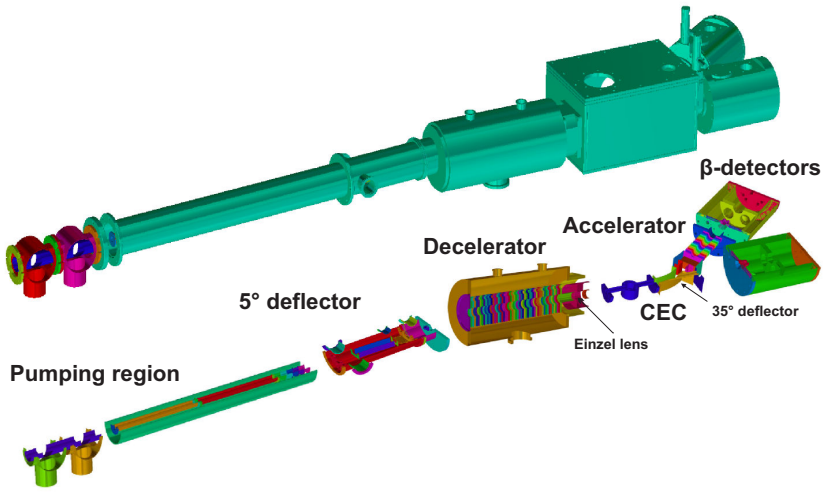

Figure 6.20: Beam line components included in the SIMION simulations. Each electrode with adjustable potential is presented with a different color. The outer chambers were included as a single electrode fixed at ground potential.

initial ion beam of mass $A = 50$ at 30 keV is focused at the entry of the light collection region. The ions are elevated from ground potential to 26 keV by a three-slope deceleration potential. The first two slopes can be controlled by changing the potential V_1 (Figure 6.21a). The parameter V_1 and the Einzel lens potential (negative with respect to 26 kV) are used to control the focus of the ion beam. After the charge exchange process, the ion beam is separated and re-accelerated to ground potential by using an accelerator of a single slope potential.

The ion beam trajectory along the different elements is shown in Figure 6.21b. Atoms and ions are separated and focused simultaneously on the different tape stations.

At the light collection region, the ion beam size is ~ 6 mm and has divergence of about 2 degrees. Due to the collimator installed at the entrance of each detector chamber, the beam size in the location of the tape stations is limited to less than 10 mm. The optimization procedure consists mainly of simultaneously maximizing the atom and ion beam transmission at the implantation point.

Figure 6.22 shows the beam transmission obtained from the SIMION ion beam simulation for different values of V_1 and Einzel lens potential, V_E. After the 35^o deflector the ion beam is re-accelerated from 26 keV to ground potential, producing a extra focusing effect. This additional focus produces a broad region

المنارة للاستشارات

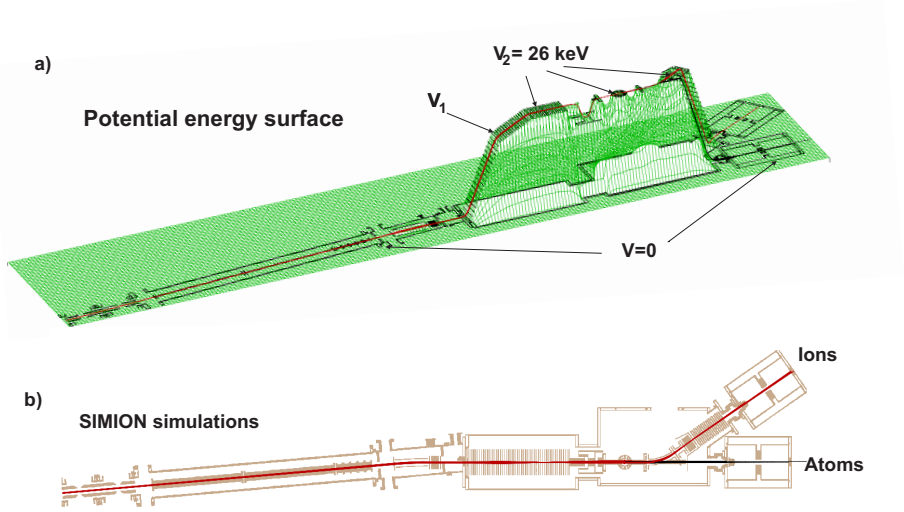

Figure 6.21: Example of a SIMION simulations for the whole ROC setup. a) Potential energy surface view, and b) particle trajectories for the ion beam. A neutralization efficiency of 50 % was assumed for the CEC process at the center of the CEC (see text for more details).

of maximum transmission for different (V_1, V_E) values (Figure 6.22).
The simulations were performed assuming different focal positions for the ion beam entering into the ROC setup. The ion-beam optics was designed to optimize the transmission of atom and ion beam within a common (V_1, V_E) region simultaneously. Figure 6.22 shows the results for atoms(left) and ions(right) for an initial ion beam with focus at two extreme positions: at the light collection region (upper figures), and at the end of the pumping region (bottom figures). The transmission in both cases is mainly defined by the parameters (V_1, V_E), but in contrast with the ions, the atom beam has a much narrower region of maximum transmission (left of Figure 6.22). The region of maximum transmission is broader when the focus of the initial beam is closer to the decelerator, but the peak (V_1, V_E) of maximum transmission does not exhibit an appreciable dependence with the focus of the initial beam, as expected from a dominant focus introduced by the deceleration potential.

Optimized values for the electrostatic potential for the main elements of the ROC setup were obtained from the ion beam SIMION simulations. The results for maximum transmission are listed in Table 6.5.

المنارة للاستشارات

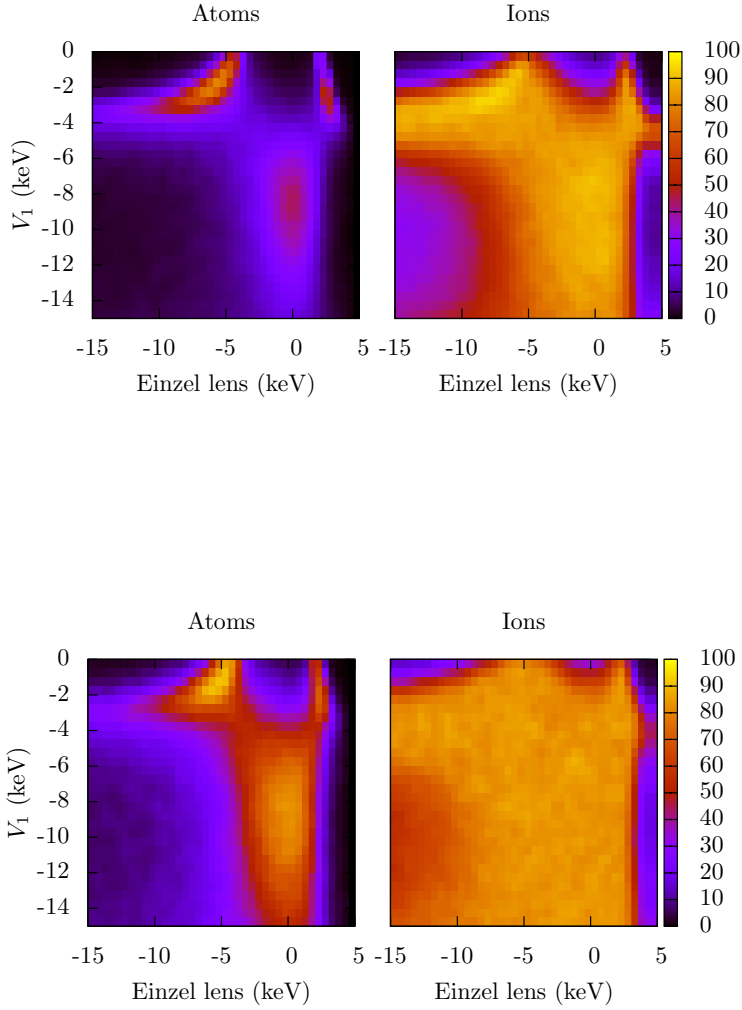

Figure 6.22: Results of ion beam SIMION simulations for both, atoms(left) and ions(right), assuming two different focal positions for the ion beam entering into the ROC setup: at the entry (upper) and at the end (lower) of the optical pumping region. Colors represent the percent of transmission simulated at the implantation point.

المنارة للاستشارات

Table 6.5: Optimum values of the main electrostatic elements of the ROC setup obtained from the ion beam SIMION simulations. The labels (i) and (ii) stands for two different regions of maximum transmission (Figure 6.22).

Parameter	Potential (V)
5^o deflector (Right)	+555
5^o deflector (Left)	-555
35^o deflector (Right)	+460
35^o deflector (Left)	-460
Top	0
Bottom	0
Right	0
Decelerator	-12000$\leq V_1 \leq$-6000 (i)
	-4000$\leq V_1 \leq$-500 (ii)
Einzel lens	-3000$\leq V_E \leq$1000 (i)
	-10000$\leq V_E \leq$-4000 (ii)

6.6 Commissioning the new ROC setup

The design and dimensions of each beam line component were chosen based on the different numerical calculations of the laser-ion interaction and ion beam simulations explained in the previous sections. The CAD files with the final design of the different parts were sent to different mechanical workshops: Pumping tube and ion beam optics components (TU Darmstadt), charge exchange chamber (MPIK-Heidelberg), and β-detector chambers (IKS-KU Leuven). In this section the installation of the different components, and the first experimental tests are presented.

6.6.1 Installation of beam line components

A photograph of the optical pumping region installed at the COLLAPS beam line is shown in Figure 6.23. The chambers, in addition to the internal parts of the pumping region, were made of aluminum. The internal parts were painted with black aluminum graphite to reduce the scattering of light around the light-collection region. The pumping region, as well as the other components sent to the different workshops were built almost identical to the original CAD designs. No appreciable changes on the shape and/or dimensions of the different

المنارة للاستشارات

Figure 6.23: Photograph of the optical pumping region installed at the COLLAPS beam line. The pumping tube connected to the light collection region (left), and a view inside the pumping tube (right).

Figure 6.24: Photograph of the installation of different beam line elements: the decelerator (left), CEC chamber (center), and HV cage (right) .

components were introduced during the production process. The tube was connected to the COLLAPS light collection region. Inside of it two independent cylindrical tubes can be maintained at different potential to implement multi-step optical pumping.

The other end of the pumping tube connects the beam line to the 5^o deflector. A photograph of the ROC setup from the deflector up to the end of the CEC chamber is shown in Figure 6.25.
A Faraday cup array and a variable aperture for beam diagnostics were installed inside the 5^o chamber. Inside the chamber, a pair of cylindrical plates are used for the deflection, and a couple of horizontal plates for vertical correction of the ion beam. The electrostatic plates are controlled by NIM power supplies located next to the beam line.
After the 5^o deflection, the laser is reflected by a 45^0 mirror, reflecting the

المنارة للاستشارات

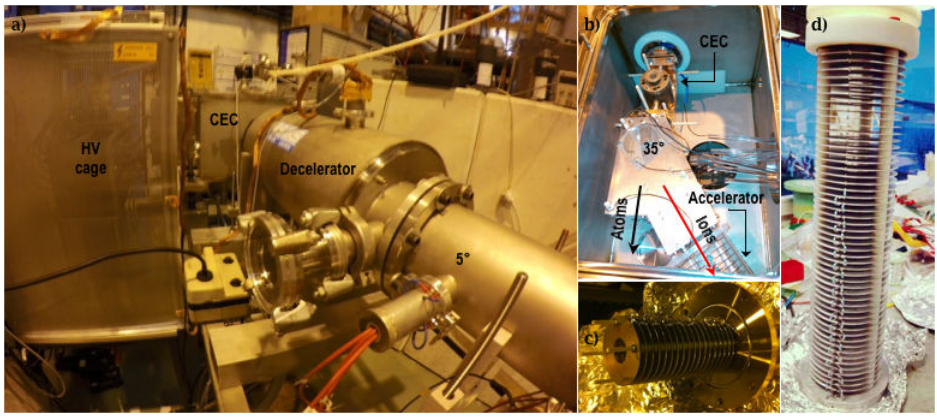

Figure 6.25: Photograph of some of the components in the ROC setup. a) A view from the 5^o deflector up to the end of the CEC chamber. The HV cage placed on one side of the CEC chamber. b) The inside of the CEC chamber. c) Re-accelerator for ions after the 35^o deflector and d) Renewed accelerator from the old ROC setup.

laser light towards outside of the vacuum chamber. A transparent window at Brewster angle reduces the reflected light into the light collection region. A photograph of inside the CEC chamber (Figure 6.25b) shows: the CEC cell, the 35^o deflector and vertical and horizontal correction plates. The accelerator and decelerator arrays are shown in Figure 6.25c and 6.25d respectively.

The inside of the HV cage is shown in Figure 6.26. An isolation transformer of 50 kV and 1 kW power (SIT 50-1000) from Stangenes was used to isolate the high voltage from the ground potential. A Heinzinger power supply PNChp-30000 provides the 26 kV to the HV platform.

The electrostatic elements inside the CEC chamber are controlled by Spellman MPS 10W power supplies. Two power supplies of -10 kV are used to control the Einzel lens and the slopes of the deceleration potential via V_1. Three power supplies of -3 kV, and three of + 3 kV are used to control the 35 degree electrostatic plates and two pairs of deflectors for horizontal and vertical corrections.
The output of each power supply is controlled by an analog signal from 0 to 10 V, obtained from a USB DAC device (USB 3106 from Measuring Computing). Figure 6.27 shows the HV output of each power supply as a function of the input signal provided by the USB DAC. The USB device is controlled by a computer outside of the HV cage via an optical link “USB 2.0 Ranger 2224 Four-port (Multi-mode Fiber)” from Icron.

المنارة للاستشارات

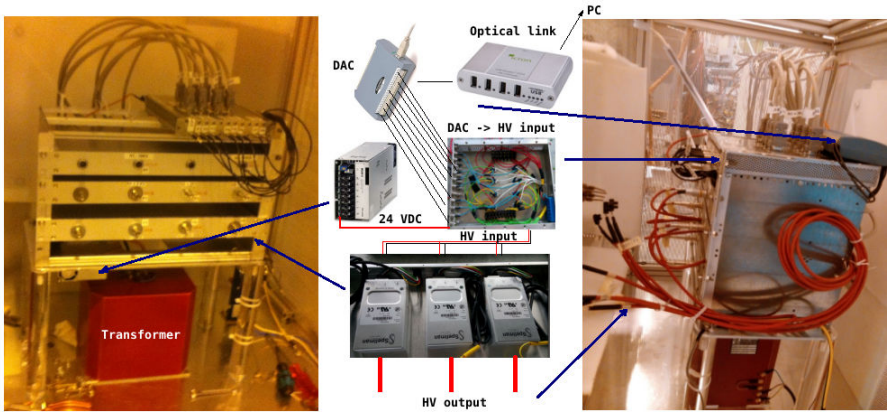

Figure 6.26: Photograph of the HV cage and the different components used to control the power supplies floating at 26 keV with respect to the ground potential.

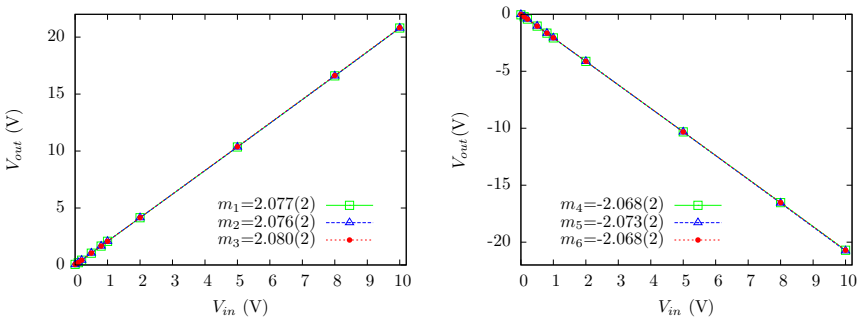

Figure 6.27: Test of linearity for the high voltage power supplies used to control the ion beam optics inside the CEC chamber. The HV output is measured as a function of the input voltage.

المنارة للاستشارات

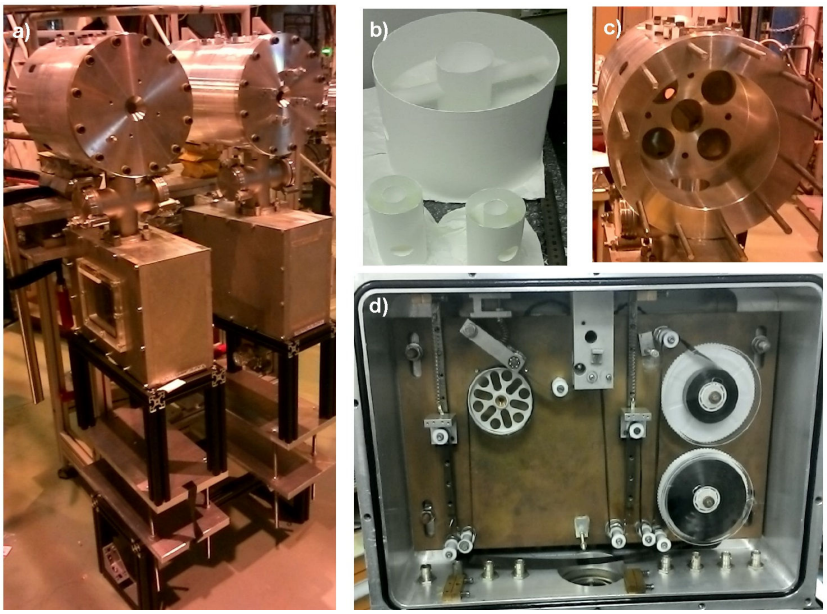

Figure 6.28: Photograph of the tape stations a) Shows both chambers assembled with the respective tape stations. b) Outer and inner scintillators. c) A view of one detector chamber. d) The inside of one of the tape stations.

A photograph of the β-detector setups and the tape stations are shown in Figure 6.28. The inner and outer cylinders and the one of the new detector chambers are shown in Figure6.28b and 6.28c, respectively. The details of the tape stations (Figure 6.28d) can be found in Ref. [254].

6.6.2 First experimental test of ion beam optics

The modifications and improvements implemented in the new ROC setup influenced mainly the ion beam optics. Testing the ion beam transmission of the new setup after the different deflections, deceleration, and post-acceleration processes was one of the critical steps to increase the sensitivity of the technique. Three main concerns were explored through the first ion beam test:

i. The ability to reduce the energy from 30 keV to 4 keV while preserving the transmission at the end of the beam line.

المنارة للاستشارات

ii. Focus control of the ion beam after the deceleration process and effective control of the ion beam optics on the top of the HV platform at 26 keV.

iii. Dependence of the total ion beam transmission with the Doppler-tunning voltage applied to the optical pumping region.

No electron suppression can be implemented for the Faraday cups currently available at the COLLAPS beam line. Thus, it was not possible to take an accurate measurement of the absolute ion beam current during the test. Instead, the same setup with Faraday cup - iris aperture commonly used at the end of the COLLAPS beam line, was moved to the end of the ROC setup. Thus, the relative measurement between the ion beam current on this cup, labelled as F_C, and the current at the entry of COLLAPS [9], F_{ISO}, can be compared directly with the values of ion beam transmission reported in previous experiments. For "standard" COLLAPS experiments F_C is installed just after the light collection region, reaching typical values of $F_C/F_{ISO} \sim 1$.

Only plasma sources were available at ISOLDE for the first experimental test, therefore only beams of noble gases were used. Although the charge exchange process and properties of the Ca atom beam could not be studied in this first test, we could achieve our main goal of understanding the general features of the ion beam optics and ion beam properties through the ROC setup. The results from both target stations, GPS and HRS, are resumed below.

At the HRS target station a beam of ^{20}Ne at 30 keV was mass separated and redirected into the COLLAPS beam line. Although plasma sources are expected to have bigger emittance than ion sources, the ion beam emittance was reduced by passing it through the ion beam cooler, ISCOOL.
The ISOLDE electrostatic elements and the beam optics before the light collection region were set to initial values registered for previous COLLAPS experiments at HRS. An ion beam current of F_{ISO} ~170 pA was measured just before the COLLAPS beam line. These initial parameters gave a good overall transmission that was quickly optimized to a maximum value on a plate used as beam diagnostic parameter located in the 5^o deflector.
The platform potential was applied to set the CEC potential at 26 kV, and all the optical components for the ROC beam line were set at the values initially predicted by the ion-beam simulations (Table 6.5). A initial transmission of $\sim$ 30% ($F_C/F_{ISO} \sim 0.3$) was immediately observed at the end of the ROC setup. After few iterations of optimizing COLLAPS and ROC electrostatic elements, a beam transmission of $F_C/F_{ISO} \sim 0.9$ was observed, which is comparable with the values reported for "standard" COLLAPS experiments.
To study the focus control of the ion beam after deceleration, the aperture in

[9] Faraday cup LA0.BFC900 of the ISOLDE beam diagnostic tools

المنارة للاستشارات

front of F_C was reduced to the minimum diameter, ~ 3 mm. By changing the slope of the deceleration, V_1, and the Einzel lens potential, V_{Einzel}, and few readjustment of the horizontal and vertical steering, a ratio $F_C/F_{ISO} \sim 0.9$ was recovered. These positive results show the ability to control the focus of the ion beam to guarantee a maximum transmission in the implantation point, and reduce the risk of implanting radioactive contamination outside the tape. The final test studied the variation of the beam transmission as a function of the potential applied to the optical pumping region. Voltages between -7 keV and +7keV were applied to the pumping region and no changes were observed in the overall transmission. The factor $F_C/F_{ISO} \sim 0.9$ was unaltered.

Table 6.6: Experimental values obtained for the main electrostatic elements of the ROC setup. Results are summarized for both target stations: HRS (second column) and GSP (third column). In both cases an ion beam transmission of 90 %, $F_C/F_{ISO} \sim 0.9$, was obtained.

Parameter	Potential (V)	
	HRS (^{20}Ne)	GPS (^{19}F)
5^o deflector (Right)	630	+624
5^o deflector (Left)	-505	-547
35^o deflector (Right)	+516	+516
35^o deflector (Left)	-516	-489
Top	-441	-210
Bottom	-345	-120
Right	+99	+87
Decelerator	-5000 (i)	-5000 (i)
Einzel lens	-2100 (i)	-2090 (i)

For the GPS target station a beam of ^{19}F was extracted from a plasma-ion source at 30 keV, mass separated and sent to the COLLAPS beam line. As expected the emittance of this beam was much larger than for the HRS source, as observed from the beam profile on the XY scanners along the ISOLDE beam line. Therefore, the extracted ion beam was collimated by using a pair of slits located before the mass separator. Although direct measurements of the beam emittance were not possible, symmetric beam profiles were recovered on the XY scanners (see Figure 6.29).

A beam current of $F_{ISO} \sim 3.7$ nA was measured just before entry of the COLLAPS beam line. Using the collimated ion beam, the obtained overall transmission from the entry of COLLAPS to the end of ROC was similar to

المنارة للاستشارات

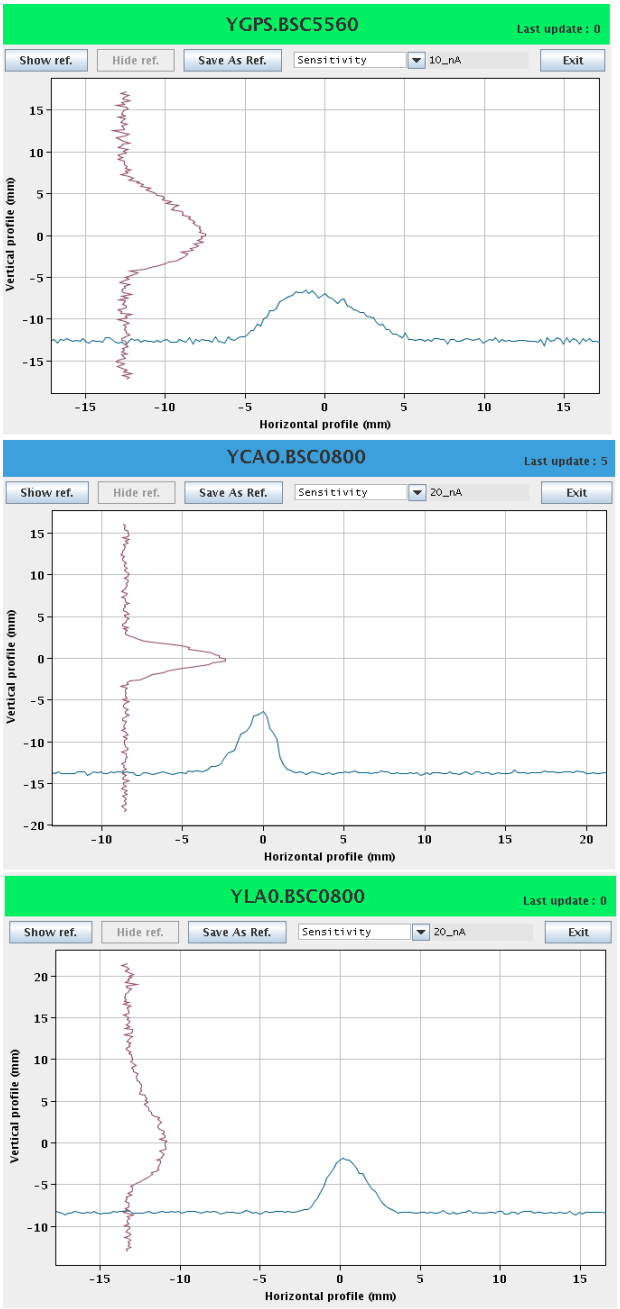

Figure 6.29: Measurements of the XY profile of a collimated ^{19}F ion beam at 30 keV, extracted from the GPS target station. The figures shows the beam profile just after the separator (upper), at midway between the separator and the COLLAPS beam line (center), and just before the COLLAPS beam line (bottom).

المنارة للاستشارات

the value obtained during the test at HRS, $F_C/F_{ISO} \sim 0.9$. The optimum experimental values obtained during the test from both target stations are shown in Figure 6.6. These values can be compared with the expected values obtained from the ion beam simulations presented in Table 6.5. Considering the multiple experimental uncertainties related with the alignment, dimensions and realistic ion beam properties, the values obtained from the simulation are consistent with the experimental ones.

The results from the tests with both target stations are equally satisfactory. Once the ion beam enters into the COLLAPS beam line, a relatively good transmission (> 90 %) can be easily achieved at the end of the ROC setup. The effectiveness of the multiple ion beam components implemented in the new setup has been proven, giving the expected ion beam transmission (> 90 %). The ion beam can be focused to less than 3 mm at the implantation point, and the focus can be controlled for atom and ions simultaneously by varying the slopes of the deceleration potential and the Einzel lens potential. Additionally, the beam transmission was not affected by the voltage applied to the optical pumping region ($\pm$ 7 kV).

6.7 Article III: Design of a sensitive setup for collinear laser spectroscopy at ISOLDE, CERN

This article, in preparation for Nuclear Instruments and Methods in Physics Research A, summarizes the different aspects involved in the technical design and the commissioning of the new ROC setup. The first experimental tests are reported and the sensitivity limits of the new setup are discussed.

I performed the numerical calculations for the ion-laser interaction. I carried out the different ion beam optics simulations that were necessary to define the size and geometry of the different beam line components. Together with Mark Bissell we designed and created the 3D drawings for all the pieces that were sent to the different mechanical workshops. I was also dedicated to the commissioning and testing of the new experimental apparatus. I prepared the draft of the manuscript. A first draft of the article, which is summarizing the above text, is included in appendix A.6.

المنارة للاستشارات

Chapter 7

Perspectives and future application of the newly designed setup

7.1 Possible physics cases for the ROC technique

The study of the neutron-deficient Ca isotopes is an obvious next step for the ROC setup. Understanding the evolution of the ground-state properties through the filling of the $d_{3/2}$ orbit is necessary to complete the description of the Ca isotopes. Especially around $N = 16$, where a signature of a new shell-closure was observed from a relatively large E_{2^+} excitation energy for ^{36}Ca [71].

The applicability of the ROC technique is constrained to the existence of a low-lying meta-stable state accessible by optical pumping, and with only one of the states (ground or meta-stable) near-resonance in the charge exchange process. This application is straightforward for alkali-earth ions Ca^+, Sr^+, Ba^+ and Ra^+.

A variation of ROC, without the inclusion of the deceleration process before neutralization, and with direct detection of ions and atoms (non radioactive detection) was applied to Sr isotopes [255], allowing hfs measurements to be extended to ^{100}Sr ($\sim 10^4$ ions/s). Measurements beyond this isotope were prevented due to a high isobaric contamination of stable isotopes in the ion beam. Implementing radioactive detection will avoid this problem and can be applied for yields as low as 10^2 ions/s. Additionally, if the beam

المنارة للاستشارات

Table 7.1: ISOLDE yields for unknown exotic isotopes that might be accessible with the ROC technique. Estimated (not measured) yields are in round brackets.

A	ISOLDE Yield (ions/μC)	Half life	Target material
^{36}Ca ($Z = 20$)	1	102 ms	Ti
^{37}Ca	15	181 ms	Ti
^{38}Ca	10^4	440 ms	Ti
^{75}Sr($Z = 38$)	2.5	88 ms	Nb
^{76}Sr	8.7 $\times 10^2$	8.9 s	Nb
^{101}Sr	($\sim$ 300)	118 ms	UC_x
^{102}Sr	30	69 ms	UC_x

energy is reduced to $\sim$5 keV before neutralization, the sensitivity would allow measurements for yields of only few ions/s [256, 231]. Of particular interest is the $Z = N$ nucleus $^{76}_{38}Sr_{38}$ [257].
The octupole-correlated nuclei Ba and Ra are of importance to understand the evolution of nuclear properties and test the validity of theoretical models calculations away from the $N = 82$ and $N = 126$ shell closures [258, 259, 260, 261].

7.2 Laser-induced nuclear orientation

A long optical pumping zone and the availability of multiple-step optical pumping can benefit other types of experiment, such as laser-induced nuclear orientation. The long interaction region guarantees a long laser-ion interaction for optical pumping and the possibility for multiple-step optical pumping can be used to maximize the polarization efficiency. In that respect, I have been participating in the design of a new beam line for Versatile Ion-polarized Techniques On-line, VITO, at ISOLDE dedicated to the use of polarized nuclei by laser-induced nuclear orientation. The main components of the new ROC setup will constitute an important part of this new beam line. VITO will make use of the optical pumping region, the charge exchange chamber and optionally the decelerator and β-detector chambers.
For cases were a suitable polarization scheme is found only in the atomic system, a charge exchange cell is required to neutralize the ion beam before the interaction region. β-NMR studies, mostly on liquid (biological) samples, will be part of the main activities that have been planned in the new beam line, and their application to different energy regimes might require post-acceleration or

المنارة للاستشارات

deceleration of polarized beams. More details on the planned experiments and the perspectives for the new beam line are presented in the following article.

7.2.1 Article IV: Perspectives for the VITO beam line at ISOLDE, CERN.

A long optical pumping zone and the availability of multiple-step optical pumping, as developed in this work, can benefit later other types of experiments, such as laser-induced nuclear orientation by optical pumping.

I have written this paper based on a presentation given by me at the Fifteenth International Symposium on Capture Gamma-Ray Spectroscopy and Related Topics (CGS15) (where I replaced Alexander Gottberg as an invited speaker, on his request and that of the VITO collaboration).

المنارة للاستشارات

EPJ Web of Conferences **93**, 07004 (2015)
DOI: 10.1051/epjconf/20159307004
© Owned by the authors, published by EDP Sciences, 2015

Perspectives for the VITO beam line at ISOLDE, CERN

R. F. Garcia Ruiz[1,a], M.L. Bissell[1], A. Gottberg[2], M. Stachura[2,3], L. Hemmingsen[3], G. Neyens[1], N. Severijns[1], and the VITO Collaboration

[1] *Instituut voor Kern- en Stralingsfysica, KU Leuven, Celestijnenlaan 200 D, 3001 Leuven, Belgium*
[2] *CERN, 1211 Geneva 23, Switzerland*
[3] *Kemisk Institut, Københavns Universitet Universitetsparken 5, 2000 København, Denmark*

Abstract. By using polarized ion beams in combination with the β-NMR technique, the Versatile Ion-polarized Techniques On-line (VITO) experiment at ISOLDE, CERN links together expertise from different fields in an unique experimental setup. An overview of the experimental techniques and a general description of the newly designed beam line are presented. Potential uses in multidisciplinary research and perspectives for future experiments are discussed.

1 Introduction

The principle of β-asymmetry detection on polarized nuclei has been established for more than half a century [1]. By implanting polarized nuclei in a medium and subsequent detection of its β-asymmetry, valuable information from either, the nucleus or the implantation medium can be inferred. With the recent developments of radioactive beam line facilities [2], the use of polarized nuclei has opened new opportunities to elucidate unexplored physical phenomena in nuclear structure [3–5], weak interactions studies [6–9] and material sciences [10].
At ISOLDE, CERN [11], polarized nuclei can be obtained by applying one of the commonly used techniques: laser-induced nuclear orientation [12], low temperature nuclear orientation [13], or the tilted foils method in combination with the post-accelerated beams from REX-ISOLDE [14]. Previous experimental programs were mainly focused on nuclear structure [4] and weak interaction studies [15–17]. Only recently, this technique has been applied successfully in the field of chemistry and bio-chemistry [18]. These latest results motivated the foundation of a new dedicated beam line for laser-induced nuclear orientation, currently known as the Versatile Ion-polarized Techniques On-line (VITO) experiment at ISOLDE. Here, we describe the general aspects of the new beam line. The basic principles of the experimental techniques are revised to illustrate its applications in different research fields. Finally, some of the planed experimental programs are briefly described.

2 VITO Beam line

On-line laser-induced nuclear orientation in combination with β-NMR was introduced for the first time at ISOLDE [12]. At present there is only one dedicated beam line for laser-induced nuclear orientation, namely at TRIUMF, Canada [19]. Besides being a unique alternative for users across Europe, VITO will include unprecedented features, such the β-NMR chamber for experiments on liquid samples, and a UHV β-NMR set-up for studies of surfaces and interfaces. The new beam line was proposed as a modification of the former UHV beam line, previously hosting the Apparatus for Surface Physics and Interfaces at CERN (ASPIC) [20]. Two major upgrades are currently under construction; i) an optical pumping zone for laser-induced nuclear orientation, and ii) three end stations for multiple users of polarized beams. The previous ASPIC apparatus is preserved as one of the end stations. A second station will include the recently developed bio β-NMR chamber [21] for experiments in biophysics and chemistry. A third open station, on a straight line, will serve for monitoring the degree of polarization, or for hosting a movable experiment.
A schematic drawing of the new beam line is shown in Figure 1. The mass separated ion beams enter the beam line, where they overlap with a laser beam in a collinear geometry. The ion velocity can be varied by changing the electric potential in the interaction region. Using the Doppler effect, the resonance laser frequency can be scanned across different hyperfine transitions. By using circularly polarized laser light, along with a weak magnetic field (~ 0.4 mT) in the direction of the beam, the quantization axis of the atomic (and nuclear) polarization is defined. For some species, the optical pumping process is desired on the atomic states rather than the ionic states. Therefore, a charge exchange cell filled with a gas of alkali atoms can be used to neutralize the incoming ion beam. Once the atoms interact with the laser beam, and nuclear polarization is achieved, the polarized atoms are re-ionized to be redirected towards the different end stations.

[a] e-mail: RonaldFernando.GarciaRuiz@fys.kuleuven.be

This is an Open Access article distributed under the terms of the Creative Commons Attribution License 4.0, which permits unrestricted use, distribution, and reproduction in any medium, provided the original work is properly cited.

Articleavailableat http .epjconferences.org or httpdx.doi.org10.1051epjconf201530004

المنارة للاستشارات

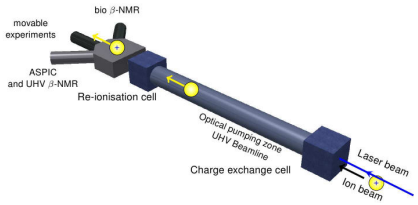

Figure 1. Schematic drawing of the VITO beam line.

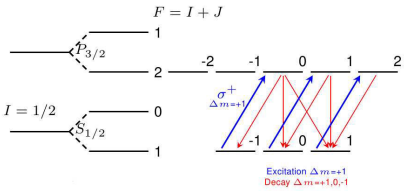

Figure 2. Scheme of optical pumping for a transition $F = 1 \rightarrow F = 2$ with circularly polarized light σ^+.

2.1 Laser-induced nuclear orientation

When atoms or ions interact with circularly polarized laser light σ^+ (σ^-), the absorption process is only allowed following the selection rules $\Delta m_F = +1$ ($\Delta m_F = -1$). Figure 2 shows an example of a hyperfine structure scheme for an atomic transition $S_{1/2} \rightarrow P_{3/2}$ for a nucleus with spin $I = 1/2$. Incident polarized light σ^+ stimulates absorption among the magnetic sub-states of the different hyperfine transitions, e.g, $F = 1 \rightarrow F = 2$. Spontaneous decay can occur following $\Delta m_F = -1, 0, +1$, but the circularly polarized light re-pumps these states with $\Delta m = +1$. As a consequence the total population is transferred to magnetic sub-states with higher magnitude of angular momentum. As the laser-atom interaction is a well known process, the polarization can be predicted with relatively good accuracy [22, 23]. A major advantage of this method is the high degree of nuclear polarization that can be achieved, typically between 10 % and 80 %, depending on the polarization scheme.

2.2 The β-NMR technique

Polarized nuclei can be implanted in a host crystal or a liquid medium for NMR experiments (see Figure 3-a). At the VITO beam line, the ions are electrostatically deflected with 90^o respect to the beam direction, while the initial direction of the polarization axis is preserved. Once the nuclei are implanted, the electron and nuclear spin are decoupled and the nuclear polarization is maintained thanks to a strong magnetic field that is applied along the polarization

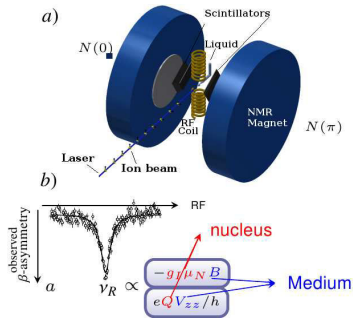

Figure 3. *a*) Sketch of the experimental setup for β-NMR experiments in liquids. *b*) Example of a β-NMR signal (see text for more details).

direction. β particles are emitted following the distribution [24]

$$W(\theta) = 1 + \frac{v}{c} A_\beta P \cos\theta, \tag{1}$$

where P is the nuclear polarization, and A_β is the β-asymmetry parameter, expressed for allowed transitions as

$$A_\beta = \begin{cases} \pm 1 & \text{for } I_f = I_i - 1, \\ \dfrac{\pm\rho^2/(I_i+1) - 2\rho\sqrt{I_i/(I_i+1)}}{1+\rho^2} & \text{for } I_f = I_i, \\ \mp\dfrac{I_i}{I_i+1} & \text{for } I_f = I_i + 1. \end{cases} \tag{2}$$

Where I_i and I_f are the initial and final nuclear spin involved in the β-decay process, respectively. ρ stands for the Gamow-Teller to Fermi mixing ratio, and the upper(lower) sign is for positron(electron) emission.
The experimental β-asymmetry, a, is obtained as the normalized difference between the β particles detected at 0^o, $N(0)$, and the β particles detected at 180^o, $N(\pi)$, given by

$$a = \frac{N(0) - N(\pi)}{N(0) + N(\pi)} \equiv \frac{v}{c} A_\beta P. \tag{3}$$

The splitting into nuclear magnetic sub-states is originating from the interaction between the fields induced by the host material with the nuclear magnetic moment, μ, and the nuclear quadrupole moment, Q. Depending on the implantation medium an electric field gradient, V_{zz}, can be produced at the site of the implanted nuclei. Together with the Zeeman splitting induced by the applied static field and the field of the host, B, a splitting into magnetic sub-levels is created. If an external radio-frequency (RF) magnetic field is applied, transitions among these magnetic sub-levels can be induced, giving rise to a loss of the nuclear spin polarization. A resonant destruction of the nuclear spin polarization can be directly measured by a change of the experimental β-asymmetry as a function of the applied RF-frequency. An example of a β-NMR signal is shown in Figure 3-b. The resonant frequency, ν_R, is a

المنارة للاستشارات

direct measurement of the energy splitting induced by the magnetic and the quadrupole hyperfine interactions and allows us to deduce the Larmor frequency, $\nu_L = -g_I \mu_N B$, or the quadrupole frequency, eQV_{zz}/h.
By measuring the Larmor frequency, ν_L, the nuclear magnetic moment can be obtained, provided that B is known [25]. However, if the nuclear moments are measured independently, the nucleus can be used as a local electromagnetic probe to obtain B and V_{zz} inside the implantation medium [26]. Additional information on the electromagnetic properties of the medium can be obtained by measuring the nuclear polarization as a function of time (spin relaxation [27]) during and after the implantation. On the other hand, the β-asymmetry parameter can be measured (eq. 2) to extract the nuclear spins and parities of ground and excited nuclear states. In addition, when the nuclear spins are established, A_β can be used to obtain ρ^2 [28], which can serve as test of the unitary of the Kobayashi-Maskawa (CKM) quark mixing matrix, via $V_{ud}^2 \propto \left(1 + \frac{f_A}{f_V}\rho^2\right)^{-1}$ [29]. An extension of the experimental methods, plans and perspectives for futures experiments in the VITO beam line are presented in the following sections.

3 First results and opportunities for future experiments

3.1 Biophysics

With the recently developed bio β-NMR chamber [21], the β-NMR technique was for the first time successfully applied to record an NMR spectrum in a solution [18], opening new possibilities for applications in general chemistry and biochemistry. A photograph of the core of the chamber is shown in Figure 4. During the experimental campaign, the chamber was tested at the end of the COLLAPS beam line, but later will be placed as one of the end stations of the VITO Beam line. The experimental setup is illustrated in Figure 3-a. Polarized ^{31}Mg ions were implanted directly into an ionic liquid. By using a RF coil around the implantation point, the external RF frequency was scanned to locate the resonance NMR signals. A MgO crystal was used as a reference sample. Details of the experimental results can be found in Ref. [18].

Two main experimental challenges are faced when liquid samples are used, i) interface between extreme vacuum environments, ranging from 10^{-6} mbar up to few mbar, ii) preservation of the nuclear polarization through the vacuum /liquid interface. An ionic liquid (EMIM-OAc) of very low vapor pressure was used during the experiment to explore systematically the behaviour of ion transmission and nuclear polarization at different pressures. Currently, improvements of the design are ongoing to allow the possibility of using water as solvent, to extend applications to general chemistry and biochemistry. When comparing β-NMR with conventional NMR, both experimental techniques provide similar information: local structure and dynamics at the probe site through detection of chemical shifts and spin relaxation times. The vast difference

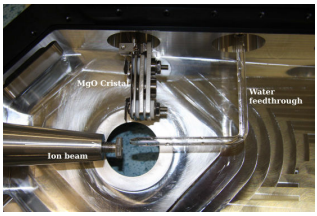

Figure 4. Photograph of the core of the chamber used for β-NMR spectroscopy on liquid samples.

lies in the sensitivity. While $\sim 10^{16}$ atoms are normally required in conventional NMR, only $\sim 10^7$ atoms are needed for β-NMR studies. In addition, the β-NMR can be used for elements which are otherwise difficult to observe spectroscopically in their closed electronic shell oxidation state such as Mg^{2+}, Ca^{2+}, Cu^{+} and possibly Zn^{2+}. These metal ions are ubiquitous in biology with functions in for example electron transport, redox reactions, enzyme catalysis, regulations of gene expression and many other reaction pathways, as well as nucleic acid biochemistry [30]. Conversely, the concentrations of most of these metal ions are maintained at highly regulated levels in cells, and the structure and functions of transmembrane proteins selectively pumping metal ions into or out of cells is a current hot topic [31–33]. Thus, there is a considerable need for spectroscopic methods that may characterize the metal site coordination geometries of these metal ions in biological systems. A letter of intent to explore the technique on these ions [34], and a full proposal to study Mg [35] and Cu [36] have already been accepted at ISOLDE. Experiments are expected to start in 2015.

3.2 Material sciences

Applications of β-NMR spectroscopy for studies on material science are rather well-known [26]. As it was previously mentioned, a nucleus with known electromagnetic properties can be used as an electromagnetic probe to extract the electric and/or magnetic properties of a given implantation or binding state [10, 37]. By controlling the implantation energy, material properties can be explored at nano-metric depths [38, 39]. Magnetic and electric properties can be separated by selecting isotopes with different nuclear spin, e.g, a nucleus with spin $I = 1/2$, and therefore no quadrupole moment, will exhibit a purely magnetic interaction with the host lattice. Furthermore, phenomena at different time scales can be studied by choosing a nucleus with an appropriate lifetime, commonly from few tens of milliseconds up to few seconds.

The previous ASPIC apparatus will be preserved as one of the end stations of the VITO beam line, providing continuity to foregoing experimental programs in the field of surface physics [40–43]. At ASPIC, state-of-the-art techniques are used for *in situ* sample preparation and characterization, to study surfaces, interfaces and layers in

المنارة للاستشارات

a UHV environment ($\sim 10^{-10}$ mbar). Radioactive nuclei are collected from ISOLDE and deposited with thermal energy on the top of the first atomic layer via soft-landing. Afterwards, electromagnetic properties of the sample can be measured using Perturbed Angular Correlation (PAC) spectroscopy [44]. A further development will adapt a chamber for β-NMR studies inside of ASPIC. Combinations of PAC and NMR have been applied in the past as complementary methods (see for example [45] and [46] for nuclear physics and biophysics applications, respectively). Albeit PAC and β-NMR provide similar information, both methods are sensitive to very different time scales. Dynamic properties can be studied in the range of 0.1 to 100 ns using PAC spectroscopy, while in β-NMR the time scale ranges from few hundreds of milliseconds to few seconds.

3.3 Nuclear structure

Polarization by optical pumping and subsequent detection of the β-asymmetry has been extensively used at ISOLDE to obtain nuclear structure information. Nuclear ground states properties as magnetic and quadrupole moments, have been previously measured on different isotopes at the COLLAPS beam line [4, 5, 23, 47, 48]. As it is not the purpose of the VITO experiment, the discussion will only be extended on alternative experiments that can take advantage of particular features of the new beam line, e.g., β-delayed spectroscopy of laser-polarized beams [49].

In addition to the ground state properties, spin and parity of excited states in the β-decay can be obtained by using β-delayed spectroscopy of polarized beams [50]. A scheme of a nuclear decay is shown in Figure 5. Excited states populated in the β-transition can decay either by particle emission (α, β, n), or γ-decay. The value $A_\beta P$ (Eq. 3) for decay to a specific excited state can be obtained by measuring the β-asymmetry in coincidence with the delayed γ-rays (or particles). As the polarization, P, is the same for all transitions, it can be obtained, e.g., by measuring the asymmetry of a pure GT decay branch (for which A_β is known to be 1). As the value A_β depends on the spins of the initial, I_i, and final state, I_f, involved in the transition (Eq. 2). Measuring the β-asymmetry of a particular transition (and thus its A_β) allows unambiguous spin and parity assignments in the daughter nucleus.

In addition to the β-counters normally employed in β-NMR, this technique requires supplementary detector arrays. γ-detectors can be used to tag low lying excited states. An experimental campaign for including such kind of experiments at the VITO beam line is ongoing [34].

3.4 Fundamental weak interaction physics

Testing the unitary of the Cabibbo-Kobayashi-Maskawa (CKM) quark mixing matrix, constitutes an important test to our understanding of the fundamental physics. A deviation from unity indicates the existence of new physics not included in the standard model [28].

The highest precision value of V_{ud}, has been obtained from

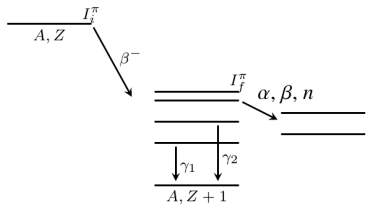

Figure 5. Nuclear decay scheme for β-delayed spectroscopy.

$0^+ \rightarrow 0^+$ super allowed β-decay, $V_{ud} = 0.97425(22)$ [51]. An alternative method to obtain an independent high precision value of V_{ud} was suggested from $T = 1/2$ nuclear mirror transitions [52]. As it was noticed (Eq. 2), for β-decay transitions with $I_i = I_f$, the β-asymmetry depends on the Gamow-Teller to Fermi mixing ratio, ρ. If the corrected Ft-value is known for the same transition, a measurement of ρ can be used to evaluate the matrix element V_{ud}, via [52]

$$V_{ud}^2 = \frac{2\pi^3\hbar \ln 2}{m_e c^2} \frac{1}{FtG_F^2(1+\Delta_R^V)} \left(1 + \frac{f_A}{f_V}\rho^2\right)^{-1}, \quad (4)$$

with m_e the electron mass, c speed of light, and G_F the Fermi constant [53]. f_V and f_A are the statistical rate functions for the vector and axial-vector part of the interaction. A radiative correction, Δ_R^V, should be applied for the respective transition [54]. In mirror transitions, V_{ud} is highly sensitive to the value of ρ. A special example is found in ^{35}Ar [55], where it was shown that a relative precision of 0.5 % on the β-asymmetry parameter, allows for a determination of V_{ud} with a relative precision of $\sim 0.07\%$. This is an impressive result, considering that in a single measurement, the obtained uncertainty is only three times less that the uncertainty of the average value extracted from the entire set of high precision measurements from super allowed $0^+ \rightarrow 0^+$ transitions.

The value $A_\beta P$ can be directly obtained from the experimental β-asymmetry (Eq. 2). Nevertheless, a precise determination of ρ relies on the precise measurement of both A_β and P. High precision measurements of such quantities impose experimental challenges on the development of laser polarization schemes, choice of suitable implantation crystals, and methods to determine the total polarization efficiency. A current project to measure the β-asymmetry parameter of ^{35}Ar has been proposed at the VITO beam line [29].

4 Conclusions

Spin-polarized beams of radioactive species represent a powerful tool to explore a large variety of physical phenomena. Versatility has been the key factor of the newly designed VITO beam line at ISOLDE. Using laser-induced nuclear orientation in combination with β-NMR opens the possibility of performing experiments in a broad

المنارة للاستشارات

spectrum of disciplines. Furthermore, a novel experimental setup was developed to apply β-NMR directly in liquid samples. This setup will allow the study of ions that are difficult to study by other spectroscopic techniques.
Thanks to the first successful results and the joint effort among experts from different fields at ISOLDE, a comprehensive experimental program is being prepared to benefit scientific research in biophysics, material sciences, nuclear structure and weak interaction physics.

Acknowledgments

This work was supported by the IAP-project P7/12, the FWO-Vlaanderen, the NSF grant PHY-1068217, BMBF(05 P12 RDCIC), the Danish Center for Scientific Computing for resources, and the Danish Council for Independent Research and Natural Sciences.

References

[1] C.S. Wu *et al*, Phys. Rev. **105**, 1413 (1957)
[2] Y. Blumenfeld *et al*, Phys. Scr. **T152**, 014023 (2013)
[3] W. Geithner *et al*, Phys. Rev. Lett. **83**, 3792 (1999)
[4] G. Neyens *et al*, Phys. Rev. Lett. **94**, 022501 (2005)
[5] R. Neugart *et al*, Phys. Rev. Lett. **101**, 132502 (2008)
[6] G. Soti *et al*, Phys. Rev. C **90**, 035502 (2014)
[7] A. Etile *et al*, EPJ Web Conf. **66**, 02034 (2014)
[8] J.R.A. Pitcairn *et al*, Phys. Rev. C **79**, 015501 (2009)
[9] D. Melconian *et al*, Phys. Lett. B **649**, 370 (2007)
[10] Z. Salman *et al*, Phys. Rev. Lett. **109**, 257207 (2012)
[11] A. Herlert *et al*, Nucl. Phys. News **20**, 5 (2010)
[12] E. Arnold *et al*, Phys. Lett. B **197**, 311 (1987)
[13] J. Wouters *et al*, Hyp. Int. **59**, 59 (1990)
[14] H. Tornqvist *et al*, Nucl. Inst. Meth. B **317**, 685 (2013)
[15] N. Severijns *et al*, Phys. Rev. Lett. **63**, 10 (1989)
[16] F. Wauters *et al*, Phys. Rev. C **82**, 055502 (2010)
[17] J.R. Stone *et al*, Phys. Rev. C **76**, 025502 (2007)
[18] A. Gottberg *et al*, Accepted in Chem. Phys. Chem. (2014)
[19] K.H. Chow *et al*, Physica B **340**, 1151 (2003)
[20] H.H. Bertschat *et al*, Hyp. Int. **129**, 475 (2000)
[21] A. Gottberg *et al*, In preparation (2014)
[22] M. Keim *et al*, Eur. Phys. J. A **8**, 31 (2000)
[23] M. Kowalska *et al*, Phys. Rev. C **77**, 034307 (2008)
[24] N. Stone and H. Postma, *Low-temperature Nuclear Orientation* (Elsevier, Amsterdam , 1986)
[25] G. Neyens *et al*, Rep. Prog. Phys. **66**, 633 (2003)
[26] B. Ittermann *et al*, Hyp. Int. **79**, 591 (1993)
[27] Z. Salman *et al*, Phys. Rev. B **70**, 104404 (2004)
[28] N. Severijns *et al*, Rev. Mod. Phys. **78**, 991 (2006)
[29] Ph. Velten *et al*, CERN-INTC-2014-062 / INTC-P-426 (2014)
[30] I. Bertini *et al*, *Biological inorganic chemistry - structure reactions* (University Science Books, 2007)
[31] M. Lu and D. Fu, Science **317**, 5845 (2007)
[32] M. Hattori *et al*, Nature **448**, 1072 (2007)
[33] P. Gourdon *et al*, Nature **475**, 59 (2011)
[34] M. Deicher *et al*, CERN-INTC-2013-013 / INTC-O-017 (2013)
[35] M. Stachura *et al*, CERN-INTC-2013-033 / INTC-P-392 (2013)
[36] M. Stachura *et al*, CERN-INTC-2013-034 / INTC-P-393 (2013)
[37] Z. Salman *et al*, Nano Lett. **7**, 1551 (2007)
[38] G.D. Morris *et al*, Phys. Rev. Lett. **93**, 157601 (2004)
[39] Z. Salman *et al*, Phys. Rev. Lett. **98**, 167001 (2007)
[40] H.H Bertschat *et al*, Phys. Rev. Lett. **78**, 342 (1997)
[41] H.H Bertschat *et al*, Phys. Rev. Lett. **80**, 2721 (1998)
[42] W. Weber *et al*, Phys. Rev. B **64**, 081404 (2001)
[43] H. Granzer *et al*, Phys. Rev. Lett. **77**, 4261 (1996)
[44] H. Frauenfelder and R.M. Steffen, *Alpha-, Beta- and Gamma-Ray Spectroscopy* (Siegbahn, North-Holland, 1968)
[45] N. Brauer *et al*, Z. Physik **244**, 375 (1971)
[46] L. Hemmingsen *et al*, J. Am. Chem. Soc. **123**, 10329 (2001)
[47] D. Yordanov *et al*, Phys. Rev. Lett. **99**, 212501 (2007)
[48] D. Yordanov *et al*, Phys. Rev. Lett. **108**, 042504 (2012)
[49] D. Yordanov *et al*, CERN-INTC-2010-021 / INTC-I-090 (2010)
[50] H. Miyatake *et al*, Phys. Rev. C **67**, 014306 (2003)
[51] I. S. Towner and J. C. Hardy *et al*, Rep. Prog. Phys. **73**, 046301 (2010)
[52] O. Naviliat-Cuncic and N. Severijns *et al*, Phys. Rev. Lett. **102**, 142302 (2009)
[53] C. Amsler *et al*, Phys. Lett. B **667**, 1 (2008)
[54] W.J. Marciano *et al*, Phys. Rev. Lett. **96**, 032002 (2006)
[55] N. Severijns *et al*, Physica Scripta **T152**, 014018 (2013)

المنارة للاستشارات

المنارة للاستشارات

Chapter 8

Conclusions

By combining state-of-the-art experiments and theory, this work is an effort to understand some of properties of the many-body problem manifested in the details of nuclear structure of the neutron-rich Ca isotopes.
A first experimental campaign used high-resolution bunched-beam collinear laser spectroscopy to measure the optical hyperfine-structure spectra of the $^{43-51}$Ca isotopes. From these results the ground-state magnetic moments of ^{49,51}Ca and quadrupole moments of ^{47,49,51}Ca were measured for the first time, and the ^{51}Ca ground-state spin $I = 3/2$ was determined in a model-independent way. The ground-state electromagnetic moments were compared with shell-model calculations using both phenomenological interactions and microscopic interactions derived from chiral effective field theory. The experimental results for the neutron-rich isotopes are in excellent agreement with predictions from valence-space interactions derived from chiral effective ïňĄeld theory including three-nucleon forces. Lighter isotopes, on the other hand, illustrate the presence of particle-hole excitations of the ^{40}Ca core in their ground state. The main results on the measurements of electromagnetic moments and the comparison with different shell-model calculations were reported in Article I.
The isotope shift extracted from the hfs spectra allowed determining the charge radii of ^{49,51,52}Ca for the first time, extending the picture of the evolution of charge radii over the three previously suggested shell closures at $N = 20$, $N = 28$ and $N = 32$. The results revealed that the charge radius of ^{52}Ca is larger than the value expected for a doubly-magic nucleus.

A separate discussion was presented by comparing the charge radii results with different theoretical calculations. Special emphasis was done on state-of-the-art *ab initio* calculations based on coupled-cluster theory. None of the available

المنارة للاستشارات

calculations can describe the relative increase of the rms charge radius of ^{52}Ca relative to ^{48}Ca, raising new questions about our understanding of the evolution of nuclear properties far away from stability

These results represent a major challenge in the search of a unified description of the atomic nucleus, which is also necessary to obtain a reliable description of neutron-rich matter. The charge radii measurements and the comparison with the different calculations are reported in Article II.

To extend our experimental knowledge beyond ^{52}Ca, a sensitive experimental setup has been designed. This new experimental apparatus is based on optical pumping and followed by radioactive detection of particles, and state selective neutralization, named the ROC technique. Although the technique was successfully applied a long time ago [17], several shortcomings were identified to improve considerably the limits of sensitivity, allowing the applicability of this technique to Ca isotopes with production yields of only few ions/s.
Numerical calculations for the laser-ion interaction allowed the determination of the optimum length of the optical-pumping region and the number of pumping steps required to maximize the pumping efficiency into the metastable states. The necessary ion-beam optical components and the respective dimensions of the different beam line components were explored through ion-beam simulations. These calculations and simulations were used to choose the optimum design and dimensions of each beam line component. The details of the experimental methods, the commissioning of the new setup, and the first experimental tests related to the comissioning of the beam line are reported in Article III.

Finally, several perspectives and future plans are expected to continue with the utilization of the newly-designed experimental setup. Most of the new beam line components will form part of the (still in development) VITO beam line at ISOLDE. An overview of the planned experiments and the perspectives for the use of laser-induced polarized nuclei were reported in Article IV.

المنارة للاستشارات

المنارة للاستشارات

Appendix A

Appendix

A.1 Collinear laser spectroscopy

To illustrate the principle of collinear laser spectroscopy, let us start by studying a gas of ions in a tunable laser field. When the laser frequency is on resonance with one of the ionic levels, the ions will start absorbing and emitting photons with the same wavelength. If we suppose a gas of ions at temperature T, and individual mass m, the Doppler broadening effect observed on the emitted photons is given by

$$\delta\omega = 2\sqrt{\ln 2}\omega_0 \frac{\delta v}{c}, \tag{A.1}$$

where ω_0 is the resonance frequency, and δv is the velocity difference between an ion energy $E_1 = 0$, and an ion with termal energy $E_2 = K_B T$, expressed as

$$\delta v = v_2 - v_1 = \sqrt{\frac{2K_B T}{m}}. \tag{A.2}$$

The ion mass, M_I, can be extracted from the atomic mass M_A by using the expression

$$M_A c^2 + E_i = m_e c^2 + M_I c^2, \tag{A.3}$$

where m_e is the mass of the electron, and E_i the ionization energy.
In the literature it is common to find the mass excess value, ΔM, which is equal to the difference between the atomic mass, m_a, and the atomic weight, $A.u$, that is

$$\Delta m_a = m_a - A.u, \tag{A.4}$$

where $u = 931.494061$ MeV$/c^2$ is the atomic mass unit.

المنارة للاستشارات

If we now introduce the gas inside a potential difference V, an additional energy eV (for single ionized ion) is added to each ion. Consequently, the new velocity difference, $\delta v'$, between the same particles will be given by

$$\delta v' = \sqrt{\frac{2(K_B T + eV)}{m}} - \sqrt{\frac{2(eV)}{m}} = \sqrt{\frac{2eV}{m}}\left[\left(1 + \frac{K_B T}{eV}\right)^{1/2} - 1\right]. \quad \text{(A.5)}$$

When the condition $k_B T \ll eV$ is satisfied, the energy spread is approximately

$$\delta v' \approx \frac{1}{2}\sqrt{\frac{K_B T}{eV}}\delta v. \quad \text{(A.6)}$$

A quantification of this effect can be calculated by inserting A.6 in A.1

$$\delta\omega' = \frac{\omega_0 K_B T}{c}\sqrt{\frac{2\ln 2}{eV.m}}. \quad \text{(A.7)}$$

It follows that if the external potential V is chosen properly, the Doppler broadening for photon emission can be reduced down to the natural width. This is the main advantage of collinear laser spectroscopy. By superimposing an ion beam with a laser beam in a collinear geometry, the energy spread of the emission process is reduced, and a high resolution measurement of the hyperfine spectra can be achieved. Notice that the frequency seen by the ion beam will be shifted by

$$\nu = \nu_0 \frac{1 \pm \beta}{\sqrt{1 - \beta^2}}. \quad \text{(A.8)}$$

With ν_0 the laser frequency in the laboratory frame, and the factor β expressed as

$$\beta = \sqrt{1 - \frac{1}{\left(\frac{eV}{mc^2} + 1\right)^2}}. \quad \text{(A.9)}$$

Hence, instead of changing the laser frequency, it is convenient to change the ion velocity by tuning the external potential. During a typical collinear laser spectroscopy experiment, the HFS spectrum is measured by observing the emitted photons as a function of the external potential (Doppler-tuning voltage).

A.2 Line shapes in fluorescence spectroscopy

The line shape observed in collinear laser spectroscopy can be described by the convolution between a Gaussian distribution associated to the Doppler

المنارة للاستشارات

broadening

$$G(x;\sigma) = \frac{1}{\sigma\sqrt{2\pi}} e^{-\frac{x^2}{2\sigma^2}}, \tag{A.10}$$

and the power broadening described by a Lorentzian distribution

$$L(x;\Gamma_L) = \frac{1}{\pi} \frac{\Gamma_L/2}{x^2 + (\Gamma_L/2)^2}, \tag{A.11}$$

resulting in a Voigt distribution

$$V(x;\sigma,\Gamma) = \int_{-\infty}^{\infty} G(t;\sigma) L(x-t;\Gamma_L) dt, \tag{A.12}$$

Inelastic collisions can reduce the ion beam energy, resulting in asymmetric Voigt profiles. For higher pressures, multiple collisions can occur and the line shape is defined by the combination of multiple-Voigt functions [262]. This effects appears notably when vapor cells are used to neutralize the ion beam [263]. As described in [263] the collision among ions (atoms) can be represented by a Poisson distribution. Consequently, multiple side peaks can contribute to the line shape, with amplitudes given by

$$P(n) = \frac{x^n}{n!} e^{-x}, \tag{A.13}$$

where n is the peak number, and x the Poisson parameter determined from the fit to the experimental data. The distance between two successive peaks depends on the transition energy of the ionic (atomic) states populated in the collision. For the different fits, this distance was fixed to account for a 3.1 eV energy difference, corresponding to the average energy value of the low-lying excited states of Ca^+. An example of a fit using multiple side peaks is shown in Figure A.1.

المنارة للاستشارات

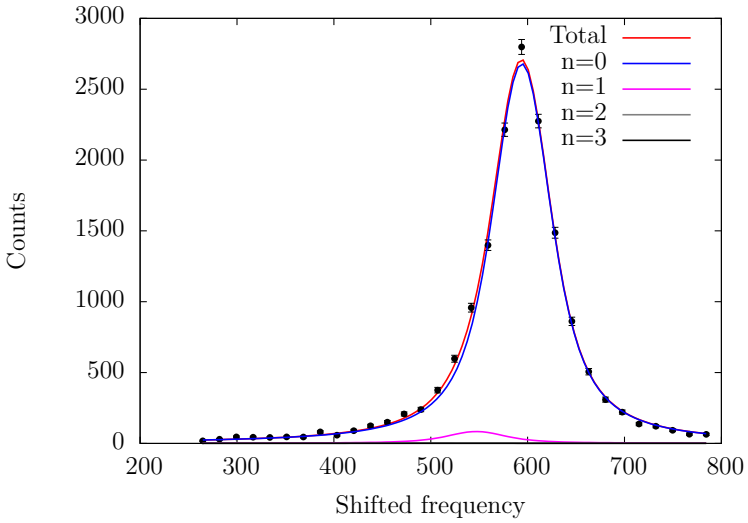

Figure A.1: Example of a fit with multiple side peaks on ^{40}Ca. Without side peaks a value of $\chi^2 = 3.2$ is obtained. When side peaks are included (red) the fit converges with a value of $\chi^2 = 2.5$.

المنارة للاستشارات

A.3 Literature values of hyperfine structure constants and ground-state electromagnetic moments of Ca isotopes

Table A.1: Selected values of hfs constants, B, reported for Ca isotopes.

A	Ca	Transition	B (MHz)	Exp	Ref.
41	I	$4s^{21}S_0 - 4s4p^3P_1$	$B(^3P_1) = 4.0(3)$	LS	[55]
	I	$4s4p^1P_1$	$B(^3P_1) = 4.337(27)$	LS+RF	[206]
	I	$4s^{21}S_0 - 4s4d^1D_2$	$B(^1D_2) = -0.4(6)$	LS	[18]
43	I	$4s4p^3P_2 - 4s5s^3S_1$	$B(^3P_2) = -5.436(8)$	ABMR+LS	[53]
	I	$4s^{21}S_0 - 4s4p^3P_1$	$B(^3P_1) = 2.6(4)$	LS	[55]
	I	$4s^{21}S_0 - 4s4p^3P_1$	$B(^3P_1) = 2.300(2)$	LS+RF	[56]
	I	$3d4s^1D_2 - 4s5p^1P_1^0$	$B(^1D_2) = -4.642(12)$	ABMR-LIRF	[264]
	I	$4s4p^1P_1$	$B(^3P_1) = 2.660(11)$	LS+RF	[206]
	II	$4s^2S_{1/2} - 4p^2P_{3/2}$	$B(^2P_{3/2}) = -6.7(1.4)$	LS	[15]
	II	$3d^2D_{3/2} - 4p^2P_{3/2}$	$B(^2P_{3/2}) = -6.9(1.7)$	LS	[204]
		$3d^2D_{5/2} - 4p^2P_{3/2}$			
	I	$4s^{21}S_0 - 4s4p^1P_1$	$B(^1P_1) = -3.48(13)$	LS	[18]
	II	$4s^2S_{1/2} - 3d^2D_{5/2}$	$B(^2D_{5/2}) = -4.241(4)$	RF-Trap	[265]
45	I	$4s^{21}S_0 - 4s4p^3P_1$	$B(^3P_1) = -2.8(7)$	LS	[55]
	I	$4s^{21}S_0 - 4s4p^1P_1$	$B(^1P_1) = 1.8(5)$	LS	[14]
	I	$4s4p^1P_1$	$B(^3P_1) = -2.5(7)$	LS+RF	[206]
47	I	$4s^{21}S_0 - 4s4p^1P_1$	$B(^1P_1) = 4.1(6)$	LS	[14]

المنارة للاستشارات

Table A.2: Reported quadrupole moments for Ca isotopes.

A	Q (b)	Ref.	Comments
41	-0.080(8)	[206]	Calculated EFG with experimental result $B(^3P_1) = 4.337(27)$ MHz.
	-0.066(2)	[207]	EFG is calculated for $^1D_2$ to obtain $Q(^{43}\mathrm{Ca})$ from $B(^1D_2) = -4.642(12)$ MHz [264]. $Q(^{41}\mathrm{Ca})$ is obtained using recalculated $Q(^{43}\mathrm{Ca})$ and ratio $B(^{41}\mathrm{Ca})/B(^{43}\mathrm{Ca})$=1.63(1) [206]
	-0.090(2)	[266]	Similar to Ref. [207], the EFG is calculated for $^1D_2$ to obtain $Q(^{43}\mathrm{Ca})$ from $B(^1D_2) = -4.642(12)$ MHz [264] and $Q(^{41}\mathrm{Ca})$ is obtained from the ratio $B(^{41}\mathrm{Ca})/B(^{43}\mathrm{Ca})$=1.63(1) [206]
43	-0.065(20)	[53]	Calculated EFG and their experimental result $B(^3P_2) = -5.436(8)$ MHz.
	-0.049(5)	[206]	Calculated EFG and their experimental result $B(^3P_1) = 2.660(11)$ MHz.
	-0.0408(8)	[207]	From EFG calculated for $^1D_2$ and experimental $B(^1D_2) = -4.642(12)$ MHz [264]
	-0.0552(11)	[266]	From EFG calculated for $^1D_2$ and experimental $B(^1D_2) = -4.642(12)$ MHz [264]
	-0.043(9)	[15]	Using their experimental value $B(^2P_{3/2}) = -6.7(1.4)$ MHz and calculated EFG.
45	0.046(14)	[206]	Calculated EFG and their experimental result $B(^3P_1) = -2.5(7)$ MHz.

المنارة للاستشارات

A.4 Nuclear mean-squared charge radii of Ca region

Table A.3: Literature values of the root-mean squared charge radii, $\langle r^2 \rangle$, of Ca isotopes.

$\langle r^2 \rangle^{A,40}$	[fm^2]	Ref.
39	-0.127(16)	[59]
41	0.0032(25)	[60]
42	0.2153(49)	[60]
43	0.124(31)	[17]
44	0.280(14)	[17]
45	0.126(18)	[17]
46	0.123(15)	[17]
47	-0.022(20)	[17]
48	-0.022(20)	[17]
50	0.273(37)	[17]

المنارة للاستشارات

A.5 Configuration Mixing

The appearance of cross terms involving admixtures between spin-orbit partners, $j_< = l - 1/2$ and $j_> = l + 1/2$, cause large deviations to the magnetic moment. These contributions were explicitly suggested in the pioneering work of Arima and Horie [267]. To first order in perturbation theory the amount of mixing is then proportional to the spin-orbit splitting [268]. Here we present a short summary for the mixing of three nucleons, and the influence of the spin-orbit partner is illustrated for the ground-state wave function of ^{51}Ca.

A.5.1 Useful relations

The magnetic moment of one state, μ, is defined as

$$\mu = \langle I, M = I | \boldsymbol{\mu_z} | I, M = I \rangle. \tag{A.14}$$

Using the notation from [269], the coupling of two wave function ψ_{I_1} and ϕ_{I_2}, with angular momentum I_1 and I_2, respectively, is given by

$$(\psi_{I_1} \times \phi_{I_2})_{IM} = \sum_{M_1 M_2} \langle I_1 I_2 M_1 M_2 | IM \rangle \psi_{I_1 M_1} \phi_{I_2 M_2} \tag{A.15}$$

where I is the total angular momentum, with projection M.
For the coupling of three angular momenta

$$((\psi_{I_1} \times \phi_{I_2})_{I_{12}} \times \gamma_{I_3})_{IM} = \sum_K \sqrt{(2I_{12}+1)(2K+1)} W(I_1 I_2 I I_3 : I_{13} K)(\psi_{I_1} \times (\phi_{I_2} \times \gamma_{I_3})_{I_{34}})_{IM}, \tag{A.16}$$

where $W(I_1 I_2 I I_3 : I_{13} K)$ are the Racah coefficients, which can be expressed in term of the 6j symbols as

$$W(j_1 j_2 j_4 j_3 : JK) = (-1)^{j_1+j_2+j_3+j_4} \begin{Bmatrix} j_1 & j_2 & J \\ j_3 & j_4 & K \end{Bmatrix}. \tag{A.17}$$

If we have n particles in the state j, coupling to IM, the wave function can be singled out using the relation ([269], pag 477)

$$\Psi_{IM\alpha}(1, ..., n) = \sum_{J\beta} \langle j^{n-1} J\beta, j | \} j^n I\alpha \rangle (\Phi_{J\beta}(1, ..., n-1) \times \phi(n))_{IM}, \tag{A.18}$$

where α indicates the additional quantum numbers required to specify the state, and $\langle j^{n-1} J\beta, j | \} j^n I\alpha \rangle$ are the fractional-parentage coefficients.

المنارة للاستشارات

A.5.2 Three valence neutron configurations

The evaluation of the magnetic matrix elements for a three-nucleon configuration occupying the same orbital j, are taken from the results of Levinson and Ford [270]:

$$\langle((\nu j)^3_I, I|\boldsymbol{\mu_z}|((\nu j)^3_I, I\rangle = g_j I, \tag{A.19}$$

where

$$g_j = g_l \pm \frac{(g_s - g_l)}{2j + 1 \mp 1}, \text{ and } j = l \pm \frac{1}{2}. \tag{A.20}$$

$$\begin{aligned}\langle((\nu j_1)^2_J \times (\nu j_2))_I|\boldsymbol{\mu_z}|((\nu j_1)^2_J \times (\nu j_2))_I\rangle = \frac{1}{2(I+1)}\Big[&g_{j_1}[I(I+1) + J(J+1) \\ &- j_2(j_2+1)]] \\ &+ g_{j_2}[I(I+1) - J(J+1) + j_2(j_2+1)]\Big]^{1/2},\end{aligned} \tag{A.21}$$

$$\begin{aligned}\langle((\nu j_1)^3_I|\boldsymbol{\mu_z}|((\nu j_1)^2_J \times (\nu j_2))_I\rangle = &-\langle j_1^2(J) j_1 I|\}j_1^3 I\rangle \frac{(g_s - g_l)}{2(2l+1)(I+1)}\delta_{l_1,l_2} \\ &\times \Big[3(J + I + l + 3/2)(J + I - l + 1/2) \\ &(J - I + l + 1/2)(I - J + l + 1/2)\Big]^{1/2},\end{aligned} \tag{A.22}$$

A.5.3 Ground state wave function of ^{51}Ca

Assuming a ground state wave function given by

$$|^{51}\text{Ca}, I = 3/2^-\rangle = a|(\nu p^3_{3/2})_{3/2}\rangle + b|[(\nu p^2_{3/2})_2(\nu p^1_{1/2})]_{3/2}\rangle + c|[(\nu p^2_{3/2})_2(\nu f^1_{5/2})]_{3/2}\rangle, \tag{A.23}$$

المنارة للاستشارات

with a, b and c the mixing coefficients, such that $|a|^2+|b|^2+|c|^2 = 1$. Therefore, the ground state magnetic moment is given by

$$\langle {}^{51}\mathrm{Ca}, I = 3/2^- | \boldsymbol{\mu} | {}^{51}\mathrm{Ca}, I = 3/2^- \rangle = |a|^2 \langle (\nu p^3_{3/2})_{3/2} | \boldsymbol{\mu} | (\nu p^3_{3/2})_{3/2} \rangle \tag{A.24a}$$

$$+ |b|^2 \langle [(\nu p^2_{3/2})_2 (\nu p^1_{1/2})]_{3/2} | \boldsymbol{\mu} | [(\nu p^2_{3/2})_2 (\nu p^1_{1/2})]_{3/2} \rangle \tag{A.24b}$$

$$+ (a^* b + b^* a) \langle [(\nu p^2_{3/2})_2 (\nu p^1_{1/2})]_{3/2} | \boldsymbol{\mu} | (\nu p^3_{3/2})_{3/2} \rangle \tag{A.24c}$$

$$+ |c|^2 \langle [(\nu p^2_{3/2})_2 (\nu f^1_{5/2})]_{3/2} | \boldsymbol{\mu} | [(\nu p^2_{3/2})_2 (\nu f^1_{5/2})]_{3/2} \rangle \tag{A.24d}$$

$$+ (a^* c + c^* a) \langle (\nu p^3_{3/2})_{3/2} | \boldsymbol{\mu} | [(\nu p^2_{3/2})_2 (\nu f^1_{5/2})]_{3/2} \rangle \tag{A.24e}$$

$$+ (b^* c + c^* b) \langle [(\nu p^2_{3/2})_2 (\nu p^1_{1/2})]_{3/2} | \boldsymbol{\mu} | [(\nu p^2_{3/2})_2 (\nu f^1_{5/2})]_{3/2} \rangle \tag{A.24f}$$

Using the free g-factor values for neutrons, $g_l = 0$, and $g_s = -3.826$ in the expression A.19

$$\langle (\nu p^3_{3/2})_{3/2} | \boldsymbol{\mu} | (\nu p^3_{3/2})_{3/2} \rangle = \frac{g_s}{2}. \tag{A.25}$$

And from A.21

$$\langle [(\nu p^2_{3/2})_2 (\nu p^1_{1/2})]_{3/2} | \boldsymbol{\mu} | [(\nu p^2_{3/2})_2 (\nu p^1_{1/2})]_{3/2} \rangle = \frac{7}{10} g_s. \tag{A.26}$$

The cross terms in A.24c is calculated from A.22

$$\langle [(\nu p^2_{3/2})_2 (\nu p^1_{1/2})]_{3/2} | \boldsymbol{\mu} | (\nu p^3_{3/2})_{3/2} \rangle = -\frac{\sqrt{10}}{5} g_s. \tag{A.27}$$

The expression A.21 is used to calculate the term A.24c

$$\langle [(\nu p^2_{3/2})_2 (\nu f^1_{5/2})]_{3/2} | \boldsymbol{\mu} | [(\nu p^2_{3/2})_2 (\nu f^1_{5/2})]_{3/2} \rangle = -\frac{5}{42} g_s. \tag{A.28}$$

The cross term A.24e and A.24f are zero, since for these terms we have $\delta_{ll'} = 0$ and $\delta_{jj'} = 0$.

المنارة للاستشارات

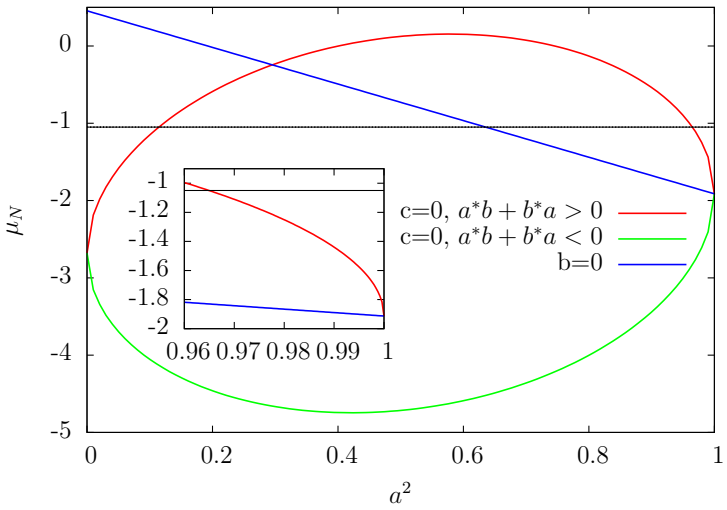

Figure A.2: Magnetic moment obtained from the expression A.29 as a function of the value $|a|^2$. In blue color the values assuming mixing with $f_{7/2}$ only ($|b| = 0$), and with red and green colors assuming the mixing is only with $p_{1/2}$ ($|c| = 0$). The huge sensitivity of the magnetic moment to the configuration mixing is mainly associated to the off-diagonal term [1]

Therefore, from A.25, A.26, A.27 and A.28, the magnetic moment for the wave function assumed in A.23, is given by

$$\langle {}^{51}\mathrm{Ca}, I = 3/2^- | \boldsymbol{\mu} | {}^{51}\mathrm{Ca}, I = 3/2^- \rangle = g_s \left[\frac{1}{2}|a|^2 + \frac{7}{10}|b|^2 - \frac{5}{42}|c|^2 - \frac{\sqrt{10}}{5}(a^*b + b^*a) \right] \tag{A.29}$$

A.6 Article III: Design of a sensitive setup for collinear laser spectroscopy at ISOLDE, CERN.

المنارة للاستشارات

A sensitive setup for collinear laser spectroscopy experiments at ISOLDE, CERN

R. F. Garcia Ruiz[a], M. Bissell[a], K. Blaum[b], C. Georges[d], W. Gins[a], H. Heylen[a], K. Lars Koenig[d], S. Kaufmann[d], M. Kowalska[c], J. Kraemer[d], S. Malbrunot[c], R. Neugart[b,d], G. Neyens[a], W. Nörtershäuser[d,e], D. T. Yordanov[1], X. Yang[a]

[a]*Instituut voor Kern-en Stralingsfysica, KU Leuven, B-3001 Leuven, Belgium*
[b]*Max-Plank-Institut fr Kernphysik, D-69117 Heidelberg, Germany*
[c]*CERN, European Organization for Nuclear Research, Physics Department, CH-1211 Geneva 23, Switzerland*
[d]*Institut fr Kernchemie, Universitt Mainz, D-55128 Mainz, Germany*
[e]*Institut fr Kernphysik, TU Darmstadt, D-64289 Darmstadt, Germany*

Abstract

An experimental setup for sensitive high-resolution measurements of hyperfine structure spectra of exotic isotopes was developed and commissioned at ISOLDE, CERN. The principle of the technique was previously demonstrated with measurements of exotic Ca isotopes produced at rates of $\sim 5\times10^4$ ions/s[1]. Here we report the improvements and new developments necessary to reach the sensitivity limits of the experimental technique, which would allow measurements of ground-state nuclear moments, spin and rms charge radii of exotic isotopes produced at rates of only few ions/s. Numerical calculations of laser-ion interaction and ion beam simulations were explored to obtained the optimum performance of the experimental setup. Among the implemented features, the new experimental apparatus includes a multi-step optical pumping region for measurements of hyperfine-split isotopes, a high-voltage platform for adequate control of low energy beams, and high efficiency β-detector setups for simultaneous β-detection of neutralized and unreacted isotopes. The commissioning of the experimental setup, and the first successful experimental tests are presented.

Keywords:

1. Introduction

The recent developments of radioactive ion beam facilities [2] have allowed to investigate nuclei far from stability, elucidating new physical phenomena not observed in stable nuclei [3, 4, 5]. Although a deeper understanding of the atomic nucleus has been reached by a joint effort between theoreticians and experimentalists, key questions remains unresolved far way from stability, where radioactive isotopes can only be produced at very low rates (<100 ions/s). Therefore, high sensitivity techniques are required to access such region of the nuclear chart.

Laser spectroscopy techniques have been widely used to extract nuclear structure information on the ground state properties of exotic nuclei [6, 7]. Nuclear moments, spins and changes in the mean squared charge radii can be measured in a model independent way [8]. One of the most common high resolution laser spectroscopic technique is based on optical detection. An ion beam overlaps a laser beam in a collinear geometry, and by changing the ion velocity, and hereby Doppler tuning the laser frequency in the atom rest frame, the transitions energy among different atomic hyperfine structure levels can be measured by detecting the fluorescent photons as function of the ion velocity [9].

Although a resolution of the order of the natural linewidth can be reach by optical detection, the overall sensitivity is reduced by the intrinsic efficiency associated to photo-detection [10]. Currently, high sensitivity experimental arrays have showed that the applicability of optical detection is limited to minimum yields of $\sim 10^3$ ions/s [11]. However, higher sensitivity can be achieved by using alternative schemes based on particle detection [12, 13, 14, 15, 16]. Such experimental approaches have been successfully applied on Ca [1], Sr [17, 18, 19], Xe [20], Kr [21] and Fr [22] isotopes.

By using optical detection techniques, a successful research program at COLLAPS-ISOLDE beam line has been focus on study the nuclear structure evolution on Ca isotopes. The optical hyperfine structure spectra and isotope shifts were measured up to ^{52}Ca. From these new experimental results, changes in the rms charge radii up to ^{52}Ca [23] and the ground state electromagnetic moments of ^{49,51}Ca [24] were determined for the first time. With production yields of less than $\sim$ 100 ions/s and $\sim$ 10 ions/s for ^{53}Ca and ^{54}Ca, respectively, these isotopes are beyond the limits of optical detection. With the aim of extending these measurements to ^{53}Ca and ^{54}Ca, this works present some of the technical developments necessary to implement a sensitive particle detection scheme [1].

The experimental method and the detection scheme are introduced in the fist section 2. A detailed explanation of the beam line and the ion beam optics simulations used to analyze and choose the proper design of each beam line component are presented in the section 5. Finally, the first successful experimental test are presented in section 8.

المنارة للاستشارات

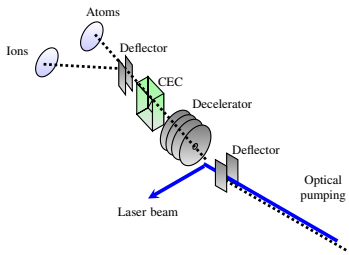

Figure 1: Layout of the experimental scheme. The method cover three main steps; *optical pumping, state-selective charge exchange*, and *radioactive detection of atoms/ions*.

2. Experimental method

The radioactive detection of optically pumped ions after state selective charge exchange (ROC) technique was proposed as a sensitive method to study the ground-state properties of exotic nuclei far from stability [1]. A layout of the experimental scheme is shown in figure 1. It consists of three main processes; *optical pumping, state-selective charge exchange*, and *radioactive detection*. First, the ions in the ground state are resonantly excited to a short-lived excited state, and subsequent spontaneous decay from this level populates a low-lying metastable state in the Ca ion (see Figure 1). An efficient population of the metastable state is achieved by superimposing the laser and the ion beam in collinear geometry along a sufficiently long optical pumping region. Afterwards, the ions (mostly in the metastable state, some in the ionic ground state) are deflected from the laser beam and decelerated in order to then be efficiently neutralized by passing the ion beam through a charge exchange cell (CEC). Finally, an electric field is applied to separate the remaining ions from the neutralized atoms. As the neutralization cross section depends on the initial state of the ionic system (the metastable state is 3 times more efficiently neutralized), the resonant interaction between the laser and the ions in the first step[1] is turned into a resonant change in the ion/atom counting rate after the charge-exchange process. Thus the hyperfine structure can be observed in the atom and ion count rate as a function of the laser frequency[2]. As the direct detection of ions and atoms can be altered by isobaric contaminants in the ion beam, the dependence on beam impurities can be removed by counting the charge particles emitted by the radioactive isotope, instead of a direct measurement of the ion beam intensity.

3. Charge exchange process

The sensitivity of the technique is dominated by the ratio between the metastable and ground state neutralization cross sections. Considering a charge exchange process of an ion A^+ colliding with an atom B, the neutralization mechanism can be expressed as

$$A^+ + (B^+ + e) \rightarrow (A^+ + e) + B^+ + \Delta E, \qquad (1)$$

where ΔE is the so called energy defect [25] given by the difference between the ionization potentials of A and B. The neutralization cross section related to this process depends on the ion impact velocity and the ionic state [26]. A semi-classical approximation to describe this charge-exchange process was introduced by Rapp and Francis [25]. The wave function for the electron, ψ, during the reaction 1 can be approximated by a linear combination of the electron wave function in both projectile, ϕ_A, and target, ϕ_B, given by [25**?**]

$$\psi = C_A(t)\phi_A \exp(-i\omega_A t) + C_B(t)\phi_B \exp(-i\omega_B t), \qquad (2)$$

$$\phi_j(r_j) = (\pi a_0^3)^{-1/2}(\gamma_j)^{3/4} \exp\left(-\gamma_j \frac{r_j}{a_0}\right), \qquad (3)$$

the electron wave function in a s-like orbital of radius r_j, bound by a potential V_j with ionization energy I_j, and $\gamma_j \equiv \sqrt{\frac{I_j}{13.6\text{eV}}}$. If the electron is not in an s orbital, the expression 3 is used only as an approximation to correlate the size of the orbital with the ionization potential.

The probability of finding the electron bound to A^+ after the charge transfer reaction, $P(b, v) = |C_B(\infty)|^2$, can be expressed as a function of the impact parameter, b, and the projectile velocity v, whose solution is obtained from the solution of the time-dependent Schrödinger equation of the wave function given in 2, with the initial conditions: $C_B(-\infty) = 1$ and $C_A(-\infty) = 0$ (electron is bound only to B^+ before the reaction). Therefore, the cross section for the charge exchange process is given by [25, 27]

$$\sigma(v) = 2\pi \int_0^\infty P(b, v) b db. \qquad (4)$$

Due to the different approximations used in the theory of Rapp and Francis [25], the derived expressions are not expected to predict the absolute value of the experimental cross sections, but they can be used to predict results of the same order of the experimental values and provide a good description of the global behaviour to study the velocity and state dependence [26]. Some examples of numerical solutions for the neutralization cross section as a function of the ion energy and initial ionic state are shown in Figure 2. The figure illustrates the dependence on the ion velocity for some inelastic channels for the reaction $Ca^+ + Na \rightarrow Ca + Na^+$, corresponding to a projectile of mass $A = 40$ at 5 keV kinetic energy.

The cross section is closer to resonance ($\Delta E \sim 0$) when the ions are initially in the metastable states D_J. Consequently, the neutralization cross section $\sigma(D_J)$ is expected to have a larger value than the neutralization cross section for ions in the ground state, $\sigma(S_{1/2})$. According to the calculated values (Figure 2), the ratio $\sigma(D_J)/\sigma(S_{1/2})$, is maximum at low

[1] It includes scanning over the hyperfine structure

[2] Here as a function of voltage, as we scan Doppler shifted observed frequency

المنارة للاستشارات

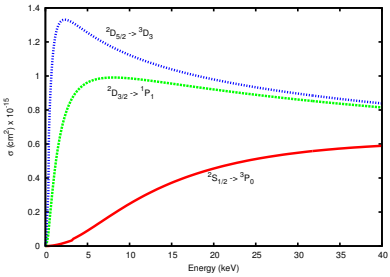

Figure 2: Example of the calculated neutralization cross section as a function of the ion energy for three different channels in the reaction $Ca^+ + Na$. The curves show the cross section for ions in three possible initial states $4s\ ^2S_{1/2}$ (red), $3\ d\ ^2D_{3/2}$ (green), or $3\ d\ ^2D_{5/2}$ (blue).

energies (<5 keV). Experimental studies of the reaction $Ca^+ + Na \rightarrow Ca + Na^+$ exhibit a maximum ratio at ~ 4 keV [26].

4. Optical Pumping

The applicability of the experimental method is restricted to the existence of a metastable state that can be optically pumped from the ground state, with a near-resonance charge-exchange reaction for only one of these states. This type of schemes is commonly found in alkaline-earth ions such as Ca, Sr, Ba and Ra. An illustration of the level scheme of CaII is shown in Figure 3. The ions, initially in the ground state, $ns^2S_{1/2}$, interact with a laser beam, and are resonantly excited to the np^2P_J states. Subsequently, spontaneous emission populates the metastable $(n-1)d^2D_J$ states.

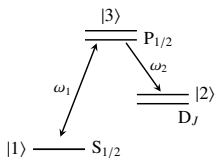

Figure 3: CaII Energy levels.

For isotopes with nuclear spin $I = 0$, approximately 100 % of the ions can be transferred to the metastable state. Therefore, the pumping efficiency depends mainly on the laser power and the interaction time (length of the optical pumping region in Figure 1). For a nuclear spin $I \neq 0$, the pumping efficiency is strongly affected by trapping into the different hyperfine components of the states involved in the pumping process.

Consider a three level system with a ground state $|\ 1\rangle$, a meta-stable state $|\ 2\rangle$, and an excited level $|\ 3\rangle$ (Figure 3), with population densities N_1, N_2, and N_3, respectively. Both spontaneous and induced emission are allowed from the excited state to the ground state, as well as spontaneous decay to the meta-stable state (this latter process will be responsible for the pumping into this level). If the frequency of the external laser field, ν_{13}, takes values around the energy difference between states $|\ 3\rangle$ and $|\ 1\rangle$, resonant excitation from the ground state to the excited state occurs. Thus, the evolution of the population for the different states can be expressed as [**?**]

$$\frac{dN_3}{dt} = -(A_{31}+A_{32})N_3 - \rho(\nu_{13})B_{31}N_3 + \rho(\nu_{13})B_{13}N_1,$$
$$\frac{dN_2}{dt} = A_{32}N_3, \quad (5)$$
$$\frac{dN_1}{dt} = A_{31}N_3 - \rho(\nu_{13})B_{13}N_1 + \rho(\nu_{13})B_{31}N_3, \quad (6)$$

with A and B the Einstein's coefficients introduced to account for the different processes of spontaneous emission (A_{31}, A_{32}), stimulated absorption (B_{13}) and stimulated emission (B_{31}). The spontaneous emission coefficients, A_{if}, between an initial state i and a final state f (with i and f characterized by their hyperfine quantum numbers I, J, F, M) [28].

For an ion exposed to a electromagnetic field with spectral energy density $\rho(\nu)$, the probability per unit time of absorption of photons, transferring the ion from the state $|\ i\rangle$ to a final state $|\ f\rangle$, is given by $\rho(\nu)B_{if}$. Only absorption from the ground state to the exited state is considered by assuming an external field with frequency values, ν_{13}, around the energy difference between the states $|\ 3\rangle$ and $|\ 1\rangle$ ($\rho(\nu_{23})B_{23} = 0$). Both, spontaneous and induced emission are allowed from the excited state to the ground state.
The population of the different states involved in the optical pumping process were calculated by numerically solving the expression 6. The final population of each state is obtained from the sum of the populations of the different hyperfine levels after a given laser-ion interaction time. In what follows, the transition $P_{3/2} \rightarrow S_{3/2}$ of Ca^+ was used as resonance transition to populate the metastable states D_J via spontaneous decay (see Figure 3).

4.1. Single-step

For isotopes with nuclear spin $I = 0$, approximately 100 % of the ions can be transferred to the metastable state. Therefore, the pumping efficiency depends mainly on the laser density power and the ion-laser interaction time.

For a nuclear spin $I \neq 0$, the pumping efficiency is strongly affected by trapping into the different hyperfine components of the states involved in the pumping process. An scheme for a laser field interaction with a CaII with nuclear spin, $I \neq 0$, is shown in Figure 5. For ions with spin $I \neq 0$, the population of the metastable state via some of the hyperfine transitions is reduced due to trapping into another hyperfine component of the ground state.

المنارة للاستشارات

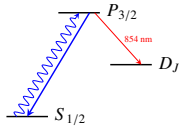

Figure 4: Level scheme of a CaII ion with nuclear spin, $I = 0$. A laser field is used to excite the ion from the ground state, $S_{1/2}$, to the excited state, $P_{3/2}$. The metastable states D_J are populated by spontaneous emission from the excited state.

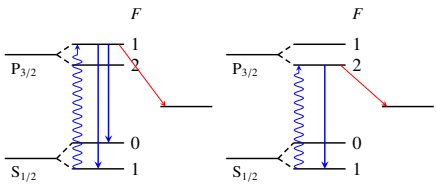

Figure 5: Level scheme of a CaII ion with nuclear spin, $I = 1/2$. A laser field of frequency 393 nm excites the ion from the ground state $S_{1/2}$ to the excited state $P_{3/2}$. When the laser is on resonances with the component $F = 1 \rightarrow F = 1$, the spontaneous emission spread the population into the metastable states D_J and the gs component $F = 0, 1$.

Figure 6 shows the population of the metastable state after resonant excitation of the ^{53}Ca ions with a single laser field, named single-step optical pumping (SSOP). The figure shows the results for different laser power densities and 6 μs interaction time, which is equivalent to an ion beam at 30 keV passing through an interaction region of 2 m long. A nuclear spin $I = 1/2$ was assumed for ^{53}Ca. When the laser is at resonance with the $F' = 1$ excited hyperfine level, by excitation from the $F = 0$ or from the $F = 1$ ground state level (see Figure 5), part of the spontaneous decay de-populates into the non-excited gs hyperfine level. This fraction of ions is lost for the remaining of the optical pumping process, which proceeds through the spontaneous decay from excited state hyperfine levels to the metastable D state. Thus, in Figure 6 only one hyperfine transition efficiently pumps the ions into the metastable state, namely the one that populates the $F' = 2$ level can not decay back to the $F = 0$ ground state. Therefore, only one of the three hyperfine transitions has a significantly large amplitude to be detected in the experiment.

A high pumping efficiency can be reached either by increasing the length of the pumping zone (interaction time) or by increasing the laser power. In practice, laser powers up to maximum 100 mW/cm^2 can be obtained for the laser frequency used to excite Ca^+ (~393 nm). At laser power densities above 40 mW/cm^2, an interaction time of about 3 μs (pumping zone of 1 m length for an ion beam at 30 keV) results in about 85 % of pumping efficiency into the meta-stable state. Higher laser power densities can be applied at the cost of power broadening,

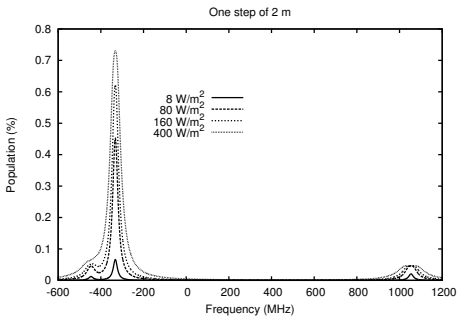

Figure 6: Population of the metastable state as a function of the laser frequency relative to the transition. The populations is calculated for different laser density powers in a single-step optical pumping of ^{53}Ca ($I = 1/2$). Ions at 30 keV enter into a beam line of 2 m length. Ion velocity ~ 1 m /(3.1 μs). See text for more details.

reducing the signal to background ratio.

4.2. Two-step

In order to observe the three hyperfine components with a similar signal strength, a two-step optical pumping (TSOP) can be applied [18, 29, 30]. Simultaneous pumping from different hfs components can be used to avoid the trapping of population. The two-step optical pumping is based on the interaction of an ion beam with two laser fields of different frequency. A comparison of the results of numerical calculations for both SSOP and TSOP are shown in Figure 7. In the SSOP process, the ion interacts during 6 μs with only one laser of variable frequency, allowing to scan the hyperfine structure but with only the $F = 1 \rightarrow 2$ transition leading to efficient pumping. The two other hyperfine transitions are very inefficient in the pumping due to their spontaneous decay into the "dark" hyperfine partner level. To apply two laser frequencies in the optical pumping section for TSOP, two different potentials will be applied along the beam path, such that the observed laser frequency is changed in subsequent pumping sections (details follow in section 5). In the first section the ion interacts with a laser field of variable frequency during 3 μs (so the potential is changed to scan the observed laser frequency), and in the next pumping section, it interacts during another 3 μs with a laser frequency fixed at the value of the dominant component, ν_2 ($F = I + 1/2 \rightarrow F' = I + 3/2$) (by applying a fixed potential).
If the frequency seen by the ion in the first step is outside of resonance, no change of population occurs. In this case only the ions observing a fixed frequency in the second section will initiate excitation of the state $F = I + 1/2$ and pumping into the meta-stable states will take place. This signal will be our base line. Then, when the first laser frequency is scanned across the

المنارة للاستشارات

hyperfine resonances, e.g. with ν_1 ($F = I-1/2 \rightarrow F' = I+1/2$), the state $F = I - 1/2$ is completely depopulated transferring some of the ions to the metastable states D_J, but most of the decay goes to the gs component $F = I + 1/2$.
When the first laser is at resonance with frequency ν_3 ($F = I + 1/2 \rightarrow F' = I - 3/2$), an opposite effect is observed. First, the state $F = I + 1/2$ is depopulated partially into the meta-stable state, but mostly to the state $F = I - 1/2$. As the state $F = I - 1/2$ can not be depopulated with the second laser field, the net population of the meta-stable state is reduced significantly. This is observed as a decrease in the meta-stable state population at ν_3 (Fig. 7).

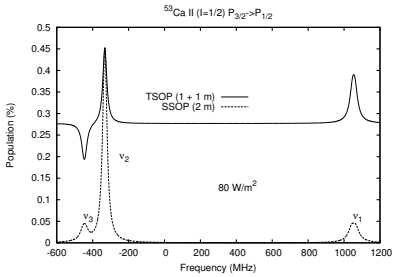

Figure 7: Population of the metastable state for single-step optical pumping (SOP) and two-step optical pumping (TSOP). A ^{53}Ca ($I = 1/2$) ion beam at 30 keV is assumed to interact with a laser beam along an optical pumping region of 2 m length. For the TSOP process, the first step was used as scanning frequency, and the frequency of the second step fixed at ν_2.

The dependence on possible fluctuations of the ion beam intensity can be reduced by measuring the asymmetry between the atom and the ion signal, defined as

$$\text{Asymmetry} \equiv \frac{\text{Atoms} - \text{Ions}}{\text{Atoms} + \text{Ions}}. \qquad (7)$$

An example of the asymmetry expected of the population of the meta-stable state in the two-step optical pumping case is shown in figure 8.

4.3. Multiple-step

More than two laser fields can be used to obtain further control for the meta-stable state population. Multiple-step optical pumping can be performed with various laser fields of different frequencies. An example for meta-stable state population of a four-step optical pumping is shown in Figure 9. The first and third laser were allowed to have variable frequency, and the second and fourth field were fixed to any of the possible values ν_1, ν_2 or ν_3. In the sequence $\nu_i - \nu_1 - \nu_i - \nu_1$ for example, the ion interacts with a laser field of variable frequency during the first step, and with a laser field of fix frequency ν_1 in the second step. The sequence is repeated, applying a variable field in the

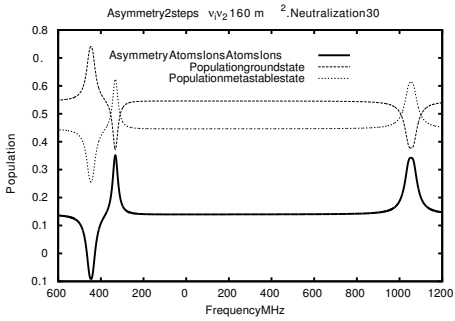

Figure 8: Asymmetry and populations of ground and metastable state with two-step optical pumping, taking as a fixed frequency the frequency ν_2.

third step, and finally a fix frequency ν_1 for the last step. An interaction time of 1.5 μs was used for each step.
As can be seen, this type of four step process is equivalent to a sequence of two TSOP, and might be used to enhance the population at frequency ν_3. Multiple steps with different values of fixed frequencies might be implemented to enhance the relative population of a specific hfs component. To summarize, TSOP produces a good balance for the signal observed in the meta-stable state population, but multiple steps with different fixed frequencies could be implemented to populate or depopulate a specific hfs component.

5. Ion Beam Optics

With the goal of improving the limits of sensitivity of the ROC technique by at least three orders of magnitude to study ^{53,54}Ca, a new experimental setup has been designed. The new ROC setup is expected to solve the shortcomings identified during previous experiments, and includes improvements on beam transmission, laser-ion interaction, β-detection efficiency, and background reduction. Furthermore, multiple-step optical pumping and simultaneous detection of atoms and ions was implemented.
The sensitivity of the previous ROC experiment on ^{50}Ca was considerably reduced due to a low S/N signal caused by radioactive isobaric contamination, which was partially implanted in the detection zone, inhibiting a possible measurement of ^{52}Ca. Thanks to the laser ionization ion source at ISOLDE, the beam contamination is now strongly reduced as compared to previous experiments using surface-ionization, allowing an improvement of the S/N signal. Energy discrimination has been implemented in the new β-detector setup to allow a clear separation of the β-counts coming from ^{54}Ca (Sec. 7). Furthermore, several ion beam optics elements have been implemented in the new setup to guarantee a safe implantation of

المنارة للاستشارات

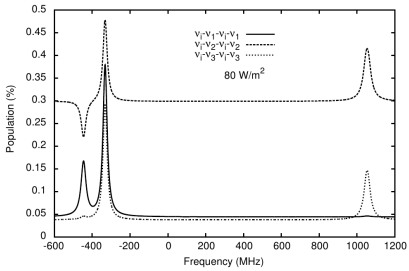

Figure 9: Population of the metastable state for four steps optical pumping. The ion beam interacts with four laser fields. First and third laser were allowed to have variable frequency, and the second and fourth field were fixed to any of the possible values ν_1, ν_2 or ν_3 (see text for more details).

both ion and atom beams on the different tape stations. The simultaneous detection of both beams allows a normalization to the total beam current, removing the dependence of the β-count signals with ion beam intensity.

An overview of the new design is shown in Figure 10. The total length of the new ROC setup is $\sim$ 4 m. The laser interacts with the ion beam along an optical pumping zone of 2 m long. A longer interaction region (2 m) guarantees $\sim$100 % pumping efficiency for transferring the ground-state population into metastable states. The introduction of multiple potentials along the pumping region allows the pumping of different hyperfine components, enhancing the signal of weakly populated hfs transitions in odd-isotopes by more than one order of magnitude, depending on the nuclear spin and the number of pumping steps (see Sec. 4).

After the optical pumping process, the ion beam is separated from the laser beam by a 5 degree deflector, and directed into the decelerator. The deflection is achieved by a couple of cylindrical lenses of long curvature radius ($\sim$ 2 m), which preserve the plane of motion for the ion beam, and minimized undesired focusing effects. This is in contrast with the previous "dog leg" deflector composed of two couples of parallel plates used to change the horizontal plane of motion and introducing a strong focus on the vertical plane, reducing the overall ion beam transmission.

After deceleration, the ion beam is passed through a charge exchange cell, and independent counting of neutralized and non-neutralized particles is performed by two independent tape stations at the end of the beam line. High transmission for the simultaneous detection of both atoms and ions after the deceleration and the neutralization processes is achieved by introducing multiple ion beam optics components floating at the CEC potential. A detailed explanation of each new beam line component is presented in the following sections.

5.1. Multi-step optical pumping and fluorescence detection

As explained in section 4, the length of the optical pumping region (interaction time) and the laser power density are critical parameters affecting the population of the metastable state. For ions with nuclear spin $I = 0$, no hyperfine components are present, and up to 100% of optical pumping efficiency can be achieved. When $I \neq 0$, the population of the metastable state is significantly reduced due to the trapping into the different hyperfine structure components, hence multi-step optical pumping needs to be employed to depopulate these "dark" states [29, 18]. In practice, multi-step optical pumping is achieved by dividing the optical pumping region in different segments maintained at different potentials. It is the equivalent to using multiple laser frequencies.

The optical pumping region for the new design is shown in figure 11. The ion beam is superimposed with the laser beam along a pumping zone divided in four segments with lengths of 40 cm, 60 cm, and two of 50 cm. The first segment corresponds to a pumping tube of 40 cm length (not shown in the figure). A light collection region is installed along the second pumping segment for monitoring the resonant fluorescence signal during the experiments. This light collection region is the same one used in the previous optical hfs experiments on Ca and K isotopes [24, 11, 9, 31].

In the experiment, the hfs spectrum of a particular nucleus is scanned by changing the potential of the optical pumping region. Regardless of the voltage applied to the optical pumping zone ($\pm$ 5 keV), the ion beam transmission up to the end of the beam line should remain unaltered. To avoid abrupt changes between the optical pumping zone and the ground potentials, a five-step accelerator(decelerator) set connects the beginning(end) of the optical pumping region with the rest of the beam line. For ions with nuclear spin $I = 0$, all pumping segments are fixed at the same potential, and the Doppler-tuning voltage is applied to the whole optical pumping region. For odd ions ($I \neq 0$), independent potentials can be applied to each pumping segment for multi-step optical pumping (see section 4). When the TSOP scheme is used, the last two sections are set at a constant voltage corresponding to the most intense resonance peak in the hyperfine spectrum. Scanning across the full hyperfine structure is then performed by scanning the voltage on the first and second section (both on the same potential).

5.2. Decelerator and focus control of atom/ion beam

As the ratio of neutralization cross section between the metastable state and the ground state reaches the maximum value at 4 keV, the initial ion energy (30 keV) should be reduced by a factor of $\sim$10. This energy reduction has the highest influence on the overall beam transport. Beam divergences, and undesired focusing points can be easily introduced during the deceleration. Besides requiring maximum beam transport efficiency, the possibility to control the focus of the decelerated beam is essential, as both ions and atoms must be separated and implanted simultaneously on two independent tape stations of 10 mm width. Radioactive nuclei were implanted outside

المنارة للاستشارات

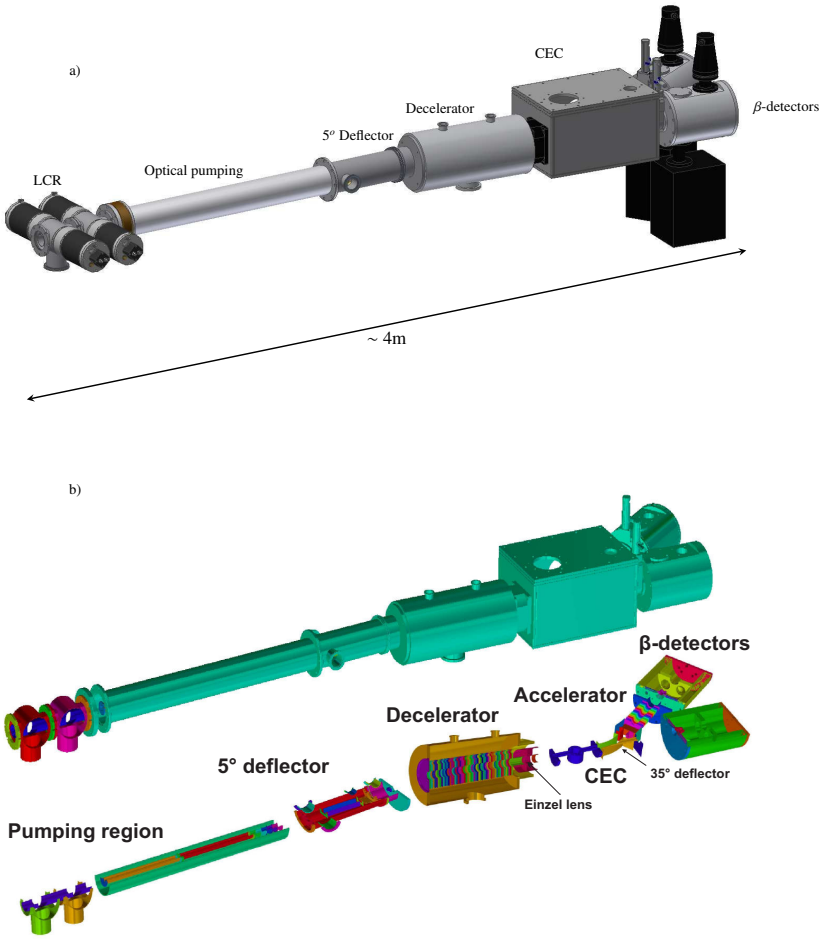

Figure 10: Complete design of the new ROC setup. a) Technical design drawing created by using Autodesk Invertor 2013. b) Beam line components included in the SIMION 3D simulations. Each electrode with adjustable potential is presented with a different color. The outer chambers were included as single electrode fixed at ground potential.

المنارة للاستشارات

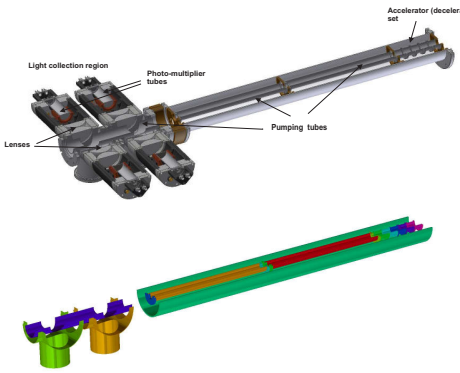

Figure 11: Design of the multi-step optical pumping region. The optical pumping region is divided in four independent segments. The first segment is not shown in the figure. A light collection region is placed along the second step for monitoring the fluorescence signals.

the tape, creating a large background due to radioactive contamination implanted around the β-detectors [1]. In order to preserve the beam quality in the deceleration process, the ion beam is passed through an array of 52 equidistant disks of 1.5 mm thickness. Each disk has an outer diameter of 14 cm, and a concentric hole of 4cm diameter. The CAD design and the 3D elements imported in SIMION are shown in Figure 10. The decelerator system is the same as used in the previous ROC setup, but an adjustable slope for the deceleration potential, and an einzel lens between the decelerator and CEC were implemented to control simultaneously the focus of both atom and ion beam.

Assuming an initial ion beam at 30 keV, the simplest approach to reduce the beam energy to 4 keV, might be feasible by applying a linear retarding potential along the beam direction, starting from the first disk at 0 V, and increasing the potential linearly up to 26 keV on the last disk. To illustrate the sensitivity of the focal point position to the shape of the retarding potential, ion beam simulations were performed for a simplified setup composed of a decelerator, an Einzel lens and a CEC cell. The results from the SIMION simulations are shown in Figure 12. As it can be seen in Figure 12a, the focal position for this case is generated after the CEC. The ion beam can be later refocused by introducing additional electrostatic elements after the CEC, but for atoms the focal point shall be fixed before the neutralization.

A common method used to control the focus introduced by a decelerator with cylindrical geometry consists in applying an exponential retarding potential field instead of a linear one [32]. Using the paraxial approximation [33], a charged particle in an axially symmetric field along the z direction, follows a trajectory, $r(z)$, described by

$$\frac{d^2r}{dz^2} + \frac{1}{2V(z)}\frac{dV(z)}{dz}\frac{dr}{dz} + \frac{r}{4V(z)}\frac{d^2V(z)}{dz^2} = 0, \tag{8}$$

where $V(z)$ is the potential along the z direction.
For an retarding potential given by an exponential form

$$V(z) = V_0(1 - e^{-\alpha z}), \tag{9}$$

with V_0 and α are constants that depend on the initial conditions. The spacial solution, $r(z)$, of equation 8 is given by

$$r(z) = 2\alpha\sqrt{(4\theta_0^2 - 2\theta_0 r_0\alpha + r_0^2\alpha^2)/3}e^{\alpha z/4}\sin(\sqrt{3}\alpha z/4 + \phi), \tag{10}$$

where θ_0 is the entrance angle, and r_0 is the initial distance from the symmetric axis. At the focal point, z_1, the distance of each particle to the symmetric axis is minimized, such that $r(z_1) = 0$. Therefore, the first focal point is located at

$$z_1 = \frac{4\pi}{\sqrt{3}\alpha}. \tag{11}$$

Hence, the focal position can be moved by varying the parameter α of the exponential function that defines the shape of the retarding potential. Experimentally, an exponential potential can be implemented by choosing appropriate resistor values connecting the different disks in the decelerator. This approach, although it is feasible, does not allow an easy control of the exponential factor, because the whole set of resistors would need to be replaced to change the focal position. Instead of using an exponential potential, a similar effect can be produced by dividing the deceleration potential in three steps of different slope. Each step is connected by a linear resistor chain of different value, and a floating power supply on the top of the CEC potential can be added to control the slopes of retarding potential. The idea is outlined in Figure 12. It can be seen as three-points linear interpolation of an exponential function, and it is equivalent to have several decelerators in series [34, 35].

The deceleration potential can be applied in three different ways: by using only one slope (figure 12a), two slopes (figure 12b) and three slopes (figure 12c). By varying the slope of each step, the focal position can be adjusted. The focus can be located inside the decelerator, an einzel lenses can be added to send the next focal point to the desired position.

In the experiment the focal position should be located at the implantation points, just in front of the tape stations, at a distance l_4 from the end of the CEC (see figure 12). For the ion beam simulations, an array of 51 disks was divided in three sets of 17 disks each one. The potential of each disk was increased linearly along the z axis, using different slopes for each set of disks. The results from the SIMION simulations are summarized in the table 1.

The results for the SIMION simulations using retarding potentials of different slopes are shown in Figure 12. For a linear potential with a single slope the focal point is located at the exit of the charge exchange cell and the beam diverges quickly at

المنارة للاستشارات

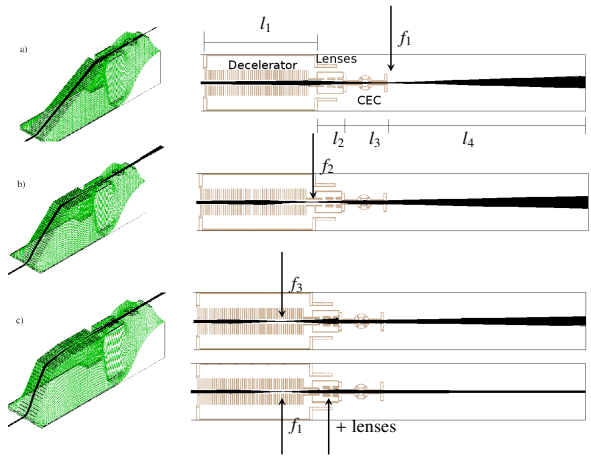

Figure 12: SIMION simulations for a simplified setup composed of a decelerator tube, an Einzel lens and a CEC cell. The retarding potential is divided in different steps: a) one slope, b) two slopes and c) three slopes. See text for more details.

Table 1: Simplified SIMION simulations for the system composed of a decelerator tube, an einzel lens and a CEC cell. A initial parallel beam at 30 keV is used to illustrate the influence of the deceleration slopes and the Einzel lens potential. The values of V_1 and V_2 are taken relative to the ground potential. The Einzel lens potential, V_L, is given relative to the platform potential (26 kV). Particle trajectories and the potential along the decelerator are shown in Figure 12.

V_1	V_2	V_L	Final beam diameter (mm)
8667	17333	0	43
13000	26000	0	23
24600	26000	0	14
24600	26000	-6500	6

short distances (Figure 12a). At the point of the tape station the beam diameter for this case is about four times the tape width (~ 40 mm). Because the focus occurs after the CEC, the Einzel lens is useless in this situation. Using two slopes (Figure 12b), the focal point can be moved to the end of the decelerator, and if three slopes are used (Figure 12c), the focal point is sent into the decelerator. Therefore, the ion beam can be re-focused by the Einzel lens, allowing full control of the focal position after the CEC. In this case the beam diameter at the implantation point can be reduced to a few millimeters, assuring a safe implantation on the tape station.

A parallel beam of 10 mm diameter entering into the decelerator tube at 30 keV was assumed in the simulations. The results are similar for a divergent ion beam as the strong focus induced in the deceleration is almost independent of the initial beam divergence. This dominant focus can be taken as an advantage for the new experimental setup. The voltage applied to the optical pumping region for the Doppler-tunning of hfs components modifies the focal point for the ion beam before the decelerator, but the focus induced in the deceleration dominates the final focal position. Consequently, very little influence on the overall beam transmission and on the focal position is expected at the tape position.

5.3. Simultaneous detection of β-decay of atoms and ions

Once the ion beam is decelerated and passed trough the charge exchange cell, the ions are separated from the neutralized particles by a pair of electrostatic cylindrical plates as shown in Figure 13. Horizontal and vertical correction plates were added to control the position of the implantation point. The atoms follow a straight path towards the tape station, located at 53 cm from the end of the CEC. The ions are deflected 35^o towards a second tape station at 68 cm from the end of the CEC. Because both β-detection stations are at ground potential, a post-accelerator can be used to gradually decrease the potential seen by the ion beam, from 26 keV to 0 keV. This re-acceleration process is accomplished by a set of 18 equidistant disks connected by resistors of equal value. As the tape station is close to the end of the accelerator, no further focus control is needed.

6. Ion beam optics simulations

The beam line components included in the ion beam optics simulations are shown in Figure 10. Electric fields and particle

المنارة للاستشارات

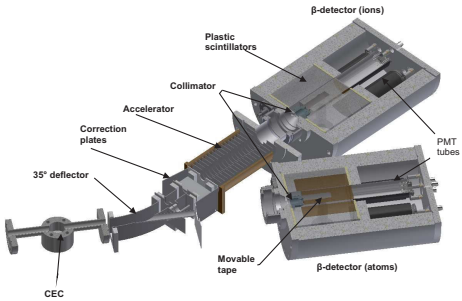

Figure 13: CAD design for the ion beam optics after the CEC cell. Independent high efficiency β-detection was implemented of atoms and ions. Details for the β-detector chambers are given in section 7.

trajectories were calculated by using the ion beam simulation software SIMION-8.1.
The 3D CAD designs of each beam line component were imported to SIMION by using the STL tools included in the same software. The outer chambers for the whole beam line were included as a single electrostatic component (electrode) fixed at ground potential. Each internal component was imported as an independent electrostatic device with an adjustable potential. The electrodes included in the ion beam simulations are shown in Figure 10. Different colors represent independent electrodes. For simulations of the whole ROC setup, a grid unit equivalent to 1.6 mm was chosen. Independent beam line segments were simulated with higher resolution (< 1 mm) to explore specific details on the beam transmission.
The simulations were performed assuming different initial conditions for the ion beam entering into the beam line. The focus of the incoming beam was placed at different positions assuming a beam emittance of around ~3-5 π mm.mrad, similar to the typical values observed at HRS [36] and GPS ion source targets [37].

An example of a SIMION simulation for the whole ROC setup is shown in Figure 14. The upper figure shows the potential energy surface view. An initial ion beam of mass $A = 50$ at 30 keV is focused at the entry of the light collection region. The ions are elevated from ground potential to 26 keV by a three-slope deceleration potential. The first two slopes can be controlled by changing the potential V_1 (Figure 14a). The parameter V_1 and the Einzel lens potential (negative with respect to 26 kV) are used to control the focus of the ion beam. After the charge exchange process, the ion beam is separated and re-accelerated to ground potential by using an accelerator of a single slope potential.
The ion beam trajectory along the different elements is shown in Figure 14b. Atoms and ions are separated and focused simultaneously on the different tape stations.

At the light collection region, the ion beam size is ~ 6 mm and has divergence of about 2 degrees. Due to the collimator installed at the entrance of each detector chamber, the beam size in the location of the tape stations is limited to less than 10 mm. The optimization procedure consists mainly of simultaneously maximizing the atom and ion beam transmission at the implantation point.
Figure 15 shows the beam transmission obtained from the SIMION ion beam simulation for different values of V_1 and Einzel lens potential, V_E. After the 35^o deflector the ion beam is re-accelerated from 26 keV to ground potential, producing a extra focusing effect. This additional focus produces a broad region of maximum transmission for different (V_1, V_E) values (Figure 15).
The simulations were performed assuming different focal positions for the ion beam entering into the ROC setup. The ion-beam optics was designed to optimize the transmission of atom and ion beam within a common (V_1, V_E) region simultaneously. Figure 15 shows the results for atoms(left) and ions(right) for an initial ion beam with focus at two extreme positions: at the light collection region (upper figures), and at the end of the pumping region (bottom figures). The transmission in both cases is mainly defined by the parameters (V_1, V_E), but in contrast with the ions, the atom beam has a much narrower region of maximum transmission (left of Figure 15). The region of maximum transmission is broader when the focus of the initial beam is closer to the decelerator, but the peak (V_1, V_E) of maximum transmission does not exhibit an appreciable dependence with the focus of the initial beam, as expected from a dominant focus introduced by the deceleration potential.

Optimized values for the electrostatic potential for the main elements of the ROC setup were obtained from the ion beam SIMION simulations. The results for maximum transmission are listed in Table 2.

Table 2: Optimum values of the main electrostatic elements of the ROC setup obtained from the ion beam SIMION simulations. The labels (i) and (ii) stands for two different regions of maximum transmission (Figure 15).

Parameter	Potential (V)
5^o deflector (Right)	+555
5^o deflector (Left)	-555
35^o deflector (Right)	+460
35^o deflector (Left)	-460
Top	0
Bottom	0
Right	0
Decelerator	-12000≤ V_1 ≤-6000 (i)
	-4000≤ V_1 ≤-500 (ii)
Einzel lens	-3000≤ V_E ≤1000 (i)
	-10000≤ V_E ≤-4000 (ii)

المنارة للاستشارات

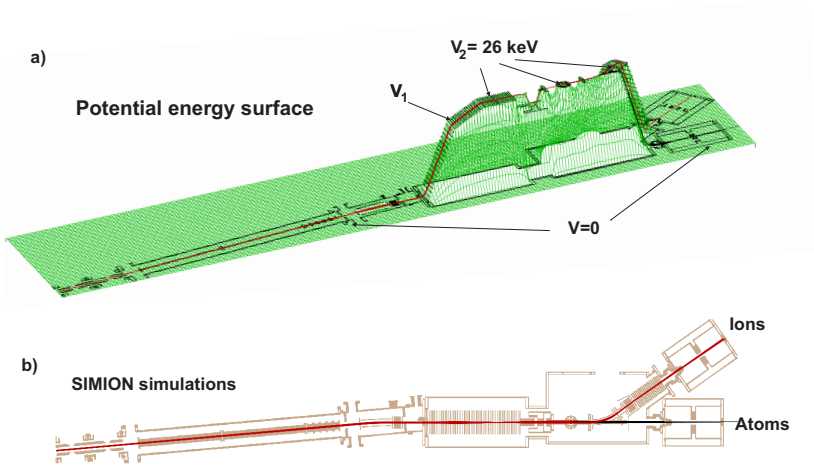

Figure 14: Example of a SIMION simulations for the whole ROC setup. a) Potential energy surface view, and b) particle trajectories for the ion beam. A neutralization efficiency of 50 % was assumed for the CEC process at the center of the CEC (see text for more details).

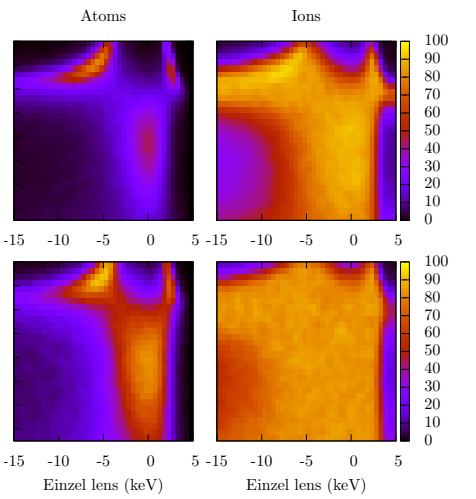

Figure 15: Results of ion beam SIMION simulations for both, atoms(left) and ions(right), assuming two different focal positions for the ion beam entering into the ROC setup: at the entry (upper) and at the end (lower) of the optical pumping region. Colors represent the percent of transmission simulated at the implantation point.

7. β-detector setup

A direct detection of atoms and ions is sensitive to isobaric contamination present in the ion beam. Nevertheless, a selective measurement of the number of particles for the ion of interest can be obtained by counting the β-particles emitted from the beta-decaying nuclei. β detection removes completely the background associated with stable contaminants. The background emanating from radioactive isobars (mainly Ti) can also be reduced if additional energy discrimination is implemented.
A view inside the β-detector chamber is shown in Figure 16. Each chamber is composed of two concentric cylindrical scintillators with inner and outer radius of 50 mm and 190 mm respectively. The axis of each cylinder coincides with the beam direction. A movable tape perpendicular to the beam direction can circulate through the center of both cylinders. This configuration allows for a geometrical efficiency of $\sim 4\pi$ at the implantation point. Particle coincidences between the inner and outer cylinder are used to discriminate the β-particles from other sources of radiation, e.g., γ-radiation. The intrinsic β-detection efficiency of this setup is expected to be $> 80\%$. The thickness of the outer detector was chosen to stop all β-particles emitted with energies below 12 MeV. It allows full energy reconstruction of the β-particles by adding the signals of all 5 PMTs. Event by event information will be obtained using the ISOLDE DAQ system, allowing the selection of different energy cuts for the offline analysis. For online monitoring, a simple DAQ system will be used to monitor β-signals. The discriminator level of each PMT signal can be adjusted to provide online "Hardware" energy cuts.

The β-particles emitted from the radioactive isotopes im-

المنارة للاستشارات

planted on the tape are recorded on the site of implantation point. After few hundreds of milliseconds [3], the contaminated part of the tape is removed, and a clean section of the tape is placed in front of the beam path at the center of the β-detectors. Each collection time is synchronized with a change of the ion velocity (Doppler-tuning of the laser frequency).
A collimator of 10 mm aperture is placed at the entrance of each chamber to prevent the implantation of the radioactive contamination outside of the tape.

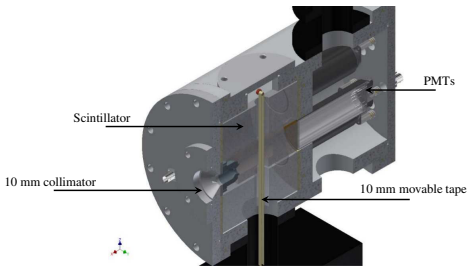

Figure 16: CAD design of the β-detector chamber. Ions are implanted on a movable tape. A collimator prevents the implantation of ions outside the tape. The β-particles are detected by two concentric cylindrical scintillators. The light from the scintillators is collected by a set of PMT tubes attached to the surface of the scinitllators.

The light resulting from the β-decaying particles passing through the scintillators is detected by a set of photomultiplier tubes. Four PMTs are attached to the surface of the outer cylinder, and one PMT on the surface of the inner cylinder.

A summary with the improvements and new features implemented in the new experimental setup are listed in Table 3.

8. Commissioning the experimental setup

The design and dimensions of each beam line component were chosen based on the different numerical calculations of the laser-ion interaction and ion beam simulations explained in the previous sections. A photograph of the optical pumping region installed at the COLLAPS beam line is shown in Figure 17. The chambers, in addition to the internal parts of the pumping region, were made of aluminum. The internal parts were painted with black aluminum graphite to reduce the scattering of light around the light-collection region. The pumping region, as well as the other components sent to the different workshops were built almost identical to the original CAD designs. No appreciable changes on the shape and/or dimensions of the different components were introduced during the production process. The tube was connected to the COLLAPS light collection

[3] For ^{54}Ca ($T_{1/2}$ = 86(7) ms) the detection time is around 400 ms

Table 3: Comparison between the previous and the new design of the ROC setup.

Parameter	Previous	New design
Interaction region	1.5 m	2 m
Light collection	No	Yes
Multi-step optical pumping	No	Yes
Deceleration	Yes	Yes
Slope control of retarding potential	No	Yes
Focus control after Deceleration	No	Yes
Atom counting	Yes	Yes
Ion counting	No	Yes
β-detection (solid angle)	$\sim$ 25	$\sim$100%
No of detectors per chamber	1	2
Protection of β-detectors against contamination	No	Yes
β-energy discrimination	No	Yes
Overall beam transmission	<70 % [4]	>90 %

region. Inside of it two independent cylindrical tubes can be maintained at different potential to implement multi-step optical pumping. The other end of the pumping tube connects the beam line to the 5^o deflector. A photograph of the ROC setup from the deflector up to the end of the CEC chamber is shown in Figure 18.

After the 5^o deflection, the laser is reflected by a 45^0 mirror, reflecting the laser light towards outside of the vacuum chamber. A transparent window at Brewster angle reduces the reflected light into the light collection region. A photograph of inside the CEC chamber (Figure 18b) shows: the CEC cell, the 35^o deflector and vertical and horizontal correction plates. The accelerator and decelerator arrays are shown in Figure 18c and 18d respectively.

9. First experimental results

The first online tests were performed by using the GPS target station at ISOLDE. A beam of $^{40}Ca^{+}$ was extracted using the RILIS ion source, accelerated up to 30 keV to be mass separated and sent to the COLLAPS beam line.

Some of the modifications and improvements implemented in the new ROC setup were expected to improve the overall ion beam transmission. Three main concerns were explored through the first ion beam test: i) The ability to reduce the energy from 30 keV to 4 keV while preserving the transmission at the end of the beam line, ii) Focus control of the ion beam after the deceleration process and effective control of the ion beam optics on the top of the HV platform at 26 keV, iii) Dependence of the overall ion beam transmission with the Doppler-tunning voltage applied to the optical pumping region.
The focus control of the ion beam after deceleration was studied by changing the slope of the deceleration potential, V_1, as a function of the the Einzel lens potential, V_{Einzel}. The region of maximum transmission coincided with the values suggested

المنارة للاستشارات

Figure 17: Photograph of the optical pumping region installed at the COLLAPS beam line. The pumping tube connected to the light collection region (left), and a view inside the pumping tube (right).

Figure 18: Photograph of some of the components in the ROC setup. a) A view from the 5^o deflector up to the end of the CEC chamber. The HV cage placed on one side of the CEC chamber. b) The inside of the CEC chamber. c) Re-accelerator for ions after the 35^o deflector and d) Renewed accelerator from the old ROC setup.

المنارة للاستشارات

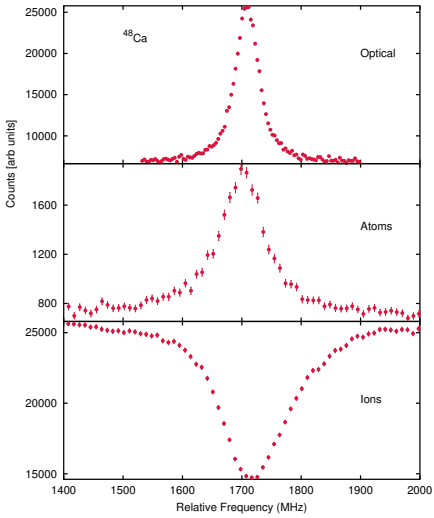

Figure 19: Example of measured spectra for the ^{48}Ca isotope. Fluorescence photons (upper) are compared with the signal of neutralized ions, atom signal (center), and the Non-neutralized, ion signal (bottom), deflected towards the 35^o chamber. All signals are measured as a function of the laser frequency in the ion rest frame. The four segments of the optical pumping region were fixed at the same potential and used as a Doppler-tuning region.

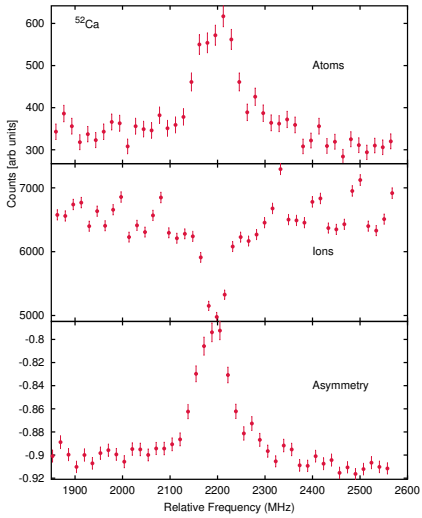

Figure 20: Example of some measured spectra for ^{52}Ca. The β-particles in both chambers were measured as function of the Doppler-tuning voltage applied to the optical pumping region and converted to the respective frequency in the ion rest frame. The upper figure shows the spectrum corresponding to the neutralized ions. In the center the spectrum for non-neutralized (ion signal) isotopes, and the asymmetry signal (see Eq. 7) is shown in the bottom panel.

from the ion beam optics simulations (see 15). The ability to localize the ion focus on the implantation point is important to reduce the risk of implanting radioactive contamination outside the tape.

The sensitivity of the ion beam transmission was studied as a function of the potential applied to the optical pumping region. Voltages between -7 keV and +7keV were applied to the pumping region and no changes were observed in the ion beam intensity measured at the implantation point.

9.1. Optical detection vs state-selective neutralization

The laser frequency was fixed around the 393-nm $4s^2S_{1/2} \rightarrow 4p^2P_{3/2}$ ionic transition of Ca^+. To benchmark the ROC measurements, fluorescence photons were detected by using the light collection region installed as part of the optical pumping region (second step). Some examples of the measured optical spectrum and the spectrum of neutralized ions as a function of the scanning frequency for the ^{48}Ca isotope are shown in Figure 19. The Doppler-tuning voltage applied to the pumping region was converted to the laser frequency in the ion rest frame.

9.2. First ROC signals

The isotope ^{52}Ca was selected to perform the first ROC measurements. Figure 20 shows the number of β-particles detected in both detector chambers, atoms and ions, measured as function of the laser frequency in the ion rest frame.

As observed in figures 19 and 20, the peak positions obtained with the optical signal are in good agreement with the values measured with the particle detection scheme. For the radioactive isotope, ^{52}Ca, the measured signals present some fluctuations (Fig. 20) that are related to changes in the proton pulse period. However, these fluctuations are reduced when the asymmetry signal is calculated.

10. Conclusions

With the aim of extending our experimental knowledge of ground state properties of calcium isotopes beyond $N = 32$, a sensitive experimental setup has been developed. The new experimental apparatus is based on optical pumping, followed by radioactive detection of particles, and state selective neutralization, named the ROC technique. Although the experimental technique was previously applied [1], several shortcomings were identified to reach the predicted the limits of sensitivity [16]. This work presented the effort to overcome these limitations, allowing the applicability of the aforementioned technique to the study of ^{53,54}Ca isotopes, which are produced at only few ions/s.

Numerical calculations for the laser-ion interaction allowed the determination of the optimum length of the optical-pumping region and the number of pumping steps required to maximize the pumping efficiency into the meta-stable states.

The necessary ion-beam optical components and the respective dimensions of the different beam line components were explored through ion-beam simulations. These calculations and

المنارة للاستشارات

the simulations were used to choose the optimum design of each beam line component.

The experimental setup was commissioned at ISOLDE and the first successful experimental tests were presented. The complete setup was tested with measurements of stable and radioactive Ca isotopes. The measurements obtained for the exotic ^{52}Ca isotope, showed the large increase of sensitivity respect to the previous measurements obtained with optical detection. Although, the high efficiency of the experimental setup has been proved, further background reduction in the β-detector setups is required to extend these measurements to isotopes produced at only few ions/s.

[1] L. Vermeeren, et al., Phys. Rev. Lett. 68 (1992) 1679.
[2] Y. Blumenfeld, T. Nilsson, P. Van Duppen, Phys. Scr. T152 (2013) 014023.
[3] A. Andreyev, et al., Phys. Rev. Lett. 105 (2010) 252502.
[4] L. Gaffney, et al., Nature 497 (2013) 199.
[5] Y. Utsuno, et al., Phys. Rev. Lett. 114 (2015) 032501.
[6] B. Cheal, K. Flanagan, J. Phys. G 37 (2010) 113101.
[7] K. Blaum, J. Dilling, W. Nörtershäuser, Phys. Scr. T152 (2013) 014017.
[8] G. Neyens, Rep. Prog. Phys. 66 (2003) 633.
[9] J. Papuga, et al., Phys. Rev. C 90 (2013) 034321.
[10] W. Nörtershäuser, C. Geppert, Lect. Notes Phys. 879 (2014) 233.
[11] J. Papuga, et al., Phys. Rev. Lett. 110 (2013) 172503.
[12] Wing, et al., Phys. Rev. Lett. 36 (1976) 1488.
[13] R. Silverans, et al., Hyp. Int. 24 (1985) 181.
[14] R. Neugart, W. Klempt, K. Wendt, Nucl. Inst. Meth. B17 (1986) 354.
[15] R. Silverans, P. Lievens, L. Vermeeren, Nucl. Inst. Meth. B 26 (1987) 591.
[16] P. Lievens, et al., Nucl. Inst. Meth. B70 (1992) 532.
[17] R. Silverans, et al., Phys. Rev. Lett. 60 (1988) 2607.
[18] P. Lievens, et al., Phys. Lett. B 256 (1991) 141.
[19] P. Lievens, et al., Phys. Rev. C 46 (1992) 797.
[20] W. Borchers, et al., Phys. Lett. B 216 (1989) 7.
[21] M. Keim, et al., Nucl. Phys. A589 (1995) 219.
[22] K. Flanagan, et al., Phys. Rev. Lett. 111 (2013) 212501.
[23] R. Garcia Ruiz, et al., Submitted.
[24] R. Garcia Ruiz, et al., Phys. Rev. C 91 (2015) 041304(R).
[25] D. Rapp, J. Francis, J. Chem. Phys. 37 (1962) 2631.
[26] L. Vermeeren, et al., J. Phys. B 25 (1992) 1009.
[27] D. Dewangan, J. Phys. B 6 (1973) L20.
[28] C. Foot, 1st Edition, Atomic Physics (Oxford University Press), 2005.
[29] L. Vermeeren, Hyper. Int. 61 (1990) 1399.
[30] P. Lievens, et al., Hyp. Int. 59 (1990) 161.
[31] K. Kreim, et al., Phys. Lett. B 731 (2014) 97.
[32] M. L. Vestal, et al., Rev. Sci. Instrum. 47 (1976) 15.
[33] B. Paszkowski, Electron Optics, 1st Edition, Elsevier, New york, 1968.
[34] Y. Ishii, et al., Nucl. Inst. Meth. B 181 (2001) 71.
[35] Y. Ishii, et al., Nucl. Inst. Meth. B 269 (2011) 2193.
[36] E. Mane, et al., Eur. Phys. J. A 42 (2009) 503.
[37] F. Wenander, et al., Nucl. Inst. Meth. B 204 (2003) 261.

المنارة للاستشارات

Bibliography

[1] R. Blin-Stoyle and M. Perks *Proc. Phys. Soc.*, vol. A67, p. 885, 1954.

[2] A. Andreyev *et al. Phys. Rev. Lett.*, vol. 105, p. 252502, 2010.

[3] K. Heyde and J. Wood *Rev. Mod. Phys.*, vol. 83, p. 1467, 2011.

[4] L. Gaffney *et al. Nature*, vol. 497, p. 199, 2013.

[5] Y. Utsuno *et al. Phys. Rev. Lett.*, vol. 114, p. 032501, 2015.

[6] D. Warner *Nature*, vol. 430, p. 517, 2004.

[7] B. Bastin *et al. Phys. Rev. Lett.*, vol. 99, p. 022503, 2007.

[8] O. Sorlin and M. Porquet *Prog. Part. Nucl. Phys.*, vol. 61, p. 602, 2008.

[9] R. V. F. Janssens *Nature*, vol. 459, p. 1069, 2009.

[10] K. Jones *et al. Nature*, vol. 465, p. 454, 2010.

[11] F. Wienholtz *et al. Nature*, vol. 498, p. 7454, 2013.

[12] D. Steppenbeck *et al. Nature*, vol. 502, p. 207, 2013.

[13] H. D. Wohlfahrt, E. B. Shera, and M. V. Hoehn *Phys. Rev. C*, vol. 23, p. 533, 1981.

[14] A. Andl *et al. Phys. Rev. C*, vol. 26, p. 2194, 1982.

[15] R. Silverans *et al. Z. Phys. D.*, vol. 18, p. 351, 1991.

[16] S. Maleki and A. Goble *Phys. Rev. A*, vol. 45, p. 524, 1992.

[17] L. Vermeeren *et al. Phys. Rev. Lett.*, vol. 68, p. 1679, 1992.

[18] W. Nortershauser *et al. Spectro. Acta Part. B*, vol. 53, p. 709, 1998.

المنارة للاستشارات

[19] A. Mortensen *et al. Phys. Rev. A*, vol. 69, p. 042502, 2004.

[20] B. Sahoo *Phys. Rev. A*, vol. 80, p. 012515, 2009.

[21] G. Sartoris and L. Zamick *Phys. Rev. Lett.*, vol. 18, p. 292, 1967.

[22] M. Vand der Merwe, W. Richter, and B. Brown *Nucl. Phys. A*, vol. 579, p. 173, 1994.

[23] L. Zamick *Ann. Phys. (N.Y.)*, vol. 66, p. 784, 1971.

[24] B. Brown, S. Massen, and P. Hodgson *J. Phys. G*, vol. 5, p. 1655, 1979.

[25] F. Trager *Z. Phys. A*, vol. 299, p. 33, 1981.

[26] J. Cole *J. Phys. G*, vol. 7, p. 25, 1981.

[27] A. Huck *et al. Phys. Rev. C*, vol. 31, p. 2226, 1985.

[28] A. Gade *et al. Phys. Rev. Lett.*, vol. 112, p. 112503, 2014.

[29] R. Machleidt and D. Entem *Phys. Rep.*, vol. 503, p. 1, 2011.

[30] J. Holt *et al. J. Phys. G*, vol. 39, p. 085111, 2012.

[31] G. Hagen *et al. Phys. Rev. Lett.*, vol. 109, p. 032502, 2012.

[32] R. Roth *et al. Phys. Rev. Lett.*, vol. 109, p. 052501, 2012.

[33] V. Somà, A. Cipollone, C. Barbieri, P. Navrátil, and T. Duguet *Phys. Rev. C*, vol. 89, p. 061301, 2014.

[34] J. D. Holt, J. Menéndez, J. Simonis, and A. Schwenk *Phys. Rev. C*, vol. 90, p. 024312, 2014.

[35] H. Geiger and E. Marsden *Proc. Roy. Soc. A*, vol. 82, p. 495, 1909.

[36] E. Rutherford *Phil. Mag. Ser. 6*, vol. 21, p. 669, 1911.

[37] C. von Weizsacker *Z. fur Phyz.*, vol. 96, p. 431, 1935.

[38] M. Mayer *Phys. Rev.*, vol. 75, p. 1960, 1949.

[39] O. Haxel, J. Jensen, and H. Suess *Phys. Rev.*, vol. 75, p. 1766, 1949.

[40] M. Goeppert Mayer, "The shell model," *Nobel lecture*, p. 20, 1963.

[41] A. G. and W. Meng, "Private comunication," *Atomic mass evaluaton 2013 (AME2013)*, 2013.

[42] E. Wigner *Phys. Rev.*, vol. 51, p. 106, 1937.

المنارة للاستشارات

[43] I. Angeli and K. Marinova *Atomic Data and Nuclear Data Tables*, vol. 99, p. 69, 2013.

[44] R. Rodriguez-Guzman *Phys. Lett. B*, vol. 691, p. 202, 2010.

[45] S. Cohen and R. Lawson *Phys. Lett.*, vol. 21, p. 306, 1966.

[46] D. T *et al. arXiv:1411.1237*, 2015.

[47] V. J. Van Oostrum *et al. Phys. Rev. Lett.*, vol. 16, p. 528, 1966.

[48] D. Ehrlich *et al. Phys. Rev. Lett.*, vol. 18, p. 959, 1967.

[49] L. Olschewski *Z. Physik*, vol. 249, p. 205, 1972.

[50] F. Neumann *et al. Z. Phys. A*, vol. 279, p. 249, 1976.

[51] J. Kowalski *et al. Z. Phys. A*, vol. 290, p. 345, 1979.

[52] U. Klingbeil *et al. Z. Phys. A*, vol. 290, p. 143, 1979.

[53] P. Grundevik *et al. Phys. Rev. Lett.*, vol. 42, p. 1528, 1979.

[54] E. Bergmann *et al. Z. Phys. A*, vol. 292, p. 401, 1979.

[55] E. Bergmann *et al. Z. Phys. A*, vol. 294, p. 319, 1980.

[56] M. Arnold *et al. Hyperfine Interactions*, vol. 159, p. 9, 1981.

[57] I. Talmi *Rev. Mod. Phys.*, vol. 344, p. 704, 1962.

[58] R. Cakirli, R. Casten, and K. Blaum *Phys. Rev. C*, vol. 82, p. 061306(R), 2010.

[59] L. Vermeeren *et al. J. Phys. G: Nucl. Part. Phys.*, vol. 22, p. 1517, 1996.

[60] C. Palmer *et al. J. Phys. B.*, vol. 17, p. 2197, 1984.

[61] K. Blaum *et al. Nucl. Phys. A*, vol. 799, p. 30, 2008.

[62] A. Klein *et al. Nucl. Phys. A*, vol. 607, p. 1, 1996.

[63] K. Kreim *et al. Phys. Lett. B*, vol. 731, p. 97, 2014.

[64] M. Avgoulea *et al. J. Phys. G*, vol. 38, p. 025104, 2011.

[65] Y. Gangrsky *et al. J. Phys. G*, vol. 30, p. 1089, 2004.

[66] A. G. and W. Meng, "Private comunication," *Atomic mass evaluaton 2011 (AME2011)*, 2011.

المنارة للاستشارات

[67] G. Neyens *Rep. Prog. Phys.*, vol. 66, p. 633, 2003.

[68] B. Castel and I. Towner, *Modern Theories of Nuclear Moments*. Oxford University Press, 1 ed., 1990.

[69] N. J. Stone *Atomic Data And Nuclear Data Tables*, vol. 90, pp. 75–176, 2005.

[70] R. Garcia Ruiz *et al. Phys. Rev. C*, vol. 91, p. 041304(R), 2015.

[71] P. Doornenbal *et al. Phys. Lett. B*, vol. 647, p. 237, 2007.

[72] K. Speidel *et al. Phys. Lett. B*, vol. 659, p. 101, 2008.

[73] P. Baumann *et al. Phys. Lett. B*, vol. 228, p. 4, 1989.

[74] NNDC, "National nuclear data center," *http://www.nndc.bnl.gov/chart/replotband.jsp*.

[75] E. Caurier *et al. Phys. Rev. C*, vol. 75, p. 054317, 2007.

[76] N. Ishii *Phys. Rev. Lett.*, vol. 99, p. 022001, 2007.

[77] B. Barrett, P. Navratil, and J. Vary *Prog. Part. Nucl. Phys.*, vol. 69, p. 131, 2013.

[78] R. Roth *Few-Body Syst*, vol. 55, p. 659, 2014.

[79] F. Jegerlenhner *Acta Phys. Polon.*, vol. B45, p. 1167, 2014.

[80] B. S. and S. Pastore *J. Phys. G Nucl . Part. Phys.*, vol. 41, p. 123002, 2014.

[81] L. Marcucci *Few-Body Syst*, vol. 55, p. 615, 2014.

[82] A. Ekström *et al. Phys. Rev. Lett.*, vol. 113, p. 262504, 2014.

[83] M. Pavon Valderrama and D. Phillips *Phys. Rev. Lett.*, vol. 114, p. 082502, 2015.

[84] S. Okubo and R. MarshakStoks *Ann. of Phys.*, vol. 4, p. 166, 1958.

[85] S. Pieper and R. Wiringa *Annu. Rev. Nucl. Part. Sci.*, vol. 51, p. 53, 2001.

[86] V. Stoks *Phys. Rev. C*, vol. 49, p. 2950, 1994.

[87] R. Wiringa, V. Stoks, and R. Schiavilla *Phys. Rev. C*, vol. 51, p. 38, 1995.

[88] R. Machleidt *Phys. Rev. C*, vol. 63, p. 024001, 2001.

المنارة للاستشارات

[89] T. Hotsuda *Oslo lectures*, 2008.

[90] J. Carlson, V. Pandharipande, and R. Wiringa *Nucl. Phys. A*, vol. 401, p. 59, 1983.

[91] P. Navratil *et al. J. Phys. G: Nucl. Part. Phys.*, vol. 36, p. 083101, 2009.

[92] C. Carlson *et al. Accepted in Rev. Mod. Phys.*, 2015.

[93] S. Barshay and G. Brown *Phys. Rev. Lett.*, vol. 34, p. 1106, 1975.

[94] S. Weinberg *Phys. Lett. B*, vol. 251, p. 288, 1990.

[95] H. Yukawa *Proc. Math. Phys. Soc. Japan*, vol. 17, p. 48, 1935.

[96] D. Furnstahl, "Lecture on nuclear forces," *TALENT 2013*, 2013.

[97] E. Epelbaum *arXiv:1001.3229[nucl-th]*, 2010.

[98] E. Epelbaum *et al. Phys. Rev. Lett.*, vol. 104, p. 142501, 2010.

[99] D. Entem and R. Machleidt *Phys. Rev. C*, vol. 68, p. 041001(R), 2003.

[100] D. Eperlbaum, W. Glockle, and U. Meibner *Nucl. Phys. A*, vol. 747, p. 362, 2005.

[101] A. Nogga *et al. Phys. Rev. C*, vol. 73, p. 064002, 2006.

[102] P. Navratil *et al. Phys. Rev. Lett.*, vol. 99, p. 042501, 2007.

[103] T. Otsuka *et al. Phys. Rev. Lett.*, vol. 105, p. 032501, 2010.

[104] A. Gallant *et al. Phys. Rev. Lett.*, vol. 109, p. 032506, 2012.

[105] S. Glazek and K. Wilson *Phys. Rev. D*, vol. 48, p. 5863, 1993.

[106] F. Wegner *Ann. Physik Leipzig*, vol. 3, p. 77, 1994.

[107] I. Talmi and S. Scherer, *Adv. Nucl. Phys.* KLUWER ACADEMIC PUBLISHERS, 27 ed., 2003.

[108] E. Caurier *et al. Rev. Mod. Phys.*, vol. 77, p. 427, 2005.

[109] K. A. Brueckner, C. Levinson, and H. Mahmoud *Phys. Rev.*, vol. 95, p. 217, 1954.

[110] B. H. Brandow *Rev. Mod. Phys.*, vol. 39, p. 771, 1967.

[111] B. R. Barrett *Czech J. Phys.*, vol. 49, p. 1, 1999.

[112] S. Bogner *et al. Prog. Part. Nucl. Phys.*, vol. 65, p. 94, 2010.

المنارة للاستشارات

[113] T. Kuo and G. Brown *Nucl. Phys. A*, vol. 85, p. 40, 1966.

[114] T. Kuo and G. Brown *Nucl. Phys. A*, vol. 114, p. 241, 1968.

[115] T. Hamada and I. Johnston *Nucl. Phys. A*, vol. 34, p. 382, 1962.

[116] A. Poves *et al. Nucl. Phys. A*, vol. 694, p. 157, 2001.

[117] M. Honma *et al. Phys. Rev. C*, vol. 69, p. 034335, 2004.

[118] M. Hjorth-Jensen, T. Kuo, and E. Osnes *Phys. Rep.*, vol. 261, p. 125, 1995.

[119] A. Zuker *Phys. Rev. Lett.*, vol. 90, p. 042502, 2003.

[120] W. Richter and M. Van Der Merwe *Nucl. Phys. A*, vol. 523, p. 325, 1991.

[121] U. van Kolck *Phys. Rev. C*, vol. 49, p. 2932, 1994.

[122] E. Epelbaum *et al. Phys. Rev. C*, vol. 66, p. 064001, 2002.

[123] A. Ekstrom *et al. Submitted to Phys. Rev. Lett.*, 2015.

[124] L. Coraggio *et al. Phys. Rev. C*, vol. 80, p. 044311, 2009.

[125] L. Coraggio *et al. Phys. Rev. C*, vol. 81, p. 064303, 2010.

[126] H. Hergert *et al. Phys. Rev. C*, vol. 90, p. 041302(R), 2014.

[127] V. Soma *et al. Phys. Rev. C*, vol. 89, p. 061301(R), 2014.

[128] S. Binder, J. Langhammer, A. Calci, and R. Roth *Phys. Lett. B*, vol. 736, p. 119, 2014.

[129] G. Jansen *et al. Phys. Rev. Lett.*, vol. 113, p. 142502, 2014.

[130] B. R. Barrett *et al. J. Phys. Conf.*, vol. 580, p. 012003, 2015.

[131] E. Dikmen *et al. arXiv:1502.00700*, 2015.

[132] P. Navratil, M. Thoresen, and B. Barrett *Phys. Rev. C*, vol. 55, p. 55, 1997.

[133] S. Pastore *et al. Phys. Rev. C*, vol. 90, p. 024321, 2014.

[134] T. A. Lahde *et al. Phys. Lett. B*, vol. 732, p. 110, 2014.

[135] T. A. Lahde *et al. arXiv:1502.06787*, 2015.

[136] R. Roth *et al. Phys. Rev. Lett.*, vol. 107, p. 072501, 2011.

المنارة للاستشارات

[137] K. A. Wendt *et al. arXiv:1503.07144*, 2015.

[138] H. Hergert *et al. Phys. Rev. C*, vol. 87, p. 034307, 2013.

[139] A. Lovato *et al. Phys. Rev. Lett.*, vol. 111, p. 092501, 2013.

[140] E. Epelbaum *et al. Phys. Rev. Lett.*, vol. 106, p. 192501, 2011.

[141] E. Epelbaum *et al. Phys. Rev. Lett.*, vol. 112, p. 102501, 2014.

[142] A. Lovato *et al. Phys. Rev. Lett.*, vol. 112, p. 182502, 2014.

[143] A. Gezerlis *et al. Phys. Rev. Lett.*, vol. 111, p. 032501, 2013.

[144] J. Lynn *et al. Phys. Rev. Lett.*, vol. 113, p. 192501, 2014.

[145] K. Tsukiyama, S. Bogner, and A. Schwenk *Phys. Rev. Lett.*, vol. 106, p. 222502, 2011.

[146] K. Tsukiyama, S. Bogner, and A. Schwenk *Phys. Rev. C*, vol. 85, p. 061304(R), 2012.

[147] S. Bogner *et al. Phys. Rev. Lett.*, vol. 113, p. 142501, 2014.

[148] H. Hergert *et al. Phys. Rev. Lett.*, vol. 110, p. 242501, 2013.

[149] V. Soma *et al. Phys. Rev. C*, vol. 84, p. 064317, 2011.

[150] C. Barbieri and M. Hjorth-Jensen *Phys. Rev. C*, vol. 79, p. 064313, 2009.

[151] V. Soma, C. Barbieri, and T. Duguet *Phys. Rev. C*, vol. 89, p. 024323, 2014.

[152] F. Coester *Nucl. Phys.*, vol. 7, p. 421, 1958.

[153] R. Bartlett and M. Musial *Rev. Mod. Phys.*, vol. 79, p. 291, 2007.

[154] G. Hagen *et al. Prog. Part. Nucl. Phys.*, vol. 77, p. 096302, 2014.

[155] G. Hagen *et al. Phys. Rev. Lett.*, vol. 101, p. 092502, 2008.

[156] S. Binder *et al. Phys. Rev. C*, vol. 88, p. 054319, 2013.

[157] A. Signoracci *et al. Phys. Rev. C*, vol. 91, p. 064320, 2015.

[158] J. Erler *et al. Nature*, vol. 486, p. 509, 2012.

[159] M. Kortelainen *et al. Phys. Rev. C*, vol. 82, p. 024313, 2010.

[160] M. Kortelainen *J. Phys. G: Nucl. Part. Phys*, vol. 42, p. 034021, 2015.

المنارة للاستشارات

[161] B. Gebremariam *et al. Nucl. Phys. A*, vol. 851, p. 17, 2011.

[162] J. Negele and D. Vautherin *Phys. Rev. C*, vol. 5, p. 1472, 1972.

[163] M. Stoitsov *et al. Phys. Rev. C*, vol. 82, p. 054307, 2010.

[164] C. Carlson and R. Schiavilla *Rev. Mod. Phys.*, vol. 70, p. 743, 1998.

[165] I. Towner *Phys. Rep.*, vol. 155, p. 263, 1987.

[166] T. Park *et al. Nucl. Phys. A*, vol. 596, p. 515, 1996.

[167] S. Pastore *et al. Phys. Rev. C*, vol. 87, p. 035503, 2013.

[168] R. Blin-Stoyle *Rev. Mod. Phys.*, vol. 28, p. 75, 1956.

[169] A. Bohr and B. Mottelson, *Nuclear Structure*, vol. 1. Benjamin, New York, 1 ed., 1969.

[170] J. M. Blatt and V. F. Weisskopf, *Theoretical Nuclear Physics*. Dover Publications, 1 ed., 1952.

[171] M. Ross *Phys. Rev.*, vol. 88, p. 935, 1952.

[172] R. Blin-Stoyle *Proc. Phys. Soc.*, vol. A66, 1953.

[173] T. Ericson and W. Weise, *Pions and Nuclei*. Oxford:Clarendon, 1 ed., 1988.

[174] L. Marcucci *et al. Phys. Rev. C*, vol. 72, p. 014001, 2005.

[175] L. Marcucci *et al. Phys. Rev. C*, vol. 78, p. 065501, 2008.

[176] M. Piarulli *et al. Phys. Rev. C*, vol. 87, p. 014006, 2013.

[177] S. Pastore *et al. Phys. Rev. C*, vol. 80, p. 034004, 2009.

[178] L. Marcucci *Few-Body Phys.*, vol. 55, p. 615, 2014.

[179] D. Gazit, S. Quaglioni, and P. Navratil *Phys. Rev. Lett.*, vol. 103, p. 102502, 2009.

[180] S. Beane *et al. Phys. Rev. Lett.*, vol. 113, p. 252001, 2014.

[181] U. Meibner *Nucl. Phys. News*, vol. 24, p. 4, 2014.

[182] S. R. Beane *et al. Phys. Rev. Lett.*, vol. 115, p. 052501, 2015.

[183] J. Friar and J. Negele *Adv. Nucl. Phys.*, p. 219, 1975.

[184] J. Friar, J. Martorell, and D. Sprung *Phys. Rev. A*, vol. 56, p. 4579, 1997.

المنارة للاستشارات

[185] P. Mohr, B. Taylor, and D. Newell *Rev. Mod. Phys.*, vol. 84, p. 1527, 2012.

[186] A. Ong, J. Berengut, and V. Flambaum *Phys. Rev. C*, vol. 82, p. 014320, 2010.

[187] B. Cheal and K. Flanagan *J. Phys. G: Nucl. Part. Phys*, vol. 37, p. 113101, 2010.

[188] A. Herlert *Nucl. Phys. News*, vol. 20, p. 4, 2010.

[189] V. Fedosseev *et al. Rev. Sci. Instrum.*, vol. 83, p. 02A903, 2012.

[190] B. Marsh and others. *Hyper. Int.*, vol. 227, p. 101, 2014.

[191] E. Mane *et al. Eur. Phys. J. A*, vol. 42, p. 503, 2009.

[192] J. Papuga *et al. Phys. Rev. C*, vol. 90, p. 034321, 2014.

[193] M. Miyabe *et al. J. Phys. Soc. Jpn.*, vol. 75, p. 034302, 2006.

[194] A. Gallant *Phys. Rev. Lett.*, vol. 109, p. 032506, 2012.

[195] J. G. Heinrich, "Coverage of error bars for poisson data," p. CDF/MEMO/STATISTICS/PUBLIC/6438, 2003.

[196] R. Kurucz, *Atomic spectral line database.* http://www.cfa.harvard.edu/ampcgi/read_pac, 1995.

[197] R. Brun and F. Rademakers *Nucl. Inst. Meth. A*, vol. 389, p. 81, 1997.

[198] F. James, "Minuit reference manual," *Computing and Networks Division*, vol. Version 94.1, 1994.

[199] C. Gorges *et al. Submitted*, 2015.

[200] A. Martensson-Pendrill *et al. Phys. Rev. A*, vol. 45, p. 4675, 1992.

[201] F. Perrot *et al. Phys. Rev. C*, vol. 74, p. 014313, 2006.

[202] B. Fornal *et al. Phys. Rev. C*, vol. 77, p. 014304, 2008.

[203] F. Arbes *et al. Z. Phys. D.*, vol. 31, p. 27, 1994.

[204] W. Nortershauser *et al. Eur. Phys. J. D*, vol. 2, p. 33, 1998.

[205] E. Brun *et al. Phys. Rev. Lett.*, vol. 9, p. 166, 1962.

[206] A. Arnold *et al. Z. Phys. A*, vol. 314, p. 303, 1983.

المنارة للاستشارات

[207] D. Sundholm and J. Olsen *J. Chem. Phys.*, vol. 98, p. 7152, 1993.

[208] Y. Kai-zhi *et al. Phys. Rev. A*, vol. 70, p. 012506, 2004.

[209] A. Martensson-Pendrill and S. Salomonson *Phys. Rev. A*, vol. 30, p. 712, 1984.

[210] M. Safronova and U. Safronova *Phys. Rev. A*, vol. 83, p. 012503, 2011.

[211] W. H. King, *Isotope Shifts in Atomic Spectra.* Plenum Press. New York and London, 1 ed., 1984.

[212] J. Menéndez, D. Gazit, and A. Schwenk *Phys. Rev. Lett.*, vol. 107, p. 062501, 2011.

[213] P. von Neumann-Cosel, A. Poves, J. Retamosa, and A. Richter *Phys. Lett. B*, vol. 443, p. 1, 1998.

[214] M. Dufour and A. Zuker *Phys. Rev. C*, vol. 54, p. 1641, 1996.

[215] A. Lisetskiy *et al. Phys. Rev. C*, vol. 80, p. 024315, 2009.

[216] A. de Shalit and I. Talmi, *Nuclear Shell Theory.* H S W Massey, 1 ed., 1963.

[217] M. Warda *et al. Phys. Rev. C*, vol. 89, p. 064302, 2014.

[218] G. Hagen *et al. Phys. Rev. C*, vol. 89, p. 014319, 2014.

[219] M. Bender *et al. Rev. Mod. Phys.*, vol. 75, p. 121, 2003.

[220] E. Caurier *et al. Phys. Lett. B*, vol. 522, p. 3, 2001.

[221] I. Talmi *Nucl. Phys. A*, vol. 423, p. 189, 1984.

[222] S. Fayans, S. Tolokonnikov, E. Trykov, and D. Zawischa *Nucl. Phys. A*, vol. 676, p. 49, 2000.

[223] N. Wang and T. Li *Phys. Rev. C (R)*, vol. 88, p. 011301, 2013.

[224] G. Fricke and K. Heilig, *Nuclear Charge Radii.* Springer, 2004.

[225] K. Hebeler *et al. Phys. Rev. C*, vol. 83, p. 031301(R), 2011.

[226] S. Goriely, N. Chamel, and J. M. Pearson *Phys. Rev. C*, vol. 88, p. 024308, Aug 2013.

[227] J.-P. Delaroche *et al. Phys. Rev. C*, vol. 81, p. 014303, Jan 2010.

المنارة للاستشارات

[228] E. Saperstein and S. Tolokonnikov *Phys. Atom. Nucl.*, vol. 74, p. 1277, 2011.

[229] M. L. Bissell *et al. Phys. Rev. Lett.*, vol. 113, p. 052502, Jul 2014.

[230] D. M. Rossi *et al. Phys. Rev. C*, vol. 92, p. 014305, Jul 2015.

[231] P. Lievens *et al. Nucl. Inst. Meth. B*, vol. 70, p. 532, 1992.

[232] D. Rapp and J. Francis *J. Chem. Phys.*, vol. 37, p. 2631, 1962.

[233] L. Vermeeren *et al. J. Phys. B*, vol. 25, p. 1009, 1992.

[234] R. Silverans *et al. Hyp. Int.*, vol. 24, p. 181, 1985.

[235] W. Silfvast, *Laser Fundamentals*. Cambridge University Press, 2 ed., 2008.

[236] C. Foot. Atomic Physics (Oxford University Press), 1 ed., 2005.

[237] D. Yordanov *PhD thesis*, vol. KULeuven, 2007.

[238] L. Vermeeren *Hyper. Int.*, vol. 61, p. 1399, 1990.

[239] P. Lievens *et al. Phys. Lett. B*, vol. 256, p. 141, 1991.

[240] R. Bruckmeier, C. WQunderlich, and H. Figger *Phys. Rev. A*, vol. 52, p. 334, 1995.

[241] D. Dewangan *J. Phys. B*, vol. 6, p. L20, 1973.

[242] NIST, "Atomic spectra database levels data," *http://physics.nist.gov/*.

[243] F. Wienholtz *Private communication*, 2013.

[244] P. Mantica *et al. Phys. Rev. C*, vol. 77, p. 014313, 2008.

[245] J. Papuga *et al. Phys. Rev. Lett.*, vol. 110, p. 172503, 2013.

[246] J. Papuga *et al. Phys. Rev. C*, vol. 90, p. 034321, 2013.

[247] M. L. Vestal *et al. Rev. Sci. Instrum.*, vol. 47, p. 15, 1976.

[248] B. Paszkowski, *Electron Optics*. Elsevier, New york, 1 ed., 1968.

[249] Y. Ishii *et al. Nucl. Inst. Meth. B*, vol. 181, p. 71, 2001.

[250] Y. Ishii *et al. Nucl. Inst. Meth. B*, vol. 269, p. 2193, 2011.

[251] I. S. Board, "Ieee recommended practices for safety in high-voltage and high-power testing," vol. IEEE Std 510-1983, 1992.

المنارة للاستشارات

[252] P. development and implementation. Essential Energy, "Electrical safety rules," vol. Issue 11, 2012.

[253] F. Wenander *et al. Nucl. Inst. Meth. B*, vol. 204, p. 261, 2003.

[254] W. Geithner. PhD Thesis, Johannes Gutenberg-Universität Mainz, 2002.

[255] R. Silverans *Phys. Rev. Lett.*, vol. 60, p. 2607, 1988.

[256] R. Neugart, W. Klempt, and K. Wendt *Nucl. Inst. Meth. B*, vol. 17, p. 354, 1986.

[257] E. Nacher *et al. Phys. Rev. Lett.*, vol. 92, pp. 232501–1, 2004.

[258] A. Mueller *et al. Nucl. Phys A*, vol. 403, p. 234, 1983.

[259] P. Butler and W. W. Nazarewicz *Rev. Mod. Phys.*, vol. 68, p. 349, 1996.

[260] L. Wansbeek *et al. Phys. Rev. C*, vol. 86, p. 015503, 2012.

[261] P. Goddard *et al. Phys. Rev. Lett.*, vol. 110, p. 032503, 2013.

[262] K. Kreim *PhD Thesis*, pp. MP–IK, 2013.

[263] N. Bendali *J. Phys. Bs*, vol. 19, p. 233, 1986.

[264] R. Aydin, W. Ertmer, and U. Johann *Z. Phys. A*, vol. 306, p. 1, 1982.

[265] J. Benhelm *et al. Phys. Rev. A*, vol. 75, p. 032506, 2007.

[266] T. Minamisono *et al. Z. Naturforsch*, vol. 57a, p. 595, 2002.

[267] A. Arima and H. Horie *Prog. Theor. Phys.*, vol. 12, p. 623, 1954.

[268] I. Talmi *J. Phys. Conf.*, vol. 20, p. 28, 2005.

[269] R. Lawson, *Theory of the nuclear shell model*. Oxford Science Publications, 1 ed., 1980.

[270] C. Levinson and K. Ford *Phys. Rev.*, vol. 99, p. 792, 1955.

المنارة للاستشارات

المنارة للاستشارات

FACULTY OF SCIENCE
DEPARTMENT OF PHYSICS AND ASTRONOMY
INSTITUTE FOR NUCLEAR AND RADIATION PHYSICS
Celestijnenlaan 200A box 2402
3001 Leuven
RonaldFernando.GarciaRuiz@fys.kuleuven.be